Dissertation zur Erlangung des Doktorgrades der Fakultät Chemie und Pharmazie
der Ludwig-Maximilians-Universtität München

The Sweet Side of the Membrane

Sugars in Biophysics, Bacterial Adhesion, and siRNA Delivery

Leonhard Karl Robert Möckl

aus

München

2015

Erkärung
Diese Dissertation wurde im Sinne von §7 der Promotionsordnung vom 28. November 2011 von Herrn Prof. Dr. Christoph Bräuchle betreut.

Eidesstattliche Versicherung
Diese Dissertation wurde eigenständig und ohne unerlaubte Hilfe erarbeitet.

München, den _____

Leonhard Möckl

Dissertation eingereicht am	01.12.2015
Erstgutachter	Prof. Dr. Christoph Bräuchle
Zweitgutachter	Prof. Dr. Thisbe K. Lindhorst
Mündliche Prüfung am	18.12.2015

Summary

This work deals with four main topics: The influence of the glycosylation of membrane proteins onto their spatiotemporal dynamics; the adhesion of bacteria to human cells; the uptake mechanism of targeted siRNA into neuronal cells; and the effect of the endothelial glycocalyx onto nanoparticle uptake.
Using metabolic labeling and high-resolution live-cell microscopy, we show that two classes of membrane glycoproteins, namely sialic acid-bearing proteins and mucin-type proteins, differ in their spatiotemporal dynamics due to different engagement into the galectin lattice. The galectin lattice is a supramolecular network that consists of the carbohydrate binding galectins and mucin-type proteins that are interconnected by them. This decreases both the spatial mobility and the turnover rate of mucin-type proteins in comparison to sialic acid-bearing proteins which are not interconnected by galectins. Furthermore, we present a straightforward method by which the spatiotemporal mobilities of membrane glycoproteins can be artificially tuned in an exact way.
Regarding bacterial adhesion, we report on a method to switch the adhesion of *E. coli* to the membrane of living cells. This is achieved by controlling the orientation of mannose, the ligand to which the bacteria bind, via a photoswitchable azobenzene. We also show that the properties of inhibitors of *E. coli* adhesion are drastically affected by shear stress and strongly differ from the properties determined under static conditions.
We further investigated how nanoparticle uptake by live endothelial cells is altered by the presence or absence of the endothelial glycocalyx. Therefore, we employed two model nanoparticle types, aminated and carboxylated ones. The first were shown to be toxic when internalized, whereas the latter were found to be inert. We reveal a clear protection effect of the endothelial glycocalyx against uptake of both types of nanoparticles. Experiments to analyze a possible link between the reduced uptake to a lower mortality are underway.

Finally, we present a detailed analysis of the uptake mechanism of siRNA targeted to the cannabinoid receptor system by the anandamide ligand and to glucose transporters by glucose. For the anandamid-modified siRNA, we show that the internalization is efficient and receptor-specific. This was proven for model neuronal cells, neuronal stem cells, and *in vivo* in a murine model. For the glucose-modified siRNA, we report on very high transfection efficiency for multiple cell lines and on the uptake mechanism.

Contents

1 Introduction

One of the main topics of this work is protein glycosylation and the glycosylation of membrane proteins in particular. Even though it has been known for a long time that almost every protein is glycosylated,[1,2] many aspects of this modification have not been elucidated. Especially, the enormous complexity of membrane protein glycosylation is still a mystery: Cells install a vast amount of sugars on their surface,[3,4] constituting the so called glycocalyx, by using numerous biosynthetic pathways and, of course, lot of energy. For some specific mutations, functional implications have been found,[5,6] however, a definitive explanation why the cell affords this has not been found so far.[7]

The main reason is the extraordinary variability of glycan structures. In contrast to DNA, RNA, and proteins, where one DNA sequence codes for exactly one RNA sequence and is eventually translated into exactly one protein,[8] sugar structures on proteins seem to be much less regulated. On different copies of one and the same protein, usually much more than one glycosylation pattern is found.[3,9] It is not clear what governs this difference, if it is governed at all and not stochastic. However, despite this "fuzzy" nature of protein glycosylation, it is not arbitrary. If strong - whereat "strong" is, again, not well defined - deviations occur, the consequences are often severe.[10] To make things even more complicated, there are also examples for the opposite case: Here, if a glycan is just slightly compromised, the cell reacts very sensitive to it.[11] Taken together, one can rightly state that for glycosylation, the link between structure and function is yet to be unraveled.

Various strategies are pursued to find an answer to this puzzle. For example, glycan profiling uses mass spectrometry to characterize glycosylation patterns on healthy as well as on e.g. cancer cells. Then, they are compared in order to find possible implications of different glycosylation patterns in a disease-related context; and great progress was made in this field.[12–14]

In this thesis, we pursue a different approach which is described in Chapter 6 and Chapter 7. We decided to investigate the relation between protein glycosylation and protein properties on a basic, biophysical level. For this, we specifically marked two classes of membrane proteins, sialic acid-bearing proteins and mucin-type proteins, by metabolic labeling, and investigated their behavior using different high resolution microscopy techniques. This allowed us to show that mucin-type proteins exhibit less spatiotemporal dynamics than sialic acid-bearing proteins due to their engagement into the so called galectin lattice. In a further step, we employed the specific labeling of glycan structures on proteins to artificially tune the spatiotemporal dynamics of the proteins.

Furthermore, a protective role is commonly assigned to the glycocalyx. It is pictured as some kind of barrier that keeps, for example, pathogens away from the cell surface, preventing infection.[15,16] In this context, we wanted to investigate the role of the glycocalyx in shielding the cell against nanoparticles. This is an important feature to be elucidated since the amount of nanosized matter in the environment increases steadily and numerous investigations claim that, with decreasing size, particles start to exhibit toxicity.[17–19] This so called nanotoxicity is likely to gain significance. Therefore, the response of cells when subjected to nanosized matter and the natural defense mechanisms need to be analyzed in order to evaluate the toxicity of nanoparticles correctly. Since the glycocalyx constitutes the interface between the cell and the exterior, the assumption seems reasonable that it plays a role in nanoparticle entry. In our experiments, we turned to a defined setting employing model endothelial cells and well-characterized model nanoparticles. Indeed, we could show that the glycocalyx protects the cell from the entry of both toxic and inert nanoparticles.

Another central topic of this thesis deals with the adhesion of *E. coli* to endothelial cells. The process of adhesion is highly important in the development of nearly all diseases caused by bacteria, often constituting the first step of the course of the disease.[20,21] Although many properties of bacterial adhesion are known, a more detailed understanding of the process is desirable. Thus, we focused on two main questions.

First, we wanted to investigate whether one can influence the adhesion of bacteria by changing the properties of the cell surface. This is possible on artificial substrates,[22] but, so far, it was not shown on live cell membranes. It turned out that, by metabolic glycoprotein engineering and incorporation of photoswitchable ligands for bacterial adhesion, we were able to increase and decrease bacterial adhesion dependent on the

orientation of the ligand. We are convinced that this will have an effect on how we judge the interaction between proteins and the cell membrane, e.g. as in our experiment between a bacterial adhesion protein and its ligand. So far, these interactions are analyzed from an electrostatic and entropic point of view. "Crude" factors like the orientation have not been in the focus of research.
We were also interested in the influence of shear flow on the properties of adhesion inhibitors. We regard this as a relevant question since antiadhesion therapy is a promising strategy to fight bacterial infections when antibiotics are not available or ineffective.[23–25] This problem is likely to increase due to the increasing number of resistant bacterial strains.[26–28] Therefore, it is important to investigate how inhibitors perform under physiological conditions. Since almost no process in a living system is truly static, the impact of shear flow on bacterial adhesion is a major aspect to be analyzed.[29,30] Here, we could show that the potency of adhesion inhibitors is strongly increased under flow conditions and, hence, underestimated under static conditions.
Finally, we investigated siRNA delivery via two targeting moieties, anandamide and glucose. We were interested in a highly specific delivery to neuronal cell in case of anandamide and in a general delivery to many different cell lines in case of glucose. The underlying idea is to use the anandamide modification[31,32] to deliver siRNA to an exact location in the body, namely to neurons and cells of the nervous system where the cannabinoid receptors are highly expressed, e.g. for gene or cancer therapy.[33,34] For the glucose modification of siRNA, we wanted to show that is a mild method to deliver any siRNA to cells. In both cases, we could verify that the targeting fulfills the requirements by dissecting the uptake mechanisms.
Taken together, the investigations presented in this thesis, all connected to sugars and the cell membrane, underline the importance of protein glycosylation for fundamental cellular processes. They point out how this key modification can be used for therapeutically relevant problems.

2 Membrane Protein Glycosylation and its Relevance in Cell Biology

2.1 Protein Glycosylation

2.1.1 Posttranslational Modification of Proteins

According to the central dogma of molecular biology, the genetic information encoded on the DNA is transcribed to messenger RNA (mRNA) which is translated to proteins.[8] The remarkable complexity of proteins is often explained by expansion of single building blocks from four nucleobases in case of DNA and mRNA to the 21 amino acids in case of proteins.[A] For example, there are $4^5 = 1024$ DNA or mRNA sequences, but $21^5 = 4084101$ (about 4000 times more) amino acid sequences of length 5. Considering that proteins are built of hundreds to thousands of amino acids, the number of possible sequences is enormous.

However, the variety of proteins is not only based on the sheer number of accessible sequences, but also on alterations that are enzymatically added during or after the protein was translated, so called posttranslational modifications.[36] Generally, a posttranslational modification is the covalent attachment of some chemical residue to the side chain of an amino acid or to the C- or N-terminus.[37] This way, the repertoire of the amino acids is expanded. Despite the fact that only few amino acids within a protein are modified and not all, the posttranslational modifications often drastically influence the functionality of a protein. In fact, for many cases it is true that the behavior of a protein is completely determined by the presence of the posttranslational modification.[38,39]

[A] Humans use the 20 canonic amino acids and selenocystein which was discovered rather late to be a part of the proteinogenic amino acids.[35]

Important examples for posttranslational modifications include:

- **Phosphorylation** is one of the most abundant posttranslational modifications.[40,41] It adds the phosphate group PO_4^{3-} to a serine, threonine, or tyrosine by so called kinases. Rarely, it can also be found on histidine, arginine, lysine, glutamate, and aspartate.
  Protein phosphorylation is a key modification with regard to cellular signaling.[42] Importantly, the addition is reversible so that the phosphate group can easily be cleaved again by phosphatases. Often, addition and cleaving of phosphate groups leads to "switching" of of a protein, turning it on or off.[43,44] Examples include G-protein coupled receptors, receptor tyrosine kinases, and epidermal growth factors: They all are controlled via phosphorylation and dephosphorylation of signaling domains and small transmitting molecules.[45]

- **Acetylation** is the reversible transfer of an acetyl group to a protein, typically on lysine residues.[46] Just as phosphorylation, it plays a central role for the regulation of protein activity. It is very prominent on the N-terminus of proteins – in humans, 85% of all proteins are acetylated there.[47] It is also crucial for the regulation of DNA transcription: DNA is wrapped around special proteins, the histones. If they are acetylated, the DNA is loosened, facilitating to start the synthesis of mRNA. Of course, the acetylation and deacetylation of histones is therefore highly regulated to avoid erroneous DNA transcription.[48,49]

- **Methylation** plays, amongst others, a very important role in epigenetics. In this case, it is not a modification of proteins, but of DNA itself typically at CpG sites, leading to the conversion of cytosine to 5-methylcytosine, which regulates transcriptional activity.[50] Methylation also occurs as posttranslational modification on protein. Usually, ariginine and lysine are the targets.[51,52] Again, like for acetylation, methylation of histones influences DNA transcription. However, in contrast to acetylation, methylation represses transcription, although it may also indirectly activate it by downregulation of transcription inhibitors.

- **ADP-ribosylation** introduces one or more ADP-ribose groups to an amine-bearing side chain of a protein like arginine with the help of the redox cofactor NAD^+.[53] The modification highly influences cellular functions related to DNA transcription and DNA repair. For example, when the cell undergoes high stress, the poly-(ADP-ribose) polymerases are upregulated, leading to increased poly-ADP-

ribosylation of proteins and depletion of NAD^+. Caspases are activated and cleave the poly-(ADP-ribose) polymerases. One fragment of the cleaved polymerases is translocated to the nucleus where it presumably acts as transcription activator for apopototic proteins and/or autoimmune targets.[54] Also, the high poisonousness of many bacterial toxins originates from erroneous ADP-ribosylation, causing e.g. cholera, diphtheria, and whooping cough.[55]

- **Ubiquitin** is a small, highly conserved globular protein of 76 amino acids with a mass of 8.5 kDa. It can be transferred to lysine residues of other proteins and is hence an example of posttranslational protein modification with another protein.[56,57] The most prominent example of ubiquitination is presumably polyubiquitination. Here, a chain of several ubiquitins linked to each other is attached to the target protein. This is a signal for the proteasome to degrade the protein, e.g. because it is not correctly folded.[58] Other tasks of ubiquitination include signal transduction and cell-cycle control.[59–61]

These are just a few examples for posttranslational modifications, and much more exist. However, in the following, we would like to single out one specific posttranslational modification since most of this thesis is somehow related to it: Glycosylation of proteins, and especially of membrane proteins.

2.1.2 Glycosylation Pathways of N- and O-Glycans

There are two major groups of glycans: N-glycans and O-glycans. As the name suggests, N-glycans are attached to the respective proteins via an N-glycosidic bond to asparagine residues whereas O-glycans are attached via an O-glycosidic bond to an oxygen atom in the amino acid sequence. The oxygen atom is provided by serine or thereonine. In the following, the central biosynthetic aspects of these two glycan classes will be shown.

N-glycans

N-glycans are attached to the protein via an asparagine which is part of the consensus sequence Asn-X-Ser/Thr where X denotes any amino acid except proline. Sometimes, N-glycans are also found at the sequence Asn-X-Cys.[62] However, not every consensus sequence is modified – in fact, up to now, it is not understood under which conditions

exactly an Asn-X-Ser/Thr sequence receives a glycan. There are examples for identical proteins where some carry a glycosylation and some do not at the same position. Nevertheless, predictions can be made. For example, if the sequence is buried inside the protein, glycosylation is very unlikely.[63]

In animals, N-acetylglucosamin (GlcNAc) in β-configuration is the sugar that almost exclusively follows asparagine. N-linked glycans feature a quite unique biosynthetic pathway. It starts with the synthesis of a precursor glycan on the cytosolic side and in the lumen of the endoplasmic reticulum (ER) on a dolichol molecule in the ER membrane. For this, phosphorylated GlcNAc from UDP-GlcNAc is added to dolichol phosphate (Dol-P) which generates Dol-P-P-GlcNAc on the cytosolic side. Subsequently, fourteen sugars are added. During the process, the precursor is flipped to the lumenal side of the ER, a process not yet understood in detail. Then, the precursor is transferred *en bloc* to the protein to be modified by a multimeric protein complex (oligosaccharyltransferase).[64] This is schematically depicted in Figure 2.1.

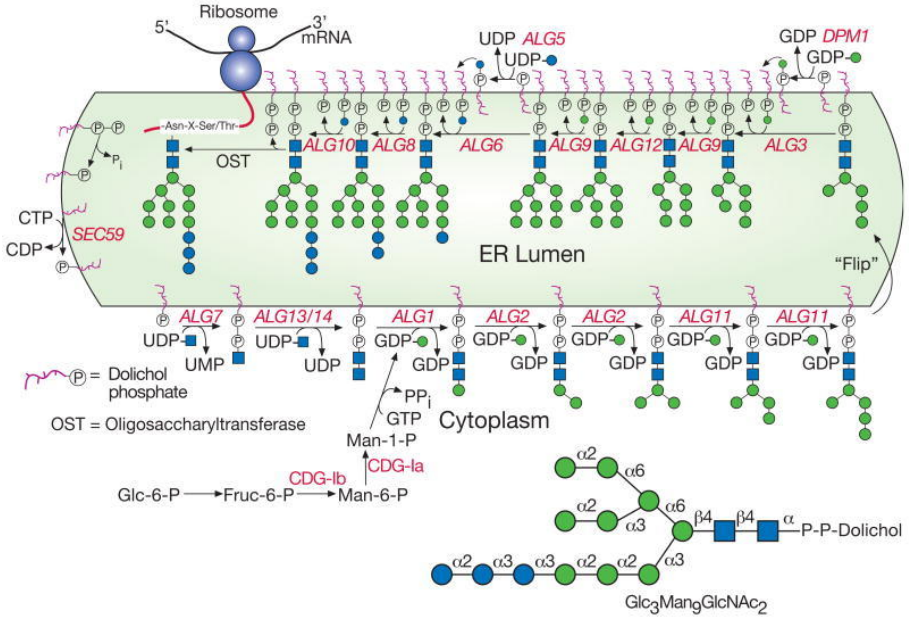

Figure 2.1: ER-associated steps in N-glycan synthesis
First, GlcNAc-P is added to Dol-P via ALG7. Then, fourteen sugar residues are added by different members of the ALG proteins. During the process, the precursor is flipped from the cytosolic to the lumenal side of the ER. After finishing the precursor synthesis, the whole glycan is transferred to the protein. The final structure of the precursor ($Glc_3Man_9GlcNAc_2$ is shown at the bottom. cf. Figure 12.1 for the key to the sugar symbols. Figure taken from reference[65]

After this, the early glycan is processed.[66,67] The first step is the removal of two glucose residues, changing $Glc_3Man_9GlcNAc$ to $GlcMan_9GlcNAc$. This is important for the quality control of protein folding and will be discussed in detail in Chapter 2.1.3. Often, additionally one mannose residue is cleaved, yielding $GlcMan_8GlcNAc$. Correctly folded proteins are transported to the Golgi apparatus where further modifications are applied. They are manifold but all include the removal of several mannose groups and the addition of one or more GalNAc residues to yield, for instance $Man_5GlcNAc_2$. The final structures of N-glycans after the processing steps are very diverse, but they all share a common sugar sequence ($Man_3GlcNAc_2$) and can be categorized into three different classes, dependent on the modification type.[65] They are depicted in Figure 2.2.

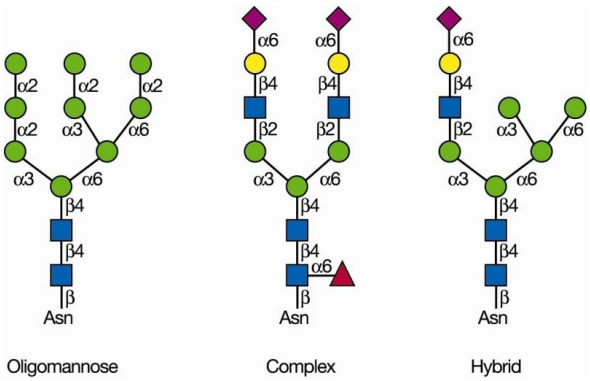

Figure 2.2: The three classes of N-glycans
Although their structural diversity is high, all N-glycans share the $Man_3GlcNAc_2$ core and can be divided into the oligomannose, the complex, and the hybrid type, dependent on the structure of the modifications that were attached during processing. Figure taken from reference[65]

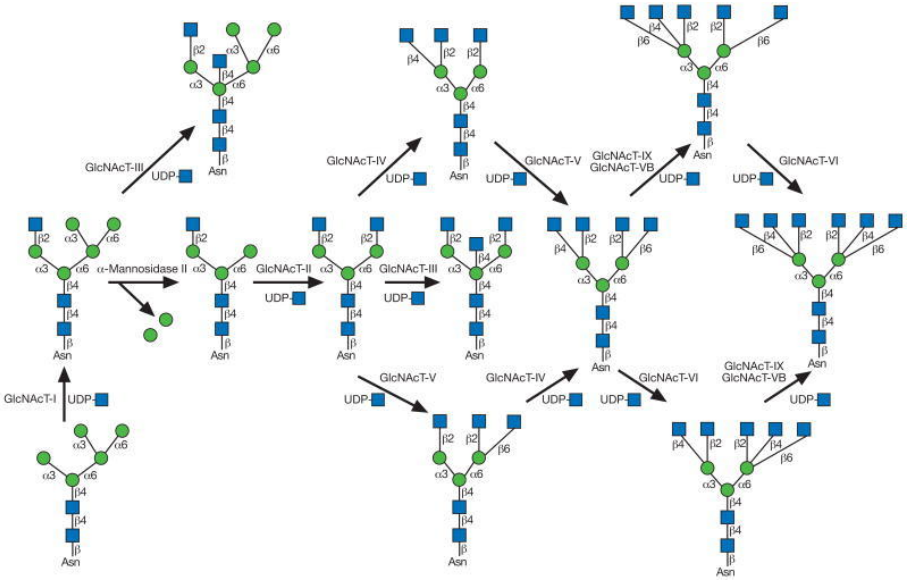

Figure 2.3: Branching of N-glycans
Multiple GlcNAc residues can be attached to the terminal mannoses of the core structure of hybrid and complex N-glycans, leading to branching of the N-glycans. These modifications depend strongly on the nutrient state of the cell and play a key role in, for example, receptor homeostasis. Figure taken from reference[65]

After completion of the processing steps, N-glycans are usually transported to the plasma membrane. It would exceed the scope of this introduction to cover even a small fraction of the various structures of N-glycans that can be found on proteins. Amongst others, branching of complex N-glycans as depicted in Figure 2.3 is highly dependent on the nutrient state of the cell and plays a central role in receptor homeostasis. This will be discussed in more detail in Chapter 2.1.4. Other ways of processing include, for example, the modification of the common core structures, the addition of sialic acids and other sugar residues to the glycan termini, and other elongations of the glycan antennae. All those alterations play important roles for the function and behavior of the modified protein, and there is a continuously growing amount of findings underlining this.[68,69]

O-glycans

O-glycosylation refers to the covalent attachment of a glycan structure to a serine or threonine residue. Amongst them, the most prominent representatives are the mucin-type O-linked glycans where an *N*-acetylgalactosamine (GalNAc) is α-linked to the OH-group of serine or threonine; but also other sugars can be used for O-glycosylation like mannose, galactose, fucose, or xylose.[69] However, in this chapter we will discuss mucin-type O-glycans because they are important representatives of the group. Furthermore, in the later described experiments we will refer to them.

At a first glance, one may suspect to find similarities between O- and N-glycosylation, but, in fact, the two processes strongly differ. First, in contrast to N-glycans, no consensus sequence for O-glycosylation has so far been identified, and the variety of sequences that is modified via O-glycosylation indicates that some amino acids are just preferred in comparison to others. For example, the vicinity of proline seems to increase O-glycosylation whereas charged amino acids are not favorable.[70]

If the OH-group of a serine or threonine is to be mucin-type O-glycosylated, the biosynthesis starts with the transfer of *N*-acetylgalactosamine from UDP-GalNAc by the enzyme polypeptide-N-acetyl-galactosaminyltransferase (ppGalNAcT). Again in contrast to N-glycosylation, the synthesis does not take place in the ER, but from the very beginning in the Golgi apparatus. Also, it does require neither a dolichol-precursor nor glycosidases that trim or process an already synthesized glycan. Importantly, the positioning of ppGalNAcT inside the Golgi apparatus strongly affects the resulting glycan structure. Roughly, the later a ppGalNAcT acts on the protein, the shorter the resulting mucin-type O-glycan will be.[71]

After the transfer of GalNAc, the synthesis continues. Once more different from N-glycosylation, the core structure common to *all* O-glycans is finished with the attachment of GalNAc. Afterwards, the synthesis routes diverge, giving rise to eight different core structures (Table 2.1 and Figure 2.4).[72] Figure 2.5 shows the stepwise synthesis of the core 1 and core 2 structure and the required enzymes as an example.

These core structures are not equally installed within all tissue types. Different glycosyltransferases are differently up- and downregulated throughout the organism, tuning the type of core structure synthesized.[69] However, the first attached sugar GalNAc only is typically not found in healthy cells, but often in tumors, suggesting that the extension and branching of O-glycans is likely to be abolished in certain cancer cells.[73] Synthesis of different O-glycan structures is mainly controlled by the affinities of the

Table 2.1: Core structures of mucin-type O-glycans

Core	Structure
Core 1 (T antigen)	Galβ1-3GalNAcαSer/Thr
Core 2	GlcNAcβ1-6(Galβ1-3)GalNAcαSer/Thr
Core 3	GlcNAcβ1-3GalNAcαSer/Thr
Core 4	GlcNAcβ1-6(GlcNAcβ1-3)GalNAcαSer/Thr
Core 5	GalNAcα1-3GalNAcαSer/Thr
Core 6	GlcNAcβ1-6GalNAcαSer/Thr
Core 7	GalNAcα1-6GalNAcαSer/Thr
Core 8	Galα1-3GalNAcαSer/Thr
Tn antigen	GalNAcαSer/Thr
Sialyl-Tn-antigen	Siaα2-6GalNAcαSer/Thr

glycosyltransferases to the substrates.[74,75] For example, in Figure 2.5 one can see that from the core 1 structure a *N*-acetylglucosamine can be attached by 2GnT or by β3GlcNAcT-3. As soon as the glycosyltransferase C2GnT has acted on the core 1 structure, β3GlcNAcT-3 cannot attach a second *N*-acetylglucosamine. Furthermore, as mentioned above, the localization of the glycosyltransferases within the Golgi apparatus limits the time they can act on the protein, roughly determining the size of the attached glycans. Other control types include classical cofactors like metal ions.[76]

2.1.3 Functions Classically Attributed to Protein Glycosylation

Although the importance of protein glycosylation is becoming clearer now, some functions were already attributed to glycosylation for a long time. In this section, we will highlight three of the most well-known tasks ascribed: Quality control during protein folding, increasing of solubility, and blood group determination.

Quality control during protein folding
Although the central dogma of molecular biology is usually termed as "DNA is transcribed to mRNA which is translated to proteins", it is often claimed that it should be expanded to "DNA is transcribed to mRNA which is translated to an amino acid chain which is folded to a protein".[77] This is to highlight the significance of protein folding

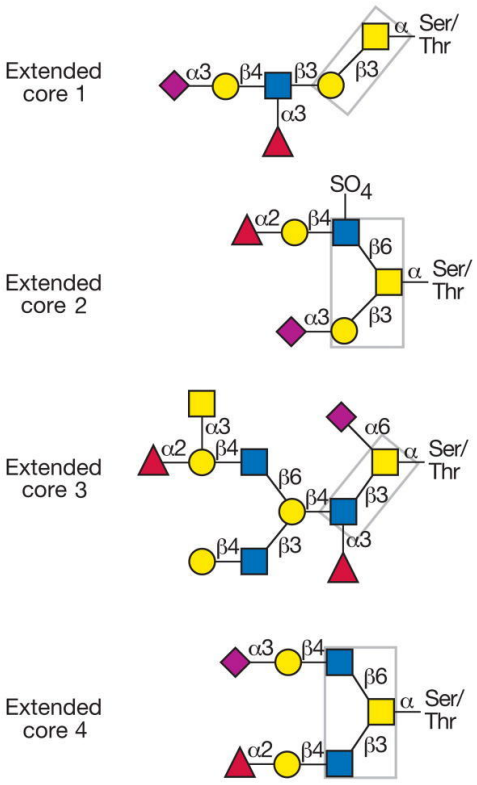

Figure 2.4: Four examples for mucin-type O-glycan cores
The respective core structure is highlighted with a gray box. For each core, a typical extension is depicted. Figure adapted from reference[65]

since without proper folding, the amino acid chain is not functional and, even worse, will tend to associate with other misfolded amino acid chains into possibly dangerous aggregates.[78,79] Therefore, in all higher organisms, sophisticated methods exist to fold amino acid chains correctly on the one hand and to detect and degrade misfolded amino acid chains on the other hand.[80,81] Here, protein glycosylation plays a very important role by regulating the calnexin-calreticulin cycle.[82] Among the many processes related to folding quality control, it is maybe the most important one.
The two chaperones calnexin and calreticulin bind to proteins that contain a single N-linked α-linked glucose residue. As it was described above, the core structure common to every newly synthesized N-glycan contains such a single α-linked glucose at the end of the ER-localized part of the synthesis. Therefore, they bind to calnexin/calreticulin and folding begins. When the last glucose residue is removed, the protein cannot bind to the calnexin-calreticulin complex anymore. If the protein was correctly folded, it is

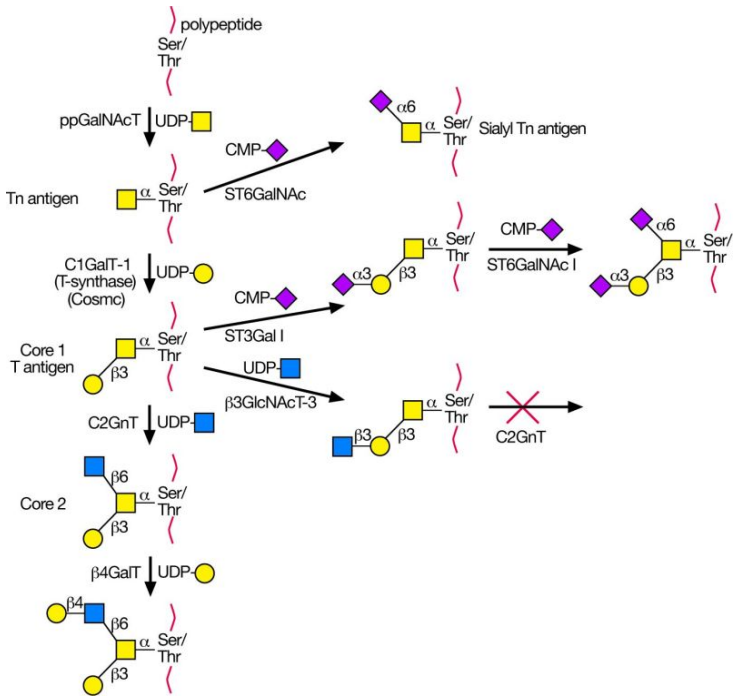

Figure 2.5: Synthesis and modification of core 1 and core 2 structures.
After the transfer of GalNAc to an OH-group of serine or threonine, the Tn antigen is obtained. This can be sialylated (both the Tn and the sialyl-Tn are common in cancer cells) or modified by galactose to yield the core 1 structure. From there, several modifications can be introduced. If an *N*-acetylglucosamine is added to the initial GalNAc via a $\beta 6$-linkage, the core 2 structure is obtained which can also be further modified. Note that two possibilities exist to add *N*-acetylglucosamine to the core 1 structure which mutually exclude each other. Figure taken from reference[65]

transported from the ER, where the N-glycan synthesis started, to the Golgi apparatus. However, if a problem occurred during folding, the incompletely folded protein is reglycosylated, again binds to calnexin and calreticulin which will try to fold the protein once more. If the protein is still misfolded after some time, the cleaving of mannose groups begins. This indicates that the protein is irreparably misfolded (so called "mannose removal clock"). In this case, the protein is exported to the cytosol and degraded by the proteasome.[83] The whole process is sketched in Figure 2.6.

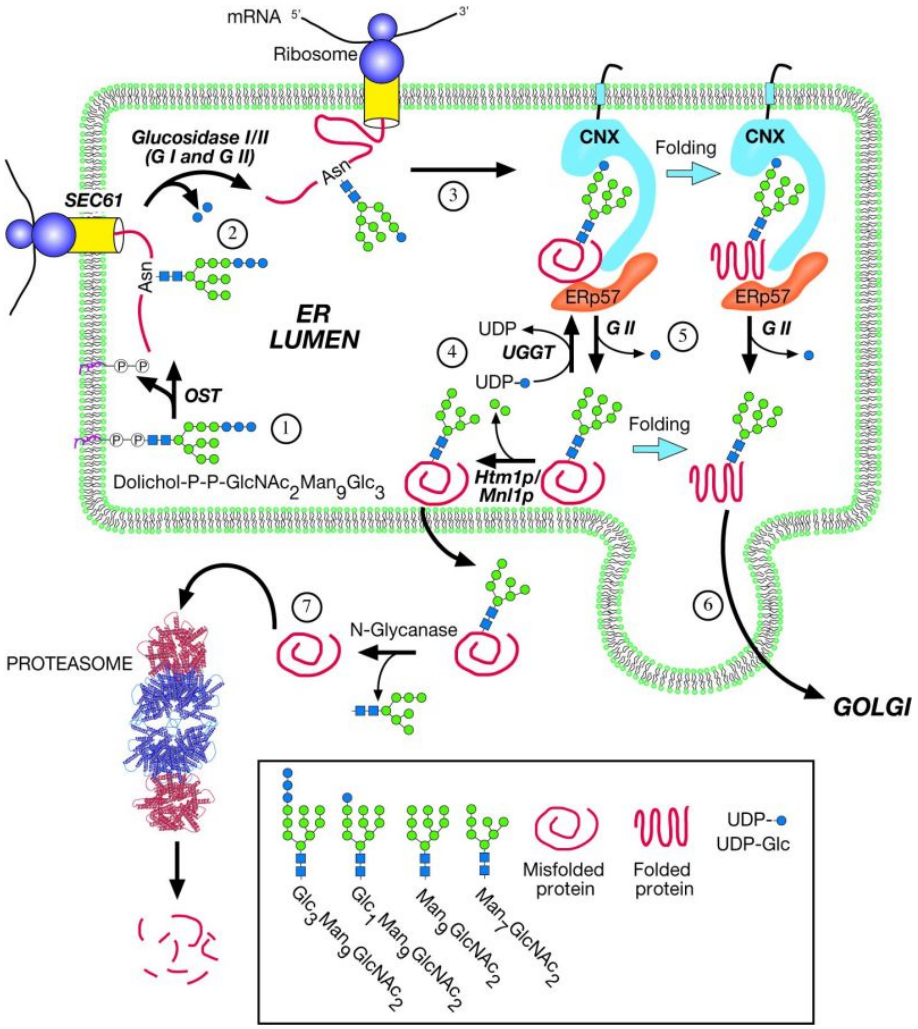

Figure 2.6: Quality control of protein folding.
Newly synthesized N-glycans are located in the ER where they are N-glycosylated with $Glc_3Man_9GlcNAc_2$. In the ER, also the first two steps of trimming of the glycan take place, i.e. the removal of two glucose units. One glucose residue is retained which, therefore, is recognized by calnexin/calreticulin. If the protein is correctly folded, it is exported to the Golgi apparatus. However, if not, the misfolded protein is reglycosylated and enters the calnexin/calreticulin cycle one more. If it stays misfolded, mannose groups are removed which is a signal for export of the misfolded protein to the cytosol where the rest of the N-glycan is removed and the amino acid chain is degraded by the proteasome. Figure taken from reference[65]

Protein solubility

Sugar molecules are hydrophilic structures and hence located at the outer, hydrophilic areas of a folded protein and not on the hydrophobic core. Therefore, it was early assumed that glycosylation helps folding and increases protein solubility,[84] either by reducing the free energy of the folded state or by increasing the free energy of the unfolded state as schematically depicted in Figure 2.7. This is an obvious idea since the folding of a protein is determined by the energy landscape of all the conformational states of the amino acid chain[85] which is in turn defined by the features of the amino acid chain. Here, it is fair to assume that glycosylation will play a role.

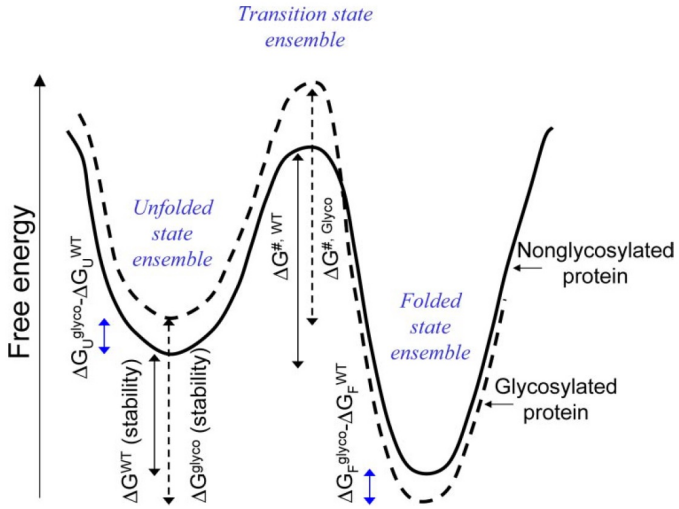

Figure 2.7: Free-energy profile of a glycosylated and non-glycosylated protein. Intuitively, a protein should be stablilized by glycosylation, either by destabilizing the unfolded state ($\Delta G^{Glyco} - \Delta G^{WT} > 0$) or by stabilizing the folded state ($\Delta G_F^{Glyco} - \Delta G_F^{WT} < 0$). Figure taken from reference[86]

However, the experimental verification is not trivial. Protein folding itself is far from being completely understood. Although all proteins (or protein subunits) are in the end made up by one amino acid chain, some of them collapse into their folded state at once, others domainwise, and again others seem to mix these ways.[87–89] It is hence not easy to single out the effect of glycosylation on the process of folding. Nevertheless, progress has been made in the last years. As an example, a recent investigation[86] using theoretical calculations should be discussed briefly.

In this study, the folding of the SH3 domain was calculated in dependence on its glycosylation state. Although SH3 is naturally not glycosylated, it is a good starting point since its folding mechanism has been extensively studied: SH3 has a size of only 56 amino acids which makes its folding path easier to access than in case of a large protein. One of the key results of this investigation is depicted in Figure 2.8.

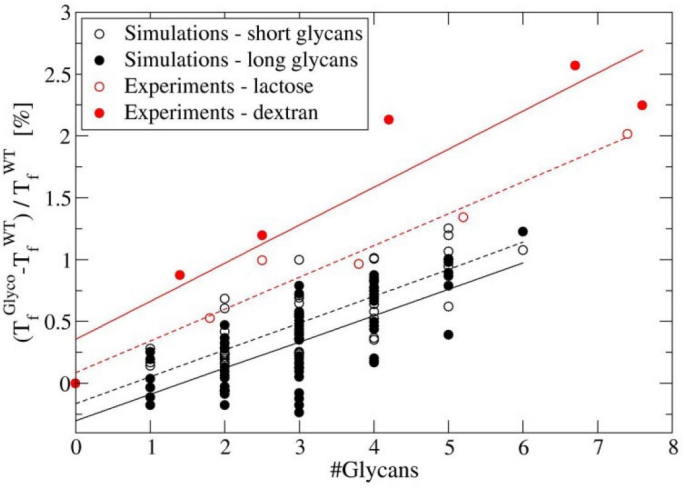

Figure 2.8: Influence of glycosylation on the folding temperature of SH3.
With increasing amounts of both short and long glycans (empty and filled circles) on the protein, the folding temperature T_f^{Glyco} increases. Experimental measurements (red circles) show good agreement. Figure taken from reference[86]

As it can be seen, adding more and more short and long glycans to the formerly not glycosylated wild-type (WT) SH3 protein leads to an increase in the folding temperature T_f^{Glyco} (i.e. the temperature at which the protein folds when being cooled down from a heat-unfolded state) which is given in relation to the folding temperature of the WT protein, T_f^{WT}. With six glycans attached (short, empty circles; and long, filled circles), the folding temperature increases by about 1%. This change may seem small, but one should consider that usually the stabilizing forces, keeping the protein folded, are just a little bit larger than the destabilizing forces that try to unfold the protein.[90] A change of 1% is hence remarkable. Moreover, a comparison with experimental data of two other studies[91,92] (red empty and filled circles), where glycans of similar sizes were attached to proteins, shows that the experimental values agree nicely with the simulated ones.

Blood group determination

A lot of ways to categorize blood groups exist, but the ABO-system is the most important and, as well, the oldest. It was established around 1900 by Karl Landsteiner.[93] He observed that blood of different patients might agglutinate when mixed. This was of course of high relevance for blood transfusions as any agglutination inside blood vessels has severe, often lethal consequences. Subsequently, four blood groups were established – A, B, AB, and O. It was found that blood group O only allows O as donor, A allows O and A, B allows O and B, and AB finally allows O, A, B, and AB. The reason for this remained a mystery for long time. It took around 60 years until the underlying biochemistry was elucidated: The reason for the different blood groups are glycans on the red blood cells.[94] They are depicted in Figure 2.9.

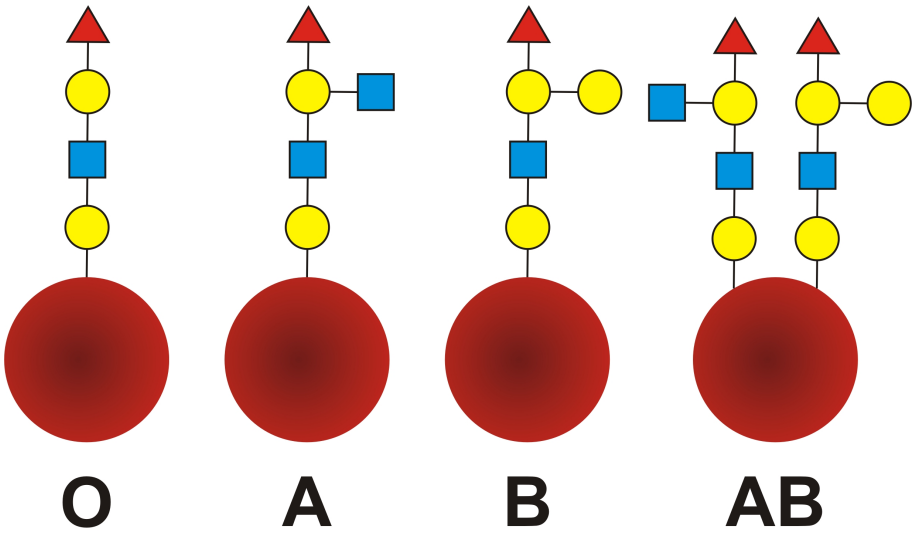

Figure 2.9: The four blood groups in the ABO-system
Sugar structures on red blood cells that give rise to the four different blood groups O, A, B, and AB.

In the blood plasma, antibodies against the glycan structure that is *not* found on the respective blood cells are present as listed in Table 2.2. If a patient with blood group O would receive, for example, blood of group A, the anti-A antibodies in her plasma would bind to the presented A-antigens on the foreign blood, causing agglutination. Therefore, she may only receive blood group O, but since there are no antigens on her blood, she can donate to anyone. On the other hand, a patient with blood group AB has no antibodies in her body, and therefore, can receive blood of any blood group. Be-

cause of this, group O is often called "universal donor" and blood group AB "universal recipient".

Table 2.2: Core structures of mucin-type O-glycans

	Group O	Group A	Group B	Group AB
Antigens on red blood cells	—	A	B	A and B
Antibodies in plasma	anti-A and anti-B	anti-B	anti-A	—

Until now, it is not understood what gave rise to blood groups.[B] Theories include, for example, exposure to environmental antigens that led to cross-reactions; labeling of own cells making it easier for the immune system to fight pathogens; or random mutations that persisted.[96]

In any case, it is remarkable that the variations in the glycan structures that determine the blood group are minimal – all antigens share the GalGlcNAcGalFuc-core which is also the glycan structure of group O. A and B have only one sugar added – GalNAc or Gal, respectively –, and AB is just a combination of A and B. Nevertheless, this small change has the described, large consequences. Considering this finding on the one hand and the vast, seemingly not strictly controlled glycan structures on proteins on the other hand, this leads to one, maybe even the most important question of modern glycobiology: Why do small changes have enormous influence in some situations whereas in other situations much larger changes have apparently no impact at all?

2.1.4 Galectin-Glycan-Interactions

Besides the above mentioned examples of functions of protein glycosylation – in which it is rather passive modification – recent investigations have elucidated that protein glycosylation is capable to fulfill various regulative tasks. This happens via a complex interplay between glycan structures and specialized proteins binding to them, called lectins.[97,98] According to textbook definitions, a lectin is a protein that is able to bind to some specific carbohydrate structure, but does not show enzymatic activity. The terminus lectin is, hence, despite their large variety and obvious relevance for many cellular processes, still rather unconventionally defined: Compared to other classes of

[B] In this context, it should be mentioned that the ABO-system is the best-known categorization of blood groups, but that it is by far not exhaustive. Many other factors determine the blood group, for example the Rhesus factor.[95]

proteins, it is remarkable that the definition is negative. This reflects that for a long time after the discovery of lectins, their regulative functions has not been known, so proteins that showed affinity to carbohydrates, but seemingly did not do anything else, were just put into the group "lectins".

In the following, we will focus on one of the most important families of proteins among lectins, the galectins. Galectins specifically bind to β-galactosides.[99] Up to now, there are 15 galectins known. 10 of them (1, 2, 3, 4, 7, 8, 9, 10, 12, and 13) have been found in humans, the others (4, 5, 6, 11, 14, and 15) as well in other mammals, but also in amphibians, fish, and fungi.[100]

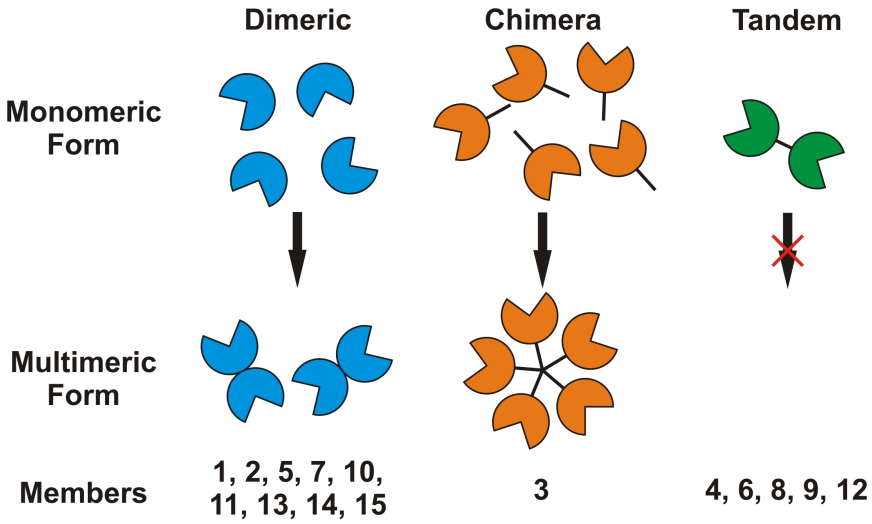

Figure 2.10: Galectin families
There are three different types of galectins: Homodimers of identical monomers (dimeric, left); pentamers of identical monomers that assemble via a non-lectin domain (chimera, middle); and a divalent form where two subunits are solidly connected via a peptide bridge and hence do not assemble (tandem, right).

One of the first detailed analysis of how the interactions between galectins and glycans influence global cellular processes was performed by Dennis *et al.* in 2006.[101] As it was discussed above, N-glycans can be processed in many different ways. A central modification is their branching from mono- to multiantennary N-glycans. Importantly, branched N-glycans act as binding partners for galectins. Since galectins exhibit more than one binding site for β-galactosides and one protein carries more than one β-galactoside if glycosylated with branched N-glycans, one glycoprotein can be bound

by multiple galectins. This gives rise to the so called galectin lattice, a supramolecular complex of glycosylated membrane proteins and galectins.[102]
Membrane glycoproteins engaged in the galectin lattice exhibit enhanced cell surface residence times and reduced internalization rates.[103,104] The degree of branching critically affects these parameters because glycoproteins carrying highly branched N-glycans (tri- or tetraantennary) show much higher affinity for galectins than lower branched N-glycans.[105] Importantly, the degree of branching is not random, but strictly controlled via the hexosamine pathway, a nutrient-sensing pathway that synthesizes amongst others N-acetylglucosmine which is required for the decoration of proteins with branched N-glycans.[106]
Strikingly, Dennis *et al.* found out that growth promoting receptors exhibit high numbers of N-glycans whereas receptors responsible for triggering of differentiation and growth arrest exhibit low numbers of N-glycans. If the nutrient state of the cell is good, this leads to high branching of growth-promoting receptors which, in turn, increases their residence time on the cell-surface due to the high affinity of highly branched N-glycans to galectins. The receptors triggering differentiation are also decorated with highly branched N-glycans, but at first not enough to increase their cell-surface residence time. However, if the nutrient state of the cell is good over a sustained time, branching of receptors carrying also low numbers of N-glycans is sufficient to let them engage in the galectin lattice in a switch-like response: They start to signal, induce growth arrest and differentiation. A schematic depiction is given in Figure 2.11. Therefore, via controlling the glycan-galectin interaction the cell is able to ensure that differentiation only starts when the time is right in terms of nutrient supply. Although proteins and posttranslational modifications of proteins are far downstream of DNA, the glycosylation type and degree together with secreted galectins lead to transcriptional control.

Of course, there are not only lectins specific for β-galactosides. For example, a prominent and very important group of lectins are the selectins which specifically bind to sialyl Lewis X structures (NeuAcα2-3Galβ1-4(Fucα1-3)GlcNAc).[107,108] They are critical to the first steps in leukocyte adhesion as depicted in Figure 2.12.[109]

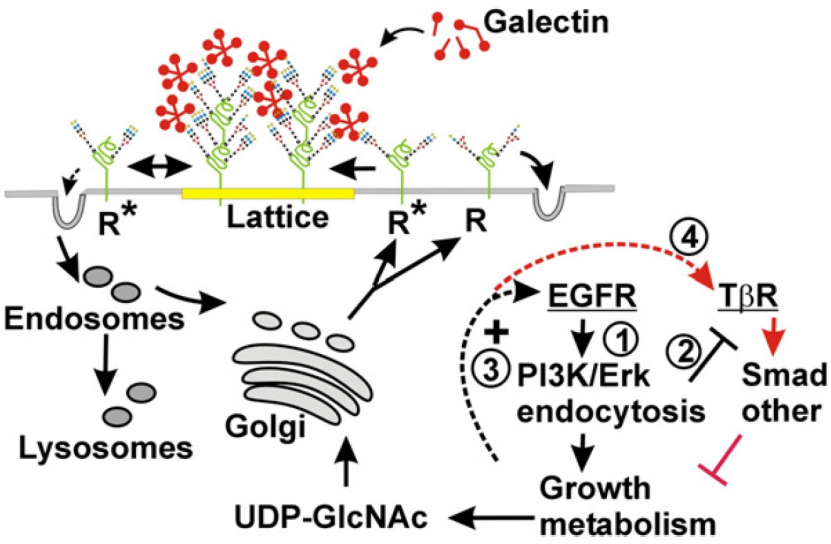

Figure 2.11: Regulation of signaling by membrane protein glycosylation and galectins.
High flux through the hexosamine pathway increases UDP-GlcNAc levels in cells, leading to stronger N-glycan branching. First, the cell surface residence time of growth promoting receptors, carrying high numbers of N-glycans, is increased (black arrows). However, as soon as a threshold is reached, also growth arresting and differentiation promoting receptors like TβR, which are decorated with few N-glycans, exhibit enough branched N-glycans to engage in the galectin lattice. In a positive feedback loop, this leads to growth arrest and differentiation (red arrows). Figure taken from reference[101]

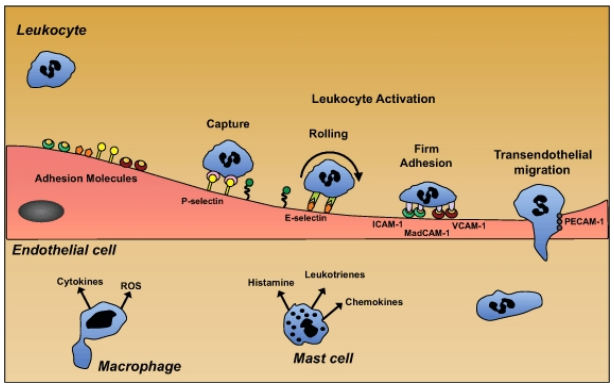

Figure 2.12: Regulation of leukocyte adhesion by selectins.
If P- and E-selectin on the surface of endothelial cells are activated, leukocytes that normally roll over the cell surface are bound. This leads to the further activation of CAM-molecules that firmly attach the leukocyte to the membrane which, in turn, triggers the migration of the leukocyte through the endothelium. Figure taken from reference[109]

2.1.5 The Glycocalyx

The totality of extracellular glyoproteins, proteoglycans, and glycolipids, both anchored and secreted, is called glycocalyx.[110] Important constituents are, for example, the glycans covalently attached to membrane proteins; long, polymeric species like glycosaminoglycans or hyaluronic acid; and sulfated polymers like chondroitin sulfate and heparan sulfate which contribute to the overall negative charge of the extracellular part of the cell membrane (Figure 2.13). Of special interest in this context is the endothelial glycocalyx that one can picture as a thick layer (several tens of nanometers up to micrometers dependent on the vessel diameter) surrounding every endothelial cell at the interface to the blood stream.[111] Since the endothelial glycocalyx is one of the most important examples for the glycocalyx, we will discuss its role briefly here.

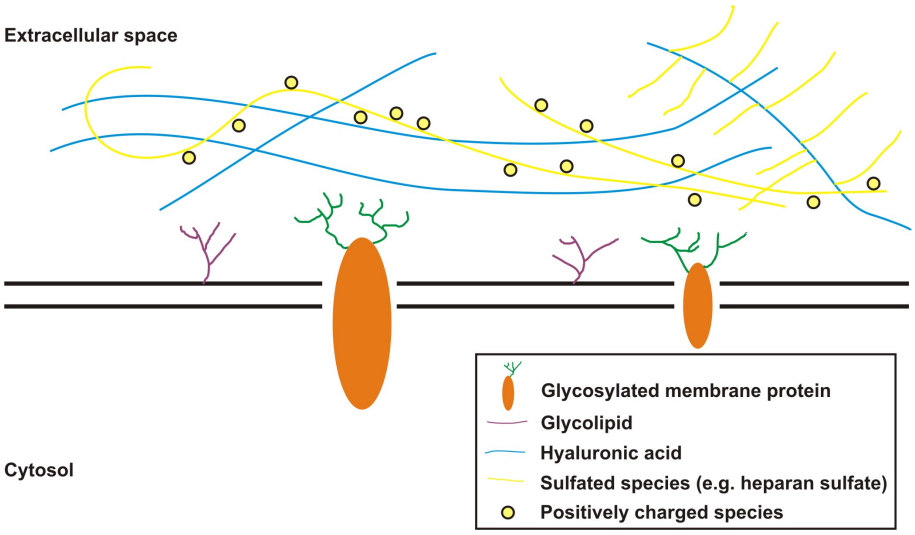

Figure 2.13: Composition of the glycocalyx
Various types of sugar structures constitute the glycocalyx: Covalently attached glycosylations of membrane proteins (green); glycolipids (violet); long, polymeric species like hyaluronic acid (cyan); or sulfated polymers like chondroitin, heparan, dermatan, or keratan sulfate (yellow) to which positively charged species like Ca^{2+} or arginine attach. From hyaluronic acid as backbone and sulfated polymers that are connected to it via linker proteins, also feather-like proteoglycans can be built.

Many observations indicated the presence of the endothelial glycocalyx long before the term was invented. For example, when investigating the rolling of leukocytes by simple light microscopy, it is evident that the moving leukocytes do not touch the vessel

wall but seem to be kept away by some barrier.[112] This is even more clearly detectable when large molecules like fluorescently labeled dextrans are injected and observed: If they exceed a certain size, they do not reach the vessel wall either.[113] Another early indication for the presence of the endothelial glycocalyx was the significantly lowered tube hematocrit (i.e. the volume fraction of red blood cells in the blood, typically around 40-45%) in microvessels in comparison to larger vessels.[114,115] It was proposed that some kind of exclusion zone reduces the diameter of microvessels such that the fraction of red blood cells has to decrease, and calculations predicted a prominent size in the range of some tens of nanometers even for the small microvessels and capillaries.[116]
Unfortunately, no experimental evidence was found when sections of blood vessels were investigated with electron microscopy (EM). This puzzling finding was not solved until it was realized that the method of probe preparation for EM destroys the glycocalyx:[117] Usually, samples to be investigated by EM are dehydrated and then treated with contrast agents. Although the glycocalyx is stable even under high flow rates in blood vessels, it is destroyed when dehydrated (Figure 2.14 bottom). Hence, the early EM investigations could not detect the true size of the glycocalyx, but just its remains. When special protocols were developed that did not perturb the hydration state of the glycocalyx, its impressive structure was quickly verified (Figure 2.14 top).

Up to now, it is an ongoing debate whether cultured cells express a glycocalyx, too. There are findings claiming that if this is the case, it is a thin, truncated form at the utmost.[111] Other studies suggest that it is again only a question of sample preparation and claim to have proven a glycocalyx even in the µm range *in vitro*.[118] This question is yet to be conclusively decided, however, investigations that found some form of a glycocalyx on cultured cells are in the majority.
Besides the rather passive function of building an exclusion zone, it quickly became clear that the glycocalyx fulfills important tasks. Many of them are closely related to mechanotransduction:[119,120] For example, the force that is created by the continuous flow of blood over the glycocalyx is sensed by the glycocalyx fibers and passed into the cell where reorganization of the actin cytoskeleton is effected. This triggers several signaling pathways that finally cause the expression and regulation of adhesion proteins, the determination of the cell's polarity, and the installation of cell-to-cell-junctions. If the glycocalyx is cleaved by enzymes, these processes are impaired or even completely blocked. Considering that cell polarity is one of the features nearly all cancer cells

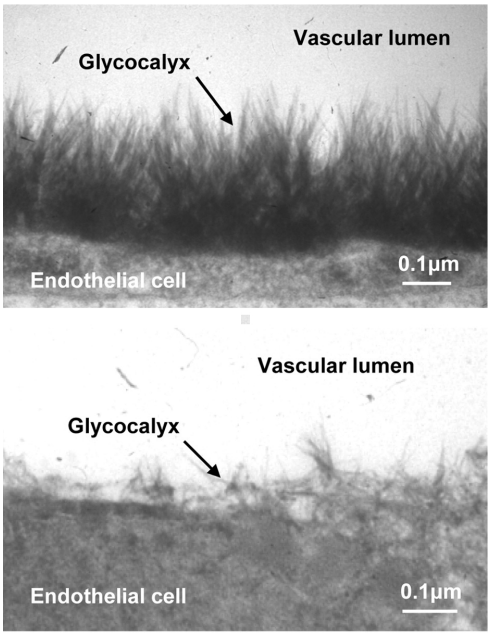

Figure 2.14: EM images of the glycocalyx in its intact state and after dehydration.
If special, protective protocols are applied, the structure of the glycocalyx is preserved (top). However, when the glycocalyx is dehydrated, in this case by ischemia, it is largely destroyed (bottom). Figure taken from reference[111]

have lost, this is an indication of how manifold the topics are where the glycocalyx plays a role.

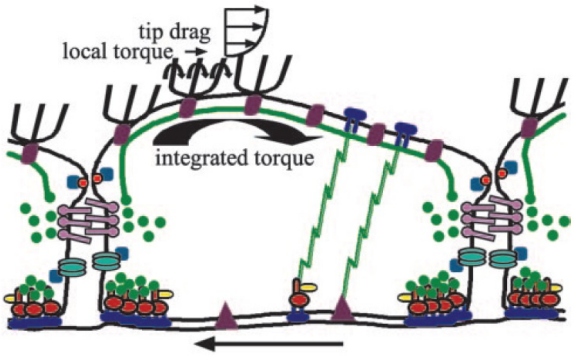

Figure 2.15: Mechanosensing and -transduction by the enothelial glycocalyx
The shear flow of the blood causes the fibers of the endothelial glycocalyx to bend, resulting in an inwards torque and reorganization of the actin cytosceleton inside the cell (green sawtooth lines). This leads to the formation of adherence and cell-to-cell junctions (purple), determining the polarity of the cell. Figure taken from reference[119]

2.2 Bacterial Adhesion and Its Inhibition

A large part of this thesis deals with bacterial adhesion to human endothelial cells and its inhibition. At the first glance, it may seem as if this has not much to do with sugars, but in fact, also in this area sugars play a central role. In the following, we will discuss the significance of sugars for bacterial adhesion and present how they can be employed to inhibit unwanted adhesion of (pathogenic) bacteria.

2.2.1 Principles and Relevance

Generally, bacteria can be classified in two different categories: On the one hand, they float freely in solution, on the other hand, they attach to a surface as single bacteria or in a group.[121] While both types may feature pathogenicity such as secretion of bacterial toxins, it is the second form of bacteria that usually causes serious infections since floating bacteria can just be washed away. Therefore, the adhesion of bacteria is one of the key steps in almost every process where bacterial colonization leads to diseases.[122,123,C] Hence, a detailed understanding of the mechanisms of bacterial adhesion is relevant.

[C] Note that not all bacterial colonization is harmful, e.g. symbiotic bacteria in the gut or on the skin.

Since we will discuss the roles of fimbriae in adhesion in the next chapter, we will focus here on other mechanisms of bacterial adhesion and cell entry. Figure 2.16 gives three examples of how bacteria attach to and enter cells.

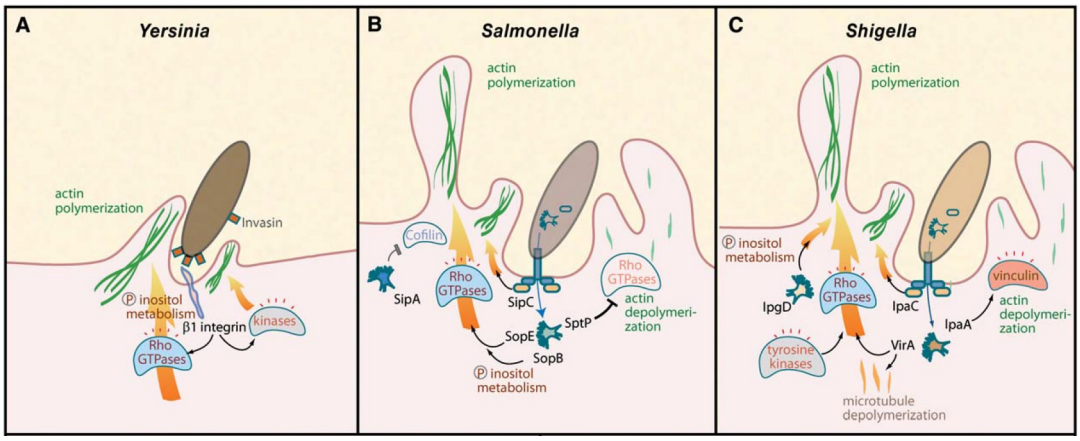

Figure 2.16: Entry of *Yersinia*, *Salmonella*, and *Shigella* into host cells.
All three bacteria attach to the cells via specialized protein complexes and secrete effectors activating cellular proteins that lead to uptake of the bacterium by the host cell. Figure taken from reference[124]

Yersinia employs invasin which interacts with $\beta 1$ integrins and activates Rac1. This causes a local change in phospatidylinositol metabolism, leading to actin polymerization and increased membrane fluidity and finally to internalization: The actin polymers act as "guide" for the membrane and the bacterium is sucked into the cell.[125]
The uptake of *Salmonella* is based upon the translocation of some type three secretion system (TTSS) proteins into the target cell. The TTSS itself functions also as an anchor, keeping the bacterium in place while SipC and SopE cause actin bundling and Rho GTPase activation. Again, actin polymerization is increased which causes the membrane to ruffle. As soon as the bacterium is internalized, the secreted SptP inhibits the Rho GTPases which helps the membrane to close behind the bacterium.[126]
Also *Shigella* adheres to the bacterium by anchoring via the TTSS. It then translocates several effectors into the cell: IpaC, nucleating actin polymerization; VirA, stimulating Rho GTPases to further induce actin bundling while inducing microtubule depolymerization to lower membrane rigidity; IpgD, promoting the ruffling of the membrane by affecting the phosphatidylinositol pathway; and IpaA, activating vinculin that depolymerizes actin in order to close the membrane once the bacterium is internalized like SptP in case of *Salmonella*.[127]

As one can see, bacteria have developed highly sophisticated methods to force cell entry by combining own attachment proteins with hijacking of cellular pathways. Once the bacteria are inside the cells, it is much harder to fight them, and the host cells are lost from the moment of entry. This highlights the importance of a deep understanding of bacterial adhesion as the prerequisite for the following entry in order to fight diseases caused by bacteria from the very start.

2.2.2 FimH-Mediated Adhesion of *E. coli*

The bacterium investigated in this thesis is *E. coli*. It adheres to cells via FimH that is located at the very tip of the fimbriae protruding from the bacterial cell wall[128] as it can be seen in Figure 2.17. The fimbrium produced by *E. coli* belongs to the type I fimbriae, exhibiting a length of up to 200 nm while being only about 7 nm think. Each bacterium carries several hundred fimbriae that together cause efficient attachment.

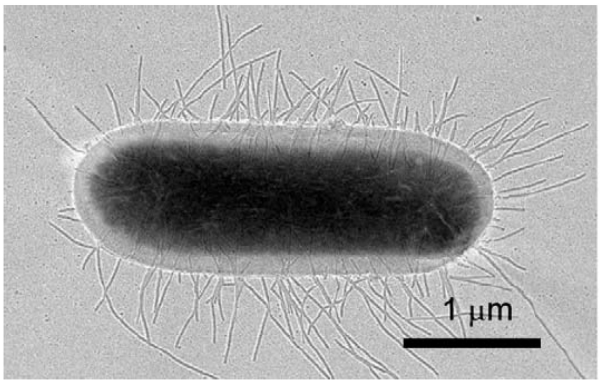

Figure 2.17: Electron micrograph of an *E. coli* bacterium with clearly visible fimbriae. Figure taken from reference[129]

The architecture of the fimbrium is quite complex. It is schematically depicted in Figure 2.18. Each Fim protein is cotranslationally injected into the periplasm of *E. coli*. FimC, a chaperone, helps folding and brings it to the channel FimD. The chaperone activity of FimC originates from an "extra" β-sheet: Every Fim protein in the fimbrium is missing one β-sheet in its core and features one extra β-sheet (with the exception of the tip protein FimH wh9ch does not exhibit an extra β-sheet). This extra β-sheet is inserted into the gap of the next Fim protein which in turn completes the subsequent Fim protein and so on, leading to high stability of the fimbrium. In case of FimC,

the extra β-sheet acts as nucleation point for folding. The fimbrium itself consists of several hundreds to a few thousand FimA subunits and the three tip proteins FimF, FimG, and FimH.[129]

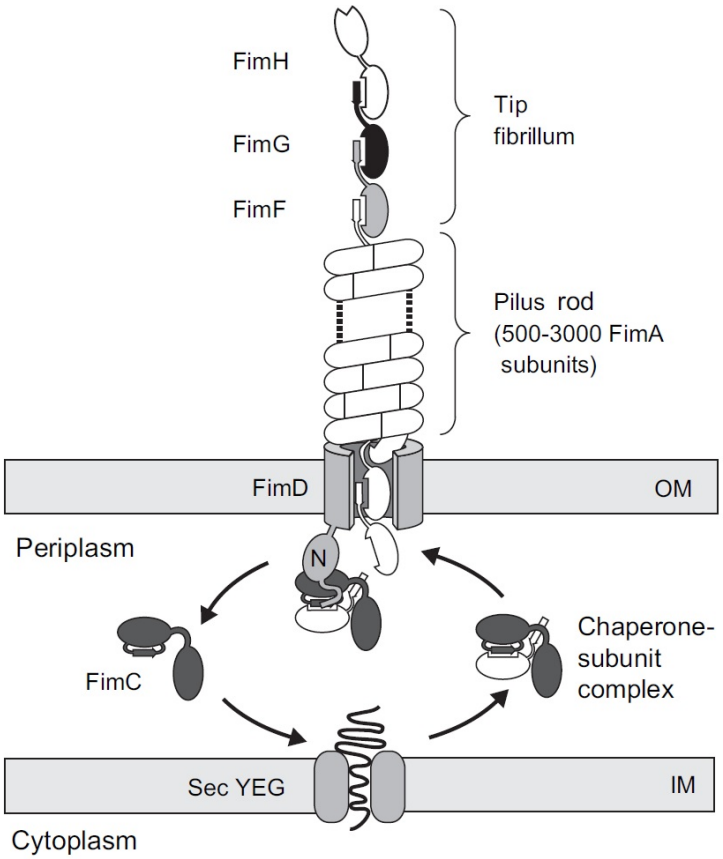

Figure 2.18: Architecture of *E. coli* fimbriae.
FimH is located at the very tip of the fimbrium. Below, FimG, FimF, and a polymer of several hundreds to a few thousands FimA units follow. Each Fim protein is cotranslationally injected in the periplasm via SecYEG where the chaperone FimC helps it folding and translocates it to the channel FimD. Figure taken from reference[129]

FimH is responsible for the attachment of the bacterium to the host cell. It binds to N-linked glycans of the high mannose type.[23,130] A crystal structure of FimH in complex with mannose is shown in Figure 2.19.[131] The interaction between FimH and mannose features a special characteristic, the so called catch bond mechanism:[132,133] The strength of normal protein-protein interactions ("slip bonds") decreases when increasing force is applied, or more precisely, the lifetime of the bond decreases with

increasing force. In contrast, the life time of catch bonds first increases with increasing force and decreases after the force exceeds a certain value. This can be compared to a person standing in a moving bus while keeping one hand on a handle. As long as the bus just drives with more or less constant velocity, the grip around the handle will not be strong. However, when the bus suddenly stops, the person will strongly hold onto the handle. If the force is finally too high, she will at some point not be able to maintain the grip any longer.
Although this is an illustrative picture, it cannot explain the molecular basis for catch bonds. In case of FimH, the catch bond mechanism is caused by a complex transition between a stressed and a relaxed state of FimH while binding to mannose. Roughly, when FimH binds to mannose with no or little force applied, FimH is in a stressed state, reducing the affinity to mannose. If force is applied, FimH undergoes a conformational change to a relaxed state which increases the affinity to mannose. If the force is increased further, the interaction between FimH and mannose is at some point too weak to persist.

2.2.3 Inhibition of Bacterial Adhesion

Since many severe diseases are caused by pathogenic bacteria, effective medication against bacterial infections is unquestionably needed. Of course, antibiotics are a common treatment for such infections, however, this therapy is not unproblematic. One of the main drawbacks of treating bacterial infections with antibiotics is the increasing number of resistant strains,[27] and the widespread use of antibiotics in the food industry has made this worse in the last decades.[134] Therefore, it seems like a good alternative to not treat the infection with bacteria after its outbreak, but to stop bacterial adhesion in the first place, preventing the infection.[135,136] For this, potent antagonists of FimH are required.
It was already discovered some decades ago that mannose alone is a rather poor ligand for FimH, but that modification of the aglycon of α-D-mannose often drastically increases the potency of the inhibitors.[137,138] However, not all modifications, even of similar size, have this effect, hence, a specific interaction was assumed. This puzzle was solved when FimH was crystallized. The structure unrevealed that at the entrance of the binding pocket (or carbohydrate recognition domain, CRD) two tyrosine residues

Figure 2.19: FimH in complex with its natural ligand mannose Figure taken from reference,[131] PDB-ID: 1KLF

are located. They can form favorable π-π-interactions with certain modifications of the aglycon.[139,140] The structure of the so called "tyrosine gate" is shown in Figure 2.20.

The understanding of the tyrosine gate makes it possible to rationally design antagonists of FimH. For example, the introduction of aromatic groups into the aglycon often leads to even better results than simple alkyl chains,[23] however, one must be careful not to overstress the tolerance of the CRD. If the modifications become too large or change the electronic density of the mannose group, the favorable π-π-stacking effect vanishes.

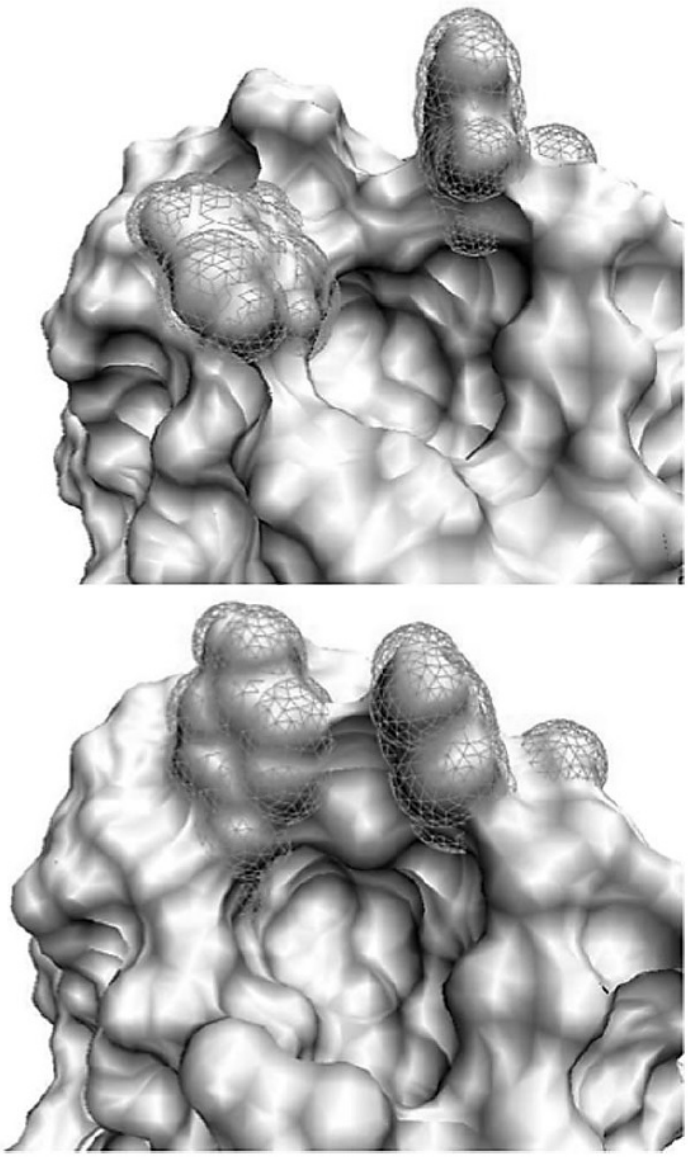

Figure 2.20: The tyrosine gate at the entrance of the CRD of FimH.
At the top, the configuration of the two tyrosine residues in the open conformation is depicted. This indicates that the ligand mannose is not inducing favorable π-π-interactions. However, if butyl mannose is used, it interacts with the tyrosines which closes the gate and increases the affinity for FimH. Figure taken from reference[23]

To investigate the potency of inhibitors, one has multiple options, however, they differ often drastically in their sensitivity and robustness. Besides established techniques like ELISA[141] or surface plasmon resonance,[142] one of the most elegant and sensitive ways is the use of a fluorescence based assay in combination with a well-defined setting[143] as depicted in Figure 2.21.

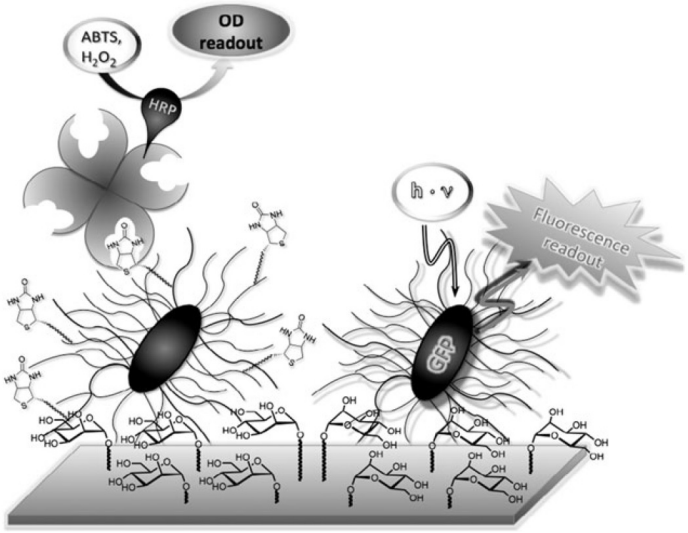

Figure 2.21: Detection of bacterial adhesion via a sandwich method and by direct fluorescent readout
E. coli adhering to an artificial, mannose-covered surface can be detected either via a sandwich-based method employing biotinylated bacteria and horseradish peroxidase-linked streptavidin (left), or directly via fluorescence readout (right). Figure taken from reference[143]

Here, the stepwise assembly of the artificial surface that is covered with the *E. coli* ligand mannose ensures that the system gives reproducible results. There are two main benefits to use fluorescence instead of a sandwich-based methods: First, biotin-modification of fimbriae may alter the adhesion properties of the bacteria. Second, detection via fluorescence is direct and does not require an intermediate step like incubation with streptavidin. This reduces the error of the system and therefore increases reliability and sensitivity. However, one must keep in mind when quantifying bacterial adhesion in such artificial environments that the situation in living systems could be strongly different. Chapter 9 will discuss one important aspect.

3 Metabolic Labeling

The technique of metabolic labeling is based on a simple, yet very effective idea: Instead of addressing a certain part of the cell with e.g. antibodies, the cellular metabolism is employed to incorporate a label into the structure that should be analyzed. If it comes to investigation of glycosylation and its effects, this approach is particularly powerful because antibodies against glycan structures often show poor affinity and selectivity[144] – in contrast to metabolic labeling where these two parameters are very good. Since we rely heavily on metabolic labeling in the experiments described in this thesis, its development and method are presented in the following chapter.

3.1 Historical Development

In the mid-90s, Werner Reutter and coworkers investigated the response of living cells when subjected to three unnatural mannosamine derivatives (Figure 3.1).[145,146] The naturally occurring *N*-acetyl mannosamine is used to synthesize sialic acids in the cell which can be found at terminal positions of many glycans on membrane proteins. The modifications Reutter *et al.* investigated were mannosamines that featured an *N*-propanoyl, *N*-butanoyl, or *N*-pentanoyl group instead of the regular *N*-acetyl group. It was surprising that the cells did not reject these unnatural derivatives: On the contrary, they were taken up and incorporated into glycans on the cell surfaces where they were easily detected after some incubation time using mass spectrometry. Reutter *et al.* rightly concluded that the intracellular synthesis machinery responsible for the construction of the sialosides on the cell membrane must be able to tolerate these modifications.

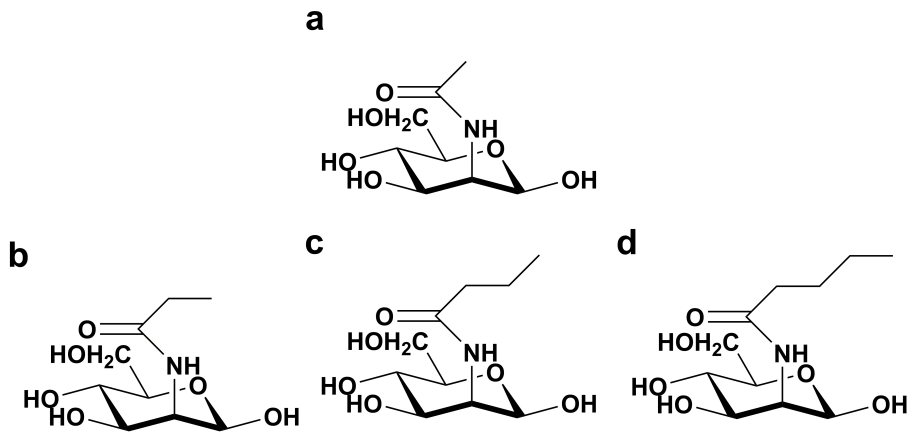

Figure 3.1: The stem compound and the three unnatural sugars introduced by Reutter *et al.* into membrane glycans
a) *N*-acetylmannosamine; b) 2-deoxy-2(porpanoyl-amido)-D-mannose; c) 2-deoxy-2(butanoyl-amido)-D-mannose; d) 2-deoxy-2(pentanoyl-amido)-D-mannose.

Of course, Reutter *et al.* were not satisfied with just to show the installation of unnatural alkyl chains onto the cell surface but wanted also to demonstrate a functional implication. They were able to show that the sialic acid-dependent interaction between the cell surface and two viruses, the B-lymphotropic papovavirus and the human polyoma virus BK, was strongly altered when the cell surface was modified with the unnatural mannosamines.[146] This effect also led to a reduced infectivity of the viruses. One may assume that this observation was just due to a general shielding effect when cells are covered with alkyl chains, but it was shown that this is not the case: Only the adhesion and infectivity of viruses interacting with the cell via sialic acids were affected. Viruses that attach employing other ligands like the also investigated SV40 did not behave differently when the cells were treated with the modified mannosamines. Moreover, the altered infectivity also vanished when cells were treated with sialidase, cleaving the modified sialic acids.
These experiments, proving that the cellular metabolism responsible for the sialylation of membrane proteins tolerates the presence of large, unnatural modifications can be seen as the birth of metabolic labeling. However, from a chemical perspective, the incorporation of alkyl chains is not very exciting due to their unreactive nature.

3.2 Metabolic Labeling with Azido Sugars

The alkyl chains incorporated by Reutter *et al.* into glycans via metabolic labeling are quite inert and do not provide a platform to perform reactions, at least under conditions compatible with living cells. To make metabolic labeling a powerful tool, it is necessary to introduce more reactive groups. However, the problem of more reactive groups is their reactivity: Such a group should have the potential to perform reactions, but must also be stable enough that it does not interfere with the molecules present in the cell which would certainly lead to toxicity. Moreover, one does not gain anything if, for example, a hydroxy group is introduced since they are abundant on the cell surface – the introduced group must be unique. All the requirements that a functional group employed for metabolic labeling must fulfill can be summed up by the term "bioorthogonality".[147] In detail, this means the following:

- Sufficient reactivity to be addressed, but not interfering with cellular components;
- Small enough to be tolerated by the synthesizing enzymes;
- Not present in the cell;
- Specifically addressable under physiological conditions, i.e. in water at ambient temperatures and pH 7 and so on.

This is schematically shown in Figure 3.2. It is not surprising that it was challenging to find such a chemical modification. However, a well-known chemical group is perfectly suited, as Bertozzi *et al.* discovered around 2000:[149] The azido group. In Figure 3.3, the underlying principle of metabolic labeling using the bioorthogonal azido group is depicted. The growth medium of cultured cells or even whole organisms[150,151] is supplemented with unnatural azido sugars ("input"). Due to the bioorthogonal nature of the modification, they are internalized by the cell and incorporated into glycans via the normal biosynthetic pathways.[152] After a while, membrane and cytosolic proteins carry an azido group at specific sugars. The sugar residue modified in the glycan on the protein (the "output") is dependent on the input: Ac_4ManNAz and Ac_5SiaNAz lead to metabolic labeling of sialic acids, $AcAc_4$GalNAz targets mucin-type O-glycans, and $AcAc_4$GlcNAz β-O-GlcNAc bearing proteins. Also, azido-modified fucose can be used to label fucose-bearing glycans.

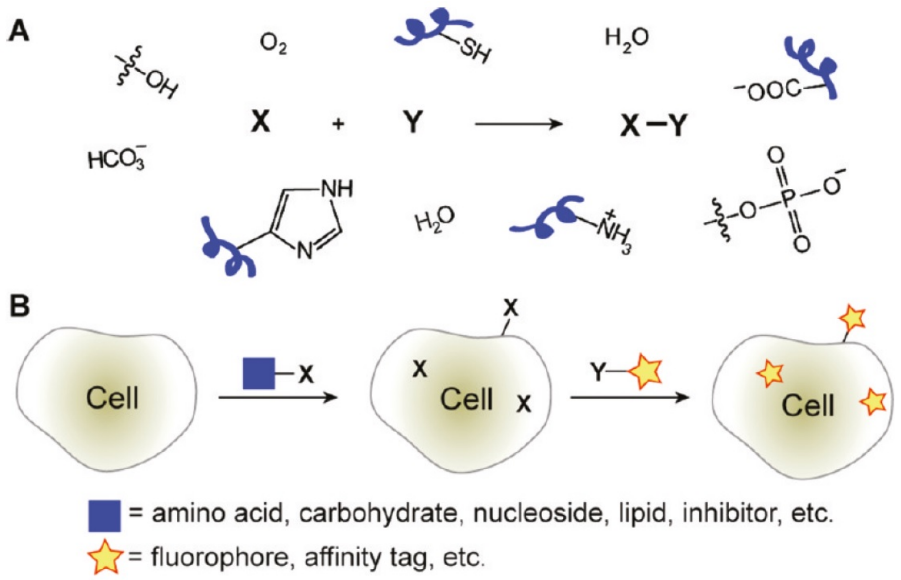

Figure 3.2: Requirements for bioorthogonal labeling of biomolecules
a) The putative bioorthogonal reaction X+Y→ X–Y must tolerate all the other functional groups like oxygen, water, amines, phosphates etc. typically present in living systems while not interacting with them. b) A typical bioorthogonal reaction is pictured as follows: A normal biomolecule is chemically modified with a group X. The biomolecule is incorporated into the cell in its usual environment since X does not interfere with the metabolism. Due to the bioorthogonal nature of X, it can be specifically addressed by a second functional group Y that reacts only with X. Y can carry any tag needed for detection, for example a fluorophore. Figure taken from reference[148]

After incorporation of the azido groups onto proteins, one must of course detect them in order to, for example, visualize the glycans via fluorescence microscopy. So far, three common options exist. They are depicted in Figure 3.4. The first method developed was the Staudinger ligation using a reactive triphenylphosphine that reacts solely with the azido groups.[149] However, the generated methanol can be a problem when it comes to live-cell experiments, moreover, the reaction rate is rather low. Another alternative is the detection via alkynes where copper-catalyzed click chemistry is employed which connects the alkyne and the azide selectively via a [3+2] Huisgen cycloaddition. The reaction is very fast, but the use of cytotoxic copper(I) is not feasible for sensitive cells.[154] Nevertheless, protocols have been developed where this detection method can be used also for live-cell experiments.[155] The main idea here is to i) shield the copper by a complexing agent, preventing it from performing toxic side-reactions; ii) reduce

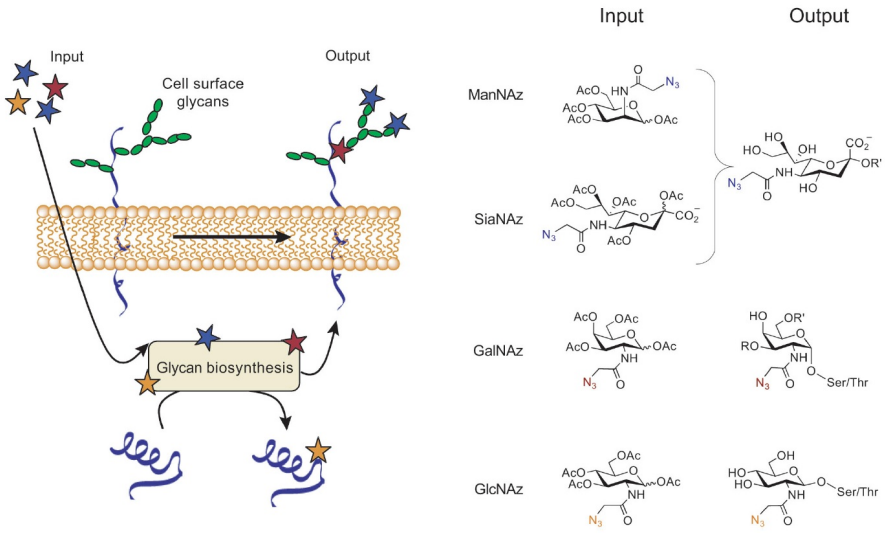

Figure 3.3: Principle of metabolic labeling
Unnatural, azido-modified sugars are internalized by the cell and incorporated into glycans where they can be detected after a while (left). The nature of the modified sugar residue in the glycan is dependent on the unnatural sugar (right). Figure taken from reference[153]

the temperature to slow down cellular processes; and iii) reduce the reaction time to a few minutes. This is possible due to the very high rate of this reaction – even at 4°C and a reaction time of five minutes, it is high enough to label all accessible azido groups on the membrane as we will show later. Finally, if one wants to avoid the use of copper(I), cyclooctynes can be used.[156] They avoid the cytotoxicity of copper(I) while still exhibit high reaction rates. In Figure 3.4, a simple cyclooctyne is depicted which exhibits low reaction rates. However, one can boost the rates by several orders of magnitudes by activating groups attached to the cyclooctyne like fluorine and benzene rings. Also in this case, the alkyne part of the cyclooctyne and the azide are connected via a [3+2] Huisgen cycloaddition.

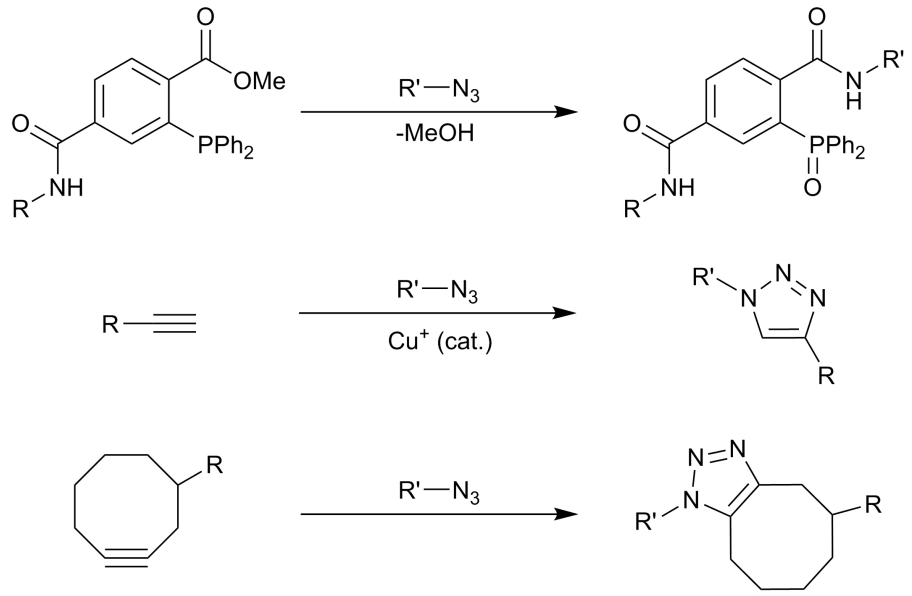

Figure 3.4: Detection of azido groups.
Shown are three common detection methods for azido groups and the resulting reaction products: Staudinger ligation with triphenylphosphines (top), copper-catalyzed click chemistry (middle), and copper-free click chemsitry with cyclooctynes (bottom). R and R' denote arbitrary chemical groups. If applied in biological systems, R is the label to be attached, e.g. a fluorophore, and R' the azide-bearing sugar on the protein.

3.3 Chemical Background of Copper-Catalyzed Alkye-Azide-Ligation

Since we do not only use copper-free click chemistry in our experiments, but also copper-catalyzed ligation of alkynes and azido groups, the mechanistic basis should be briefly highlighted here as shown in Figure 3.5.

Several studies suggest the existence of a dynamic equilibrium between different copper(I) acetylides in solution.[158] These are formed via the attack of copper on the π-system of the alkyne which strongly acidifies the proton. It is suggested that the pK_a is lowered by almost 10 units, making water a sufficiently strong base to deprotonate the alkyne. When the azide attacks, it first coordinates a second copper ion that is not part of the acetylide. It seems like this second atom fulfills two tasks: On the one hand, it activates the copper(I) from the acetylide, on the other hand, it serves as first binding

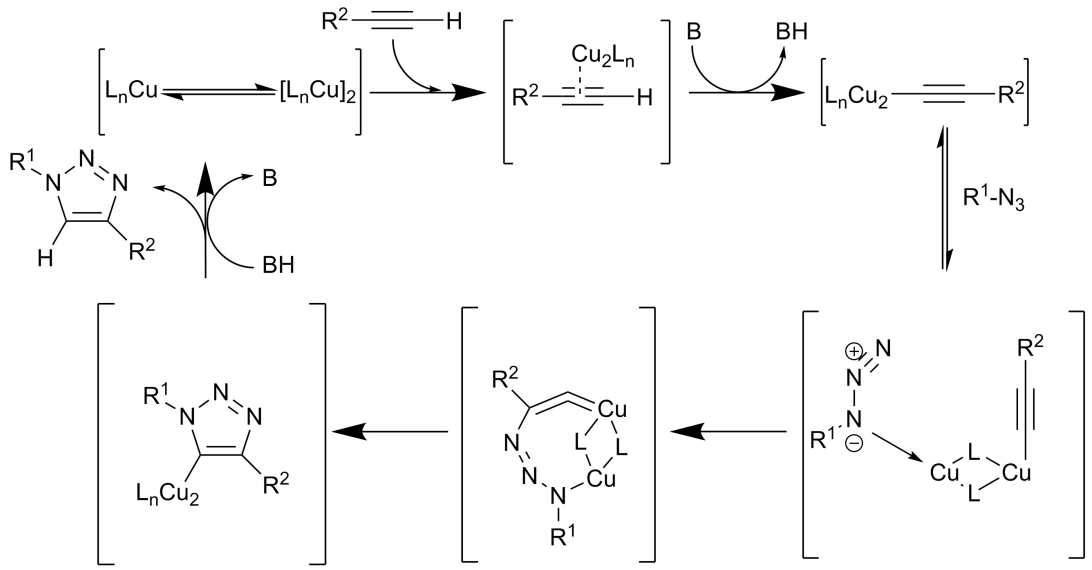

Figure 3.5: Simplified mechanism of the copper-catalyzed reaction between alkynes and azides

The catalyzing Cu^+ is complexed by some ligand and binds to the triple bond of the alkyne. Some base cleaves the acidified hydrogen, yielding the copper(I) acetylide. Then, the azide attacks. Via several intermediate steps, the final product of the cycloaddition is formed and the catalyzing species as well as the base are regenerated. R^1 and R^2 denote an arbitrary chemical residue. Figure adapted from[157]

partner for the azide. This coordination reduces the electron density of the alkyne, making it possible for the azide to attack it, leading to cyclization.

4 siRNA in Cell Biology and Therapeutic Applications

Chapter 11 deals with the internalization of targeted small interfering RNA (siRNA) into model neuronal stem cell and into live mouse brains. We will in this chapter briefly introduce the mechanism of siRNA-mediated gene expression and how it can be utilized for gene therapy.

4.1 siRNA-Mediated Control of Gene Expression

After the transcription of DNA to mRNA, the mRNA is prepared for translation by processes like splicing, polyadenylation, and capping.[159] The processed mRNA is then translated many times. However, at some point it will be desirable to decrease again the synthesis of the protein encoded by the mRNA. Also, it may happen that the situation of the cell changes in a way that the production of the respective protein is no longer wanted. Since the proteins translated in excess would be useless or even harmful, cells have developed several mechanisms to intercept mRNA. Among them, siRNA-mediated posttranscriptional control of gene expression is the most common.[160]

The molecular basis of siRNA-mediated gene expression, commonly termed RNA interference (RNAi), is schematically depicted in Figure 4.1. siRNAs are RNA molecules that are encoded on the DNA just as normal mRNA.[161–163] Usually, they consist of 21 nucleotides with two unpaired nucleotides at each end and 17 paired nucleotides in the middle. RNA Pol II or III transcribe the RNA that will later become siRNA. However, right after transcription, the synthesized RNA is several thousand nucleotides long and features a cap and poly-A tail just like normal mRNA. This so called primiRNA is exported from the nucleus into the cytoplasm by Drosha or RNase III and

the cofactors DGRCS and Exportin 5.[164] There, the endonuclease Dicer with its helper proteins TRBP and PACT specifically cleave the pri-miRNA into small pieces.[165] This yields siRNA.
The resulting siRNA has two strands. One of the strands is complementary to the target mRNA. It is therefore called antisense-strand or guide strand. The other strand has the same sequence as the mRNA and is termed sense-strand or passenger strand, underlining that this strand just comes together with the antisense strand. The double-stranded siRNA is recognized by the RISC loading complex (RLC) and loaded into RNA-induced silencing complex (RISC).[166] RISC unwinds the siRNA and splits it. The sense-strand is degraded in the process while the antisense-strand stays in the RISC.
With this, everything is set for RNAi. In case of perfect match between the mRNA and the siRNA, the mRNA is cleaved by AGO2 which completely shuts down translation. In case of a two to seven matching nucleotides, the mRNA is not degraded, but stays bound to RISC, which in turn reduces translation.[167]

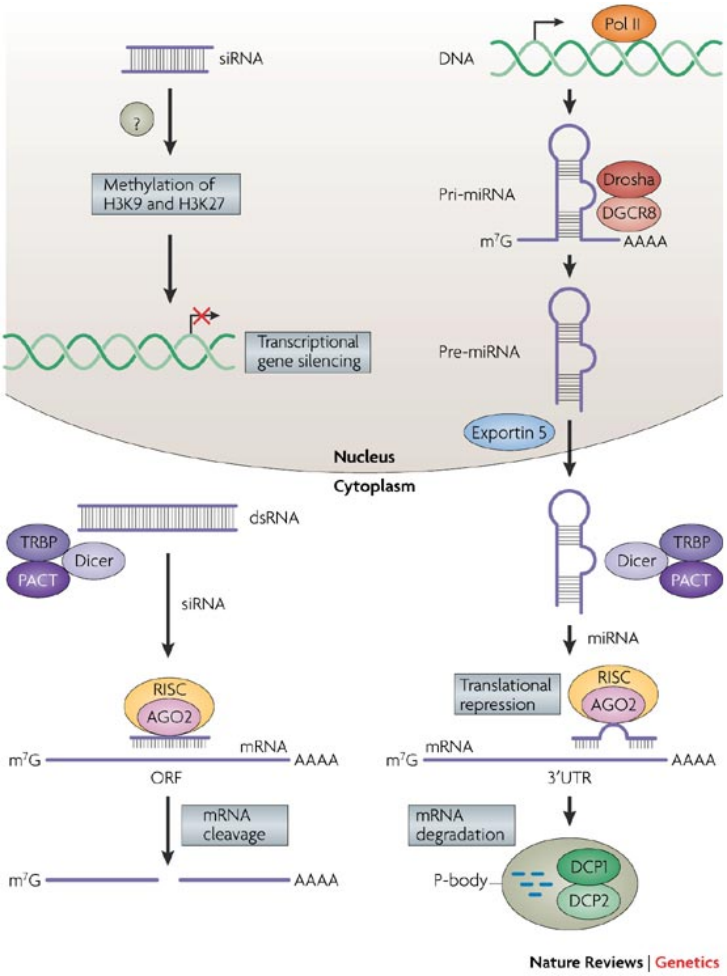

Figure 4.1: Processes during RNAi.
After synthesis of pri-miRNA, it is exported into the cytosol where it gets processed by Dicer. The resulting siRNA is loaded into RISC by RLC. The corresponding mRNA is recognized. In case of perfect match, the mRNA is degraded, otherwise, it stays in the RISC. In the first case, complete silencing, in the second case, reduction of translation results. Figure taken from[81]

4.2 siRNA in Therapeutic Applications

The possibility to alter gene expression by RNA interference makes siRNA an interesting tool to treat diseases: After identification of proteins crucial for a disease or infection, the respective translation can in principle just be shut down by RNA interference which fights the disease. About 15 siRNA constructs are currently investigated in clinical phases I-III.[168]

One of the first drugs employing RNA interference, Bevasiranib, is a simple siRNA directed against the vascular endothelial growth factor (VEGF).[169] VEGF activity is mainly responsible for neovascularisation of the macula, leading to age-induced macula degeneration.[170] The idea behind the treatment is to downregulate VEGF expression in order to suppress neovascularisation, hence fighting the main cause for macula degeneration.

Another example is Miravirsen (SPC3649) which is a miRNA-based drug currently in phase II.[171] The RNA interference is directed against miR-122, a mRNA crucial for the development of the Hepatitis C virus.[172] Miravirsen is built by so called locked nucleic acid ribonucleotides which are spaced throughout a DNA phosphorothioate sequence. It was shown that Miravirsen binds to mature miR-122 which blocks interaction with hepatitis C virus RNA. This inhibits assembly of the virus, fighting the infection.

An important aspect of siRNA-mediated therapy is the delivery of the siRNA to the target cell. For this, various possibilities exist.[173–176] In this work, targeting employing anandamid (*N*-Arachidonylethanolamid, AEA), a derivate of arachidonic acid, was prominently used.[31] AEA binds to the cannabinoid receptors 1 and 2 which are G-protein coupled receptors.[32,177,178] Cannabinoid receptor 1 is predominantly located in neuronal cells, especially in the hippocampus. The cannabinoid receptor 2 is found on cells related to the immune system, osteoblasts, and osteoclasts. Corresponding to their location, the cannabinoid receptor 1 is involved in brain plasticity and neurotransmission, whereas cannabinoid receptor 2 plays an important role in immune response.

5 Fluorescence Microscopy, Diffusion, and Single-Molecule Tracking

5.1 Principles of Fluorescence Microscopy

Fluorescence microscopy is a powerful tool to elucidate processes within living systems.[179,180] Although microscopy in general and also fluorescence microscopy are techniques established already some time ago, they are still pushed further. New methods with increased capacity and applicability are continuously developed. The most prominent example amongst them may be the discovery of super-resolution microscopy about 15 years ago which was awarded with the Nobel Prize for Chemistry in 2014.[181] However, all fluorescence microscopy techniques have a common basis: The principles of optics and the physical processes underlying fluorescence. As almost all experiments described in this thesis are connected to fluorescence microscopy, its basics are introduced in the following.

5.1.1 Fluorescence

The ability of certain physical systems like e.g. atoms, molecules, or quantum dots to emit light after excitation with electromagnetic radiation is called fluorescence. These systems are generally termed fluorophores. Although atoms, molecules, and quantum dots differ strongly in their properties, they have in common that, in order to function as fluorophores, they need to possess one or more electrons that are able to be excited by photons. In the following, we will discuss the phenomenon of fluorescence for molecules since most fluorophores used in this thesis were organic dyes like the

AlexaFluor dyes.[A] The central processes underlying fluorescence can be visualized and explained using the so called Jablonski diagram (Figure 5.1).[182] It schematically depicts the relevant energy levels of the molecule influencing the process of fluorescence.

In order to emit a photon, i.e. fluoresce, a molecule must first absorb energy. In the diagram, this is depicted by the blue arrow: An electron is excited within femtoseconds, for example from the highest occupied molecular orbital to the lowest unoccupied molecular orbital. The system is hence transferred from the electronic ground state S_0 to a vibrational state of an excited electronic state, e.g. S_2. From this high-energy level, the system does not return to the ground state immediately: It first undergoes vibrational relaxation (dark red arrow) and internal conversion (light red arrow). These two processes occur within picoseconds and are therefore about three orders of magnitudes faster than fluorescence. Via vibrational relaxation, the system loses energy to its environment, e.g. via collisions with other molecules, and arrives in the vibronic ground state of S_2. From there, it crosses into energetically overlapping, highly excited vibrational states of S_1. Again, the system undergoes vibrational relaxation and arrives at the vibrational ground state of S_1. From there, it falls down to the electronic ground state S_0 within nanoseconds, emitting a photon that can be detected as fluorescence (green arrow). Usually, the system does not arrive in the vibronic ground state, but in an excited state from where it is again transferred to the vibronic ground state via vibrational relaxation. Because the system therefore loses energy due to the relaxation processes, the emitted wavelength is usually shifted towards lower energies, i.e. higher wavelengths, which is called Stokes' shift.[183]

Besides this path, there exists the possibility that the system undergoes a transition from the vibronic ground state of S_1 to the triplet ground state T_1 (yellow arrow). This is a rare event because the process is forbidden by quantum mechanics, hence, it is also not meaningful to give a timescale for this process. However, if it occurs, the system

[A] For some experiments, quantum dots were used. The basis of fluorescence in their case is different than of organic dyes, however, the underlying principle is rather simple: The size of a quantum dot is in the range of the wavelength of an electron ($\lambda = h/\sqrt{2m_e k_B T} \approx 7.7\ nm$ at 22°C), hence, quantum confinement of the electron-hole pair after excitation occurs. This electron-hole pair can be modeled as one particle, an exciton, that is positioned in a potential well. The resulting energy levels, defining the emitted fluorescence, can be approximated using the simple particle in a box model. Considering this, it is also easily understandable why the emission wavelength of a quantum dot depends mainly on its size.

is "trapped" in T_1 because the emission of a photon to return to S_0 is now of course also forbidden. Hence, the related phosphorescence (orange arrow) takes much longer (microseconds to minutes). Since these photons are often not usable for the detection of fluorescence due to their long delay, phosphorescence is an unwanted effect in many applications.

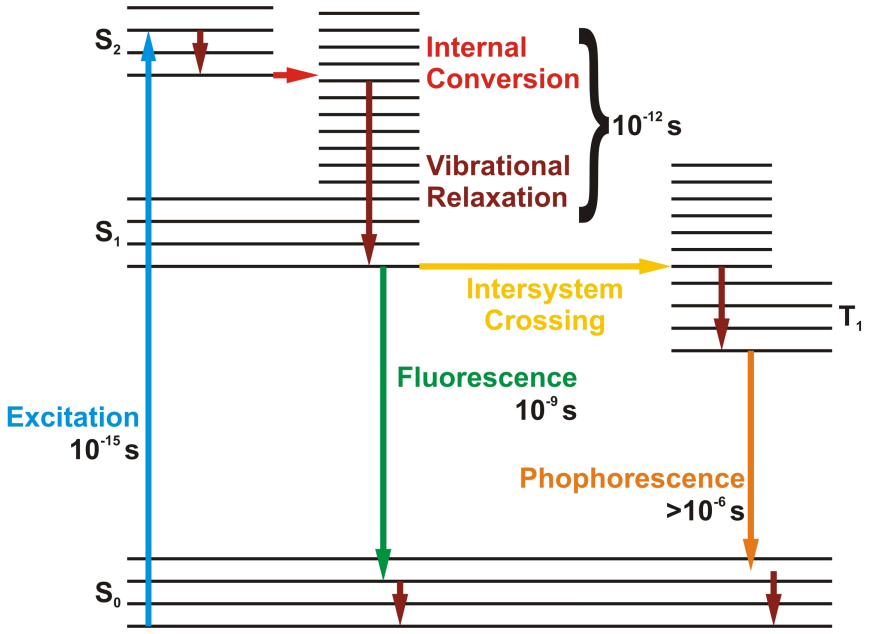

Figure 5.1: Jablonski diagram
The system is excited from the electronic ground state S_0 to an excited electronic state like S_2. Then, it undergoes internal conversion to reach the vibronic ground state of S_1. From there, it usually returns to S_0, emitting a photon which is detected as fluorescence. Sometimes, it may undergo intersystem crossing into the triplet state T_1, a process forbidden by quantum mechanics. From there, the system falls back to S_0, but on a much longer time scale than in case of fluorescence since the return from T_1 to S_0 is again forbidden.

5.1.2 Optical Imaging and Resolution

If the signal of a fluorescent emitter is recorded using an optical system like a microscope, diffraction occurs. This has an important consequence: The microscope does not show the actual size of the fluorophore, but a blurred spot of much larger size. In the following, the physical reason for diffraction will be discussed using the most simple example for diffraction: Light diffracted at a small aperture.

Light can be described as an electromagnetic wave.[184] Therefore, it must satisfy the wave equation

$$\nabla^2 \vec{E}(x,y,z,t) = \frac{1}{c^2} \frac{\partial^2 \vec{E}(x,y,z,t)}{\partial t^2}, \tag{5.1}$$

where $\vec{E}(x,y,z,t)$ is the electric field (the magnetic field can be treated equally), c is the speed of light, and t is time. To solve this equation, we assume harmonic plane waves traveling from the aperture to describe the propagation of the field

$$E(x,t) = E_0 cos(\vec{k}x - \omega t) = \Re\mathfrak{e}(E_0 e^{i(\vec{k}x-\omega t)}), \tag{5.2}$$

where ($\vec{k}$ is the wave vector or spatial frequency and ω is the temporal frequency. If we put this ansatz into the wave equation, we get:

$$-\vec{k}^2 E = -\frac{\omega^2}{c^2} E. \tag{5.3}$$

Considering that ω is related to the frequency f via $\omega = 2\pi f$ and the wave vector to the wavelength via $k = 2\pi/\lambda$, we obtain

$$\frac{4\pi^2 f^2}{c^2} = \frac{4\pi^2}{\lambda^2}, \tag{5.4}$$

which results in a well-known equation:

$$c = \lambda f. \tag{5.5}$$

Therefore, the ansatz is a solution of the wave equation. In order to evaluate how the field evolves, we consider that the electrical field needs to fulfill the Helmholtz equation:

$$(\nabla^2 + \vec{k}^2) E(x,y,z) = 0. \tag{5.6}$$

For simplicity, we switch to the frequency domain via a 2D-Fourier transformation. The waves travel in the x-y-plane whereas they are constant in z:

$$E(x,y,z) = \int\int \overline{E}(\vec{k}_x,\vec{k}_y,z)e^{i(\vec{k}_x x+\vec{k}_y y)}d\vec{k}_x d\vec{k}_y. \tag{5.7}$$

Hence, we obtain:

$$\nabla^2 \int\int \overline{E}(\vec{k}_x,\vec{k}_y,z)e^{i(\vec{k}_x x+\vec{k}_y y)}d\vec{k}_x d\vec{k}_y + \vec{k}^2 \int\int \overline{E}(\vec{k}_x,\vec{k}_y,z)e^{i(\vec{k}_x x+\vec{k}_y y)}d\vec{k}_x d\vec{k}_y = 0. \tag{5.8}$$

This equation can be solved with the following ansatz:

$$\overline{E}(\vec{k}_x,\vec{k}_y,z) = \overline{E}(\vec{k}_x,\vec{k}_y,0)e^{\pm i\vec{k}_z z}. \tag{5.9}$$

This implies that, from the field at $z = 0$, we can calculate the field at any position along z. Since this sort of transfers the field at $z = 0$, the term $e^{\pm i\vec{k}_z z}$ is often called optical transfer function. With this, we have in principal already obtained the reason for diffraction. It is hidden in the term k_z in the optical transfer function which is defined as follows:

$$k_z = \sqrt{k^2 - {k_x}^2 - {k_y}^2}. \tag{5.10}$$

This means that if ${k_x}^2+{k_y}^2 \leq k^2$, k_z is real. The resulting wave is called the propagating wave. However, if ${k_x}^2 + {k_y}^2 \geq k^2$, k_z is imaginary and the resulting wave is called evanescent wave. It decays exponentially in z-direction. This means that in the far field the original wave at the aperture loses all frequencies for which ${k_x}^2 + {k_y}^2 \geq k^2$. Hence, at the aperture, we started with a narrow signal in real space, corresponding to a broad signal in the k-space. As the wave propagates, most frequencies in k-space are lost, causing a narrow signal. This leads to a broad signal in real space which causes spatial broadening. This diffracted image is called point spread function or Airy function.
The diffraction implies that there is an upper limit for the resolution of an optical system. The equation describing the minimal distance Δx_{Abbe} that a microscope can still resolve in an illuminated sample (i.e. not an ensemble of fluorescent emitters!) was first derived by Ernst Abbe in 1873:[185]

$$\Delta x_{Abbe} = \frac{\lambda}{2n \sin \alpha}, \tag{5.11}$$

where λ denotes the wavelength of the light used for illumination, n is the refractive index of the medium, and α half the aperture angle of the objective.
However, for fluorescence microscopy, the situation is a little different. Here, not a sample is illuminated with light, but the diffraction-limited spots of emitters itself give rise to the detected signal. Resolution is in this case defined by the so called Rayleigh criterion[186] which is schematically depicted in Figure 5.2. It states that if two fluorescent emitters are to be resolved, the maximum of the one emitter must lie above the first minimum of the second emitter or further away.[B] The corresponding equation for the minimal resolvable distance $\Delta x_{Rayleigh}$ is given by:

$$\Delta x_{Rayleigh} = \frac{1.22\lambda}{2n \sin \alpha}. \tag{5.12}$$

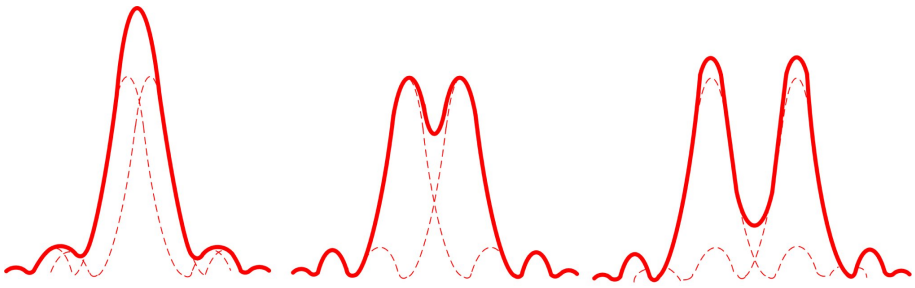

Figure 5.2: Rayleigh criterion
The maxima of two fluorescent emitters are not resolved when they are closer to each other than the distance between a maximum and the first minimum (left). If the maximum of the first is positioned above the first minimum of the second, they are just resolved (middle). If they are separated even more, they can be well resolved (right). Figure taken from reference[188]

5.1.3 Wide-Field and Scanning Confocal Microscopy

In this work, we apply two microscopy techniques: On the one hand wide-field fluorescence microscopy, on the other hand scanning confocal microscopy. Since the latter

[B] There also exists the so called Sparrow limit[187] which assumes two emitters to be resolved if there is a clear decrease of signal strength between the two maxima. However, it is not used as often as the Rayleigh criterion, maybe because its definition is not as precise.

can be seen as a special case of the first, we will first describe the principle of wide-field microscopy.
In wide-field microscopy, usually an epifluorescent illumination is used. This means that the laser employed for the excitation of the fluorophores is passing through the objective (the condenser) which also collects the fluorescence from the sample. The intensity of the laser can be tuned with an acusto-optical tunable filter (AOTF). Basically, it employs that certain materials change their permittivity upon the presence of a mechanical strain, hence, by changing the strain, the transmitted laser light can be set. To couple the laser into the objective, a dichroic mirror which reflects light below and transmits it above a certain wavelength is used. The properties of the mirror are chosen in a way that the excitation light, if it is reflected by the specimen, is again reflected by the mirror and only the emission from the fluorophore is collected. To make sure that all excitation light is blocked, filters are incorporated. If more than one laser is employed for excitation, additional dichroic mirrors and filters are used. To detect the emitted fluorescence, an array detector is used. Nowadays, it is usually a charge coupled device (CCD) camera. The biggest advantages of wide-field microscopy are the high sensitivity and the fast acquisition time which makes it, for example, suitable for single-molecule detection.[189,190] A schematic representation of the wide-field microscope used for some experiments in this thesis is given in Figure 5.3.

However, the high sensitivity and time resolution of the wide-field microscope also determines its main drawback: The low spatial resolution, especially in the axial direction. This has led to the development of the confocal microscope.[180] Here, two pinholes are introduced at the camera and at the sample which efficiently block the emission and the detection of molecules that are not in focus of the objective both in lateral and axial directions. Therefore, the sensitivity of the wide-field setup is retained while its spatial resolution is drastically improved. However, since the field of view of the detector is typically at least some microns whereas the detected area now is only the focus of the objective, i.e. in the size of a few hundred nanometers, the focus must be scanned across the sample in order to obtain the full image. Unfortunately, this makes the acquisition very slow: One image needs now seconds to be acquired. For the spectral investigation of molecules in solids at low temperatures,[191,192] for example, this is tolerable, but considering the fast dynamics of cellular components, the low temporal resolution poses a problem. For this, confocal spinning-disk microscopy has been developed. It is a compromise between the high spatial resolution of scanning

confocal microscopy and the high time resolution of wide-field microscopy. The central element of such a microscope is a spinning-disk unit as it is schematically depicted in Figure 5.4.

The laser light passes through the first disc where lenses focus the light. The second disc, which is synchronous to the first lens, features the pinholes that block out-of-focus excitation and, when the emission light passes through the disc again, also out-of-focus emission. The two discs rotate fast (several thousand revolutions per minute). Hence, the focuses are scanned very often across the sample which reduces the acquisition time down to milliseconds. However, a large fraction of the fluorescence is lost in comparison to wide-field microscopy which explains the lower sensitivity. Nevertheless, when the signal strength is not the central problem as it is in single-molecule detection, scanning-disc microscopes are the most powerful instruments, especially when it comes to life-cell imaging. In Figure 5.5, the setup of commercial spinning-disc microscope used in our experiments is schematically depicted.

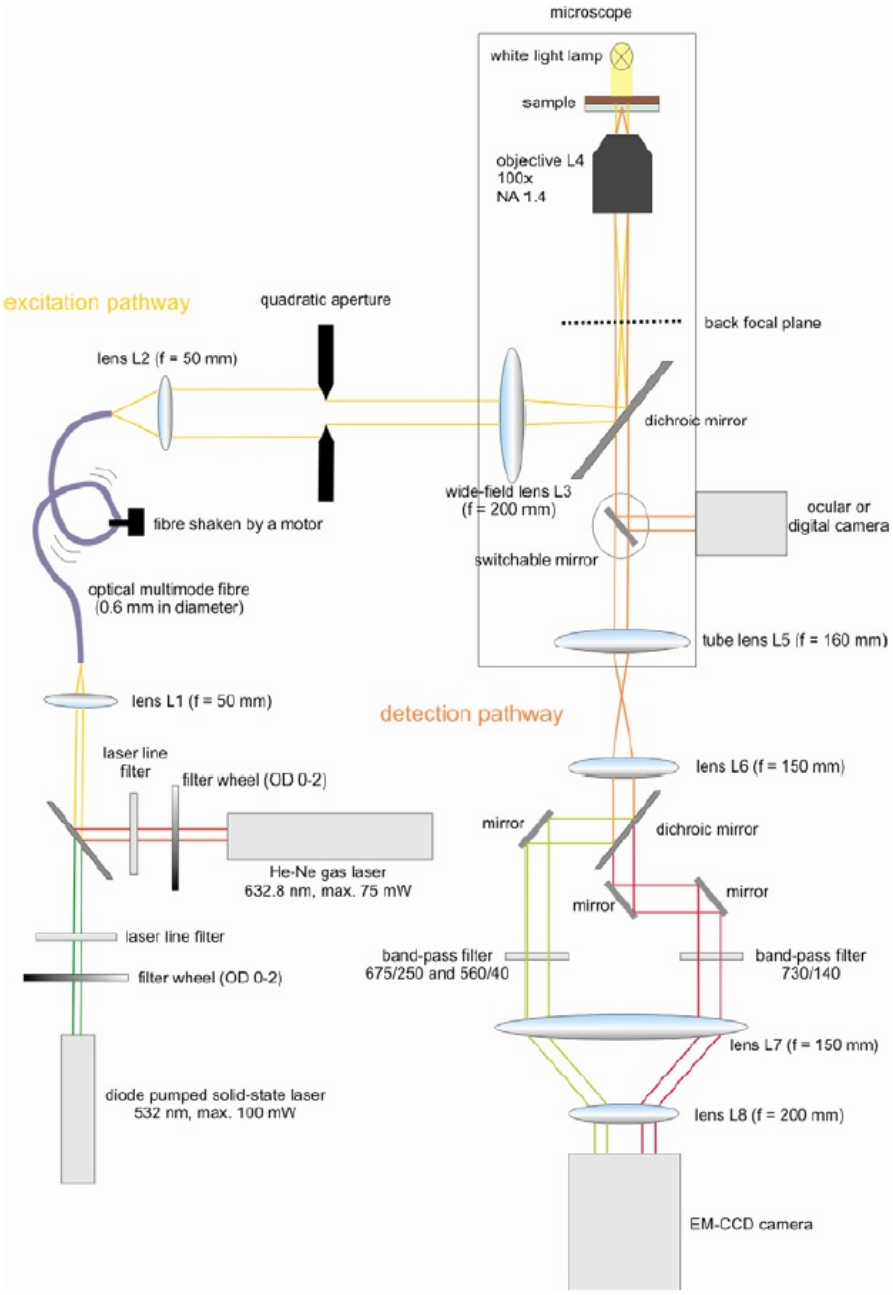

Figure 5.3: Wide-field microscope for single-molecule detection
Two lasers with wavelengths of 532 nm and 633 nm are used for excitation. They are directed through a shaken fiber. Behind the fiber, the beam is parallelized and passed through an aperture from where it is directed through a 100x objective with a numerical aperture of 1.4 to the sample. A dichroic mirror and filters are used to separate the emission before the signal is collected by an EM-CCD camera.

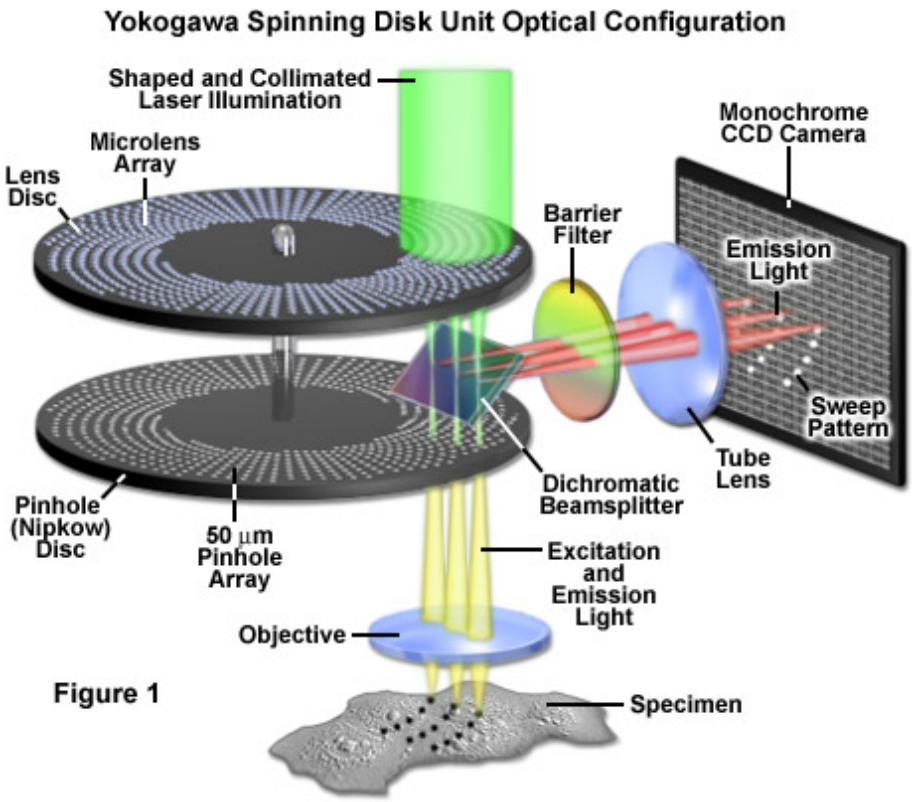

Figure 5.4: A spinning-disk unit
Laser light passes through a lens and a pinhole disc which create several focuses. They are scanned in parallel across the sample, reducing the acquisition time. Figure taken from reference[193]

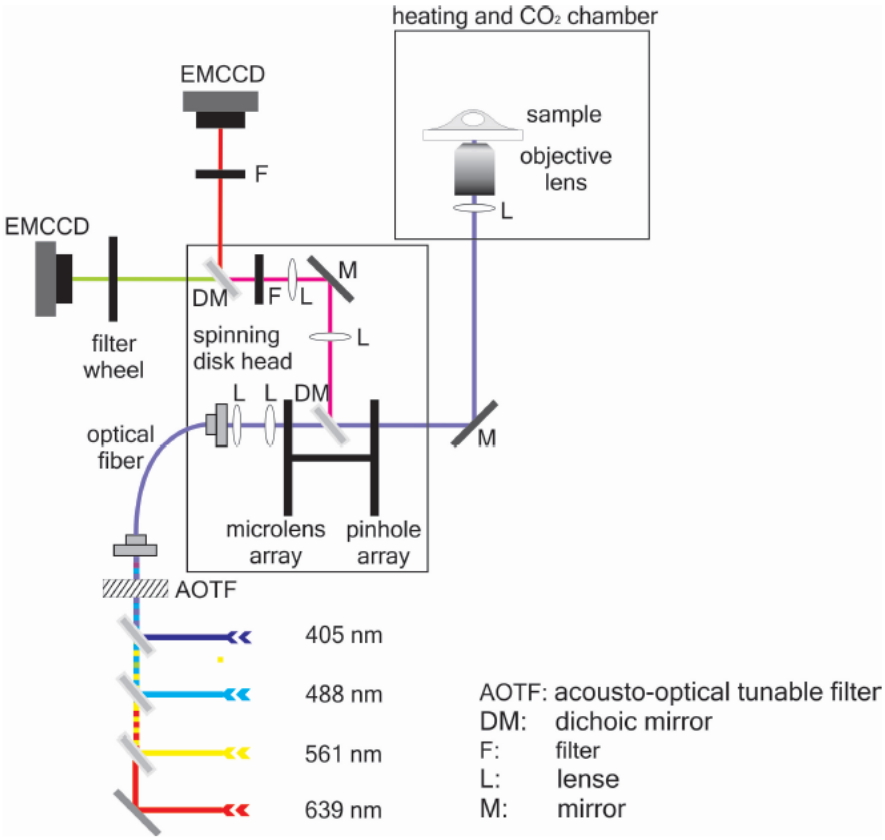

Figure 5.5: Representation of the Zeiss Cell Observer SD
Laser light of four different wavelengths is transferred to the spinning-disc unit via an optical fiber. From there, it is brought to the specimen where it excites fluorophores in epifluorescent mode. The emission light is collected, filtered, and detected by two EMCCD cameras, allowing for parallel detection of up to four fluorophores. For life-cell imaging over extended periods of time (up to days), the system features also a heated sample chamber with CO_2 atmosphere.

5.2 Principles of Single-Molecule Tracking

Tracking single particles or molecules and evaluating the recorded trajectories makes it possible to investigate the properties of a system in much more detail than methods averaging over the whole observed ensemble.[194,195] The reason is that within the average the behavior of single members of the ensemble is buried. In contrast, the investigation of individual representatives of the ensemble allows for the detection of e.g. small subpopulations or local variations. Since single-molecule tracking plays an important role in this thesis, we will describe the basis of this method briefly in the following.

5.2.1 Macroscopic Description of Diffusion

Diffusion is caused by random the thermal movement of molecules or particles in a gas, a solution, or even in solids. According to Fick's first law,[196] the flow J of particles in an ensemble caused by diffusion is proportional to the concentration gradient $\partial c/\partial x$ (here in one dimension) which runs in the direction opposite to the flow. The proportionality constant is the diffusion coefficient $D(x)$:

$$\vec{J_x} = -D(x)\frac{\partial c(x,t)}{\partial x}. \tag{5.13}$$

For the general case of three dimensions one obtains:

$$\vec{J} = -D\nabla c. \tag{5.14}$$

Returning to the one-dimensional case, one obtains, considering the conservation of mass

$$\frac{\partial c(x,t)}{\partial t} = -\frac{\partial J_x}{\partial x}. \tag{5.15}$$

This means that, for any change of concentration at a certain position, the flow must change in time accordingly. Amongst others, this states that the flow vanishes when the concentration gradient has disappeared. Substitution of Fick's first law yields:

$$\frac{\partial c(x,t)}{\partial t} = \frac{\partial}{\partial x}\left(D(x)\frac{\partial c(x,t)}{\partial x}\right). \tag{5.16}$$

If $D(x)$ is constant it follows:

$$\frac{\partial c(x,t)}{\partial t} = D\frac{\partial^2 c(x,t)}{\partial x^2}. \tag{5.17}$$

In analogy, the general term for three dimensions is given by:

$$\frac{\partial c}{\partial t} = \nabla \cdot (D\nabla c). \tag{5.18}$$

The solution of this equation quickly becomes very challenging and can often be only numerically approached. However, if one makes some simplifying assumptions (i.e. constant diffusion coefficient, no boundaries, and N particles starting to diffuse all at $t = 0$ and $x = 0$ along x and do not influence each other) the solution of this equation is not too complicated:

$$c(x,t) = \frac{N}{\sqrt{4\pi Dt}} e^{-x^2/4Dt}. \tag{5.19}$$

The solution is a Gaussian distribution with a mean of zero and variance $2Dt$. Considering the definition of the variance, one obtains:

$$\left\langle x^2(t) \right\rangle = \int x^2 c(x,t) dx = 2Dt. \tag{5.20}$$

We should keep this result in mind for a moment. Now, we turn to the microscopic description of diffusion using random walks.

5.2.2 Diffusion as Random Walk

We consider a particle that is located at $x = 0$ at time t_0. Its movement consists of single steps s that are either in direction of $+x$ or $-x$, i.e. the probability for each direction is 1/2. Furthermore, it moves with a characteristic velocity with the absolute value $|v|$. Since the particle behaves randomly, its velocity vector is $\pm\vec{v}$. Finally, we define a

certain time τ the particle needs to make one step. The distance the particle moves is then:

$$\delta = \pm |v| \tau. \tag{5.21}$$

If τ and $|v|$ are constant over all steps s (which does not need to be the case and, in fact, almost never seems to be true in complex systems[197]), the particle is at $x(s)$ after s steps, where $x(s)$ is given by:

$$x(s) = x(s-1) \pm \delta = x(s-1) \pm |v| \tau \tag{5.22}$$

or

$$x(s) = \Delta x_s + \Delta x_{s-1} + ... + \Delta_1 = \sum_{i=1}^{s} \Delta x_i. \tag{5.23}$$

Because the probability for the particle to move in direction of $+x$ is the same as moving in $-x$ (1/2), the expected mean displacement $< x >$ is of course zero. One could compare it with flipping a fair coin many times: Heads and tails will appear about equally often. Hence, every particle moves about as often to the left as to the right. However, this does not mean that the system does not evolve. Only the mean displacement is zero. To account for the evolution of the system, one introduces the mean square displacement (MSD):

$$x^2(s) = \left(\sum_{j=1}^{s} \Delta x_j \right) \left(\sum_{k=1}^{s} \Delta x_k \right) = \sum_{j,k=1}^{s} \Delta x_j \Delta x_k = \sum_{j=1, j=k}^{s} \Delta x_j^2 + \sum_{j,k=1, j \neq k}^{s} \Delta x_j \Delta x_k. \tag{5.24}$$

Since every step has the same length δ, we can rewrite as follows:

$$x^2(s) = s\delta^2 + \sum_{j,k=1, j \neq k}^{s} \Delta x_j \Delta x_k. \tag{5.25}$$

Because the probability of the particle to move left is the same as to move to the right (1/2) and we assume the movement of each particle to be independent of other parti-

cles, the second term becomes zero if we consider a large number of particles. Hence, we obtain:

$$\left\langle x^2 \right\rangle = s\delta^2. \tag{5.26}$$

Above, we have introduced a characteristic time τ that the particle needs to perform one step. It is obvious that the number s of steps the particle makes within a certain time t is equal to t/τ. It follows:

$$\left\langle x^2 \right\rangle = s\delta^2 = \frac{\delta^2}{\tau} t. \tag{5.27}$$

The values of τ and δ were both assumed to be constant, so we can define that $\delta^2/\tau := 2D$. Hence:

$$\left\langle x^2 \right\rangle = 2Dt. \tag{5.28}$$

Therefore, we obtain exactly the same result for the value of the MSD as if we analyze the problem from the perspective of the single particle which of course should be the case. However, we so far considered only one-dimensional diffusion of a freely moving particle. Next, we turn towards more realistic environments and discuss which consequences they have on the MSD curves.

5.2.3 Mean Square Displacement Curves

The movement of freely diffusing particles in isotropic environment results in the so called normal diffusion. However, diffusion usually does not take place along one, but in two or three dimensions. Considering the isotropy of the environment, one can separate the dimensions. Hence, the position vector can be split into two components: $\vec{r} = \vec{x} + \vec{y}$. For the MSD, we obtain in two dimensions:

$$\left\langle {r^2}_{2D} \right\rangle = \left\langle x^2 \right\rangle + \left\langle y^2 \right\rangle = 2Dt + 2Dt = 4Dt. \tag{5.29}$$

For three dimensions, $\vec{r}$ can be split into three components ($\vec{r} = \vec{x} + \vec{y} + \vec{z}$), hence the MSD is in this case $\left\langle r^2{}_{3D} \right\rangle = 6Dt$.

Extension to more than one dimension is of course not sufficient to cover diffusion in complex systems. In fact, normal diffusion is not the normal case – usually, one finds deviations from this behavior. Generally, four different types of diffusion are distinguished.[194,198] They are schematically depicted in Figure 5.6a-d. The corresponding equations for the MSD curves are given in Table 5.1 and the MSD curves in Figure 5.6e.

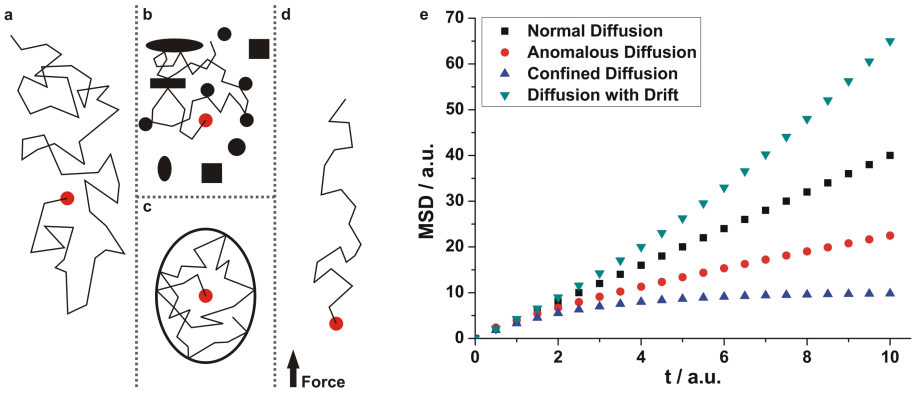

Figure 5.6: Types of diffusion

a) Normal diffusion: The diffusing particle does not encounter any barriers. b) Anomalous diffusion: The particle encounters obstacles. c) Confined diffusion: The particle is trapped in a region. d) Diffusion with drift: The particle diffuses freely and does not encounter barriers, but a constant force drives it in a certain direction. e) MSD curves: Normal diffusion (black squares) results in a straight line whereas the MSD curve for confined diffusion (red circles) bends down. However, it does not reach a limit, in contrast to confined diffusion (blue triangles). Finally, diffusion with drift (cyan triangles) yields a parabola. Parameters: $d = 2$, $D = 1$, $\alpha = 0.75$, $C = 10$, $A_1 = A_2 = 1$, $v = 0.5$

Table 5.1: Diffusion Types and MSD Curves
$d = 1, 2, 3$ for one-, two-, or three-dimensional diffusion. v is the drift velocity caused by the external force.

Diffusion Type	MSD Curve	
Normal Diffusion	$\left\langle r^2 \right\rangle = 2dDt$	
Anomalous diffusion	$\left\langle r^2 \right\rangle = 2dDt^{\alpha}$	$0 < \alpha < 1$
Confined Diffusion	$\left\langle r^2 \right\rangle = C\left(1 - A_1 e^{\frac{-2dA_2Dt}{C}}\right)$	$A_1, A_2 > 0$
Diffusion with Drift	$\left\langle r^2 \right\rangle = 2dDt + (vt)^2$	

In case of normal diffusion, the MSD curve is a straight line and follows the ideal case we derived above. As soon as obstacles are present and influence the movement of the diffusing particle, the MSD curve bends down. The more obstacles exist, the more convex is the MSD curve, proportional to t^{α} where α takes values between 0 and 1 and is the lower the more obstacles are in the way of the diffusing particle. Hence, one could picture normal diffusion just as a special case of anomalous diffusion where $\alpha = 1$. Confined diffusion is reached if the obstacles are so close to each other that the diffusing particle cannot escape a certain region. Note, however, that there is a sharp transition between anomalous and confined diffusion: No matter how small the value of α is in case of anomalous diffusion, the MSD curve has no upper limit. In contrast, in case of confined diffusion, such a limit exists (C) since the term in brackets approaches to 1 for sufficiently large t. The two constants A_1 and A_2 account for the geometry of the confinement. Finally, if an external force is present that induces a drift – like an electric field or a flow of the medium in which the diffusion occurs – the MSD curve is no longer linearly dependent on t, but quadratic. For increasing t, the quadratic term naturally dominates.

5.2.4 Tracking and Positioning Accuracy

As discussed in Chapter 5.1.2, an emitting molecule with a size of a few nanometers appears on a detection screen or a camera as a blurred spot with a size of several hundreds of nanometers due to diffraction within the optical imaging system. The key idea underlying single-molecule tracking is that although the signal of the molecule is blurred, one is able to determine its position with much higher accuracy.[199,200] The

only requirement is that one really detects a single emitter, but this can be ensured easily by dissolving the fluorescent species to low concentrations (typical concentrations are 10^{-9} to 10^{-12} M). Provided that the emission originates from a single molecule and detection takes place in two dimensions, a 2D-Gaussian can be fitted to the fluorescence signal where the x- and y-coordinates are the spatial dimensions and the z-coordinate encodes the fluorescence intensity:[C] The formula for the 2D-Gaussian is given by:

$$f(x,y) = Ae^{-\left(\frac{(x-x_0)^2}{2{\sigma_x}^2}+\frac{(y-y_0)^2}{2{\sigma_y}^2}\right)}, \tag{5.30}$$

where A is the amplitude, x_0 and y_0 are the coordinates of the center in x and y and σ_x and σ_y are the spreads in x and y. The center of the Gaussian is then used as the position of the emitter as schematically depicted in Figure 5.7. If this way the movement of a fluorophore is recorded over time, for example a fluorescent label attached to a protein diffusing in a cell membrane, a trajectory T is obtained. Recording many trajectories is required to reduce statistical variations naturally occurring. From the coordinates of the emitter at each point in time the MSD can then easily be extracted:

$$\left\langle r^2(\tau)\right\rangle = \lim_{n\to\infty}\frac{1}{N}\sum_{i=1}^{N}[\vec{T}_i(\tau)-\vec{T}_i(0)]^2. \tag{5.31}$$

Since the localization accuracy is of high relevance not only for single molecule tracking, but also for super-resolution microscopy, the basis of localization microscopy should be discussed briefly in the following. As it was derived above, the resolution in conventional fluorescence microscopy is limited because emitters cannot be separated if they are too closely together. On the other hand, if one can be sure to detect the signal of a single emitter only, its position can be determined with nanometer accuracy. The key idea of all super-resolution techniques is to enforce the emitters densely labeling a

[C] As we described above, the signal of the emitter is in fact not a Gaussian, but a PSF. However, for three reasons fitting with a Gaussian is justified: First, the main contribution of the PSF is the central maximum, already the first side maximum is very small. The error is therefore small if one neglects the side maxima. Second, a Gaussian exhibits radial symmetry around the center just as the PSF. Hence, the error even becomes smaller if one is only interested in determining the position of the center. Third, a Gaussian is easy to fit which results in low computation times.

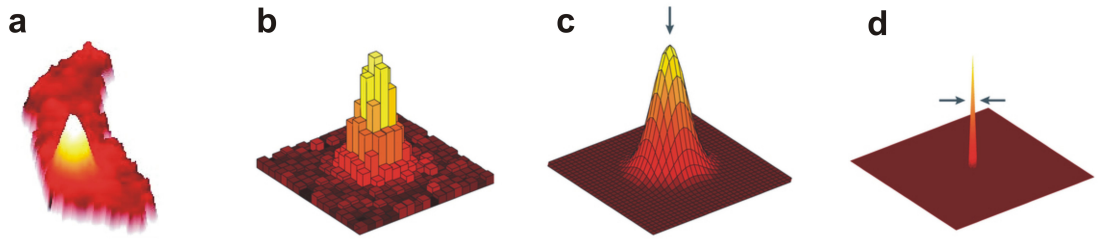

Figure 5.7: Diffraction limited detection and localization accuracy.
When photons are detected from a single emitter, they form a diffraction-limited pattern called the PSF. The above figures show (a) the original PSF of a single YFP molecule in a bacteria cell, (b) the pixelated PSF measured on the camera, (c) a two-dimensional Gaussian fit to the PSF and (d) the high-precision localization of the emitter determined from the center of the PSF. Figure taken from references[201,202]

structure[D] not to emit all at the same time (which would result in a diffraction limited image), but sequentially. This can either be in space (localization microscopy)[200] or in time (depletion microscopy).[205,206] In depletion microscopy (stimulated emission depletion, STED, microscopy), only a very narrow area of emitters is allowed to fluoresce normally at a time while the emitters around are forced to emit with a defined wavelength which is filtered. This allows to image with higher resolution than in conventional fluorescence microscopy. Localization with high precision does not play a role here. In contrast, precise determination of the position of a single emitter is the basis common to all localization microscopy techniques (Figure 5.7).

The following text follows "Nobel Prize in Chemistry 2014 for Erik Betzig, Stefan Hell, and William E. Moerner" by Leonhard Möckl, Don C. Lamb, and Christoph Bräuchle, Angewandte Chemie 2014

Although the intensity profile of a single fluorescent emitter is subject to diffraction, its center can be localized with much higher precision: Whereas the size of the emitter molecule is about 1 nm, the fluorescent spot produced by diffraction within the microscope is actually 200 nm. Figure 5.7a/b shows the intensity profile of such a diffraction-limited signal referred to as the point spread function (PSF), which can be

[D] The dense labeling is necessary because otherwise the structure would not be represented correctly. The reason for this is the Nyquist sampling criterion[203,204] which was originally formulated for signal processing applications and time frequencies, but also holds for imaging. It states that a signal in time can only be represented by a discrete sequence if the distance between the points of the sequence is not too large, i.e. the sampling rate must not be too low. This can be fully translated to spatial frequencies.

approximated by a two-dimensional Gaussian function (Figure 5.7c). Provided the detected signal is generated by only one emitter (i.e. a single molecule), the center of the PSF determines the position of the emitter with very high accuracy (often called super localization). As the number of photons detected from a single emitter increases, the accuracy with which the peak position of the PSF can be determined improves and the position of a single emitter can be localized more precisely. Hence, Abbe's formula can be modified to incorporate the enhanced localization precision:

$$\Delta x_{min}, \Delta y_{min} = \frac{\lambda}{2n \sin \alpha} \cdot \frac{1}{\sqrt{N}} \tag{5.32}$$

where N is the total number of photons detected. Thus e.g. with 100 detected photons, the resolution for the localization of a single emitter is increased by a factor of 10 (Figure 5.7d). This high-resolution microscopy paved the way for tracking single molecules with nanometer localization accuracy (FIONA, 1.5 nm) unraveling, for example, the hand-over-hand movement of the motor protein Myosin V[208] or the three-dimensional movement of mRNA particles in yeast cells.[209]
Whereas one emitter is sufficient for single molecule tracking, microscopy of complex structures needs many emitters (labels) in order to visualize their features correctly (Figure 5.8a). However, when all the labels are excited simultaneously (Figure 5.8b), high-precision localization of the individual emitters is no longer possible due to the overlapping of the PSFs, leading to a blurred or non-resolved image. This is what is measured in a conventional optical fluorescence microscope. Unfortunately, sparse or diluted labeling of the structures, resulting in separated PSFs, is not sufficient for imaging the structure correctly due to under sampling of the image as described by the Nyquist-Shannon-criterion.[203,204] In other words, one needs a high concentration of emitters to resolve the features of the structure correctly while, at the same time, a low concentration is needed in order to separate the PSFs of the individual emitters for performing high-precision localization microscopy.
It was Erik Betzig who first made a valuable suggestion[210] for a solution to this contradiction. His idea was to isolate the emitters by some spectral property. The separated subsets of emitters each form a sparse set in space. Hence, the position of the emitters within one subset can be determined with high accuracy. By sequentially measuring all the subsets, a super-resolution image can be generated by combining all the high-precision localizations. At that time, the optical property Betzig suggested for sepa-

rating the individual subsets was the inhomogeneity in the absorption wavelength.[211] However, this turned out to be difficult to realize.
It was W. E. Moerner who, after getting the ball rolling, contributed to an alternate solution. When he investigated mutants of the green fluorescent protein (GFP), he encountered a strange photophysical behavior of the T203F mutant.[212] The mutant fluoresced when illuminated with 488 nm light and eventually switched into a non-fluorescent dark state. Amazingly, it was not irreversibly photobleached but could be reactivated by 405 nm illumination (Figure 5.8c). This finding triggered the search for other GFP mutants with similar photophysical switching characteristics, although they were not originally designed with subdiffractive microscopy in mind.[213]
It took Betzig, returning to university after some years of working in industry, to "connect the dots" and make the final step towards super-resolution microscopy. He recognized that such photoactivable (pa) fluorescent proteins are capable of solving the problem of sparse and dense labeling in the following way: The sample is labeled densely with paGFP molecules that are in a dark state at the beginning of the experiment. With a low-powered laser pulse having the appropriate wavelength, a few fluorescent proteins are stochastically transferred to the active state so that they form a sparse subset. They are subsequently visualized by 488 nm excitation in a single molecule manner until they completely photobleach. After photobleaching, new fluorescent proteins are activated in the following frames and the cycle starts over again (Figure 5.8d). Finally, one obtains the full, complex picture in high resolution by summing up all the highly resolved single emitters of each frame (Figure 5.8e). The tremendous gain in resolution is best visualized by two images taken from Betzig's 2006 landmark publication[214] where he introduced the technique as Photo-Activated Localization Microscopy or PALM with a resolution of typically about 20 nm (Figure 5.9).

In summary, two key elements are required to create a super-resolution image of a complex structure by localization microscopy. First, the fluorophores labeling the structure must be actively controllable in such a way that in every image frame only a sparse subset of labels are emitting and that hence their diffraction-limited signals are spatially well separated. Second, each diffraction-limited PSF of a single molecule has to be fitted with an appropriate model function in order to estimate the position of the emitter with high precision. The collection of molecular positions determined with high accuracy allows then the reconstruction of the structure in a pointillist fashion.

Besides PALM, two other ways of producing super-resolved images by localization microscopy using different actively controlled fluorophore switching mechanisms were introduced in 2006: fPALM,[215] and STORM.[216] In the meantime, numerous sophisticated approaches using actively controlled fluorophore switching mechanisms have been developed.[217] However, there are also limitations to be overcome. One is that high-quality super-resolution images need a lot of individual localizations, limiting the overall time resolution. Moreover, image reconstruction needs time-consuming post processing. In addition, life does not take place in two dimensions, but is three-dimensional. Numerous new schemes have been developed to account for this. Among others, astigmatism-[218] and double helix PSF-based imaging[219] were introduced to provide super-resolution localization in the z-dimension. Additional advances include multicolor imaging[220] and faster data collection and analysis methods for video-rate imaging.[221]

Considering that the high positioning accuracy was known for a long time, it is maybe a little surprising that it took until the mid 90s for the technique of localization microscopy to be theoretically described and another 10 years for it to be experimentally implemented. However, since then it has become a powerful method to elucidate processes otherwise not accessible with fluorescence microscopy techniques. Because of this, and because it changed the way we think about optical resolution, the discovery of super-resolution optical microscopy was awarded the Nobel Prize in Chemistry 2014.[181]

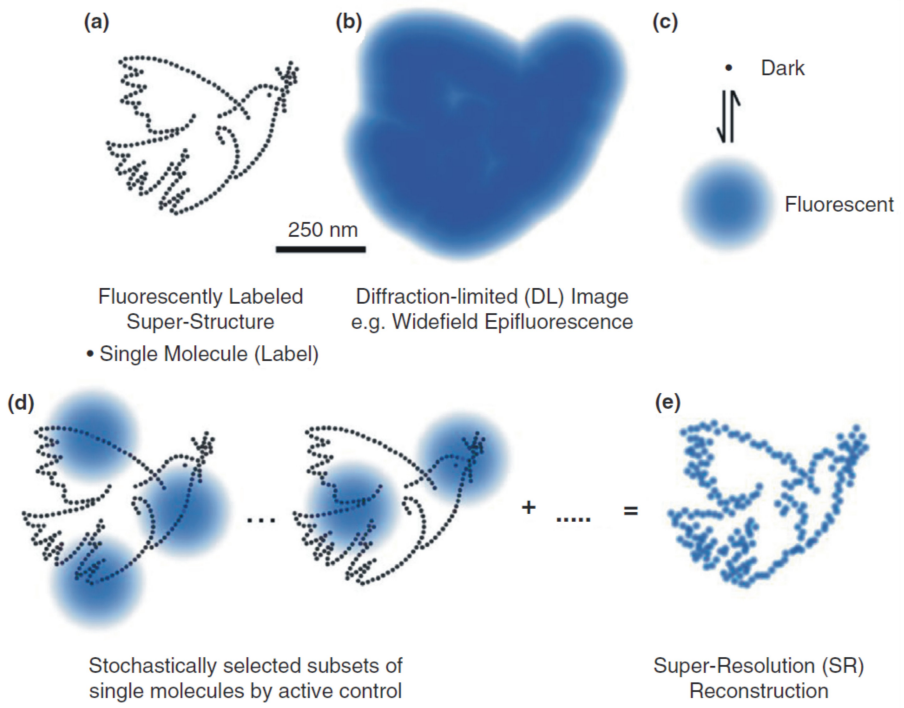

Figure 5.8: The principle of localization microscopy.
(a) An arrangement of fluorescent molecules representing La Paloma de la Paz (P. Picasso, 1961) with a spatial frequency below the diffraction limit. (b) Were this structure to be visualized by conventional microscopy, Abbe's criterion forbade resolution of the individual features. (c,d) However, by stochastically switching molecules between a fluorescent state and a dark state, the PSF of a few sparse emitters can be acquired in each acquisition step. Their positions are determined with high precision and (e), in a pointillist approach, the results of all localizations are combined to obtain a super-resolved reconstruction of the object. Figure taken from reference[207]

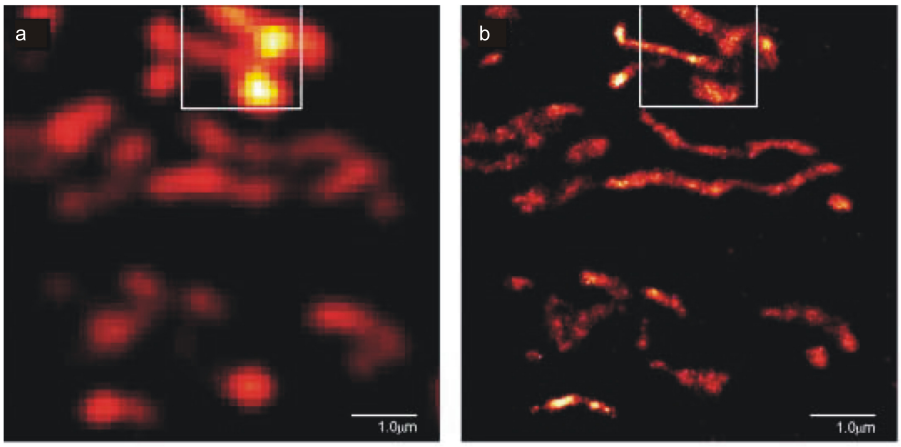

Figure 5.9: Super-resolved images of mitochondria in COS-7 cells.
(a) A Total Internal Reflection Fluorescence (TIRF) microscopy image and (b) the PALM super-resolution image of mitochondria in COS-7 cells. The mitochondria were labeled using a photoactivable fluorescent protein (dEosFP) targeted to the matrix of the mitochondria. Whereas only the approximate shape of the mitochondria can be resolved using TIRF microscopy, PALM microscopy exhibits features on the length scale of some tens of nanometers, well below the diffraction limit. Figure taken from reference[214]

6 Glycosylation Influences Spatiotemporal Membrane Protein Dynamics

This chapter is based on: **"Microdomain Formation Controls Spatiotemporal Dynamics of Cell-Surface Glycoproteins"** by Leonhard Möckl, Andrea K. Horst, Katharina Kolbe, Thisbe K. Lindhorst, and Christoph Bräuchle
ChemBioChem **16**, 2023 (2015)[222]

Acknowledgements:
LM conducted and evaluated the experiments and wrote the manuscript.
AK, KK, TKL, and CB wrote and corrected the manuscript.

6.1 Abstract

The effect of galectin-mediated microdomain formation on the spatiotemporal dynamics of glycosylated membrane proteins in human microvascular endothelial cells (HMEC-1) was studied qualitatively and quantitatively by high-resolution fluorescence microscopy and artificially mimicked by metabolic glycoprotein engineering. Two types of membrane proteins, sialic acid-bearing proteins (SABPs) and mucin-type proteins (MTPs), were investigated. For visualization they were metabolically labeled with azido sugars and then coupled to a fluorescent dye, conjugated to cyclooctyne, by click chemistry. Both spatial (diffusion) and temporal (residence time) dynamics of SABPs and MTPs on the membrane were investigated after treatment with exogenous galectin-1 or -3. Strong effects of galectin-mediated lattice formation were ob-

served for MTPs (decreased spatial mobility), but not for SABPs. Lattice formation also strongly decreased the turnover of MTPs (increased residence time on the cell membrane). The effects of galectin-mediated crosslinking was accurately mimicked by streptavidin-mediated crosslinking of biotin-tagged glycoproteins and verified by single-molecule tracking. This technique allows the induction of crosslinking of membrane proteins under precisely controlled conditions, thereby influencing membrane residence time and the spatial dynamics of glycans on the cell membrane in a controlled way.

6.2 Introduction

The dynamics of proteins on the cell membrane are essentially characterized by two processes: diffusion inside the membrane resulting in lateral movement (spatial dynamics), and membrane- protein transportation to their destinations on the membrane after biosynthesis and retraction back into the cell after a certain time, thus resulting in a membrane residence time as a function of the incorporation and internalization kinetics (temporal dynamics). These spatiotemporal dynamics are influenced by the formation of microdomains, caused by a complex molecular interplay at the cell surface.[101,223–225] One way for the cell to control microdomain organization is glycosylation of membrane proteins.[104,226] Glycosylated cell-surface proteins can assemble into supramolecular structures by interacting with highly abundant lectins such as galectins.[227–229] Both galectin-1 and -3 are N-acetyllactosamine (LacNAc)-specific; galectin-1 exists as a divalent homodimer, whereas monomeric galectin-3 can self-associate into multimeric complexes.[230,231] It is known that the interaction between galectins and glycans is highly regulated.[232,233] Importantly, galectins as scaffold proteins build up the "galectin lattice", thereby leading to, for example, regulation of receptor signaling.[228,232] However, the effects of galectin lattice formation on spatial and temporal dynamics have not been studied. It is important to understand the full dynamics of membrane proteins, including the formation of microdomains as this influences many crucial cellular processes.

6.3 Results and Discussion

We used fluorescence microscopy with human microvascular endothelial cells (HMEC-1) and galectin-1 and -3 to demonstrate the effect of the galectin lattice on the spatiotemporal dynamics of glycoproteins. LacNAc-containing mucin-type glycoproteins (MTPs) were investigated as galectin ligands and compared to sialic acid-bearing glycoproteins (SABPs), which are not interconnected by galectins. We also established streptavidin (SA)-mediated crosslinking of biotinylated MTPs and SABPs as an artificial and robust, galectin-independent method to induce lattice formation and investigated its influence on spatiotemporal membrane protein dynamics (Figure 6.1).

We employed metabolic labeling to visualize cell-surface glycoproteins by fluorescence microscopy.[149,156,234,235] HMEC-1 were incubated with tetraacetylated *N*-azidoacetyl-D-mannosamine (Ac_4ManNAz) to target SABPs, or with tetraacetylated *N*-azidoacetyl-*d*-galactosamine (Ac_4GalNAz) to target MTPs. In a second step, the azido groups were addressed by a membrane-impermeable cyclooctyne-AlexaFluor647 derivative in a bioorthogonal conjugation reaction. This procedure resulted in fluroescence-labeled SABPs and MTPs, respectively (Figure 12.2, Figure 12.3, Figure 12.4, Figure 12.5), whereat there may be proteins belonging to both groups (Figure 12.6). In the next step, 3.3 µg mL^{-1} galectin-1 or-3 was added to the fluorescence-labeled cells to induce additional galectin lattice formation with cell-surface MTPs. FRAP experiments then were performed to measure spatial mobility of the labeled glycoproteins (Figure 6.2).[236] The bleaching spot was localized at the cell membrane, and each cell was measured once. Due to carbohydrate- independent mechanisms that decrease the mobility of all membrane proteins, such as attachment of membrane proteins to the cytoskeleton, the mobile fraction does not reach a ratio of 1.[237,238]

Thus, even prior to the addition of exogenous galectin, the SABP mobile fraction reached only about 0.3, and for MTPs it was approximately 0.23. The difference might be a consequence of the MTP-galectin lattice on cultured HMEC-1, thus leading to reduced MTP mobility. Indeed, we confirmed the expression of galectins-1 and -3 by immunohistochemistry (Figure 12.7). Also, galectin expression by HMEC-1 has been reported before.[239–241] However, exogenous addition of galectin-1 and -3 induced a further, significant decrease in the MTP mobile fraction as expected, whereas the SABP mobile fraction did not decrease significantly. This also indicates that the fraction of proteins belonging both to SABPs and MTPs is not dominant, as galectin treatment

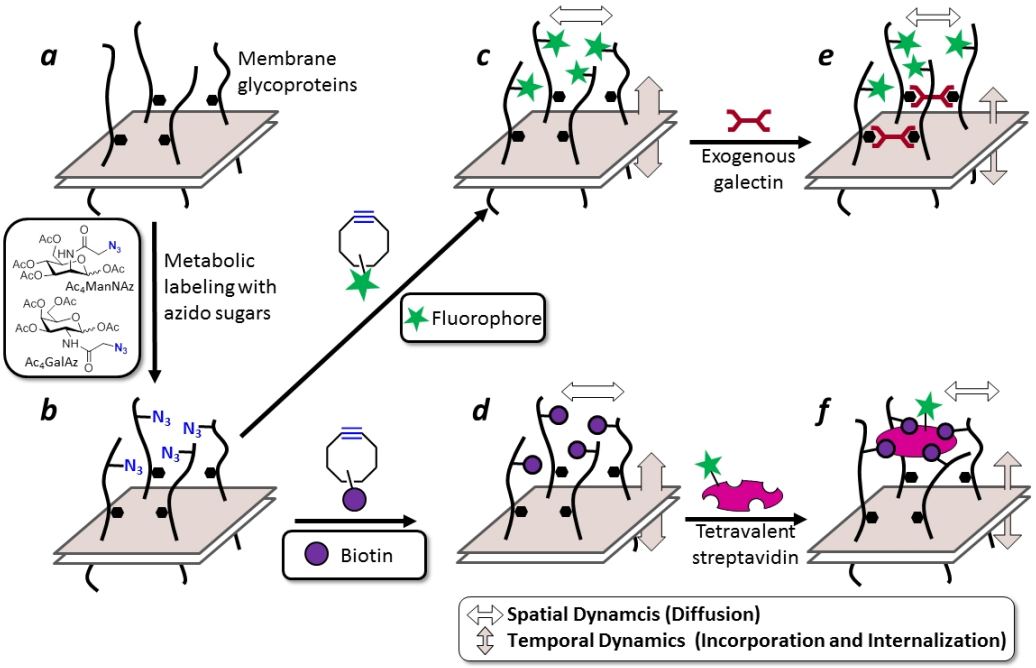

Figure 6.1: Experimental approach.
Membrane glycoproteins (a) were tagged with azido groups by labeling with Ac_4-ManNAz or Ac_4GalNAz (b). In a second step, either a fluorescent dye (c) or a biotin (d) was coupled to the azido groups by copper-free click chemistry. The fluorescence of the specifically labeled membrane glycoproteins was used to investigate their spatial dynamics (diffusion inside the membrane) and temporal dynamics (incorporation into the membrane and internalization back to the cell interior) as a function of galectin-induced microdomain formation (e). The biotin tag was employed to induce artificial, streptavidin-mediated crosslinking of membrane proteins (f). Visualization of the spatiotemporal dynamics used fluorescently labeled streptavidin.

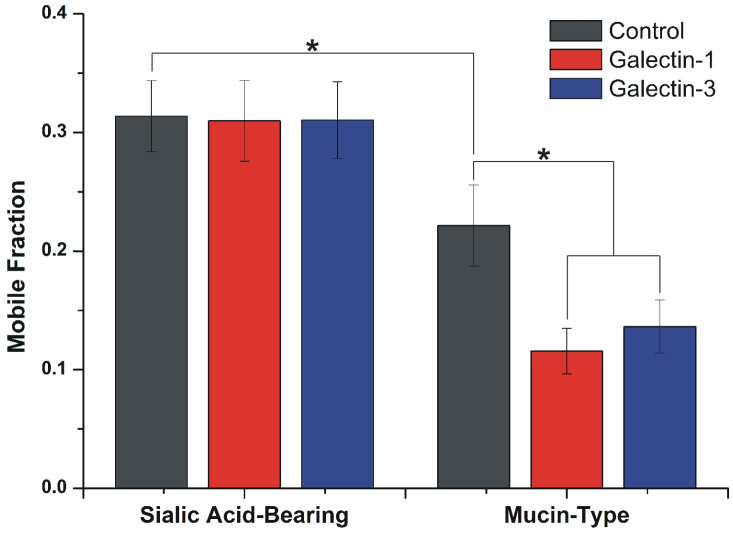

Figure 6.2: Effects of exogenous galectin-1 or -3 on spatial mobility of membrane glycoproteins determined by FRAP
The mobile fraction of MTPs (galectin ligands) decreases upon addition of 3.3 mg mL^{-1} galectin-1 or -3, caused by crosslinking (formation of galectin lattices). For SABPs, only small decreases are visible. Data are mean ±SEM (n=29 or 30); t-test $^{*}p<0.1$.

affects only proteins labeled by Ac_4 GalNAz (MTPs) and not by Ac_4ManNAz (Figure S5). Our results are in line with previous studies where the influence of glycosylation on the behavior of specific proteins was investigated.[242–244]

To further demonstrate the functional importance of microdomain formation on cell membrane protein dynamics, we designed a set of experiments to mimic the effects of galectin lattice formation, again by employing metabolic glycoprotein engineering. A cyclooctyne-biotin conjugate was added to azidemodified glycoproteins (Figure 6.1b), thereby yielding biotintagged membrane glycoproteins (Figure 6.1d). The modified proteins could be crosslinked by SA displaying four binding sites for biotin (Figure 6.1f), and thus this multivalent interaction enabled lattice formation. By prior addition of free biotin, the degree of SA-induced lattice formation could be controlled: for example, the natural tetravalency of SA homotetramers can be switched to a mean valency of two, resulting in reduced binding capacity for biotin-tagged glycoproteins. This allowed us to measure glycoprotein mobility as a function of the valency of the crosslinking SA. Biotin-tagged membrane proteins were incubated with 1.25 mm fluorescent di- or tetravalent SA for 20 min to induce artificial SA-mediated network

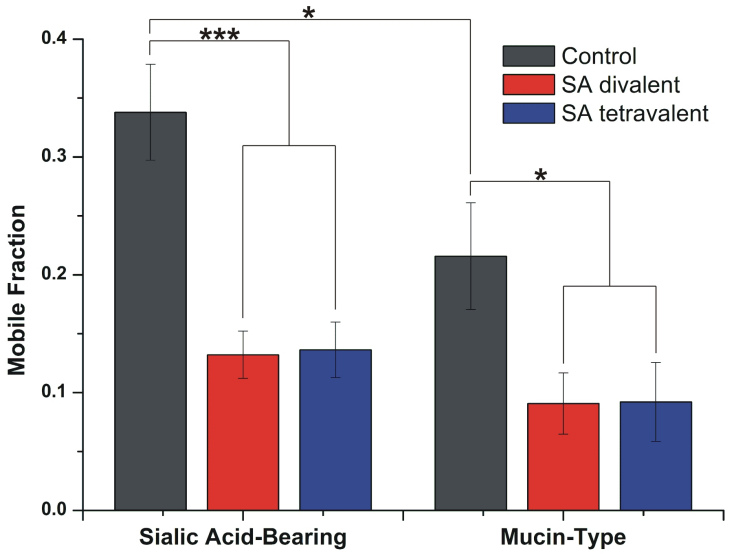

Figure 6.3: Effect of di- and tetravalent SA on spatial mobility of biotin-tagged membrane glycoproteins.
Both di- and tetravalent SA lead to a significant decrease in the mobile fraction. Data are mean ±SEM (n=27-29); t-test, *p<0.1, ***p<0.0001

formation, then spatial mobility was measured by FRAP. Other than in the case of carbohydrate-specific galectin crosslinking (Figure 6.2), SA-mediated crosslinking reduced the mobile fractions of biotin-tagged SABPs and biotin-tagged MTPs comparably (Figure 6.3). Notably, divalent SA (two ligand-binding sites like galectin-1) resulted in effective reduction of the mobile fraction of membrane proteins: the mobile fractions of SABPs and MTPs are reduced to about 0.1. crosslinking actually form a network, we investigated the movement of individual SA molecules labeled with Alexa-Fluor647 by single-molecule tracking.[194,198,245–249] For this, we used two types of SA: tetravalent (capable of forming networks) and monovalent (no crosslinking capability, but able to bind and label biotin-conjugated glycans). Biotin-tagged membrane proteins were incubated for 20 min with 1.25 mm mono- or tetravalent SA. The concentration of fluorescent SA was 0.1 nm, typical for single molecule experiments. Then, the movement of single SA molecules on the cell surface was tracked (0.0513 s/frame) and their trajectories were recorded (representative examples in Figure 6.4a; several hundred to a few thousand trajectories for each condition).[194,198,248,249]

The single-molecule tracking data corroborated the results obtained from the bulk measurement by FRAP. Clearly, tetravalent SA resulted in much lower spatial mobil-

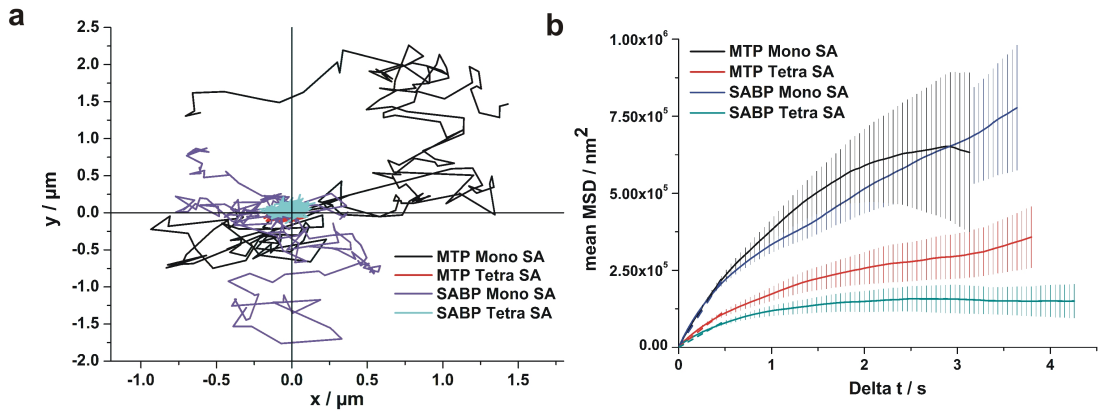

Figure 6.4: Representative tracks of SA on the surface of HMEC-1 with biotin tagged MTPs or SABPs.

a) Five tracks for each glycoprotein type, shifted to a common origin. b) MSD (mean square displacement) analysis. The trajectories of tetravalent SA cover a much smaller area (largely overlapping) than those of monovalent SA, thus indicating low spatial mobility as a result of effective crosslinking. Accordingly, the slopes of the MSD curves are significantly lower for tetravalent SA-mediated crosslinking than for monovalent SA. Dashed lines indicate the linear fit to the linear part at the beginning of the curves. Error bars are given as the weighted standard deviation divided by the square root of the number of degrees of freedom.

ity than monovalent SA, as indicated by the small, mostly overlapping area that is covered by the trajectories displayed in Figure 6.4a. Furthermore, the mean square displacement (MSD) curves (Figure 6.4b) obtained from the single-molecule trajectories[194,198,249] show three different types of diffusion for monovalent and tetravalent SA: 1) for very short times (dashed lines in Figure 6.4b), diffusion is normal with much higher slopes for monovalent SA (diffusion coefficient $D = 1.21 \cdot 10^{-5}$ nm^2 s^{-1} for MTPs, $1.18 \cdot 10^{-5}$ nm^2 s^{-1} for SABPs) than for tetravalent SA ($D = 5.98 \cdot 10^{-4}$ nm^2 s^{-1} for MTPs, $4.32 \cdot 10^{-4}$ nm^2 s^{-1} for SABPs); 2) anomalous diffusion over larger time ranges for monovalent SA, with comparable behavior for MTPs and SABPs; and 3) confined diffusion for longer time ranges for tetravalent SA, again with comparable behavior for MTPs and SABPs (confinement area=$3.71 \cdot 10^{-5}$ nm^2 for MTPs, $1.55 \cdot 10^{-5}$ nm^2 for SABPs). Our results are in good agreement with a recent study investigating the mobility of glycans in the membranes of cancer cells.[250] The confined diffusion of tetravalent SA can be attributed to the simultaneous binding of several biotinylated membrane proteins, thereby restricting their movement to a limited area.[194,198] From the data we obtained on the effects of natural and artificial crosslinking on the spatial dynamics

of cell-surface proteins, the question arose as to whether lattice formation also influences the temporal dynamics of membrane proteins (incorporation of glycans into the cell membrane and internalization back into the cell). The internalization can be followed more directly than incorporation, as the latter is blurred because of the complex biosynthetic pathways (Figure 12.9). This was done by fluorescent labeling of the azide-tagged membrane glycoproteins once, followed by observation of the decay of membrane fluorescence after labeling caused by the internalization of the membrane proteins. Enhanced galectin lattice formation on the cell membrane should lead to stronger interconnection of membrane glycoproteins, and hence their relative internalization rate should decrease because of the more difficult internalization of the crosslinked membrane proteins. Therefore, we fluorescently labeled MTPs and SABPs once, incubated them with 0, 0.3, 1.3, or 3.3 mg mL^{-1} galectin-1 and -3, and measured the residual membrane fluorescence after 5 h. The values were compared, that is, normalized to the decreased membrane fluorescence of untreated cells after 5 h.

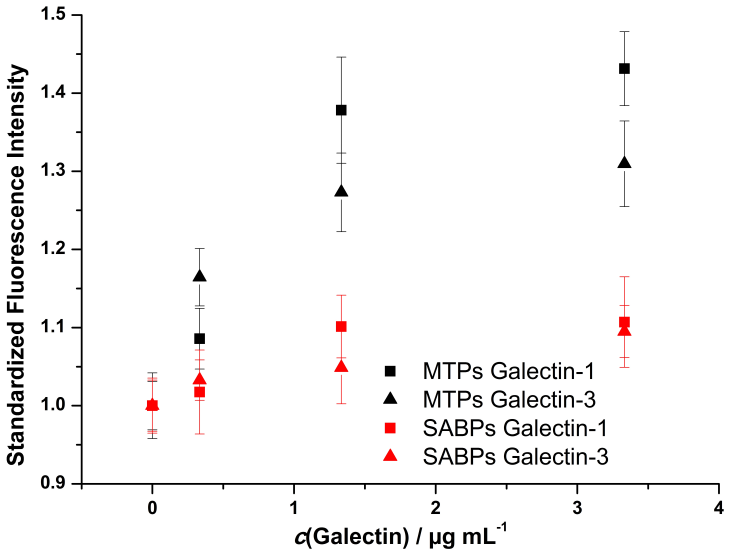

Figure 6.5: Effects of exogenous galectin-1 and -3 on membrane protein internalization. Internalization of MTPs, and to a lesser extent SABPs, is slowed by increasing amounts of galectin-1 and -3. Normalized fluorescence intensity: ratio of membrane fluorescence of galectin-treated cells to untreated cells after 5 h. Data are mean ±SEM (n=28-30).

The membrane fluorescence of galectin-treated cells decreased more slowly than that of untreated cells; we measured an increase in the normalized membrane fluorescence, which reached a constant at approximately 1.3- to 1.4-times higher than that of un-

treated control cells (Figure 6.5). The relative internalization rates of SABPs were also affected, albeit to a much lesser extent, as expected. (The measured effect is again attributed to some galectin-binding sites on SABPs.) Hence, not only spatial mobility on the cell surface, but also internalization of MTPs was strongly reduced by exogenous addition of galectin-1 and -3. We also wanted to demonstrate that artificial lattice formation leads to a decelerating effect on membrane protein internalization. For this, biotin-tagged membrane proteins were interconnected with 1.25 mm fluorescent di- or tetravalent SA. Membrane fluorescence was quantified after 5.5 h or directly after SA-treatment (0 h). The ratio of mean membrane fluorescence after 5.5 h to that at 0 h represents the amount of proteins that remains on the membrane after 5.5 h (Figure 6.6).

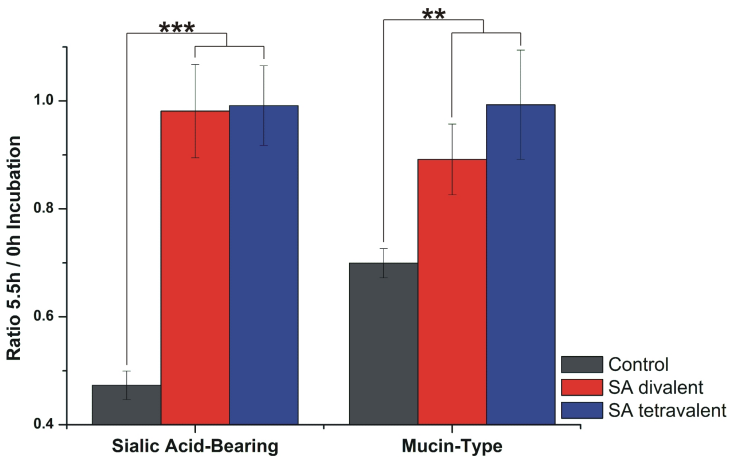

Figure 6.6: Effects of di- and tetravalent SA on internalization of biotin-tagged membrane proteins.
For both SABPs and MTPs internalization is strongly slowed by addition of di- or tetravalent SA. The ratio (0.88-0.96) between membrane fluorescence at 5.5 h and 0 h indicates that little internalization occurred over this time. Untreated cells showed much higher internalization. Data are mean ±SEM (n=29-30); t-test:**$p<0.01$, ***$p<0.0001$.

Addition of both di- and tetravalent SA to biotin-tagged SABPs and MTPs slowed glycoprotein internalization drastically (very little decrease in membrane fluorescence was seen within 5.5 h), whereas untreated cells showed a significant decrease in membrane fluorescence (Figure 12.8). Furthermore, the change in internalization rate will certainly affect the incorporation process similarly, as these processes are metabolically coupled (Figure 6.7). In a model we simulated the mutual dependence of the

processes (Figure 6.7, Figure 12.10, Figure 12.11). As mentioned above, we chose to observe internalization because it can be measured directly. Nevertheless, we also detected higher relative incorporation rates for SAPBs than for MTPs (Figure 12.12 and Figure 12.13). This finding is fully consistent with our simulations. Taken together, our experiments confirm that the spatiotemporal dynamics of membrane glycoproteins is causally linked to their glycosylation type and their engagement into scaffoldinduced lattice formation. As glycoproteins of the mucin type show higher affinity to galectin-1 and -3 than SABPs, their incorporation into galectin lattices is enforced, thereby resulting in prolonged residence on the cell membrane and lower spatial mobility relative to untreated cells. Using metabolic labeling, we were able to experimentally separate the two protein types. Artificial, SA-induced lattice formation has the same effect, however, for both glycoproteins (MTPs and SABPs), as lattice formation in this case is not carbohydrate-specific. The SA-based approach to mimic lattice formation is a versatile, artificial, and precisely controllable technique to influence and manipulate mobility, location, and clustering of cell-surface proteins. As the spatiotemporal dynamics of particular cell-surface proteins regulate important cellular processes (e.g., cellular signaling), this method will allow researchers to influence key functions of a cell. In future experiments we intend to employ the regulating potential of artificial microdomain formation to further investigate the influences of cell-surface glycoprotein dynamics on cell biology.

6.4 Simulation of Membrane Protein Internalization

This work was not part of the published article.

As mentioned above, in order to investigate the interplay between membrane protein internalization and incorporation in more detail, we set up a simple model to test how the simulated behavior matches the observations. Here, we will describe it in more detail. In the model, we considered the relevant compartments for glycosylation and physiologically reasonable correspondence between them. This is schematically depicted in Figure 6.7.

From this, we derived a straightforward system of coupeled differential equations that fully describe the system and can be solved numerically with arbitrary accuracy:

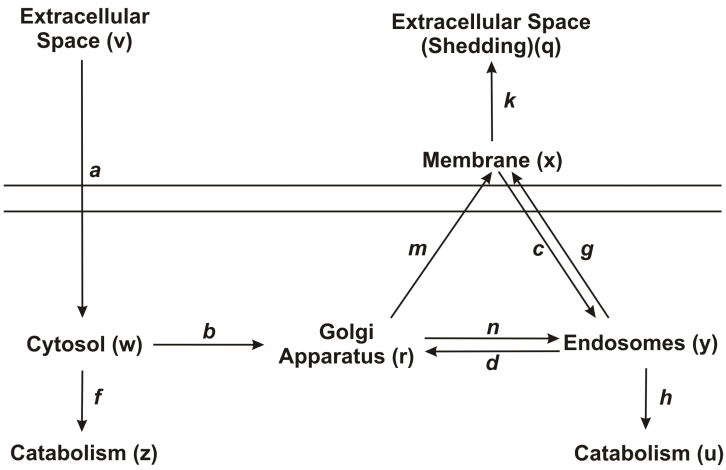

Figure 6.7: Simulation of cellular compartments and metabolite flow through them. We assume that a constant flow of metabolites is presented from the extracellular environment. They are internalized and then either used to generate energy or to build glycan structures.

```
With[{a = 1, b = 0.5, c = 0.1, d = 1, f = 0.1,
g = 0.05, h = 0.1, k = 0.1, m = 0.1, n = 0.1},
sol = NDSolve[{
v'[t] == -a ,
w'[t] == a - b w[t] - f w[t],
x'[t] == m r[t] - c x[t] + g y[t] - k x[t],
y'[t] == c x[t] - g y[t] - d y[t] - h y[t] + n r[t],
z'[t] == f w[t], u'[t] == h y[t],
q'[t] == k x[t],
r'[t] == b w[t] - m r[t] - n r[t] + d y[t],
v[0] == 0, w[0] == 0, x[0] == 0, y[0] == 0,
z[0] == 0, u[0] == 0, q[0] == 0, r[0] == 0},
{v, w, x, y, z, u, q, r},
{t, 0, 100}]]
```

The variables are defined as follows: q = Extracellular space (shedding), r = Golgi Apparatus, u = Catabolism from endosomes, v = Extracellular Space, w = Cytosol, x = Membrane, y = Endosomes, z = Catabolism from Cytosol, a = $k_{\text{Extra-Cytosol}}$, b = $k_{\text{Cytosol-Golgi}}$, c = $k_{\text{Membrane-Endosomes}}$, d = $_{\text{kEndosomes-Golgi}}$, f = $k_{\text{Cytosol-Catabolism}}$, g = $k_{\text{Endosomes-Membrane}}$, h = $k_{\text{Endosomes-Catabolism}}$, k = $k_{\text{Membrane-Shedding}}$, m = $k_{\text{Golgi-Membrane}}$,

n = $k_{\text{Golgi-Endosomes}}$, which is also depicted in Figure 6.7. Solving this system gives the result depicted in Figure 6.8.

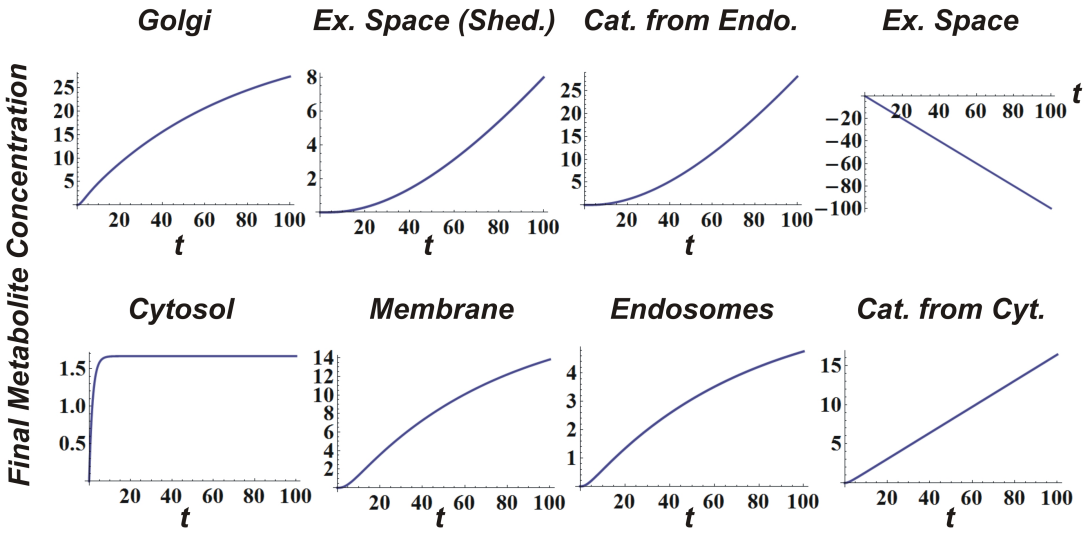

Figure 6.8: Development of metabolite concentration in the model.
Parameters: a=1, b=0.5, c=0.2, d=1, f=0.1, g=0.05, h=0.1, k=0.01, m=0.1, n=0.1, v(0)=0, w(0)=0, x(0)=0, y(0)=0, z(0)=0, u(0)=0, q(0)=0, r(0)=0

Hence, we set the starting concentrations of all compartments to 0 and defined a continuous flow with $\frac{1}{t}$ from the extracellular space into the cell: The extracellular space is the only source.[A] Therefore, the concentration of metabolites there decreases linearly with slope −1. The metabolites first arrive in the cytosol. There, a stationary state is reached quickly because the arriving metabolites are not staying there. Two routes are possible: The metabolites are either directly used for energy generation (catabolism from cytosol, which increases linearly after a short lag phase that it takes the first metabolites to arrive in the cytosol) or they enter the Golgi apparatus. Hence, the metabolite concentration there starts to rise after a little longer lag phase compared to the cytosol. Again, a stationary state is reached because from the Golgi apparatus, the metabolites are either transferred to endosomes or to the membrane. From the membrane, they can be shedded off into the extracellular space or be retracted into the endosomes. From the endosomes, the metabolites can then be transported to the Golgi apparatus, back to the membrane, or fed into the catabolism.

[A] Since the influx is not limited, we set the concentration of metabolites in the extracellular space to 0. The resulting negative concentrations are of course only mathematically meaningful. One can, however, just consider the absolute values as amount of internalized metabolites.

The simulation shows that for the only source of the system, the extracellular space, the metabolite concentration continuously decreases whereas for all sinks (catabolism and shedding) the concentration rises linearly after a short delay. All other compartments have influx and drains, therefore, their curves show a sigmoid development, tending to a limit. Notice also that the lag phases correspond to the position in the system, i.e. the "distance" from the metabolite source: The lag phases for the sinks can be ordered according to catabolism from endosomes ≈ extracellular space from shedding > catabolism from cytosol. Equally, the lag phases of the compartments reaching a limit in concentration can be ordered according to membrane ≈ endosomes > Golgi apparatus > cytosol. Moreover, the rates all together define the metabolite concentrations at a given point in time. In this case, from the 100 metabolites that entered the cell within 100 time units about 28% are found in the Golgi apparatus, 8% in the extracellular space due to shedding, 27% in the catabolism from endosomes, 1.5% in the cytosol, 15% on the membrane, 4.5% in endosomes, and 16% in the catabolism from the cytosol.
If, for example, the rates are set to values where every metabolite is directed fast to the membrane, the curves match the situation exactly as depicted in Figure 6.9. Now, the metabolite concentrations after 100 time units is for all compartments low except for two: First, as it should be, on the membrane, but second and perhaps a little surprising also in the extracellular space due to shedding. However, if one considers the high metabolite concentration on the membrane (over 50%), it is reasonable that the low shedding rate of 0.01 still has a significant effect. A very distinct behavior shows the curve for the metabolite concentration in the Golgi apparatus. This is because now the rate between cytosol and Golgi apparatus is, although it is with 0.5 quite large, a bottleneck: The rate from the Golgi apparatus to the membrane is with 1 even higher. Therefore, the concentration in the Golgi apparatus increases fast within the first time units, but then, the arriving metabolites are brought to the membrane, causing the curve to flatten fast.
Taken together, our model is capable of describing the metabolite flow through cellular compartments quantitatively. Therefore, we used it to investigate how the incorporation and internalization rates of membrane proteins are connected and compared it to the experimental results. These simulations are shown in Figure 12.10, Figure 12.11, and Figure 12.13.

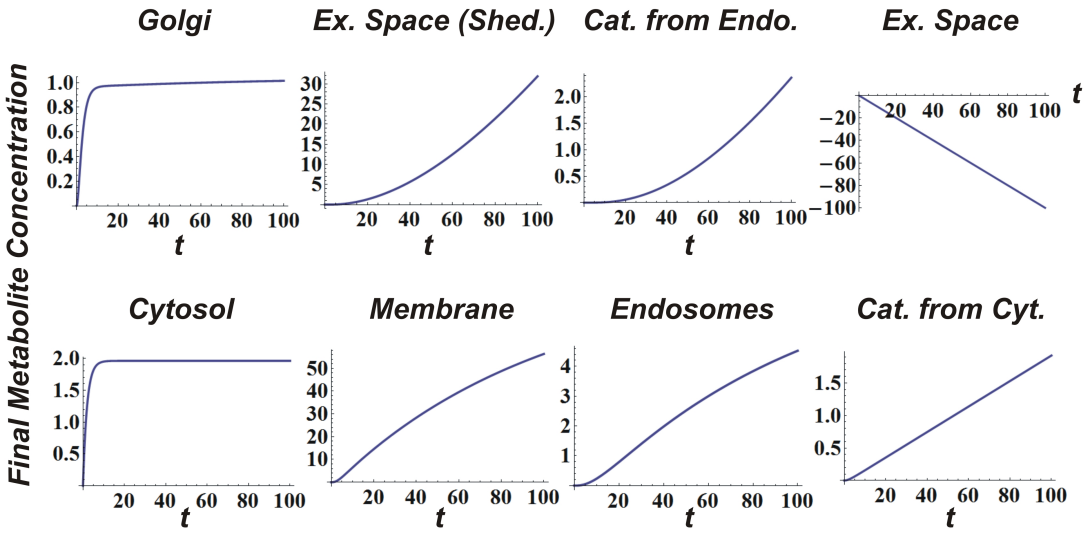

Figure 6.9: Development of metabolite concentration in the model.
Parameters: a=1, b=0.5, c=0.01, d=0.01, f=0.01, g=0.1, h=0.01, k=0.01, m=1, n=0.01 v(0)=0, w(0)=0, x(0)=0, y(0)=0, z(0)=0, u(0)=0, q(0)=0, r(0)=0

6.5 Experimental Section

Cell culture: HMECs (variant 1, CDC, Atlanta, GA) were seeded in collagen coated 8-well LabTek slides (Nunc, Rochester, NY) with a density of $1.5 \cdot 10^4$ or $1 \cdot 10^4$, respectively, in 400 µL growth medium, dependent on whether the experiment was performed two or three days after seeding, in order to yield subconfluent cells. The cells were cultured in MDCB-131 medium with 1% Glutamax, 10% fetal bovine serum (FBS), 10 ng/mL hEGF (all Life Technologies, Carlsbad, St. Louis, MO), and 1 µg/mL hydrocortisone (Sigma-Aldrich, St. Louis, MO) at 37°C in 5% humidified CO_2 atmosphere. Cells were fixed with 4% paraformaldehyde (Sigma-Aldrich) in DPBS+Ca^{2+}/Mg^{2+} (Life Technologies). Before and after fixation, it was washed three time with DPBS+Ca^{2+}/Mg^{2+}.

Metabolic Labeling: Growth medium was supplemented with 50 µM Ac_4ManNAz or Ac_4GalNAz (Life Technologies). For fluorescent labeling, cells were incubated for 45 min with Click-IT Alexa Fluor 647 DIBO Alkye (350 µL, 5 µM (Life Technologies).

Fluorescence microscopy: Confocal images were obtained using a commercially available spinning-disk inverted microscope (Carl Zeiss). Single molecule images were obtained on a custom-built Nikon epi-fluorescence TE200 microscope (Nikon) with a Nikon PlanApo100 objective (NA=1.4). Laser power was constant for each set of experiments and repeatedly controlled.

Quantification of membrane fluorescence: The obtained images for each set of experiments were randomized. Background was defined as the mean gray value of 5 out-of-cell regions and subtracted. Then, a line (width=667.5 nm) was drawn manually on the fluorescing cell membrane image, and the mean gray value along this line was determined. This was defined as the membrane fluorescence intensity.

SA-mediated lattice formation: After biotin-tagging of membrane glycoproteins, AlexaFlour647-labeled SA (1.25 μM; Life Technologies) was added and incubated for 20 min. For single-molecule measurements, the concentration of non-fluorescent SA was also 1.25 μM, with 0.1 nM fluorescent SA. For blocking of SA binding sites, biotin solution was added dropwise in a stoichiometric ratio with thorough mixing.

Immunostaining: HMEC-1 were fixed and incubated for 50 min with goat serum (2%) in DPBS+Ca^{2+}/Mg^{2+} followed by incubation for two hours at room temperature with rabbit monoclonal antibodies against galectin-1 or galectin-3 (1:100; ab108389/ab76245, Abcam, Cambridge, UK). Cells were then incubated for 40 min with secondary antibody (1:200).

Statistical methods: Data were first tested for normal distribution, which was always positive. The F-test always resulted in unequal variances, therefore a two-tailed student's t-test for unequal variances was performed to determine p-values.

Software: Images were analyzed using ImageJ. With the Matlab program uTRACK, tracking was performed.[251] Tracks were analyzed with the program @msdanalyzer.[252] For data visualization and analysis, OriginPro 8G was used. Simulations were carried out in Mathematica 7 (Wolfram, Hanborough, UK). FRAP analysis was performed with easyFRAP.[253]

7 Artificial, Tunable Interconnection of Membrane Glycans

This chapter is based on: **"Artificial Formation and Tuning of Glycoprotein Networks on Live Cell Membranes: A Single-Molecule Tracking Study"** by Leonhard Möckl, Thisbe K. Lindhorst, and Christoph Bräuchle
accepted for publication by *ChemPhysChem*

Acknowledgements:
LM conducted and evaluated the experiments and wrote the manuscript.
TKL and CB wrote and corrected the manuscript.

7.1 Abstract

We present a method to artificially induce network formation of membrane glycoproteins and show the precise tuning of their interconnection on living cells. For this, membrane glycans are first metabolically labeled with azido sugars and then tagged with biotin by copper-free click chemistry. Finally, the so obtained biotin-tagged membrane proteins are interconnected with streptavidin (SA) to form an artificial protein network in analogy to a lectin-induced lattice. The degree of network formation can be controlled by the concentration of SA, its valency, and the concentration of biotin on membrane proteins. This was verified by investigation of the spatiotemporal dynamics of the SA-protein networks employing single-molecule tracking. It was also proven that this network formation strongly influences the biologically relevant process of endocytosis as it is known from natural lattices on the cell surface.

7.2 Introduction

The formation of lattices and networks is a crucial mechanism in every living cell. Examples include the nuclear lamina,[254] the cytoskeleton,[255] the galectin-glycoprotein lattice,[103] or the flat clathrin lattice.[256] From the wide thematic area of these examples, ranging from nucleus structure to mechanical stability of the cell and membrane protein organization, the relevance of protein interconnection can be seen. Therefore, it is not astonishing that the formation and properties of protein networks are in the focus of both experimental[104,257,258] and theoretical research.[259–261] Moreover, they are also an inspiration for the development of techniques that allow the assembly of cellular components into defined structures.[262–265] However, so far there are only a few attempts to actively influence and control the formation of physiological lattices, such as membrane-localized lattices[266] which are relevant in signaling, metabolism, or cellular communication.[101,243] Much more research deals with the manipulation of other features of the cell membrane employing, for example, cyclodextrins,[267] cavitation,[268] nanotubes,[269] or optical tweezers.[270] In a recent paper,[222] we have investigated the effects of the galectin lattice on membrane protein dynamics and have described a method to artificially induce network formation on the membrane of living cells. Here, we have systematically changed all parameters responsible for artificial network formation and report the results of a detailed analysis performed by single-molecule tracking. Furthermore, we reveal the influences of this artificial network formation on endocytosis.

Our method relies on a robust three-step protocol as schematically depicted in Figure 7.1. First, metabolic labeling with azido-modified sugars is employed to introduce the azido group into glycosylated membrane proteins, suited for bioorthogonal labeling.[153] In the second step, biotin is coupled with the azido groups by click chemistry[271] and finally, formation of artificial protein networks is effected by incubation with streptavidin (SA) that can bind up to four biotin moieties. We chose to target the glycosylation of membrane proteins because this modification is abundant on the cell surface.[69] Therefore, most membrane proteins can be addressed this way and are then available for the following modifications required for artificial network formation. For metabolic labeling, we supplemented the growth medium of human microvascular endothelial cells (HMEC) with tetra-O-acetylated *N*-azidoacetyl-D-mannosamine (Ac_4ManNAz) or tetra-O-acetylated *N*-azidoacetyl-D-galactosamine

(Ac_4GalNAz). These azidosugars are taken up by the cell and processed along the normal biosynthetic pathways to be incorporated into cell surface glycoproteins.[153] This leads to azido-modified sialic acid-bearing proteins (SABPs) in case of Ac_4ManNAz or mucin-type proteins (MTPs), respectively, in case of Ac_4GalNAz.[272,273] For biotin tagging, DIBO-biotin was employed, a cyclooctine-biotin conjugate reacting solely with azides in a copper-free click reaction;[156] no other functional groups present on the cell surface are involved in this conjugation step. To induce artificial network formation, SA was used, mainly for two reasons: First, the mechanism of SA-biotin binding is well understood[274] and can even be modified to tune the properties of the interaction.[275,276] Second, the SA-biotin complex is very strong (KD$\approx 10^{-15}$ M)[277] allowing for the formation of a stable network. It is important to keep in mind that especially SABPs often carry more than one sialic acid,[278] resulting in more than one biotin bound to the protein. Therefore, the same protein can be bound by different SAs, which is of course relevant for network formation. To allow investigation of protein networks by single-molecule tracking we employed fluorescent AlexaFluor647-SA at suitable concentrations.

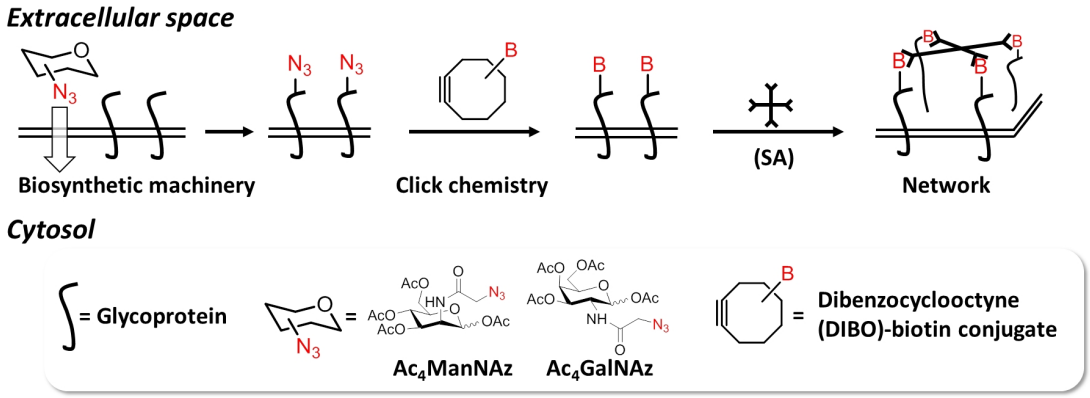

Figure 7.1: Schematic representation of the protocol employed for artificial network formation.
Supplementation of the cellular growth medium with azido sugars (Ac_4ManNAz or Ac_4GalNAz) leads to metabolic labeling of membrane-bound glycoproteins with azido groups. This allows tagging with biotin (B) by click chemistry using a cyclooctyne-biotin conjugate. The resulting biotin-tagged membrane proteins can then be interconnected by tetravalent SA.

In order to explore tuning of artificial network formation, we systematically modified the parameters that determine the degree of protein interconnection and investigated the associated changes in spatiotemporal dynamics of the artificial network. These parameters are the valency of network-forming SA (free biotin binding sites), SA concentration, and biotin concentration on cell surface proteins. They can be easily tuned in our system by blocking biotin binding sites of SA via preincubation of SA with free biotin, by varying the concentration of used SA, and by varying the concentration of used DIBO-biotin, respectively (Figure 7.2). We changed each of these parameters at a time while keeping the other two constant.

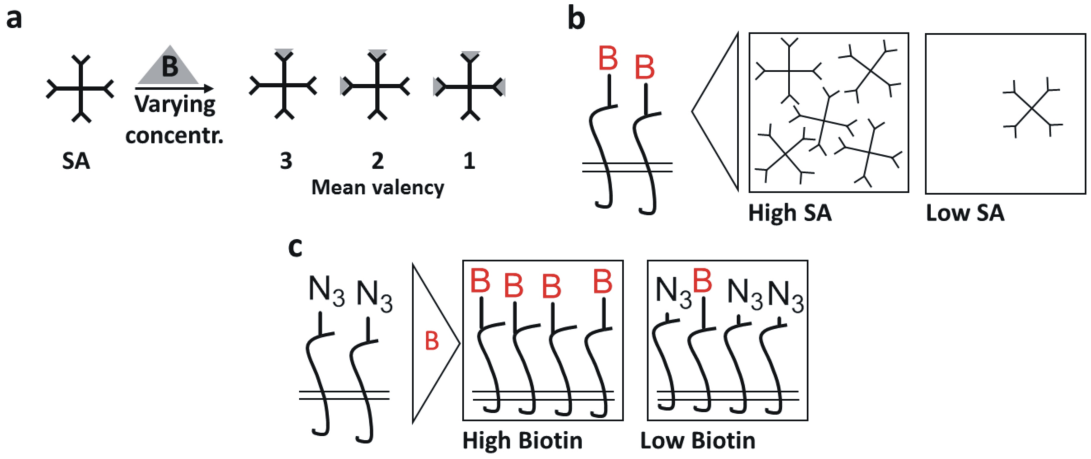

Figure 7.2: The factors that influence artificial network formation.
(a) Statistical tuning of SA valency by preincubation of SA with biotin; increasing biotin amounts result in gradually reduced SA mean valency from four to three, two, and one. (b) Tuning of SA concentration was effected by incubation of the biotin-tagged cells with different amounts of SA. (c) The concentration of available binding sites for network-forming SA was tuned by incubation of the azido-tagged cells with different amounts of DIBO-biotin.

7.3 Results and Discussion

First, we investigated the influence of the valency of network-forming SA on glycoprotein network formation. For this, we incubated HMECs with 50 µM Ac_4ManNAz or Ac_4GalNAz, respectively, for two days. After this time, a steady state is reached in which all natural sugars that can possibly be modified in our approach have been

replaced by azido sugars.[222] Then, we addressed the azido groups by incubation with 5 µM DIBO-biotin, followed by interconnection of the biotin-tagged membrane proteins with SA. For incubation with SA, a total concentration of 1.25 µM was employed with a concentration of fluorescent AlexaFluor647-SA of $5 \cdot 10^{-9}$ M, a typical concentration for single-molecule experiments (cf. Figure 12.14 for exemplary images). The SA mean valencies varied from four to one (cf. Figure 7.2a). We subsequently tracked the movement of the fluorescent SA on the membrane of several cells (20-30 for each experiment) and recorded their trajectories over time.
The changing mobility of glycoproteins upon interconnection by SA of different valency can directly be seen from the trajectories of the single SA units on the cell membrane. Whereas incubation of biotin-tagged membrane proteins with tetravalent SA leads to trajectories that mostly cover only a small area (Figure 7.3a), incubation with SAs of mean valency of one results in many long trajectories covering a large area (Figure 7.3b). Some trajectories show a deviating nature, such as strong confinement in case of monovalent SA and low confinement in case of tetravalent SA. This can be attributed to SA of a divergent valency, present in the applied samples due to the stochastic nature of the biotin blocking process of tetravalent SA, or to tetravalent SA bound to only one protein, respectively.

To quantitatively investigate membrane protein network formation with SA, we extracted mean square displacement (MSD) curves[194,198,279,280] from the trajectories (Figure 7.4a/b left). From this, it is clearly visible that for increasing mean valencies of SA the corresponding MSD curves bend more, corresponding to less mobility and increasing confinement (see Figure 12.15 for a simple simulation of the relation between network formation and confinement).

From the MSD curves also additional information on the nature of the membrane protein diffusion process can be extracted. Since the MSD curves show strong bending for SA valencies larger than one and also tend towards a limit, we decided to fit the MSD curves following the model of confined diffusion.[194,198] The formula that describes the MSD in dependence of the delay time is

$$MSD = C\left(1 - A_1 e^{-\frac{4A_2 Dt}{C}}\right) \tag{7.1}$$

where C stands for the size of the confinement, A_1 and A_2 are geometrical constants defining the shape of the confinement, and D is the diffusion coefficient (cf. Chap-

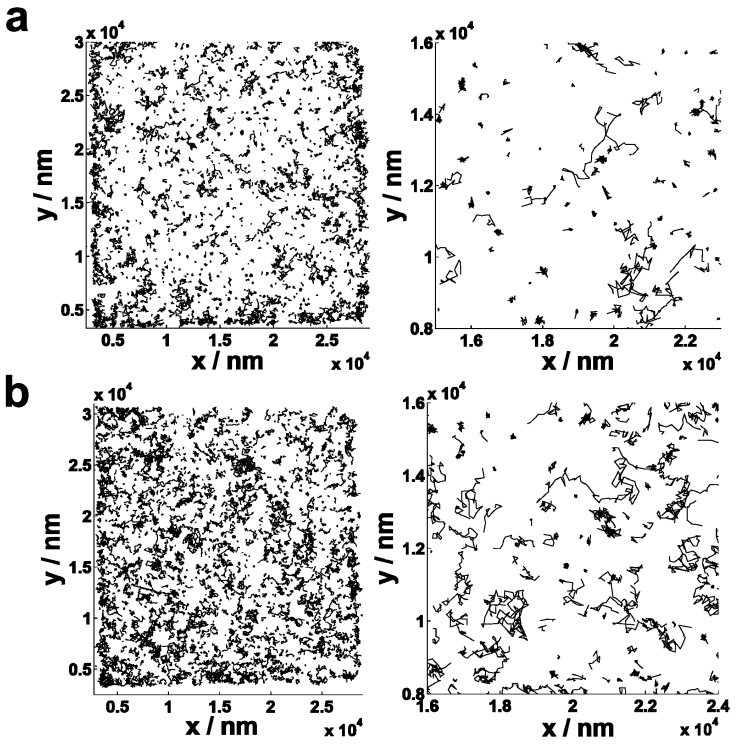

Figure 7.3: Trajectories of SA on the membrane of HMECs after metabolic labeling with Ac_4ManNAz and tagging with DIBO-biotin.
Left: All trajectories recorded. Right: Zoom in. (a) Incubation with tetravalent SA results in trajectories that mostly show a high confinement, visible from the small area that is covered. (b) In contrast, incubation with SA of a mean valency of one leads to many trajectories that cover a large area, displaying lower confinement and higher mobility. n=2300-2600 trajectories.

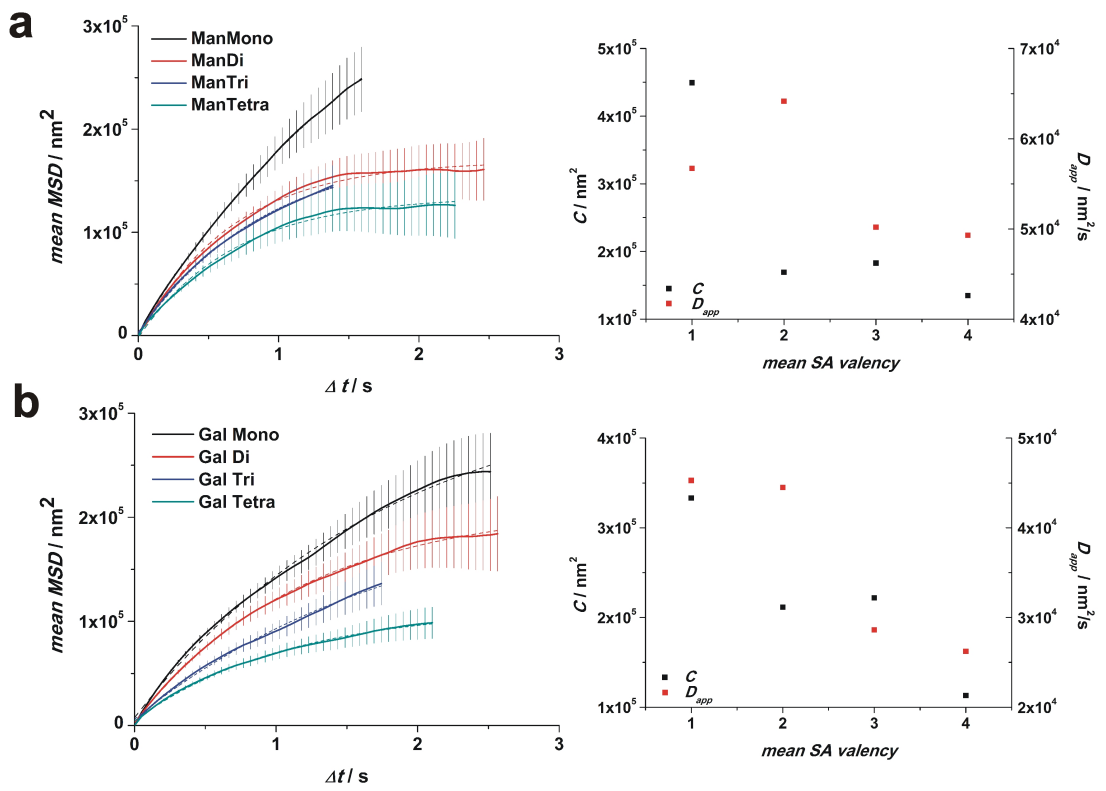

Figure 7.4: Effect of mean SA valency on network formation.
Both, for incubation with Ac_4ManNAz (a) and Ac_4GalNAz (b), the MSD curves (left) bend stronger with increasing mean valency of interconnecting SA. Correspondingly, the apparent diffusion constants Dapp and the confinement area C decrease (right). Error bars are given as the weighted standard deviation divided by the square root of the number of degrees of freedom. Dashed lines indicate fit curves. 2300-4700 trajectories/MSD curve.

ter 5.2.1 and Table 5.1). Unfortunately, one cannot obtain the values of the two free constants A_2 and D just by fitting the MSD curve, only the value of their product is accessible. However, since it is our goal to qualitatively compare the diffusion constants of SA in different networks relative to one another, we combined the numerator to the apparent diffusion coefficient D_{app} and used the formula:

$$MSD = C\left(1 - A_1 e^{-\frac{D_{app} t}{C}}\right) \tag{7.2}$$

The thus obtained values for the confinement area and for the apparent diffusion constants (Figure 7.4a/b right) corroborate the trend that was already displayed by the

MSD curves. With increasing valency of interconnecting SA molecules, the confinement area and the apparent diffusion coefficient decrease. The fit curves in Figure 7.4 are given as dashed lines which nicely overlap with the experimental data, indicating that the model of confined diffusion is well chosen. The variation in the C- and D_{app}-values is understandable from the overlapping error bars in the MSD curves. Importantly, the decreasing tendency and the significant difference between monovalent SA (no network formation) and tetravalent SA (maximal network formation) is clearly visible.

Confinement is also detected when monovalent SA is applied, although it is not capable of forming an artificial membrane protein network. This finding is not surprising as diffusion of cell membrane proteins has been found to be confined already without artificial interconnection as shown by numerous studies.[225,281,282] Also, SA of higher valency that may be present in the sample due to the stochastic blocking of biotin binding sites could contribute. Clearly, however, SA of higher valency effects artificial network formation, thus reducing the mobility of the membrane proteins and further decreasing their confinement area.

It is interesting to compare the effects of artificial network formation depending on whether the initial azido labeling was performed with Ac_4ManNAz, leading to azido-bearing SABPs, or Ac_4GalNAz, leading to azido-bearing MTPs. When monovalent SA was applied (no artificial network formation), the confinement area of SABPs is larger than in case of MTPs and also its apparent diffusion coefficient is slightly higher. This observation can be explained by natural lattice formation. Cultured HMECs express galectins as proved by immunostaining (see Figure 12.16). These GalNAc-specific lectins interconnect MTPs to form lattices, whereas SABPs are not involved in this natural network formation process due to the nature of their glycan portions. Consequently, as long as no artificial network is induced, the mobility of MTPs is lower than that of SABPs due to their engagement in the natural galectin lattice.[222] However, if the interconnecting SA has a mean valency of two, three, or four, respectively, artificial networks are formed in all cases and thus the confinement area and the apparent diffusion coefficients of both SABPs and MTPs decrease: In this case, the artificial network formation dominates over the other cellular mechanisms that lead to confinement (such as the formation of galectin lattices). Next, we went on to characterize the effect of SA concentration on network formation. For this, HMECs were again labeled with biotin after incubation with 50 μM Ac_4ManNAz and 5 μM DIBO-biotin as described above.

Then, we incubated with 0, 1.25, 2.5, or 5 µM tetravalent SA and recorded trajectories of fluorescent SAs (c=$5 \cdot 10^{-9}$ M) on the cell membrane. The MSD curves (Figure 7.5 left), the values for the respective confinement area, and of the apparent diffusion coefficient (Figure 7.5 right) show that SA concentration also affects the formation of an artificial network: Higher concentrations of interconnecting SA lead to stronger bending of the MSD curves and, correspondingly, to smaller confinement areas and lower apparent diffusion coefficients

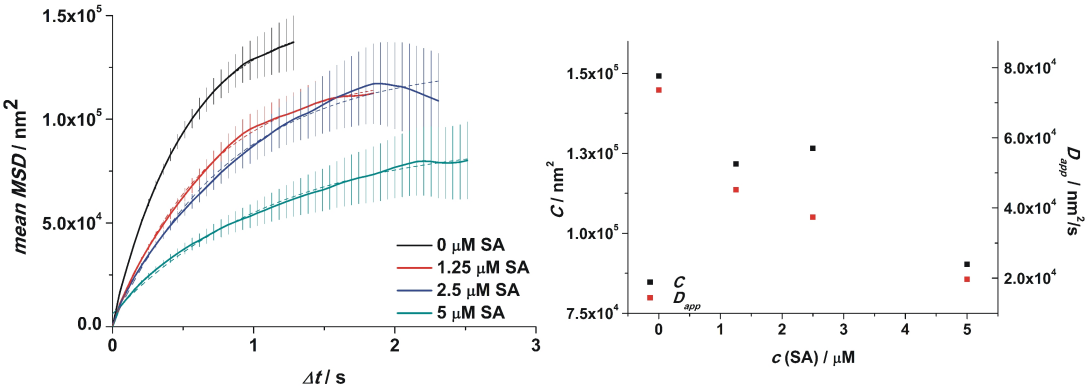

Figure 7.5: Effect of SA concentration on network formation
The bending of the MSD curves increases with increasing SA concentration, displaying decreasing mobility (left) as reflected in the obtained values for the apparent diffusion constant and the confinement area (right). Error bars are given as the weighted standard deviation divided by the square root of the number of degrees of freedom. Dashed lines indicate fit curves. 5100-6100 trajectories/MSD curve.

Finally we investigated the influence of biotin concentration on artificial network formation. Biotin concentration determines the number of binding sites for interconnecting SA. For this, we first incubated the cells with 50 µM Ac_4ManNAz for two days as before and then addressed the azido-tagged membrane proteins with 1, 5, 10, 25, 50, or 75 µM DIBO-biotin. To induce network formation, we incubated with 5 µM tetravalent SA. However, in this case the fluorescent species was not SA, but SA-coated quantum dots (QDs) at a concentration of $5 \cdot 10^{-9}$ M (see Figure 12.14 for example images). They are incorporated into the artificial network just as AlexaFluor647-SA, but other than AlexaFluor647 they virtually do not bleach. This advantage makes it possible to follow their movement over a long period of time which allows to observe the MSD curve

to reach the plateau.[A] From the MSD curves it is readily visible that the membrane biotin concentration strongly affects the formation of the artificial network (Figure 7.6 left). For DIBO-biotin concentrations of 1 to 10 μM, the confinement increases with increasing concentration. However, at 25 μM and above, a threshold is reached with MSD curves remaining at a very low level, displaying strongly confined diffusion. This is reflected in the values of the apparent diffusion constant and the confinement area (Figure 7.6 right), both decreasing with increasing DIBO-biotin concentrations.
It is worth mentioning that the concentration of biotin has by far the strongest effect on membrane protein mobility and artificial network formation, when compared to the effect of SA valency and SA concentration. When the latter two parameters were varied, the effects on confinement and apparent diffusion were less pronounced and showed larger variations, presumably due to other cellular mechanisms that affect membrane protein mobility. In contrast, when medium and high biotin concentrations were applied in our experiment, movement of proteins within the network could be almost completely shut down. This can be seen from the confinement areas that remain constant at a very low level from 25 μM biotin onwards. The apparent diffusion constants decrease first, but stay at a medium level before also dropping to a very low value at 75 μM. This observation can be reasoned by two transitions: Between 5 and 50 μM biotin proteins show very strong confinement, but are still able to move a little within this confinement, which results in the low values for C and the medium values for D_{app}. At 75 μM the confinement is very strong as before, but now the proteins are almost completely immobile, further decreasing D_{app}.

Having shown that our method is suited to artificially induce network formation on cell membranes in a defined way, we also wanted to secure its relevance in a biological environment. Hence, we chose to investigate its effect on endocytosis, a fundamental cellular process. For this, we first induced artificial network formation by incubating HMECs for two days with 50 μM Ac_4ManNAz, followed by incubation with 5 or 50 μM DIBO-biotin and 0, 1.25, 2.5, or 5 μM tetravalent SA. Then, we added 0.75 mg/mL fluorescent 10 kDa dextran, a common endocytosis probe, incubated for 15 minutes, and

[A] In the preceding two experiments SA-coated QDs could not be employed as the number of SA molecules on one QD ranges from 5 to 10. Thus, it is impossible to exactly control SA valency and SA concentration in this case. Here, we can use them because we investigate the effect of biotin concentration and not that of interconnecting SA. Furthermore, they are only applied at a very low concentration.

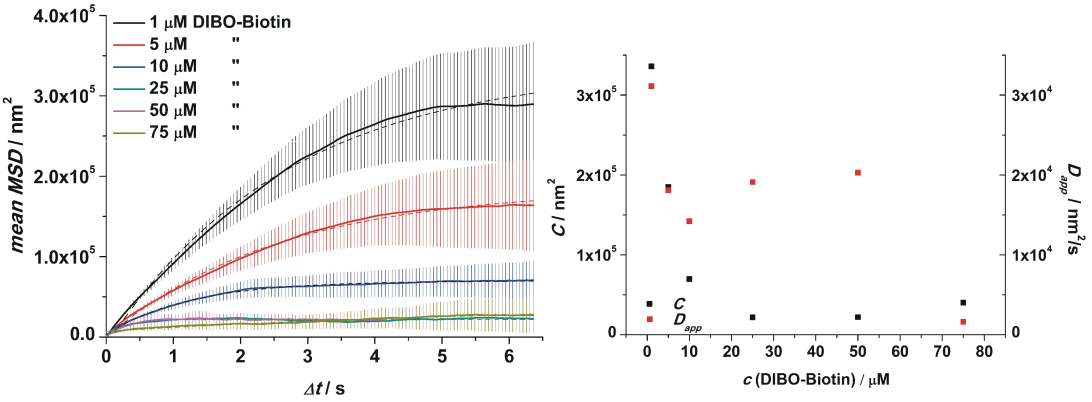

Figure 7.6: Effect of cell surface biotin concentration on network formation.
With increasing DIBO-biotin concentration, the MSD curves increasingly bend, indicating a more and more confined movement. At concentrations ≥ 25 µM DIBO-biotin, the MSD curves remain constant at a very low level, displaying very high confinement (left). Consistently, the apparent diffusion constant and the confinement area decrease with increasing DIBO-biotin concentration (right). Error bars are given as the weighted standard deviation divided by the square root of the number of degrees of freedom. Dashed lines indicate fit curves. 800-3400 trajectories/MSD curve.

fixed the cells. Then, we quantified the fluorescence signal of several cells within one confocal slice at the lower part of the cells. The integrated fluorescence density per slice divided by the number of cells is then a measure for the ability of the cells to internalize the dextran (Figure 7.7). From the endosomal signals it is clearly visible that upon artificial network formation, the endocytosis is strongly slowed down. In case of incubation with 5 µM DIBO-biotin, the signals from the endosomes decrease from about 22500 a.u. for no addition of SA, i.e. no artificial network formation, to about 2500 a.u. for the presence of 5 µM SA. In case of incubation with 50 µM DIBO-biotin, the endosomal signal for no addition of SA is lower compared to incubation with 5 µM DIBO-biotin, presumably due hindered endocytosis as a consequence of the high degree of DIBO-biotin modification. However, it also decreases strongly with rising SA concentrations, again indicating a significant reduction of the endocytosis rate. Therefore, artificial network formation physically blocks endocytosis by introducing large protein clusters on the cell surface that are difficult to internalize for the cell. Over the time we performed the experiments (one to two hours), we did not detect adverse effects on the cells. However, one can assume that membrane rigidification, as in case

of strong artificial network formation, will alter the behavior of a cell, e.g. during cell division. Therefore, this is an interesting approach to influence cellular behavior. Experiments to elucidate this in various ways are currently underway.

Our results prove that the spatiotemporal dynamics of membrane glycoproteins can be easily and reliably tuned by SA-mediated interconnection employing metabolic labeling and biotin modification of cell surface glycans. In our approach, the formation of an artificial network on the cell membrane is effected and can be systematically tuned, as verified by single-molecule tracking. In general, the mobility of the interconnected proteins decreases with increasing SA valency, SA concentration, and membrane biotin concentration. However, these three parameters influence the proteins not equally. The concentration of biotin has by far the strongest effect on protein mobility whereas increasing SA valency and SA concentration, respectively, decrease protein mobility less strongly. By careful setting of these parameters, the mobility of membrane proteins can be adjusted and tuned from physiological values to an almost frozen condition. Furthermore, we were able to show that artificial network formation also influences the biologically relevant process of endocytosis which strongly decreases with increasing network formation. We are confident that our method of artificially influencing glycoprotein networks can be helpful to control membrane protein mobility in a broad context.

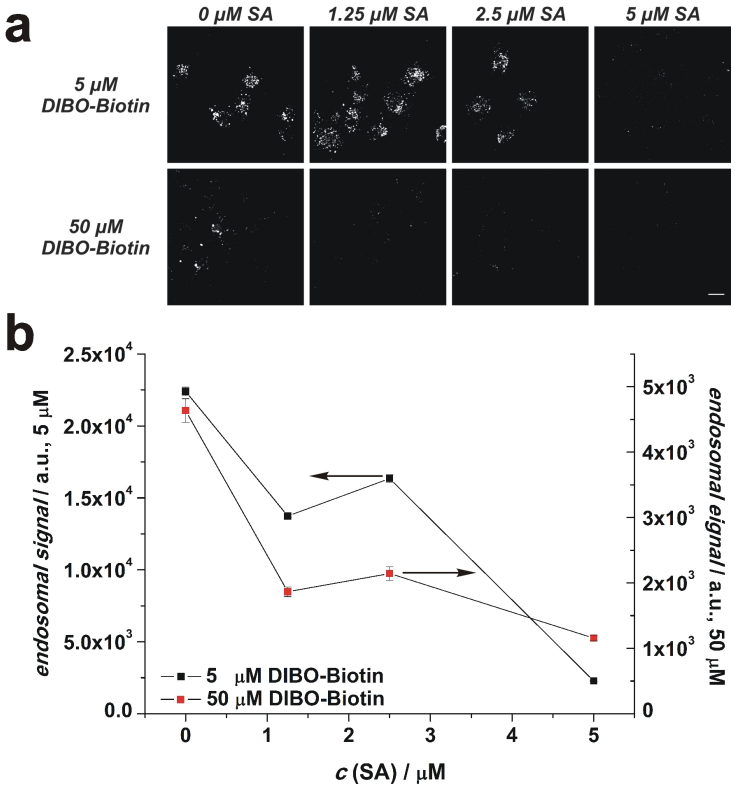

Figure 7.7: Effect of artificial network formation on endocytosis.
(a) Representative images of HMECs incubated with fluorescent 10 kDa dextran after artificial network formation with the indicated DIBO-biotin and SA concentrations. It is clearly visible that for both cases (5 and for 50 µM DIBO-biotin) the endosomal signal decreases when rising amounts of SA are used for network formation. At 50 µM DIBO-biotin and 0 µM SA (i.e. no artificial network formation) endocytosis is lower than in the analogous experiment at 5 µM DIBO-biotin. This observation is presumably due to the high number of biotin residues present on the cell surface at 50 µM DIBO-biotin that already hinders endocytosis. Nevertheless, addition of SA further decreases the endocytosis rate also in this case. (b) Quantification of the endosomal signal reflects the strong influence of artificial network formation on the endocytosis rate. n=25-94, Scale bar = 30 µm. Error bars indicate the standard error of the mean and arrows the y-axis corresponding to 5 and 50 µM biotin, respectively.

7.4 Step Length Analysis

This work was not part of the published article.

Calculation of the MSD is a very efficient way to characterize the motion of diffusing particles. However, it may be desirable to have a more intuitive way of describing the diffusion of a particle. One way is to investigate the number of consecutive steps in one direction. We will call this a "chain" in the following (Figure 7.8).

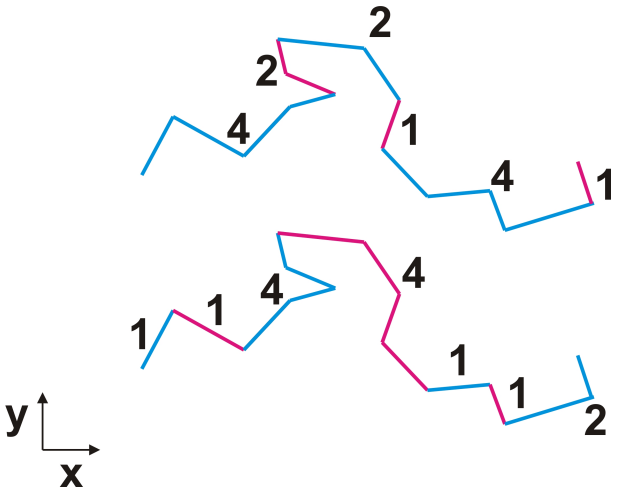

Figure 7.8: Definition of chains as consecutive steps in one direction.
Shown is two times the same part of a trajectory. At the top, it is color-coded for increasing (cyan) and decreasing (magenta) x-values, at the bottom the same way for y-values. From this, consecutive steps in one direction of "chains" are easily determined.

Let's consider the movement of a particle undergoing normal diffusion. If we define any direction $\vec{a}$, then the particle has, as described above, ideally the probability 1/2 to make a step in $+\vec{a}$ (i.e. the coordinate of the particle along $\vec{a}$ increases). Equally the particle has also the probability 1/2 to make a step in $-\vec{a}$ (i.e. the coordinate of the particle along $\vec{a}$ decreases). This means that, for example, the probability for the particle to make five steps into one direction (i.e. chain length 5) is $0.5^5 = 0.03125$. The other values for chains for a particle undergoing normal diffusion are listed in Table 7.1.

Table 7.1: Probability of chain lengths for idealized normal diffusion

Chain length	Probability
1	0.5
2	0.25
3	0.125
4	0.0625
5	0.03125
6	0.015625
7	0.0078125
8	0.00390625
9	0.00195313
10	0.00097656
11	0.00048828
12	0.00024414
13	0.00012207
14	$6.1035 \cdot 10^{-5}$
15	$3.0518 \cdot 10^{-5}$
16	$1.5259 \cdot 10^{-5}$

However, this is not true for a particle undergoing confined diffusion. Since the particle diffuses inside a confinement, the more steps it makes in the same direction, the more likely it is that it hits a boundary. Therefore, for confined diffusion, if the particle has made a step in $+\vec{a}$, the probability for the particle to make a step in $+\vec{a}$ again is smaller than to make a step in $-\vec{a}$ and the other way around. Of course, the longer the chain is, the more unlikely it becomes in comparison to a freely diffusing particle: Sometimes, this is called "memory" of the particle.
Before we investigated our experimental data, we simulated trajectories for particle undergoing diffusion inside a confinement of different sizes to validate our approach. For this, we used the same model that is described in Figure 12.15 where particles can diffuse freely inside a potential L that drives them back to their original position. Therefore, we varied the size of the potential.[B] First, we calculated how often chains of lengths from 1 to 16 occurred. The results are given in Figure 7.9

[B] Other parameters: $N_{Particles}$=1000, N_{Steps}=500, dimensions=2, $D = 1 \cdot 10^{-3}$ $\mu m^2/s$, T=37°C, L=0.05µm

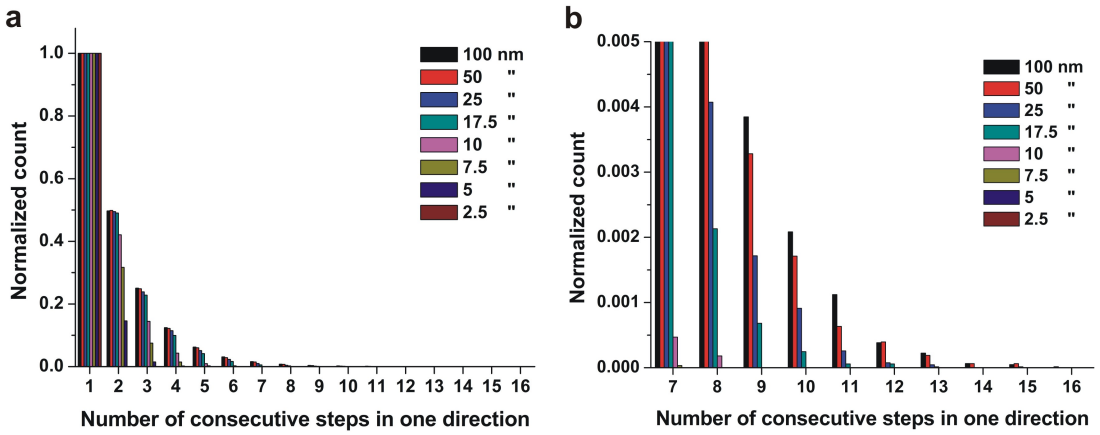

Figure 7.9: Number of consecutive steps in one direction for different simulated potentials
(a) Normalized histogram for all chains of steps. (b) Detail for longer chains. As it can be clearly seen, the probability of longer chains decreases the narrower the potential becomes.

The simulation shows two important aspects of the diffusion process. On the one hand, for all potential sizes the chain length with the highest probability is one, meaning that it is always most likely that a particle performs first a step forward and then back. This is expected, because otherwise a preferred direction would exist: For example, if two steps in one direction were more likely than one, this would imply drift. On the other hand, for large confinements, long chain lengths occur whereas they are becoming more and more unlikely for narrower confinements until for very narrow confinements they do not occur at all anymore. This is nicely seen in Figure 7.9b. Since the data are normalized, it follows that the probability for shorter chains increase when longer chains vanish.
One can also compare the probabilities for the different chains in case of idealized normal diffusion with the histograms for the simulated diffusion by calculating the ratio between them. For this, the ideal case of normal diffusion (Table 7.1) just has to be normalized. The result is given in Figure 7.10.

For large confinement sizes (50 and 100 nm), the ratio is close to one, indicating that the deviation from the ideal case is small – the particle undergoes pseudonormal diffusion. When the confinement sizes decrease, the ratio deviates more and more from 1 and tends for long chain length to zero, indicating that for increasing confinement long chain length become highly unlikely. Only at very long chain lengths, the data points deviate from this trend and start to behave erratically. This can be attributed to

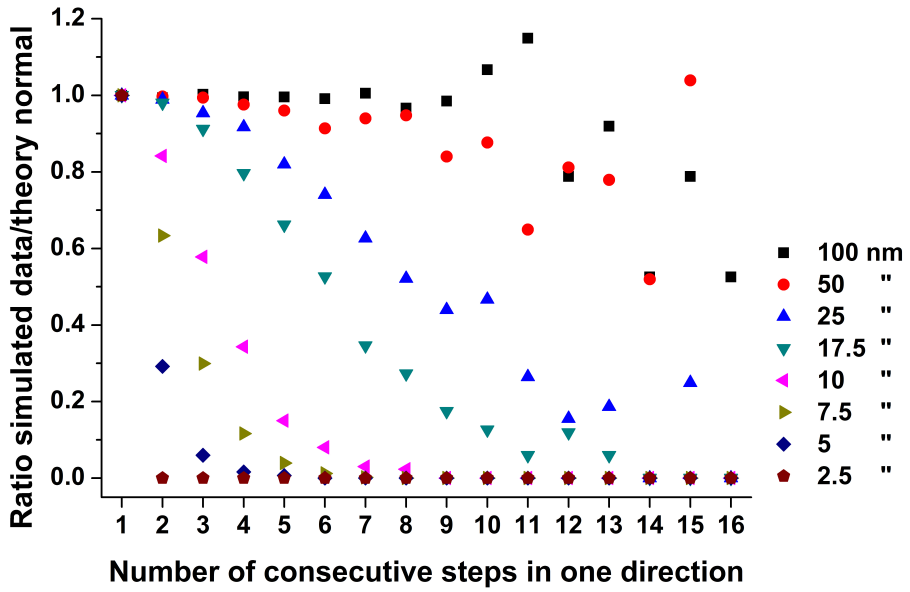

Figure 7.10: Comparison of chain lengths between the simulated data and idealized normal diffusion
With decreasing potential size, the ratio deviates towards smaller ratios, indicating that longer chain lengths become more unlikely. The deviations from the trend at long chain lengths can be attributed to the low statistical power in this region.

the low statistical power – these chain lengths are anyway highly unlikely, so a small deviation has a big impact on the ratio.

Finally, one can also calculate the cumulative weighted chain length (CWCL). This is done by multiplying the normalized frequency f_i of a certain length i with the respective length and then summing up over all the products until the longest observed chain N_{max}:

$$CWCL = \sum_{i=1}^{N_{max}} f_i \cdot i \tag{7.3}$$

This value is, as one can easily derive, 4 for idealized normal diffusion. It decreases for confined diffusion (until it reaches zero for a completely immobile particle) and increases for diffusion with drift. The result for the simulated data is depicted in Figure 7.11. It can be clearly seen that for increasing confinement the cumulative

weighted chain length decreases. For the potential size of 100 nm, it is close to 4, confirming the result depicted in Figure 7.10 that for this confinement size the diffusion is pseudonormal. Moreover, the development is not linear: There is a sharp transition at a potential size of about 20 to 25 nm, above which the cumulative weighted chain length is close to four and below which it decreases rapidly. This can be understood when considering the physical setting: As soon as the confinement exceeds a certain size, the particle is unlikely to encounter it. In this case, it makes not a big difference if the confinement is then even larger. On the other hand, as soon as the particle is affected by the confinement, a further decrease in confinement size has a big impact. For the parameters of our simulation, the critical size is at about 25 nm.

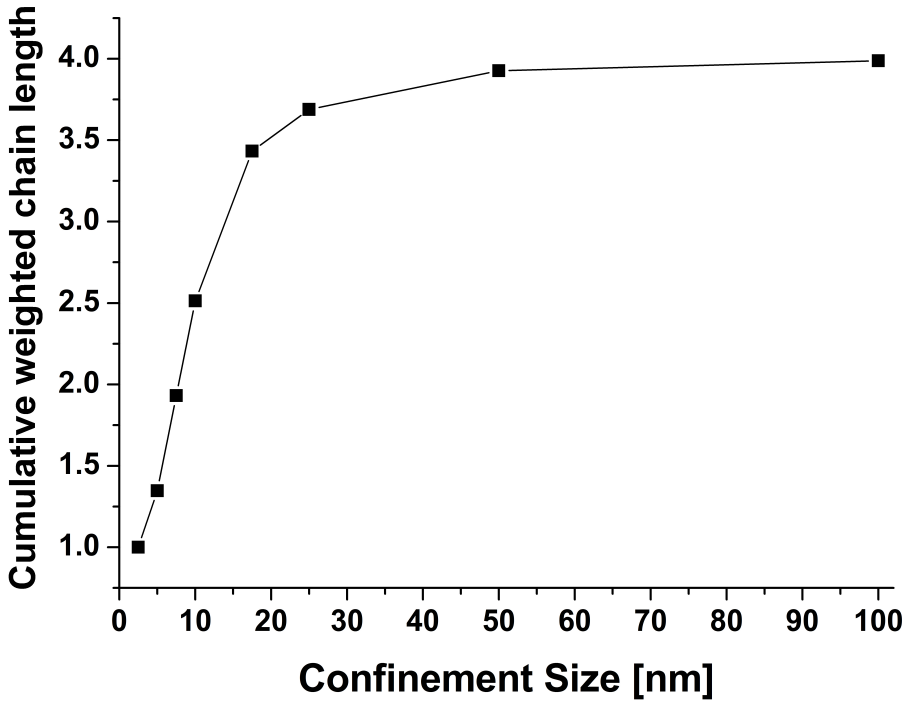

Figure 7.11: Cumulative weighted chain length
For large confinement sizes, the cumulative weighted chain length is close to 4 which is the expected value for idealized normal diffusion. For smaller confinements, it decreases first slightly, then rapidly.

Having validated the analysis method, we turned to the experimental data described above. Since we detected the strongest effects for the variation of DIBO-biotin concentration, we decided to analyze the steps for this experiment. Naturally, we investigated the movement along the two Cartesian coordinates that we obtained for the trajectories

along $\vec{x}$ and $\vec{y}$. In Figure 7.12 the histograms for the chains with lengths from 1 to 16 are given. As it can be easily seen from the histograms, the most likely case is a chain with length one. However, with increasing DIBO-biotin concentration, the probability for long chains decreases. This can both be seen from the decreasing probability to make a certain number of steps for rising DIBO-biotin concentrations as well as the decrease in the longest observed chain which can be nicely seen in Figure 7.12b: For example, the longest chain for 1 µM DIBO-biotin is 16, but only 9 for 75 µM DIBO-biotin, indicating more and more confined diffusion.

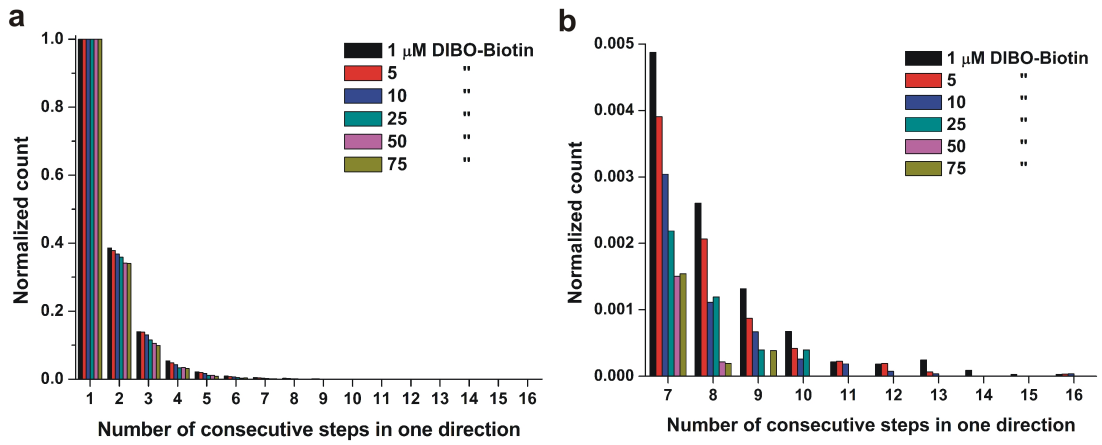

Figure 7.12: Number of consecutive steps in one direction for varying DIBO-biotin concentrations
(a) Normalized histogram for all chains of steps. (b) Detail for longer chains. As it can be clearly seen, the probability of longer chains decreases for increasing DIBO-biotin concentrations.

As described for the simulated data, one can also compare the probabilities for the different chain lenghts to the development in case of idealized normal diffusion. For the experimental data, the result is depicted in Figure 7.13. For all DIBO-biotin concentrations, the ratio between the experimentally observed frequency and the theoretical frequency for normal diffusion is below 1 and tends to zero as it was also observed for the simulated data. However, in contrast to the simulation, the ratio drops not steadily to zero, but decreases first and then reaches a limit before reaching zero. This limit decreases with increasing DIBO-biotin concentrations. This indicates that the situation in the environment of the artificial network is more complex than just confined diffusion. One possibility would be that not all particles are completely engaged in the network, but that some diffuse more or less normal, which elevates the ratio at longer

chain lengths. Again, at very high chain lengths and low DIBO-biotin concentrations, some data points do not follow the trend, which can be attributed to the low statistical power.

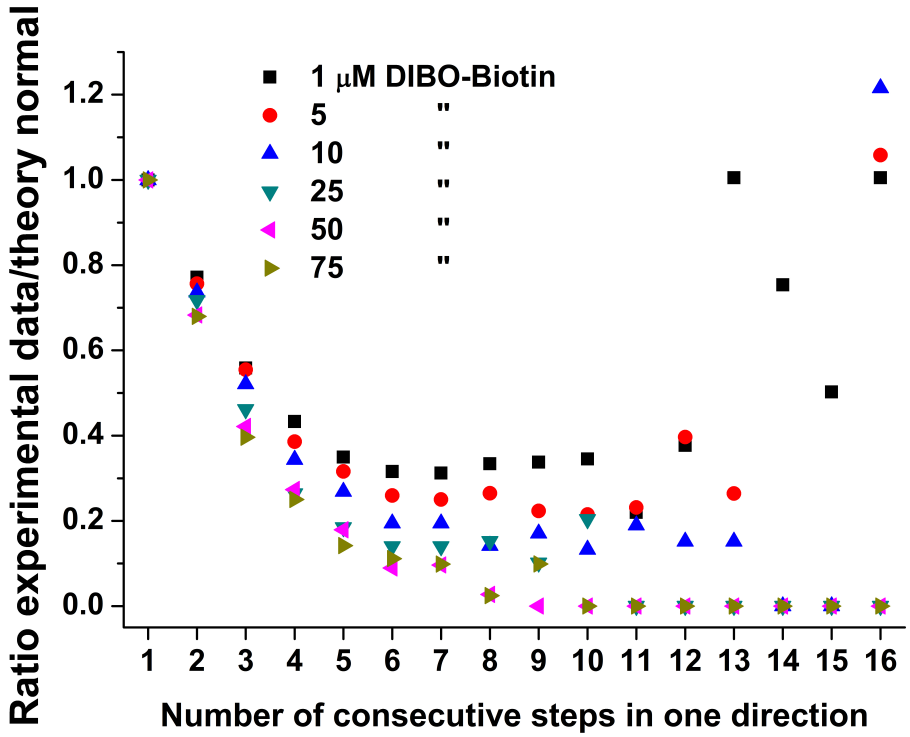

Figure 7.13: Comparison of chain lengths between the experimental data and idealized normal diffusion
For all chain lengths, the ratio is well below 1 (except for very high lengths where the statistical power is low). This indicates that all diffusion processes are strongly deviating from normal diffusion towards confined diffusion. This tendency increases for increasing DIBO-biotin concentrations.

Finally, the calculation of the cumulative weighted chain length shows increasing confinement for increasing DIBO-biotin concentrations (Figure 7.14). Note that the value varies between about 2.1 and 2.7, which was for the simulated data the steepest part of the curve.

Taken together, we could show that by analysis of the distribution of chain lengths one can easily determine a variety of parameters that further characterize the nature of the diffusion process. In our case, the values are fully consistent with the above described MSD analysis and corroborate the results obtained there.

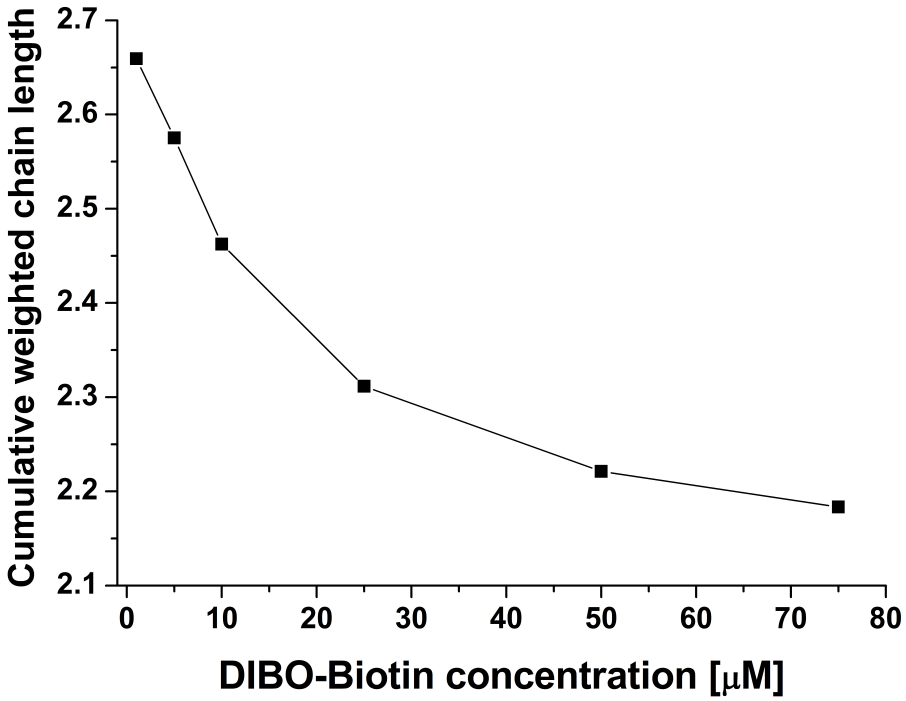

Figure 7.14: Cumulative weighted chain length
The value of the cumulative weighted chain length decreases for increasing DIBO-biotin concentrations, indicating stronger confinement.

7.5 Experimental Section

Cell culture: HMECs (variant 1, CDC, Atlanta, GA) were seeded in collagen coated 8-well LabTek slides (Nunc, Rochester, NY) with a density of $1.5 \cdot 10^4$ or $1 \cdot 10^4$, respectively, in 400 µL growth medium, dependent on whether the experiment was performed two or three days after seeding. The cells were cultured in MDCB-131 medium with 1% Glutamax, 10% fetal bovine serum (FBS), 10 ng/mL hEGF (all Life Technologies, Carlsbad, St. Louis, MO), 1 µg/mL hydrocortisone, and 1% of a penicillin-streptomycin solution containing 10,000 U/mL penicillin and 10 mg/L streptomycin (both Sigma-Aldrich, St. Louis, MO) at 37°C in 5% humidified CO_2 atmosphere. Cells were fixed with 4% paraformaldehyde (Sigma-Aldrich) in DPBS+Ca^{2+}/Mg^{2+} (Life Technologies). Before and after fixation, it was washed three time with DPBS+Ca^{2+}/Mg^{2+}.

Tagging of membrane glycans with biotin: For metabolic labeling, growth medium was supplemented with 50 µM Ac_4ManNAz or Ac_4GalNAz (Life Technologies) for at least two days. Cells were washed three times with warm growth medium and incubated with 400 µL DIBO-biotin (Life Technologies) solution at the desired concentration for one hour.

Artificial network formation: After tagging of membrane glycans with biotin, cells were washed three times with warm growth medium. Then, it was incubated with 350 µL SA solution at the desired concentration for 15 minutes. The concentration of fluorescent SA or of SA-coated QDs, respectively, was $5 \cdot 10^9$ M. It was washed two times with CO_2-independent medium (room temperature) supplemented with 10% FBS (both Life Technologies). For microscopy, cells were kept in CO_2-independent medium and immediately measured at room temperature (21°C) within less than one hour.

Endocytosis assay: HMECs were incubated for two days with 50 µM Ac_4ManNAz, followed by incubation with 5 or 50 µM DIBO-biotin and 0, 1.25, 2.5, or 5 µM tetravalent SA as described above. 0.75 mg/mL 10 kDa dextran-AlexaFluor647 conjugate (Life Technologies) in 400 µL growth medium was added for 15 minutes. Cells were fixed to ensure a defined time within endocytosis could occur. Then, fluorescence images of several cells within one confocal slice in the lower part of the cells were collected and the fluorescence signal within the endosomes was quantified.

Fluorescence microscopy: Single molecule images were obtained with a custom-built Nikon epifluorescence TE200 microscope and a Nikon PlanApo100 objective, NA=1.4. Confocal images for the quantification of endocytosis were obtained using a commercially available spinning-disk inverted microscope from Zeiss.

Software: Images were acquired and converted to tif images with Andor SOLIS 4.9. Tracking was performed with the Matlab Program uTrack.[251] MSD analysis was performed with the Matlab Class @msdanalyzer.[252] Simulations were carried out with Matlab. Images were analyzed using ImageJ. For data visualization and analysis, OriginPro 8G was used. Figures were prepared with CorelDraw12.

8 Photocontrol of E. coli Adhesion to Human Cells

This chapter is based on: **"Switching first contact: photocontrol of E. coli adhesion to human cells"** by Leonhard Möckl, Anne Müller, Christoph Bräuchle, and Thisbe K. Lindhorst
ChemComm **52**, 1254 (2016)[283]

Acknowledgements:
LM and AM conducted and evaluated the experiments and wrote the manuscript.
LM, AM, CB, and TKL wrote and corrected the manuscript.

8.1 Abstract

We have shown previously that carbohydrate-specific bacterial adhesion to a non-physiological surface can be photocontrolled by reversible E/Z isomerization using azobenzene-functionalised sugars. Here, this approach is applied to the surface of human cells. We show not only that bacterial adhesion to the azobenzene glycoside-modified cell surface is higher in the E than in the Z state, but add data about the specific modulation of the effect.

8.2 Introduction

Cell adhesion is a fundamental principle of biology. Many of its aspects have been elucidated,[284,285] but the molecular details of cell interactions are not fully under-

stood. As the first contact of cells is mediated through their glycosylated surfaces, our research on cell adhesion is focused on carbohydrate recognition. All organisms can recognize and distinguish between carbohydrates with the help of specialised proteins, the lectins.[137] Lectin function has been described in the context of, i.a., signaling, trafficking, and quality control, thus involving indispensable processes of life.[286–288] Also bacterial cells utilize their own lectins to mediate adhesion to glycosylated surfaces such as the membrane of the target cells.[289,290] Furthermore, bacterial adhesion enables bacterial colonization, biofilm formation, biofouling, or it precedes infection of cells.[121,291] Hence, investigation and control of bacterial adhesion is important, especially in a medical context, given the high incidence rates of infectious diseases worldwide.[292]

In recent years we have studied the α-D-mannoside-specific adhesion of *Escherichia coli* bacteria,[23,293] which is mediated by the bacterial lectin FimH. FimH is located at the tips of adhesive organelles, called type 1 fimbriae,[294] which are projecting from the bacterial cell surface. Previously we have shown that type 1 fimbriae-mediated bacterial adhesion to a non-physiological surface can be photochemically controlled. In this specific case azobenzene-functionalised α-D-mannoside derivatives were assembled on a gold surface in the form of a glyco-SAM (self-assembled monolayer).[22,295] Photochemical isomerization of the azobenzene moiety between its E and its Z state then allowed to reversibly switch the orientation of the attached carbohydrate ligands between two defined states. In parallel with this E/Z isomerization, the adhesiveness of the surface was altered leading to reduction of bacterial adhesion in the Z state of the SAM by 80 % in comparison to the E state.

While the azobenzene photoswitch is long known[296] and has been used before for switching of the properties of designer surfaces,[297–300] our work on the control of bacterial adhesion through re-orientation of carbohydrate presentation is unprecedented. Here it has been our goal to challenge our system in the context of cell-cell adhesion, thus changing the artificial glyco-SAM surface against the plasma membrane of human cells. For this, we had to incorporate azobenzene mannosides in the cell surface of live cells, effect their E/Z isomerization to switch the orientation of the attached mannoside moieties, and to finally test the influence of this isomerization on *E. coli* adhesion.

8.3 Results and Discussion

Our experimental approach is explained in Figure 8.1: Metabolic oligosaccharide engineering (MOE)[148,301] was employed to install bioorthogonal azido functional groups on the cell surface. This allows their subsequent modification with alkyne-functionalised azobenzene glycosides by well-known click chemistry.[302–305] In a final step, photochemical E/Z isomerization of the installed azobenzene moiety was effected by irradiation with light of the appropriate wavelength, and subsequently bacterial adhesion was measured via high-resolution live-cell fluorescence microscopy. For these experiments, human microvascular endothelial cells, variant 1 (HMEC-1) and GFP-fluorescent type 1 fimbriated *E. coli* PKL1162[143] were used.

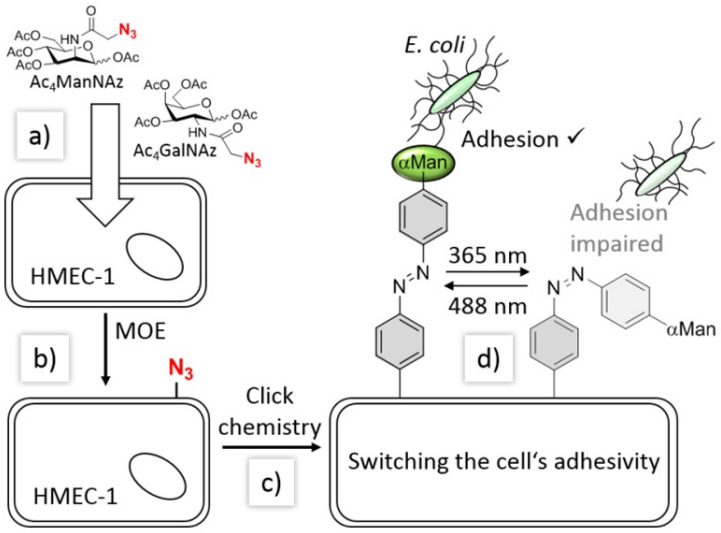

Figure 8.1: Our approach of switching the adhesivity of cells.
Azido functional groups can be incorporated into cell surface glycoconjugates employing the synthetic carbohydrates Ac_4ManNAz or Ac_4GalNAz, respectively, according to a known methodology called metabolic oligosaccharide engineering (MOE). The peracetylated azido sugars are taken up by the cells (HMEC-1) (a), and processed by the biosynthetic machinery to lead to azido-functionalization of the cell surface (b). Bioorthgonal click chemistry then allows conjugation of the cell surface with azobenzene glycosides (such as α-D-mannosides, αMan). Reversible E/Z isomerization of the azobenzene moiety employing UV or visible light, respectively, allows to change the orientation of the conjugated sugar. This experimental approach allowed to test if adhesion of *E. coli* to live human cells can be photochemically controlled.

To install the required bioorthogonal azido functional groups on the cell surface of HMEC-1, cells were incubated with 50 µM tetraacetylated *N*-azidoacetyl-D-mannosamine (Ac_4ManNAz, Figure 8.1). Ac_4ManNAz is taken up by the cells and according to the oligosaccharide metabolism leads to azido labelling of terminal sialic acid units of membrane glycoproteins. When Ac_4GalNAz is employed on the other hand, the azido label is incorporated into mucin-type glycoproteins.[156] For the chemical functionalization of the azido-modified cells, the azobenzene derivatives **5**-**7**, carrying an alkyne functional group were required (Scheme 1). Synthesis of the azobenzene glycosides **5** and **6** started from the known p-aminophenyl glycosides **1**[143] and **2**,[306] which were subjected to a classical azo coupling with phenol to furnish the respective hydroxyazobenzene derivatives **3** and **4**.[307] Then, Williamson etherification with propargyl bromide led to the desired alkyne-functionalised azobenzene glycosides **5** and **6**. The azobenzene alkyne **7** was needed as control and was directly obtained from hydroxyazobenzene.[308] As normal, the synthesised azobenzene derivatives were obtained in the more stable *E*-configuration.

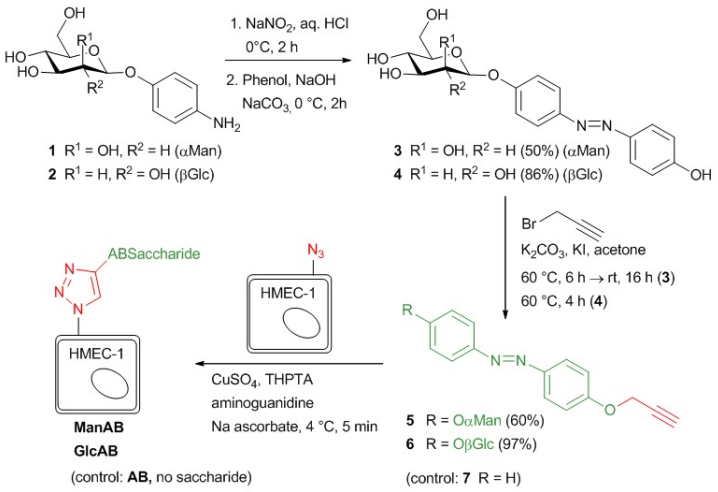

Figure 8.2: Synthesis of alkyne-functionalised azobenzene glycosides and labelling of engineered human cells (HMEC-1).
α-D-Mannosides were used as specific ligands for bacterial adhesion, whereas β-D-glucosides and simple propargylated azobenzene (7) are needed as control compounds. Azido-functionalised HMEC-1 were ligated with azobenzene (AB) derivatives **5**-**7** in a Cu(I)-catalyzed click reaction.

First, the azobenzene α-D-mannoside **5** was conjugated to azido-functionalised HMEC-1 after Ac_4ManNAz labelling. For this reaction, 200 µM azobenzene α-D-mannoside,

50 μM $CuSO_4$, 250 μM tris(3-hydroxypropyltriazolylmethyl)amine, 1 mM aminoguanidine, and 2.5 mM sodium ascorbate in buffered saline solution were employed at 4°C for 5 minutes according to the literature.[155] Copper (I), which is produced during the reaction, is known to exhibit toxic side effects after some time, however, we applied conditions that were shown earlier not to be harmful for cells. Azobenzene mannoside **5** was employed as 200 μM solution to ensure complete labelling of all azido groups on the cell surface, based on a control experiment with a fluorescent alkyne (cf. Figure 12.17). After labelling, cells were split into two portions. To effect $E \rightarrow Z$ isomerization of the conjugated azobenzene moiety, both sets of labelled HMEC-1 were irradiated with UV light of 365 nm. Then, cells were incubated with GFP-fluorescent *E. coli* (1:10 dilution of a suspension with OD_{600}=0.1, cf. Figure 12.18, Figure 12.19, Figure 12.20, Figure 12.21) and the number of adhered bacteria was counted employing high-resolution live-cell fluorescence microscopy. For both sets of HMEC-1 the number of adhered bacteria is similar low at this stage, as it is expected (Figure 8.3). In a subsequent step, only one of both cell sets was irradiated again; this time with green light (488 nm) to reverse the initial isomerisation and thus effect $Z \rightarrow E$ isomerization of the azobenzene configuration. Then, a second incubation with fluorescent *E. coli* was performed as before, and adhesion again quantified by counting the number of adhered bacterial cells. Whereas the adhesivity of the cells without a second irradiation treatment remained the same, a significant increase of bacterial adhesion was measured for the cells that were irradiated at 488 nm (about 50%). We attribute this observation to the mode of mannose orientation, which is changed with the isomerization of the azobenzene hinge. In accordance with the observation made with photoswitchable glyco-SAMs, the adhesivity of the azobenzene mannoside-modified cell surface is higher in the E than in the Z state, where the carbohydrate ligand is more hidden. At first, the azobenzene α-D-mannoside **5** was conjugated to azido-functionalised HMEC-1 after Ac_4ManNAz labelling. For this reaction, 200 μM azobenzene α-D-mannoside, 50 μM $CuSO_4$, 250 μM tris(3-hydroxypropyltriazolylmethyl)amine (THPTA), 1 mM aminoguanidine, and 2.5 mM sodium ascorbate in buffered saline solution were employed at 4°C for 5 minutes according to the literature.[155] Copper (I), which is produced during the reaction, is known to exhibit toxic side effects after some time, however, we applied conditions that were shown earlier not to be harmful for cells. Azobenzene mannoside **5** was employed as 200 μM solution to ensure complete labelling of all azido groups on the cell surface, based on a con-

trol experiment with a fluorescent alkyne (cf. Figure 12.17). After labelling, cells were split into two portions. To effect $E \rightarrow Z$ isomerization of the conjugated azobenzene moiety, both sets of labelled HMEC-1 were irradiated with UV light of 365 nm. Then, cells were incubated with GFP-fluorescent *E. coli* (1:10 dilution of a suspension with OD_{600}=0.1, cf. Figure 12.18, Figure 12.19, Figure 12.20, Figure 12.21) and the number of adhered bacteria was counted employing high-resolution live-cell fluorescence microscopy. For both sets of HMEC-1 the number of adhered bacteria is similar low at this stage, as it is expected (Figure 8.3). In a subsequent step, only one of both cell sets was irradiated again; this time with green light (488 nm) to reverse the initial isomerisation and thus effect $Z \rightarrow E$ isomerization of the azobenzene configuration. Then, a second incubation with fluorescent *E. coli* was performed as before, and adhesion again quantified by counting the number of adhered bacterial cells. Whereas the adhesivity of the cells without a second irradiation treatment remained the same, a significant increase of bacterial adhesion was measured for the cells that were irradiated at 488 nm (about 50%). We attribute this observation to the mode of mannose orientation, which is changed with the isomerization of the azobenzene hinge. In accordance with the observation made with photoswitchable glycoSAMs, the adhesivity of the azobenzene mannoside-modified cell surface is higher in the E than in the Z state, where the carbohydrate ligand is more hidden. At first, the azobenzene α-D-mannoside **5** was conjugated to azido-functionalised HMEC-1 after Ac_4ManNAz labelling. For this reaction, 200 µM azobenzene α-D-mannoside, 50 µM $CuSO_4$, 250 µM tris(3-hydroxypropyltriazolylmethyl)amine, 1 mM aminoguanidine, and 2.5 mM sodium ascorbate in buffered saline solution were employed at 4°C for 5 minutes according to the literature.[155] Copper (I), which is produced during the reaction, is known to exhibit toxic side effects after some time, however, we applied conditions that were shown earlier not to be harmful for cells. Azobenzene mannoside **5** was employed as 200 µM solution to ensure complete labelling of all azido groups on the cell surface, based on a control experiment with a fluorescent alkyne (cf. Figure 12.17). After labelling, cells were split into two portions. To effect $E \rightarrow Z$ isomerization of the conjugated azobenzene moiety, both sets of labelled HMEC-1 were irradiated with UV light of 365 nm. Then, cells were incubated with GFP-fluorescent *E. coli* (1:10 dilution of a suspension with OD_{600}=0.1, cf. Figure 12.18, Figure 12.19, Figure 12.20, Figure 12.21) and the number of adhered bacteria was counted employing high-resolution live-cell fluorescence microscopy. For both sets of HMEC-1 the number of adhered

bacteria is similar low at this stage, as it is expected (Figure 8.3). In a subsequent step, only one of both cell sets was irradiated again; this time with green light (488 nm) to reverse the initial isomerisation and thus effect $Z \rightarrow E$ isomerization of the azobenzene configuration. Then, a second incubation with fluorescent *E. coli* was performed as before, and adhesion again quantified by counting the number of adhered bacterial cells. Whereas the adhesivity of the cells without a second irradiation treatment remained the same, a significant increase of bacterial adhesion was measured for the cells that were irradiated at 488 nm (about 50%). We attribute this observation to the mode of mannose orientation, which is changed with the isomerization of the azobenzene hinge. In accordance with the observation made with photoswitchable glycoSAMs, the adhesivity of the azobenzene mannoside-modified cell surface is higher in the E than in the Z state, where the carbohydrate ligand is more hidden. At first, the azobenzene α-D-mannoside **5** was conjugated to azido-functionalised HMEC-1 after Ac_4ManNAz labelling. For this reaction, 200 µM azobenzene α-D-mannoside, 50 µM $CuSO_4$, 250 µM tris(3-hydroxypropyltriazolylmethyl)amine, 1 mM aminoguanidine, and 2.5 mM sodium ascorbate in buffered saline solution were employed at 4°C for 5 minutes according to the literature.[155] Copper (I), which is produced during the reaction, is known to exhibit toxic side effects after some time, however, we applied conditions that were shown earlier not to be harmful for cells. Azobenzene mannoside **5** was employed as 200 µM solution to ensure complete labelling of all azido groups on the cell surface, based on a control experiment with a fluorescent alkyne (cf. Figure 12.17). After labelling, cells were split into two portions. To effect $E \rightarrow Z$ isomerization of the conjugated azobenzene moiety, both sets of labelled HMEC-1 were irradiated with UV light of 365 nm. Then, cells were incubated with GFP-fluorescent *E. coli* (1:10 dilution of a suspension with OD_{600}=0.1, cf. Figure 12.18, Figure 12.19, Figure 12.20, Figure 12.21) and the number of adhered bacteria was counted employing high-resolution live-cell fluorescence microscopy. For both sets of HMEC-1 the number of adhered bacteria is similar low at this stage, as it is expected (Figure 8.3). In a subsequent step, only one of both cell sets was irradiated again; this time with green light (488 nm) to reverse the initial isomerisation and thus effect $Z \rightarrow E$ isomerization of the azobenzene configuration. Then, a second incubation with fluorescent *E. coli* was performed as before, and adhesion again quantified by counting the number of adhered bacterial cells. Whereas the adhesivity of the cells without a second irradiation treatment remained the same, a significant increase of bacterial adhesion was measured for the

cells that were irradiated at 488 nm (about 50%). We attribute this observation to the mode of mannose orientation, which is changed with the isomerization of the azobenzene hinge. In accordance with the observation made with photoswitchable glyco-SAMs, the adhesivity of the azobenzene mannoside-modified cell surface is higher in the E than in the Z state, where the carbohydrate ligand is more hidden. At first, the azobenzene α-D-mannoside **5** was conjugated to azido-functionalised HMEC-1 after Ac_4ManNAz labelling. For this reaction, 200 µM azobenzene α-D-mannoside, 50 µM $CuSO_4$, 250 µM tris(3-hydroxypropyltriazolylmethyl)amine, 1 mM aminoguanidine, and 2.5 mM sodium ascorbate in buffered saline solution were employed at 4°C for 5 minutes according to the literature.[155] Copper (I), which is produced during the reaction, is known to exhibit toxic side effects after some time, however, we applied conditions that were shown earlier not to be harmful for cells. Azobenzene mannoside **5** was employed as 200 µM solution to ensure complete labelling of all azido groups on the cell surface, based on a control experiment with a fluorescent alkyne (cf. Figure 12.17). After labelling, cells were split into two portions. To effect $E \rightarrow Z$ isomerization of the conjugated azobenzene moiety, both sets of labelled HMEC-1 were irradiated with UV light of 365 nm. Then, cells were incubated with GFP-fluorescent *E. coli* (1:10 dilution of a suspension with OD_{600}=0.1, cf. Figure 12.18, Figure 12.19, Figure 12.20, Figure 12.21) and the number of adhered bacteria was counted employing high-resolution live-cell fluorescence microscopy. For both sets of HMEC-1 the number of adhered bacteria is similar low at this stage, as it is expected (Figure 8.3). In a subsequent step, only one of both cell sets was irradiated again; this time with green light (488 nm) to reverse the initial isomerisation and thus effect $Z \rightarrow E$ isomerization of the azobenzene configuration. Then, a second incubation with fluorescent *E. coli* was performed as before, and adhesion again quantified by counting the number of adhered bacterial cells. Whereas the adhesivity of the cells without a second irradiation treatment remained the same, a significant increase of bacterial adhesion was measured for the cells that were irradiated at 488 nm (about 50%). We attribute this observation to the mode of mannose orientation, which is changed with the isomerization of the azobenzene hinge. In accordance with the observation made with photoswitchable glyco-SAMs, the adhesivity of the azobenzene mannoside-modified cell surface is higher in the E than in the Z state, where the carbohydrate ligand is more hidden.

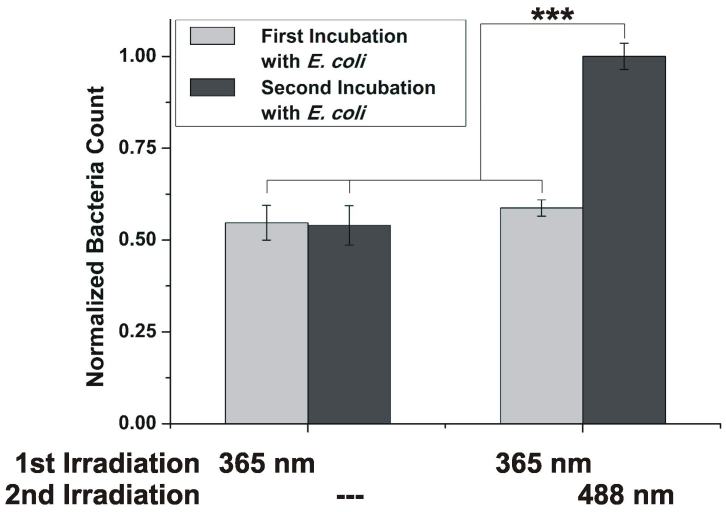

Figure 8.3: Switching of ManAB configuration allows to control adhesion of E. coli to HMEC-1.
After incubation of two sets of cells bearing azido groups at terminal sialic acids with **5** in *Z*-configuration, the adhesion of bacteria is similar for both sets. However, photoswitching of **ManAB** configuration to *E* increases the adhesion significantly (second incubation). If **ManAB** remains in *Z*-configuration, no increase is observed. Error bars are given as standard error of the mean (SEM) of experiments with four independent sets of cells/condition. *** = $p < 0.001$.

So far, photoswitching of the adhesivity of azobenzene mannoside-labelled cells was investigated under static conditions. In order to investigate photoswitching of cell adhesion in real-time, flow-based experiments[132] were performed next. This has the advantage that one can follow adhesion in real time and that testing is closer to physiological conditions where flow is often present. Thus, HMEC-1 were cultivated in flow chambers, again incubated with Ac_4ManNAz and labelled with azobenzene mannoside **5** in analogy to our experiments under static conditions. Then, a bacterial suspension (1:50 dilution of a suspension with OD_{600}=0.1) was employed at continuous flow with a shear rate of 1.5 dyn/cm^2 a typical shear rate for microvascules). It is worthwhile to note, that the flow was not interrupted during irradiation (300 seconds). Adhering bacteria were monitored by fluorescence microscopy while switching the configuration of azobenzene mannosides conjugated on HMEC-1 multiple times between *E* and *Z* (Figure 8.4). The development of the recorded bacterial GFP-fluorescence is then a direct measure for the adhesion of *E. coli*.

The obtained curves clearly show that alternating irradiation using light of 365 nm and 488 nm has a strong effect on bacterial adhesion (Figure 8.4a). After irradiation of the flow chamber with 488 nm light, the slopes of the bacterial GFP signal are significantly higher than after irradiation with 365 nm. This is also clearly seen after fitting of the curves, assuming a linear development of fluorescence (Figure 8.4b). Only after several switching events (starting at 1500 s), the measured slopes are no longer correlated with azobenzene configuration. This can be attributed to increasing coverage of HMEC-1 with bacterial cells and more and more bacteria adhering to other to bacteria. This is clearly seen in the obtained microscopic images (cf. Figure 12.22). Thus, when bacteria are adhering to bacterial cells and not to HMEC-1, the adhesion is naturally not sensitive to E/Z isomerization. As under static conditions, the results obtained in the flow experiments indicate that the orientation of mannoside **5** conjugated to the surface of HMEC-1 has a strong influence on the adhesion of bacteria. Again, the results suggest that the bent Z form is less accessible for bacteria than the E form. Thus, adhesion is reduced after $E \rightarrow Z$ isomerization. Next, two important control experiments were performed in order to understand the observed effects in greater detail. First, the question of carbohydrate specificity of the observed effects was addressed. Thus, the azobenzene derivative **7** (**AB** in Figure 8.5), devoid of a carbohydrate, and the β-D-glucoside **6** (cf. Figure 8.2) were employed for HMEC-1 labelling instead of the mannoside **5** which was used so far. The glucoside **6** exhibits a similar structure and polarity as **5** but is no ligand for the bacterial lectin FimH. Labelling of HMEC-1 was again performed with Ac_4ManAz, click chemistry carried out with **6** and **7** as before, and then bacterial adhesion was measured after irradiation. All experiments were compared to azido-labelled HMEC-1, which had not been reacted with either of the azobenzene derivatives (control, Figure 8.5). These experiments show that adhesion of *E. coli* to cells reacted with either **6** or **7**, is significantly decreased compared to untreated cells. This observation suggests a shielding effect for both derivatives, prohibiting bacterial adhesion to the surface of HMEC-1 to some extent. On the other hand, this effect is not significantly sensitive to E/Z isomerization. This finding indicates that the adhesion of bacteria to cells treated with **5** is indeed carbohydrate-specific and results from the interaction between the bacterial lectin FimH and its α-D-mannosidic ligand. Unspecific polar interactions, e.g., do not account for bacterial adhesion. Control cells showed a slight response to irradiation with 365 nm light, but the effects caused by **6** or **7** are more significant. At this stage of the project, we were asking how the orientation of a

rather small molecule (such as an azobenzene glycoside) within the complex environment of a cell's surface can exert such a pronounced effect on cell adhesion. Hence, we performed a second control experiment in which the azobenzene mannoside ligand is positioned differently on the surface of HMEC-1. This is possible by labelling HMEC-1 with Ac_4GalNAz instead of Ac_4ManNAz. Whereas Ac_4ManNAz leads to labelling of sialic acids, which are almost exclusively found at the terminal position of cell surface glycans, Ac_4GalNAz labels mucin-type glycoproteins. These are characterised by LacNAc moieties, which are localised deeper within the glycosylated cell surface.[306] Interestingly, bacterial adhesion to HMEC-1, labelled with Ac_4GalNAz and modified with mannoside **5** is increased in comparison to control cells. This observation can be rationalised on the increased concentration of mannoside present on the cell surface after modification; other than in case of modification with **6** or **7**, which does not change the mannosylation pattern of HMEC-1. However, the observed increased adhesion is not dependent on the configuration of the azobenzene moiety, thus insensitive to irradiation. In this case it seems, that the orientational change of the mannoside ligand is not effective within the complex environment of the HMEC-1 surface. As LacNAc groups are typically not localised at terminal positions of glycans, the azobenzene mannoside moieties might be buried under a layer of other glycoconjugates.

Taken together, we show that the azobenzene mannoside **5** can be employed to influence adhesion of *E. coli* to HMEC-1. We postulate the following mechanism that underlies this photocontrol: i) mannose binds to FimH and serves as ligand for specific interaction between the bacterium and the modified cell surface (cf. Ac_4ManNAz+**5** vs. Ac_4ManNAz+**6**). ii) If no mannose ligand is present or if it adopts a disadvantageous orientation (Z-configuration), the azobenzene groups shield the cell, leading to reduced binding of *E. coli* (cf. Ac_4ManNAz+**5** vs. Ac_4ManNAz+**AB**). iii) The FimH ligand mannose must be localised at the terminus of glycans to ensure that the change in configuration upon a Z-E-transition is not small (Ac_4ManNAz+**5** vs. Ac_4GalNAz+**5**). It is surprising that this orientation effect can be found not only on an artificial, ordered glyco-SAM as we described before, but even in the complex, in comparison rather chaotic setting of the cell surface. Of course, this finding bears implications for the way how cells recognize and are affected by their environment. Further experiments will have to investigate how the exact processes and consequences of e.g. orientational variances are, but we hope that our work is a first step in this direction.

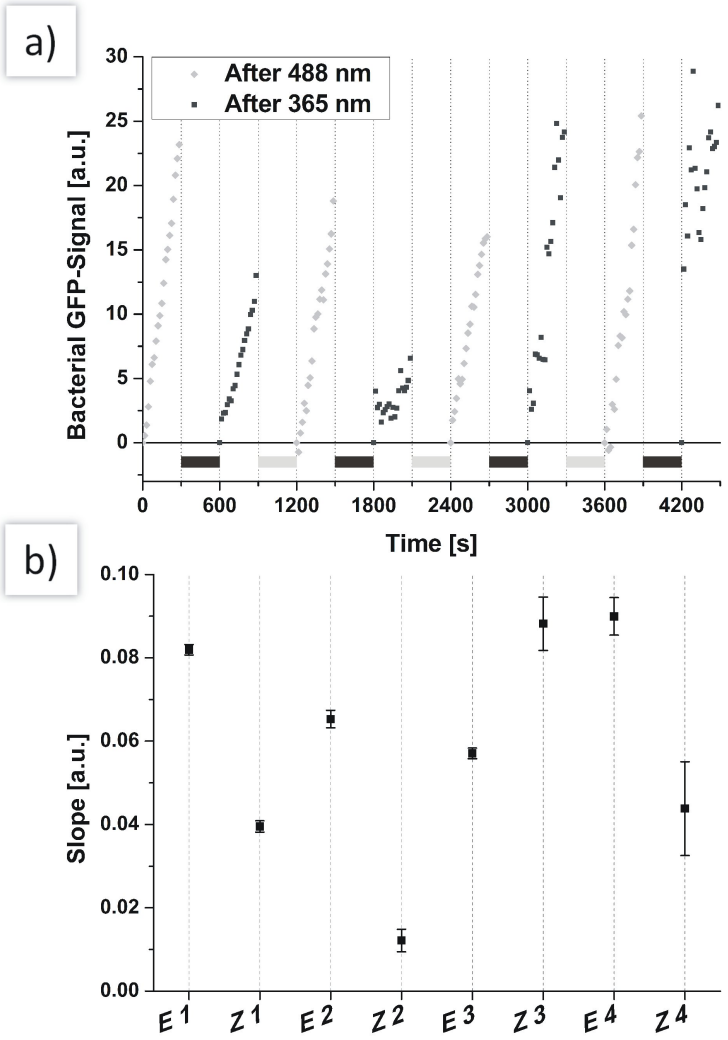

Figure 8.4: Adhesion of *E. coli* to switchable cell surfaces under flow.
a) The azobenzene **5** was switched several times between *Z* and *E* while flowing a continuous stream of bacteria solution over the cells. The adhesion of bacteria was lower if **5** was in *Z*-configuration. Only after several switching cycles this tendency was no longer observed, caused by increasing coverage of the cells with bacteria, leading to a high amount of adhering to other bacteria and not to the cell surface. During irradiation with 365 nm (light grey bars) or 488 nm (dark grey bars), the flow was not stopped. b) The slopes of linear curves that were fitted to the data of the middle panel clearly resembles the effect of the reversible switching. Error bars are given as SEM of the fitting. For easier comparison, the slopes are set to start at a common origin by subtraction of the fluorescence intensity of the first frame from the subsequent frames.

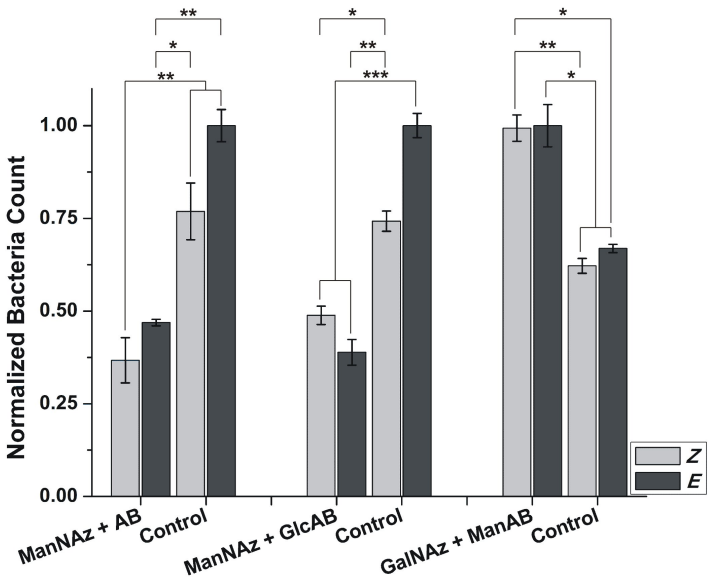

Figure 8.5: Control experiments.
If the azobenzene lacks a mannose group (**AB**, left) or exhibits a glucose group to which FimH cannot bind specifically (GlcAB, middle), adhesion is reduced in comparison to control cells independent of the configuration of the azobenzene, indicating a shielding effect of **AB** and **GlcAB**. If **ManAB** is attached to mucin-type proteins (right) and hence not at the terminal position of glycans, the adhesion is increased but not dependent on the configuration of the azobenzene. Errors are given as SEM. Experiments were carried out with four independent sets of cells for each condition. * = $p < 0.1$, ** = $p < 0.01$, *** = $p < 0.001$

8.4 Experimental Section

General methods: Analytical thin layer chromatography (TLC) was performed on silica gel plates (GF 254, Merck). Visualization was achieved by UV light and/or with 10% sulfuric acid in ethanol followed by heat treatment at 180°C. Flash chromatography was performed on silica gel 60 (Merck, 230-400 mesh, particle size 0.040-0.063 mm) by using distilled solvents. Melting points (mp) were determined on a Büchi M-56 apparatus. Optical rotations were measured with a Perkin-Elmer 241 polarimeter (sodium D-line: 589 nm, length of cell: 1 dm) in the solvents indicated. Proton (1H) nuclear magnetic resonance spectra and carbon (13C) nuclear magnetic resonance spectra were recorded on a Bruker DRX-500 and AV-600 spectrometer. Chemical shifts are referenced to the residual proton of the NMR solvent. Data are presented as follows: chemical shift, multiplicity (s=singlet, d=doublet, t=triplet, q=quartet, m=multiplet, and br=broad signal), coupling constant in hertz (Hz) and, integration. Full assignment of the peaks was achieved with the aid of 2D NMR techniques (1H/1H COSY and 1H/13C HSQC. All NMR spectra of the E-isomers of the azobenzene derivatives were recorded after they were kept for 16 h in the dark at 40 °C. Infrared (IR) spectra were measured with a Perkin Elmer FT-IR Paragon 1000 (ATR) spectrometer and were reported in cm-1. ESI mass spectra were recorded on an Esquire-LC instrument from Bruker Daltonics. UV-vis absorption spectra were performed on Perkin-Elmer Lambda-241 at a temperature of 20 °C ± 1 °C.

Bacterial Culture: E. coli (strain pPKL1162) were inoculated in LB medium (10 mL) (Sigma-Aldrich, St. Louis, MO) in presence of chloramphenicol (50 mg/L) and ampicillin (100 mg/L) (both Sigma-Aldrich) and grown at 37°C overnight under constant agitation. Then, the bacteria were centrifuged and washed two times with DPBS $+Ca^{2+}/Mg^{2+}$ (Life Technologies, Carlsbad, St. Louis, MO) and once with cell medium. Then, the bacteria were resuspended in cell medium (10 mL) and the optical density at 600 nm was determined. For the experiments under static conditions, a 1:10 or 1:20 dilution of a suspension with OD600=0.1 was used. Under flow conditions, the dilution was 1:50.

Cell Culture: HMEC-1 (CDC, Atlanta, GA) were seeded in collagen coated 8-well LabTekII-slides (Nunc, Rochester, NY) or in collagen coated Luer $I^{0.8}$ channels (IBIDI, Martinsried, Germany) and grown to confluency. The cells were cultured in MDCB-131 medium with 1% glutamax, 10% FBS, hEGF (10 ng/mL) (all Life Technologies), and hydocortisone (1 µg/mL) (Sigma-Aldrich) at 37°C in 5% CO_2-atmosphere.

Fluorescence Microscopy: Confocal fluorescence images were obtained with a commercially available spinning-disk inverted microscope (Zeiss).

Software: Images were analyzed using ImageJ. For data visualization and analysis, OriginPro 8G was used. Figures were prepared with Corel Draw 12.

9 Flow Changes the Properties of E. coli Adhesion Inhibitors

This chapter is based on: **"En route from artificial to natural: Evaluation of inhibitors of mannose-specific adhesion of *E. coli* under flow"** by Leonhard Möckl, Claudia Fessele, Christoph Bräuchle, Thisbe K. Lindhorst
Under revision at *Biochimica et Biophysica Acta (BBA)*

Acknowledgements:
LM and CF conducted and evaluated the experiments and wrote the manuscript.
TKL and CB wrote and corrected the manuscript.

9.1 Abstract

We investigated the properties of four *E. coli* adhesion inhibitors under static and under flow conditions. On mannan-covered model substrates and under static conditions, all inhibitors were able to almost completely abolish lectin-mediated *E. coli* adhesion. On a monolayer of living human microvascular endothelial cells (HMEC-1), the inhibitors reduced under static conditions adhesion as well, but a large fraction of bacteria still managed to adhere even at highest inhibitor concentrations. In contrast, under flow conditions *E. coli* did not exhibit any adhesion to HMEC-1 already at inhibitor concentrations where significant adhesion was detected under static conditions. This indicates that the presence of shear stress strongly affects inhibitor properties and must be taken into account when evaluating the potency of bacterial adhesion inhibitors.

9.2 Introduction

The adhesion of bacteria to surfaces is one of the key steps in processes where bacteria exhibit pathogenic effects. Examples include harmful triggering of cellular signaling cascades,[309] invasion of host cells,[310] or biofilm formation.[311] One of the most common infectious diseases caused by bacterial adhesion are urinary tract infections (UTI). It is estimated that every second woman and 5% of the male population suffers from a UTI at least once in their lifetime. Uropathogenic *E. coli* (UPEC) are the primary reason for these infections.[312] The first contact between the eukaryotic cell and the bacterium, crucial for the subsequent development of the disease, is mediated by adhesive organelles anchored on the outer membrane and projecting from the surface of UPEC. These so-called fimbriae consist of various protein units with a lectin domain at the very end. One of the best characterized fimbriae and among the most important virulent factors of *E. coli* are the type 1 fimbriae. Their associated lectin is FimH which is specific for α-D-mannosides. FimH is known to bind to high-mannose type oligosaccharides of the glycocalyx of eukaryotic cells. Multivalency of this specific protein-carbohydrate interaction leads to adhesion of bacterial cells.[313] To fight bacterial infections like UTI, antibiotics are commonly used. However, one of the main problems resulting from the widespread use of antibiotics is the appearance of resistant bacterial strains.[314] An alternative therapeutic strategy against bacterial infection is an antiadhesion therapy[315] in which carbohydrate inhibitors are employed to prevent bacterial adhesion. Numerous FimH antagonists have been developed for the inhibition of type 1 fimbriae-mediated bacterial adhesion.[140,143,316] Recently, bioisosters glycosides were shown to be promising drugs against UI.[317] In spite of the unquestionable success of the antiadhesion approach, antiadhesion therapy has not yet led to general solutions against infectious diseases. The reason might be that it is still challenging to consider all different aspects of a complex natural environment in the development of antiadhesives. Typically inhibitors of bacterial adhesion are evaluated in a microtiter plate-based assay under static conditions (Figure 9.1A). However, a glycosylated microplate or any other artificial glycoarray cannot resemble the full complexity of a cell surface. Thus it is important to also test the potency of, here, FimH antagonists in cell-based assays (Figure 9.1B).[318] In addition, natural conditions of cell-cell interactions are characterized by flow and shear stress, respectively.[30] Flow is a critical parameter in bacterial adhesion as it has been described for the bacterial lectin FimH that it exerts

so-called catch bonds under flow.[319] In catch bonding, FimH ligands are bound more tightly as a consequence of an allosteric process, in which FimH adopts a conformation of increased mannose affinity.[320] Although adhesion of bacteria under shear stress has been investigated since some time,[321–324] the influence of shear stress on inhibition of bacterial adhesion is not yet in the focus of research.[325] Therefore, we commenced a study to compare the effect of FimH antagonists in an artificial environment, that is a microtiter plate-based adhesion inhibition assay, with a cell-based assay under physiological conditions (Figure 9.1C). As bacterial adhesion under physiological conditions is almost never static, it is important to compare inhibition of bacterial adhesion under static conditions with testing under flow. An improved knowledge of inhibition of cell adhesion processes will eventually facilitate the development of new antiadhesive inhibitors.

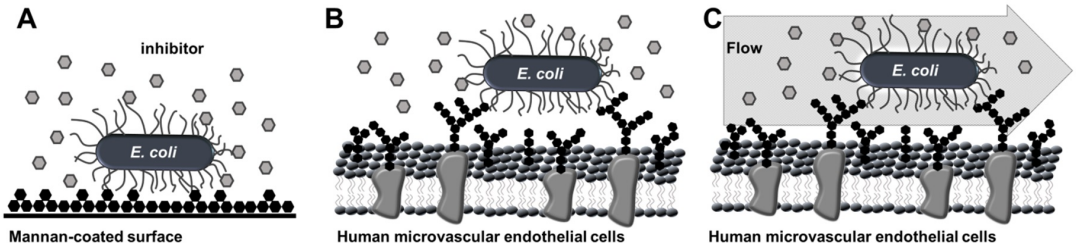

Figure 9.1: En route from artificial to natural.
The mannose-specific fimbriae-mediated adhesion of bacterial cells to surfaces depends on the conditions. (A) Adhesion to artificial surfaces such as mannan-coated microtiter plates has been regularly used to evaluate the potency of sugar inhibitors under static conditions. (B) In bacterial adhesion to the glycosylated surface of human cells (HMEC-1) inhibitors compete with a more complex carbohydrate environment. (C) Under natural flow conditions, shear forces activate catch bonding of the bacterial lectins and thus, for inhibitors of bacterial adhesion different potencies might be found than under static conditions.

For our study, four known α-D-mannosides with interesting properties as inhibitors of type 1 fimbriae-mediated adhesion of *E. coli* were selected (Figure 9.2). Based on their IC_{50} values as inhibitors of bacterial adhesion to a mannan-coated polystyrene model surface (microplate), we were interested to measure their inhibitory potency in a more physiological environment by testing their ability to shut down *E. coli* adhesion on a monolayer of human microvascular endothelial cells, variant 1 (HMEC-1). In an important third step the static testing conditions were changed to flow conditions

to investigate how the presence of shear stress affects the potency of the inhibitors to abolish *E. coli* adhesion.

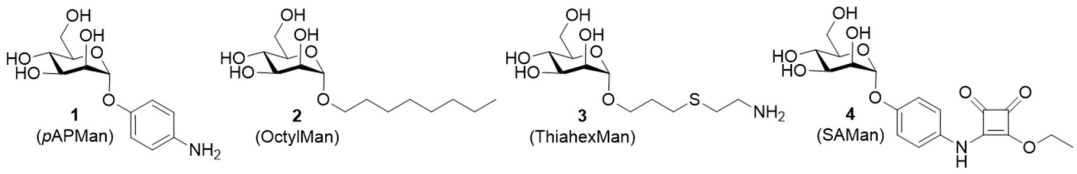

Figure 9.2: Structures of FimH ligands 1-4, employed for inhibition of type 1 fimbriae-mediated bacterial adhesion.

9.3 Results and Discussion

9.3.1 Inhibition of *E. coli* adhesion to mannan surfaces under static conditions

All four mannosides under investigation, **1**-**4**, were tested in parallel using the well-known adhesion-inhibition assay.[143] Bacteria which express GFP where used to correlate the fluorescent intensity, recorded with a microplate reader, with the bacterial adhesion. In every assays methyl α-D-mannoside (MeMan) was tested in parallel as reference inhibitor. From the obtained fluorescence data and the resulting sigmoidal inhibition curves (cf. Figure 12.23) we determined IC_{50} values and the corresponding RIP (relative inhibitory potential, based on MeMan). For all tested inhibitors, the RIP value was larger than 1 (Table 9.1). Thus, all tested inhibitors were more potent as inhibitors of type 1 fimbriae-mediated bacterial adhesion to mannosylated surfaces than the standard MeMan.

Table 9.1: Inhibition of type 1 fimbriae-mediated *E. coli* adhesion to mannan-coated microtiter plates.
IC50 and RIP values are averaged from mean values from three independent tests. SD: standard deviation

Inhibitor	IC_{50} [μM (SD)	RIP (SD)	total inhibition (%)
*p*APMan (**1**)	321 (0.23)	25.4 (0.02)	98 %
OctylMan (**2**)	124 (0.87)	62.7 (0.79)	98 %
ThiahexMan (**3**)	3120 (1.23)	2.1 (0.37)	94 %
SAMan (**4**)	6.65 (0.75)	1169.3 (2.46)	96 %

The measured potencies are in accordance with reported data.[140,143,326,327] Due to the aromatic aglycone, mannosides 1 and 4 are 25 times and almost 1200 times more potent inhibitors of type 1 fimbriae-mediated bacterial adhesion than MeMan. In particular the special potency of **4** has been reported and explained earlier.[328,329] ThiahexMan is the weakest of the tested four. Interestingly, OctMan (2) is the best inhibitor in the tested series which might be due to micelle formation. Glycomicelles can exert multivalency effects, leading to improved inhibitory potency of this compound.[279] Overall, the inhibitor potencies decrease in the order of **4**>**2**>**1**>**3**. All four mannosides could inhibit bacterial adhesion to mannan by almost 100 % at concentrations 5 mM with the exception of ThiahexMan which leaves 5 % of adhered unaffected until even at a concentration 200 mM.

9.3.2 Inhibition of *E. coli* adhesion to HMEC-1 under static conditions

Inhibition of *E. coli* adhesion to a mannan surface has shown once again, that mannosides **1**-**4** are antagonists of FimH. Next, we went on to test their inhibitory power under physiological conditions, i.e. using cells. Mannosides **1** and **4** were tested earlier as inhibitors of bacterial adhesion to the human colorectal cancer cell line HT-29 cells.[318] Here, we used immortalized human microvascular endothelial cells (HMEC-1) which are closer to the physiological situation. Hence, HMEC-1 were cultivated in 96-well plates and incubated with a suspension of *E. coli* in presence of the four inhibitors **1**-**4**. Each concentration for each inhibitor was tested in four independent wells. Inhibitor concentrations were chosen around the IC_{50}-value determined in the adhesion inhibition assays with mannan-coated microtiter plates. Thus **1**-**4** were employed 0.1-

10 mM, 0.05-0.5 mM, 0.5-20 mM, and 0.001-1 mM. This time, bacterial adhesion was investigated using high-resolution live cell microscopy and the inhibitory potencies of the employed mannosides was determined by counting adhered bacteria after inhibition and washing (cf. Figure 12.24 for example images). As negative controls, two sets of cells were employed: On the one hand, untreated HMEC-1; and on the other hand, HMEC-1 treated with the highest DMSO concentration occurring in the experiments. This was done because for live-cell experiments, inhibitor stock solutions in DMSO were prepared. For both sets of controls, bacterial adhesion was identical. We hence defined the ratio between cells treated with inhibitors and control cells as the relative adhesion. The results are shown in Figure 9.3.

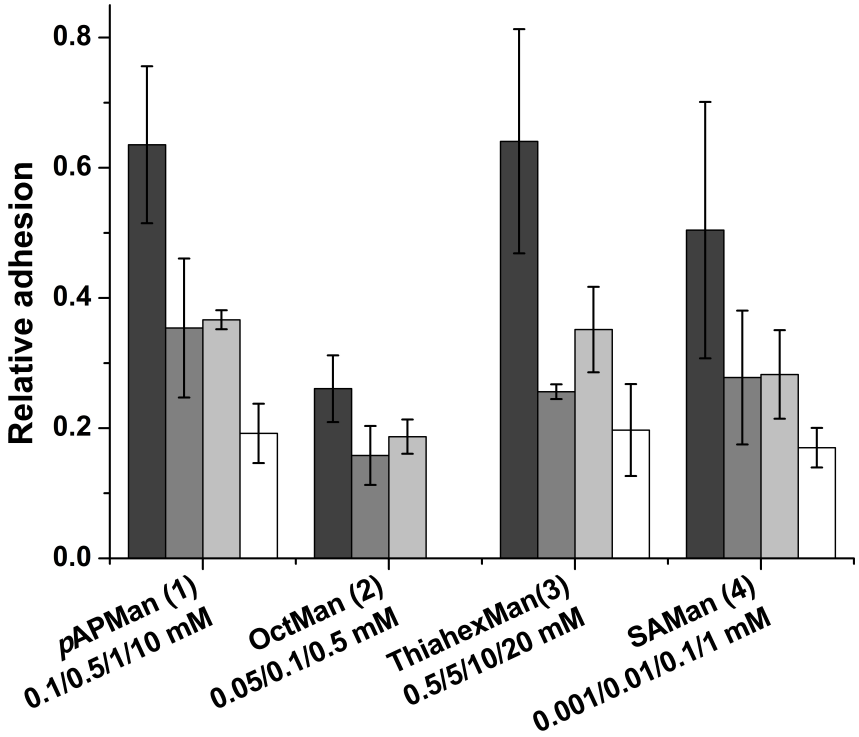

Figure 9.3: Adhesion of *E. coli* to HMEC-1 under static conditions.
All four inhibitors are able to reduce adhesion of *E. coli* to HMEC-1, visible from the lower relative adhesion. However, for none of the inhibitors the relative adhesion reaches 0. It remains constant at a relative adhesion of about 0.2. Errors are given as standard error of the mean (SEM). Each bar represents the mean of four independent wells.

From these results it can be seen that the relative inhibitory potencies of the four tested mannosides show similar ranking as inhibitors of *E. coli* adhesion to HMEC than of *E.*

coli adhesion to mannan: **4**≈**2**>**1**>**3**. At the fourth tested concentration of 15 mM for **2**, it did not stay in solution when dissolved in cell medium, which is why the respective bar is not depicted here. As usual for experiments with life cells, error bars are relatively large, larger than those obtained with the mannan-coated polystyrene surface: Nevertheless, it can be clearly seen that the relative adhesion settles at a value of about 0.2 in all cases. This implies that adhesion is even at highest inhibitor concentrations not completely abolished. In any case, a 20 % fraction of bacteria compared to control cells remained adhering even when inhibitory mannosides much higher than the IC_{50}-value were applied. Since the residual bacterial adhesion is not dependent on the inhibitor concentration, it is reasonable to attribute his effect to interactions between bacterial surface structures the surface of HMEC. Considering that in the artificial environment of a microtiter plate unspecific, non-FimH dependent interactions are deliberately minimized, it is not astonishing that they play a much bigger role in the very complex setting of the cell surface.[330] Thorough washing of the samples in order to remove unspecifically adhered bacteria did not change the situation. Although we extensively rinsed the samples to remove residual bacterial adhesion, the fraction of remained bacteria stayed the same. We were interested to see if constant flow conditions would change the situation.

9.3.3 Inhibition of *E. coli* adhesion to HMEC-1 under flow

Bacterial adhesion to eukaryotic cells under physiological conditions normally occurs under flow. We therefore moved to a flow-based setup where *E. coli* are streamed at a physiological shear rate of 1.5 dyn/cm^2 continuously over HMEC-1 in presence or absence of inhibitors. Due to the characteristics of the flow setup, we had to investigate slightly higher inhibitor concentrations than under static conditions, however, the tested concentration ranges overlap in both cases. Bacterial adhesion was again followed via fluorescence microscopy (cf. Figure 12.25 for example images). The increase of the recorded fluorescence signal is a direct measure for the bacteria adhering over time: The more bacteria adhere, the faster the signal rises. We evaluated this development by fitting a straight line to the obtained curves and calculated its slope, representing the adhesion rate for this condition. Analogous to the static condition, the relative adhesion was defined as the ratio between the slope of treated cells and untreated cells. Of course, for the investigation of one inhibitor a single bacterial sus-

pension was used where inhibitor solution was added to yield the respective concentrations in order to exclude any variations in adhesion due to different concentrations. Under these conditions, we expected unspecific adhesion to be reduced. The results are depicted in Figure 9.4.

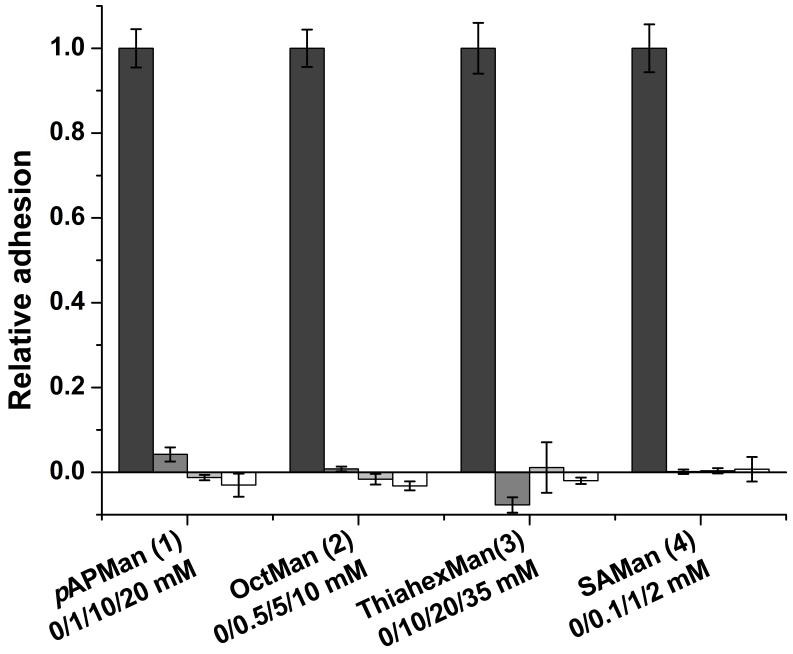

Figure 9.4: Adhesion of *E. coli* to HMEC-1 under flow conditions.
For inhibitor concentrations that could not abolish bacterial adhesion under static conditions, adhesion was under flow close to zero and remained at this level also for the higher concentrations. It is clearly visible that the relative adhesion is close to zero for all four inhibitors already at these concentrations. Errors are given as the SEM of the fit.

The strong effect of shear stress on the effect of the inhibitors on bacterial adhesion is evident. For all investigated inhibitor concentrations, adhesion was almost completely abolished under shear stress. This can be attributed to a significantly lower unspecific binding: Under the continuous force generated by the shear stress, bacteria are only able to adhere when they can form specific interactions between FimH and mannose groups on the cell surface. If they are blocked by an inhibitor, the unspecific interactions that are sufficient to retain the bacteria on the cells under static conditions are not strong enough to prevent the bacteria from being washed away by the flow.
Taken together, we could show that the potency of the tested four *E. coli* adhesion inhibitors is strongly affected by the presence of shear stress. Under static conditions

and on a model substrate, inhibitors are able to abolish bacterial adhesion almost completely whereas they are only able to diminish adhesion on a monolayer of HMEC-1. A significant amount of *E. coli* is able to adhere to the cells even at very high inhibitor concentrations, presumably due to unspecific interactions. In contrast, the presence of shear stress strongly decreased unspecific adhesion. At inhibitor concentrations where significant adhesion was detected under static conditions, adhesion was shut down completely under flow conditions. We would like to point out that this finding has consequences for the evaluation of inhibitor potencies: Whenever they are determined under static conditions whereas the physiological state exhibits flow conditions or the other way around, it is based on our results possible that the obtained values do not correspond to the actual values. Therefore, it is of high relevance to investigate inhibitor potencies not only under static, but also under flow conditions.
Taken together, our experiments show that bacterial adhesion to human cells occurs in a complex setting where a variety of factors interfere with each other. This has consequences for the evaluation of inhibitor potencies. Normally, the assessment is performed in a simplified, clearly defined and artificial environments to yield reproducible and robust results. Although this is a powerful method to investigate new inhibitors and rank their potencies, our results strongly suggest that the actual performance under physiological conditions is very likely to deviate. Therefore, it is based on our findings crucial to not only investigate inhibitors of bacterial adhesion in an idealized environment, but also in realistic settings in order to judge their potency correctly and elucidate the underlying mechanisms. We hope that our experiments are a first step in this direction.

9.4 Experimental Section

Selection and synthesis of inhibitors: Structures of the employed FimH antagonists are depicted in Figure 9.2. They differ with regard to their aglycon. The aromatic moiety of p-aminophenyl mannoside **1** (pAPMan) is known to improve FimH affinity based on $\pi\pi$-stacking with the lectin's tyrosine residues Y48 and Y137, which are located at the entrance of the carbohydrate binding site of the lectin FimH due to its affinity promoting aglycon.[139] The octyl mannoside **2** (OctMan) resembles an example of a series of potent alkyl mannosides.[140] In addition, the octly group was shown to form glycomicelles in solution which might result in multivalency effects in inhibition of bacterial adhesion. The 6-amino-thiahexyl mannoside **3** (ThiahexMan) was recently shown to be toxic when applied in high concentrations (> 12.5 mmol).[326] Fially, the squaric acid derivative **4** (SAMan) completes the selection of tested mannosides. It

has been reported to exceed the inhibitory potency of **1** by a factor of 16 due to its affinity promoting aglycon.[328] All inhibitors were synthesized according to known procedures.[139,323–325,327–329,331,332] The obtained analytical data were in full accordance with those reported.

Bacterial culture: GFP-fluorescent *E. coli* (strain pPKL1162)[143] were inoculated in 10 mL LB medium (Sigma-Aldrich, St. Louis, MO) in presence of chloramphenicol (50 mg/L) and ampicillin (100 mg/L) (both Sigma-Aldrich) and grown at 37°C overnight under constant agitation. For the inhibition on mannan surfaces the bacteria were centrifuged and washed with PBS two times. Then, a suspension with OD_{600}=0.4 in PBS was prepared for further use. For the inhibition on HMEC-1 the bacteria were centrifuged and washed two times with DPBS +Ca^{2+}/Mg^{2+} (Life Technologies, Carlsbad, St. Louis, MO) and once with cell medium. Then, the bacteria were suspended in 10 mL cell medium and the optical density at 600 nm was determined. For the experiments under static and under flow condition, a 1:50 dilution of a suspension with OD_{600}=0.1 was used.

Cell culture: HMEC-1 (CDC, Atlanta, GA) were seeded in 96 well microtiter plates (Corning, Corning, NY) or in collagen coated Luer $I^{0.8}$ channels (IBIDI, Martinsried, Germany) and grown to confluency. The cells were cultured in MDCB-131 medium with 1 % glutamax, 10 % FBS, 10 ng/mL hEGF (all Life Technologies), and 1 µg/mL hydrocortisone (Sigma-Aldrich) at 37°C in 5 % CO_2-atmosphere.

Inhibition of bacterial adhesion: Inhibition on mannan surfaces. Mannan coated 96 well microtiter plates (Nunc) were blocked with a solution of PVA (1 % in PBS) for 2 hours with 200 rpm at room temperature. The inhibitors were dissolved in PBS and added in a serial dilution. The bacterial solution was added and the plates were incubated at 37°C with 100 rpm for 1 hour. The plates were washed with PBS (3 x 300 µL/well) and the fluorescence intensity was determined.[315]

Inhibition under static conditions on HMEC-1: Cells were grown to confluency in 96-well plates (Corning). A 1:50 dilution of *E. coli* was prepared, inhibitors at the respective concentrations were added, and it was incubated for 20 minutes. The medium was removed from the cells and 200 µL of the bacteria suspension was added. It was incubated for 30 minutes at 37°C on a shaker (400 rpm). Then, it was washed with 200 µL DPBS +Ca^{2+}/Mg^{2+} (Life Technologies) for 20 minutes (37°C, 400 rpm). The DPBS was removed and replaced by CO_2-independent medium (Life Technologies).

Inhibition under flow conditions on HMEC-1: Cells were grown to confluency in Luer $I^{0.8}$ channels (IBIDI). For each inhibitor, a single suspension was used. First, bacteria (1:50 dilution of a suspension with OD_{600}=0.1) were flown over the cells without inhibitor (shear rate=1.5 dyn/cm^2). Then, the channel was changed and inhibitor was added to the respective concentration. Afterwards, the channel was changed again and inhibitor was added to the next concentration and so on.

Fluorescence microscopy: Confocal fluorescence images of the GFP-fluorescing bacteria were obtained with a commercially available spinning-disk inverted microscope (Zeiss).

Software: Images were analyzed using ImageJ. For data visualization and analysis, OriginPro 8G was used. Figures were prepared with Corel Draw 12.

10 The Endothelial Glycocalyx is a Barrier for Nanoparticle Entry

This chapter is based on: **"The Endothelial Glycocalyx Protects Cells from Nanoparticle Entry"** by Leonhard Möckl, Stefanie Hirn, Adriano de Andrade Torrano, Christoph Bräuchle, and Fritz Krombach
In preparation

Acknowledgements:
LM, SH, and ATT conducted the experiments.
LM, SH, ATT, CB, and FK wrote and corrected the manuscript.

10.1 Introduction

Already shortly after the discovery of the endothelial glycocalyx, it has been assumed that it fulfills a barrier and/or filter function for metabolites, small molecules, and ions. Considering that it is up to several hundreds of nanometers thick, this seems to be a reasonable assumption. Indeed, it has been shown that the glycocalyx excludes certain molecules like albumin or dextrans.
However, the term "barrier" is also related to defense against toxic species. Among others, certain nanometer-sized particles seem to easily penetrate cells and cause unwanted, possibly harmful reactions. Since they are also often found in the blood stream, we decided to investigate whether the endothelial glycocalyx is able to protect endothelial cells from nanoparticle entry. For this, we decided to use fluorescently labeled, 50 nm sized particles of two different types: On the one hand, we employed amino-functionalized particles, on the other hand carboxy-functionalized. The first have been described to be harmful for cells and cause stress and apoptosis whereas the

latter have been reported to be inert and not to affect cells. Also, we decided to use a cell-based *in vitro* assay employing human umbical vascular endothelial cells (HUVECs). They are cells quite close to the physiological case and have also been reported to express a glycocalyx *in vitro*.

10.2 Results and Discussion

First, we wanted to demonstrate that HUVECs indeed express a glycocalyx under the conditions we applied. For this, we cultured HUVECs one, three, five, seven, and ten days after seeding with medium exchange every two days. After this, cells were fixed and immunostaining against heparan sulfate, one of the central components of the glycocalyx, was performed. The result is given in Figure 10.1. It is evident that the fluorescence intensity is very low after one day of incubation, then increases, and remains constant after five days. This indicates that in our setting glycocalyx components are indeed expressed and that this process takes about five days.

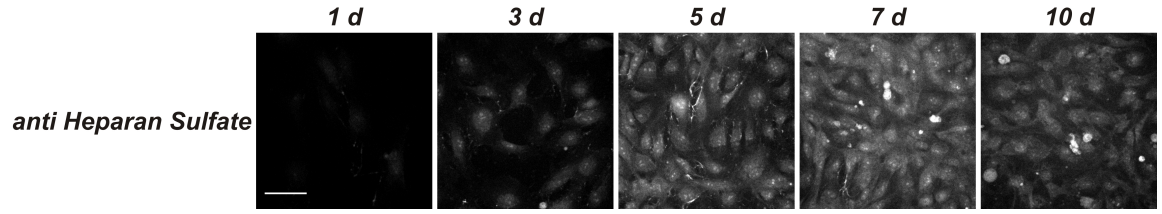

Figure 10.1: Development of heparan sulfate expression on HUVECs cultured for the indicated time.
Clearly, after one day, almost no heparan sulfate signal is detected. However, it increases gradually and remains approximately constant from five days culture time onwards. Therefore, the key glycocalyx component heparan sulfate is expressed within several days in our setting.
Contrast settings equal for all images. Scale bar = 50 μm.

Having shown that HUVECs indeed express a glycocalyx, we investigated its effect on the internalization of the amino- and carboxy-nanoparticles. For this, we incubated HUVECs cultured for ten days for 24 h with 0.5, 1, or 5 μg/mL particles. To analyze the effect of the glycocalyx, we applied a cocktail of heparinase III (2U/mL), neuraminidase (0.83 U/mL), and hyaluronidase (25 U/mL) in cell medium for 1 h before

incubation with particles. These enzymes cleave of the three main glycocalyx components. The result of the quantification of intracellular fluorescence originating from internalized particles is given in Figure 10.2. Representative images can be found in Figure 10.3.

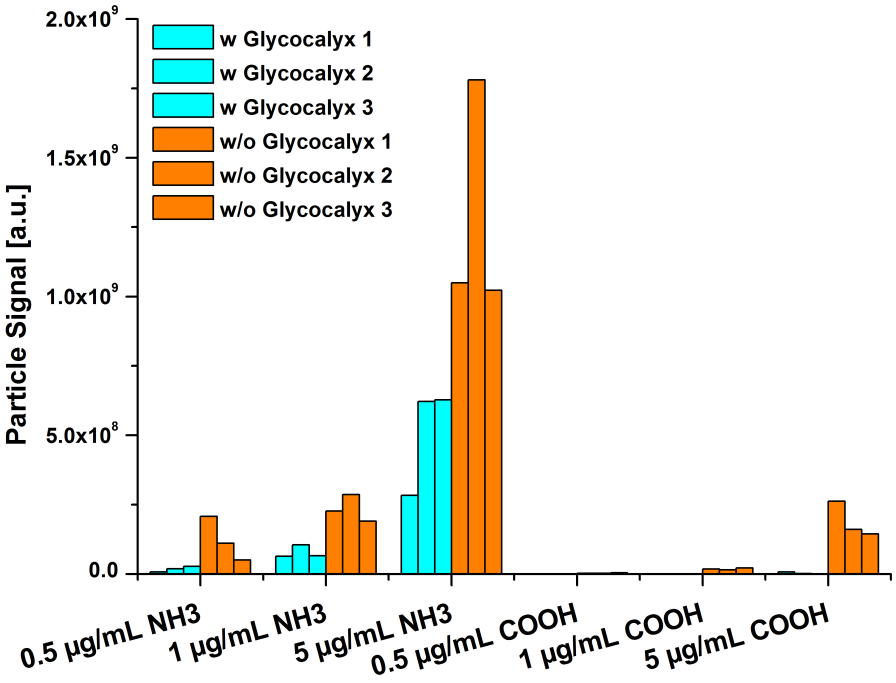

Figure 10.2: Uptake of amino- and carboxy-nanoparticles into HUVECs in presence and absence of the glycocalyx.
Both particle types enter HUVECs and sufficiently high concentrations. Amino-particles show higher internalization rates than carboxy-particles. However, in presence of the glycocalyx, the uptake is for both particle types lower. Each triplicate is shown separately. In each triplicate, four individual wells of a 96-well plate were investigated.

As it can be clearly seen from the quantification, both particle types are internalized. However, there are differences between the two types and also between the cells with intact and with shedded glycocalyx: The amino-particles generally show higher internalization than the carboxy-particles. This is expected since amino-particles are rather positively charged in cell medium whereas carboxy-particles are negatively charged. Since many glycocalyx components carry negatively charged functional groups like sulfates, amino-particles should exhibit a higher affinity in comparison to carboxy-particles. However, for cells with intact glycocalyx, the uptake is for all concentrations

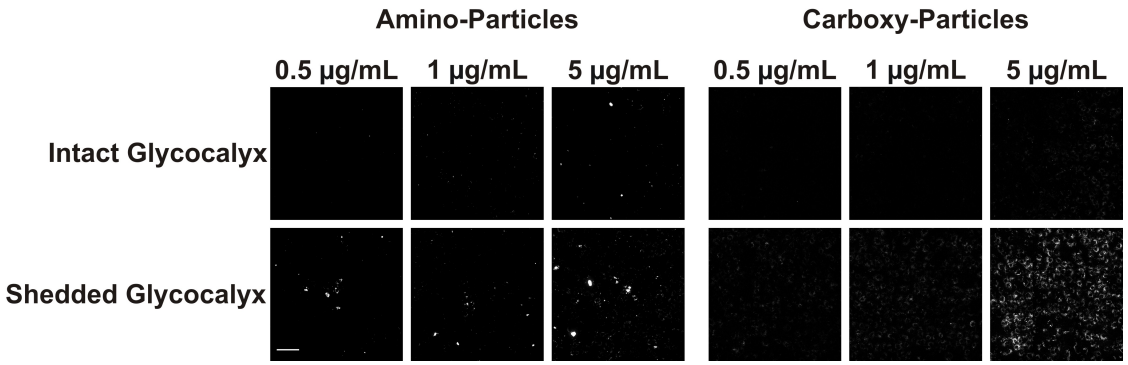

Figure 10.3: Representative Images of Uptake of amino- and carboxy-nanoparticles into HUVECs in presence and absence of the glycocalyx.
It can be clearly seen that for both particles the amount of internalized particles is much higher when the glycocalyx is shedded (bottom tow) in comparison to the intact glycocalyx (top row). Also, amino-particles are internalized stronger than carboxy-particles. Contrast settings are equal for each particle type. Scale bar = 100 µm.

and for both particle types significantly lower than for cells with shedded glycocalyx. Especially, this can be seen for carboxy-particles which are practically not internalized if the glycocalyx is present, but significantly when the glycocalyx is shedded. From these results we conclude that the endothelial glycocalyx indeed functions as a barrier against nanoparticle uptake.

11 Uptake of Targeted siRNA into Model Cells and *in vivo*

This chapter is based on: **"Cell-Penetrating and Neurotargeting Dendritic siRNA Nanostructures"** by Korbinian Brunner, Johannes Harder, Tobias Halbach, Julian Willibald, Fabio Spada Felix Gnerlich, Konstantin Sparrer, Andreas Beil, Leonhard Möckl, Christoph Bräuchle, Karl-Klaus Conzelmann, and Thomas Carell
Angewandte Chemie Int. Ed. **54 (6)**, 1946 (2015)[333]

Acknowledgements:
KB, JH, TH, JW, FS, FG, KS, AB, and LM conducted the experiments.
KB, JH, TH, JW, FS, FG, KS, KKC, and TC wrote the manuscript.
KB, JH, TH, JW, FC, FG, KS, AB, LM,CB, KKC, and TC corrected the manuscript.

11.1 Abstract

We report the development of dendritic siRNA nanostructures that are able to penetrate even difficult to transfect cells such as neurons with the help of a special receptor ligand. The nanoparticles elicit strong siRNA responses, despite the dendritic structure. An siRNA dendrimer directed against the crucial rabies virus (RABV) nucleoprotein (N protein) and phosphoprotein (P protein) allowed the suppression of the virus titer in neurons below the detection limit. The cell-penetrating siRNA dendrimers, which were assembled using click chemistry, open up new avenues toward finding novel molecules able to cure this deadly disease.

11.2 Introduction

RNA interference is a powerful tool that allows the sequence-specific suppression of gene expression by small interfering RNAs (siRNAs).[162,334,335] The major obstacle preventing the widespread use of siRNA-based therapeutics is the lack of efficient, specific, and nontoxic delivery systems to transport siRNA duplexes into cells and tissue.[168,336] Commonly used siRNA-delivery vehicles, such as liposomes or cationic polymeric systems, are heterogeneous in size and composition, and severe cytotoxic effects are observed in sensitive cell types such as neurons.[176,337–342] Recently we reported the ability of all-cis-configured anandamide (arachidonoylethanolamin, AEA) to target siRNA to cannabinoid receptors, thus leading to the efficient receptor-mediated internalization of the siRNA-AEA adducts.[343] As cannabinoid receptors are expressed on immune and neural cells, this approach enables the efficient delivery of siRNAs into these sensitive cell types.[32,177,178]

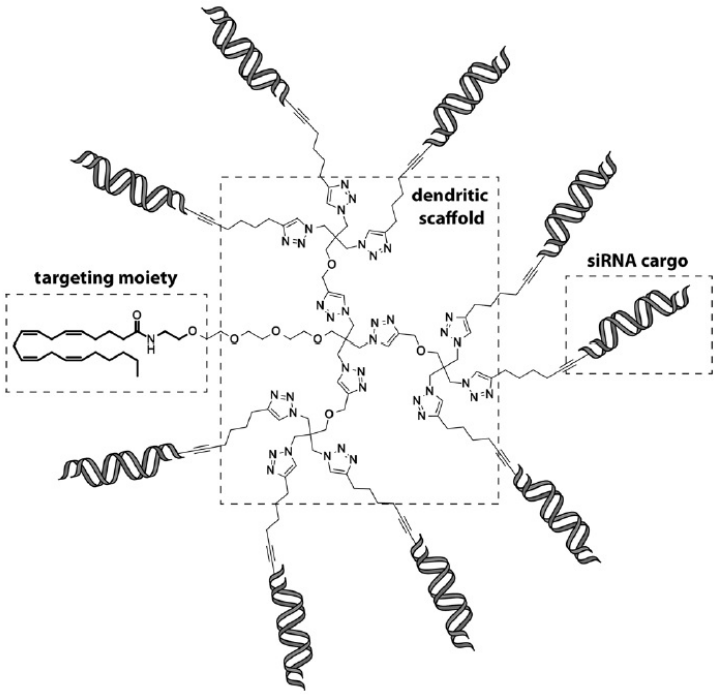

Figure 11.1: A dendritic siRNA nanostructure with an anandamide targeting unit. The siRNA passenger strands are covalently connected to a dendritic framework, while the siRNA guide strands are hybridized to the nanostructure.

One important problem associated with receptor-mediated siRNA uptake is the limited expression of some receptors on cell surfaces. This leads to the rapid saturation of receptors, which limits the amount of siRNA that can be delivered. Here, we show that one AEA ligand is able to induce the receptor-mediated uptake of dendritic siRNA nanostructures with up to nine siRNA duplexes per ligand. Efficient RNA silencing is thus observed despite the complex structure (Figure 11.1). In principle this allows us to circumvent the saturation effect and to extend the uptake of siRNA.

11.3 Results and Discussion

A click-chemistry-based approach enabled the efficient synthesis of the required monodisperse siRNA nanostructures (see Figure 11.1).[6] The synthetic strategy that enabled the assembly of the siRNA structures is depicted in Figure 11.2.

The starting material pentaerythritole was converted to the corresponding triazide 1 in two steps. Compound **1** was next reacted with mono-Boc-mono-Ts-functionalized tetraethyleneglycole **2**, which provided the key branching molecule **3**. Using CuI-catalyzed click reactions, compound 3 was extended with the additional alkyne-containing branching molecules **4** and **5**, which were both obtained in two steps (Figure 11.2). The tosylates **6** and **7** were next converted into the corresponding azides **8** and **9**. Subsequently, we cleaved the Boc groups in **3**, **8**, and **9** and reacted the amines with arachidonic acid. These reactions provided the dendritic anandamide azides **10**, **11**, and **12**. The products of this reaction were next connected to the alkine-modified siRNA passenger strands using a CuI-catalyzed click reaction to give the dendritic nucleic acid nanostructures.[344–349] In all three cases we obtained one main product after the click reaction. These compounds were isolated using reversephase semipreparative HPLC. The correct structure and monodispersity of the dendritic siRNA assemblies was next confirmed by analytical HPLC and MALDI-TOF-analysis (for two examples, see Figure 11.3). In all cases, we obtained the dendritic structures in excellent purity. The correct molecular weights were obtained within the experimental limits of the MALDI-TOF measurements, proving the expected monodispersity of the nanoparticles. The final siRNA dendrimers ready for transfection were obtained by hybridizing the corresponding numbers of guide strands to the dendritic structures.

To investigate the biological activity of the siRNA dendrimers, we utilized a reporter assay in RBL-2H3 cells.[343,350] As depicted in Figure 11.4, all prepared siRNA dendrimers dendrimers showed strong silencing effects. For the experiments, we kept the amount of siRNA duplexes constant by reducing the concentration of the dendritic structure to the reciprocal of the number of siRNA duplexes per nanoparticle. The dendrimer AEA-[3siRNA] with three siRNA strands attached showed by far the strongest silencing effect, even though the concentration of the dendrimer was reduced to one third compared to the anadamide-functionalized siRNA duplex. Surprisingly, even the dendrimer AEA-[9siRNA] showed a strong efficacy compared to the monomeric siRNA, despite its large size and the small total concentration (Figure 3).

The 3' end of the siRNA guide strand allows further functionalization.[351,352] This modification can stabilize the RNA inside the cell, which should lead to a better silencing effect.[349,353,354] In order to exploit this possibility, we next functionalized the siRNA duplexes of the dendrimers with a glucose molecule at the 3' ends.[355] Glucose forms H-bonds with the RNA duplex and increases the water solubility. The introduction of the 3' modification was achieved by hybridizing the passenger-strand-containing dendrimers with the corresponding glucose-modified guide strands. Indeed, the glucose-end-capped dendrimers showed a significantly enhanced efficacy. It is likely that the large siRNA dendrimes suffer from serious degradation in the endosomes after internalization.[353,356] This may be retarded by glucose capping.[357] The advantage of capping of the trimeric siRNA dendrimer is quite large, as shown in Figure 3B. The threefold glycosylated structure finally gave a silencing effect of approximately 80%. Thus, in comparison to the monomeric duplex, the silencing efficiency was increased by a factor of 2.5, despite the reduced total concentration. We next investigated the possibility of utilizing the dendritic siRNA structure to induce silencing in difficult to transfect cells such as neurons (Figure 4). Consequently, we tested the uptake of the nanoparticles into neural stem cells. We prepared siRNA dendrimers in which we replaced the glucose units at the 3' end of the guide strand by Alexa Flour 647. Indeed, when we added the fluorophore-modified siRNA trimer to the neural stem cells, efficient uptake was detected by confocal microscopy (Figure 4A).

In order to prove the ability of the siRNA dendrimers to silence an endogenous gene, we next transfected the neural stem cells with a trimeric siRNA dendrimer targeting Tet1. This enzyme was recently shown to oxidize 5-methylcytosine to 5-hydroxy-

methylcytosine and 5-carboxycytosine, which is essential for the differentiation process.[358–360] Using qPCR, we monitored the expression level of Tet1 (Figure 4 B). Indeed, the siRNA dendrimer led to a significant reduction of the level of endogenous Tet1 expression, proving the effect of the siRNA despite it being incorporated into a dendritic structure. Again, we observed the strongest silencing effect with the trimeric siRNA structure. Finally we were interested in the ability of our dendritic siRNA structures to exhibit a medicinally relevant function in primary neurons that are hard to transfect by normal methods.[341,361] As a target, we chose the neurotropic rabies virus (RABV), which causes over 55000 deaths per year and is not treatable after the onset of clinical symptoms.[362,363] For this study, we infected mouse E14 cortical neurons with the RABV and subsequently treated the cells with two siRNA dendrimers (AEA-[3siRNA]-Glc) against the mRNAs of the viral nucleoprotein (N protein) and the phosphoprotein (P protein). The siRNA sequences were designed in silico using the program siDESIGN. Both proteins are essential for viral transcription and replication and are therefore considered promising targets to efficiently counteract RABV infection.[364–367] In addition, the P protein of RABV is an important antagonist of the innate immune system, completely suppressing both IFNb induction and signaling pathways.[368,369] Down-regulation of P protein expression should consequently promote the innate immune response, thereby further restricting RABV infection. The data of the experiment clearly show that treatment of the infected neurons with either one of the dendrimers AEA-[3siRNA]-Glc (anti-P and anti-N) lead to a strongly reduced viral titer (Figure 4C; for data of targeting N protein Figures S2 and S3). The titer was reduced by two orders of magnitude in relation to the control experiment performed with a nontargeting anandamidemodified siRNA. The trimeric dendrimer was able to reduce the viral titer to a level close to the detection limit of the experiment. Important are also the observations that the reduction of the viral titer is dose-dependent and that with the standard lipofectamin 2000-based transfection, only a tenfold reduction of the viral titer was observed. These results show the improved efficacy of the siRNA dendrimers. In summary, we have presented novel dendritic siRNA nanostructures that allow the transfection of difficult-totransfect cells, such as stem cells and primary neurons.[370] A click-chemistry-based approach, in which the passenger strands of the siRNAs are covalently bound to the dendritic structure, allowed us to exactly control the monodispersity of the particles, which enabled the control of the number of siRNA duplexes bound to one AEA ligand for receptormediated uptake. The dendritic siRNA

nanostructures allow the effective control of gene expression in neural stem cells and in primary neurons. We were also able to use the system to reduce the viral titer of the rabies virus in primary neurons to close to the detection limit, thus illustrating a possible way to a novel siRNA-based therapy of this deadly disease.

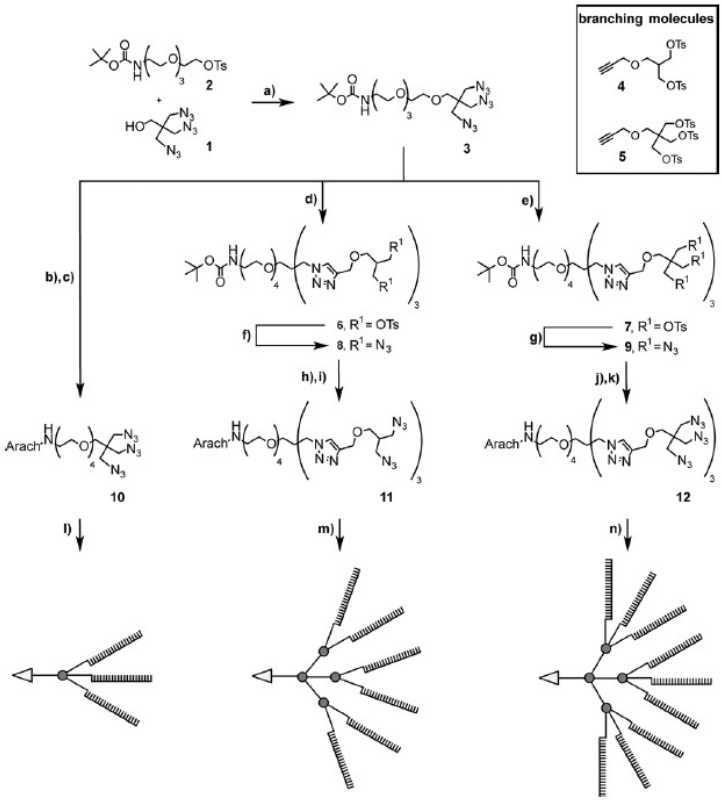

Figure 11.2: Synthesis of the siRNA dendrimers AEA-[3ORN], AEA- [6ORN], and AEA-[9ORN].a) NaH, 15-crown-**5**, DMF, RT, 46%; b) TFA, $CHCl_3$, RT, 94%; c) arachidonic acid, TBTU, DIPEA, DMF, RT, 95%; d) **4**, $CuSO_4$, sodium ascorbate, H_2O/THF (1:1), RT, 80%; e) **5**, $CuSO_4$, sodium ascorbate, H_2O/THF (1:1), RT, 65%; f) NaN_3, DMF, 110°C, 85%; g) NaN_3, DMF, 110°C, 97%; h) TFA, $CHCl_3$, RT, 71%; i) arachidonic acid, HATU, DIPEA, DMF, RT, 81 ; j) TFA, $CHCl_3$, RT, 76%; k) TBTU, DIPEA, DMF, 40°C, 70%; l) alkyne-modified oligonucleotide (ORN), CuBr, TBTA, DMSO/H2O, 89%; m) alkyne-modified oligonucleotide (ORN), CuBr, TBTA, DMSO/H_2O, 78%; n) alkynemodified oligonucleotide (ORN), CuBr, TBTA, DMSO/H_2O, 65%.

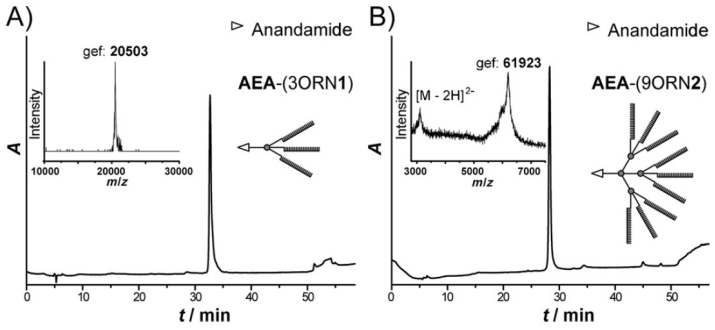

Figure 11.3: HPL chromatograms of the purified dendrimers obtained with 10and 12.
The inserts show the MALDI-TOF spectra. MALDI-TOF data: A) calc. (AEA-[3ORN1]): m/z 20506, found: 20503. B) calc. (AEA- [9ORN2]): m/z 62124, found 61923 (broad signal).

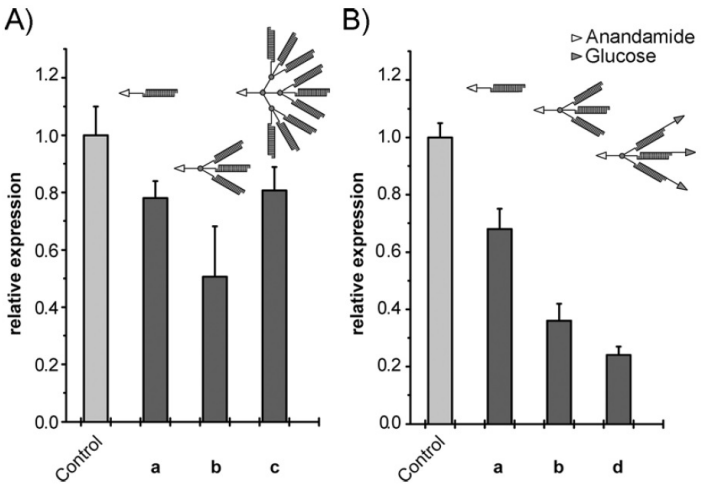

Figure 11.4: Relative silencing of the Renilla luciferase compared to the silencing of Firefly luciferase mediated by dendritic anandamidesiRNAs in RBL-2H3 cells.
Investigated was: A) the influence of branching (1, 3, 9 siRNA duplexes per ligand) on silencing efficacy mediated by novel dendritic structures; B) the influence of additional glucose modifications introduced by modified siRNA guide strand. In all cases the total amount of siRNA duplexes was normalized to the monomeric structure. Quantification was achieved by luciferase activity. a: AEA-[1siRNA-Luc], b: AEA-[3siRNA-Luc], c: AEA-[9siRNA-Luc], d: AEA- [3siRNA-Luc]-glucose.

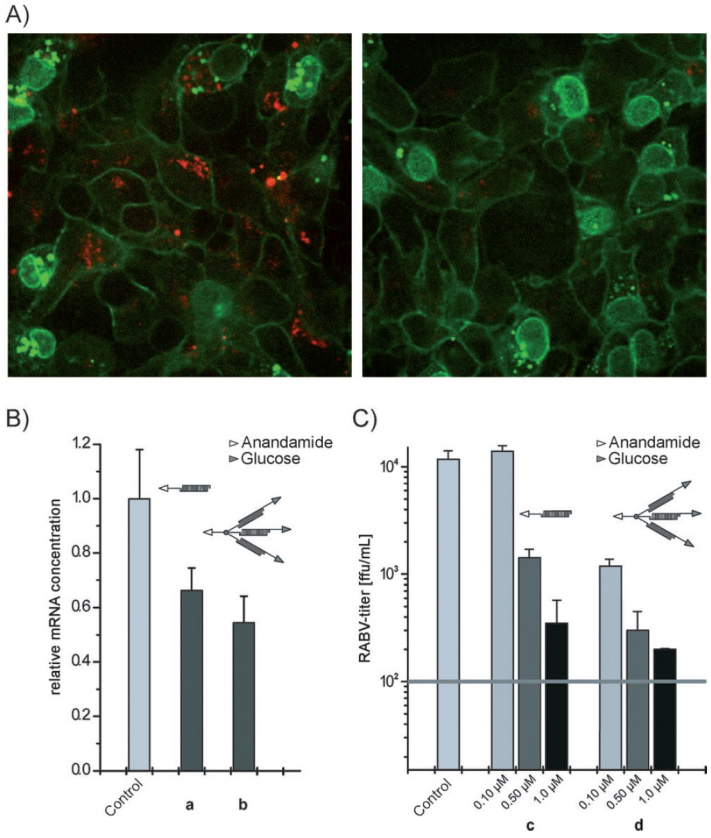

Figure 11.5: Anandamide-mediated delivery of dendritic siRNA nanostructures to neural stem cells.

A) Left: trimeric siRNA modified with Alexa Fluor647 was incubated with neural stem cells. Right: As a negative control the stem cells were incubated with siRNA lacking the ligand modification (red: siRNA, green: cell membranes. The contrast settings for siRNA signals were equal for both images). B) Successful delivery of nanostructures to stem cells was additionally demonstrated by regulation of Tet1 monitored by real-time PCR. a: AEA-[1siRNA-Tet1], b: AEA-[3siRNA-Tet1]-Glc. C) Down-regulation of RABV titers in E14 cortical neurons by treatment with different AEAmodified siRNA structures targeting the P protein of rabies virus. c: AEA-[1siRNA-P-protein], d: AEA-[3siRNA-P-protein]-Glc.

11.4 Investigation of Uptake Kinetics and Mechanism of Targeted siRNA

This work was not part of the published article.

In additional experiments, we investigated different targeting types of siRNA constructs in order to determine their uptake mechanism and kinetics. The siRNA employed is shown in Figure 11.6.

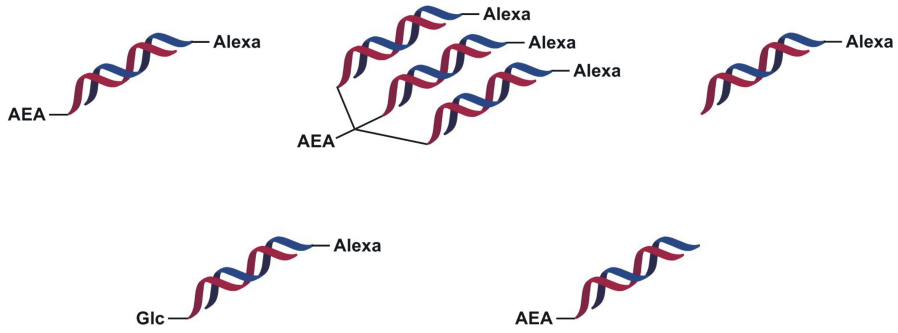

Figure 11.6: siRNA used in additional experiments
In the top row, the simple, fluorescently labeled siRNA duplex targeted with AEA, a construct with three siRNA-arms ("tripod"), and the untargeted siRNA used for control experiments are shown. In the bottom row, a glucose-modified siRNA and an AEA-targeted, but not fluorescently labeled siRNA are depicted.

11.4.1 Uptake Mechanism and Kinetics of AEA-Targeted siRNA

First, we determined the uptake of AEA-targeted siRNA into RBL2H3 cells, a murine model cell line for neuronal stem cells. For this, we compared the intracellular fluorescence intensity 1, 8, and 20 hours after addition of siRNA. Investigated constructs were the duplex-siRNA, the tripod siRNA-construct, and untargeted siRNA. The concentration of siRNA strands was always 125 nM, i.e. the concentration of the tripod siRNA-construct was 41.7 nM since the strand concentration is then 125 nM. The result is given in Figure 11.7. Representative fluorescent images can be found in Figure 12.26.

For all investigated time points, untargeted siRNA is no internalized significantly. Targeted siRNA, in contrast, is already after 1 h taken up and the amount increases for

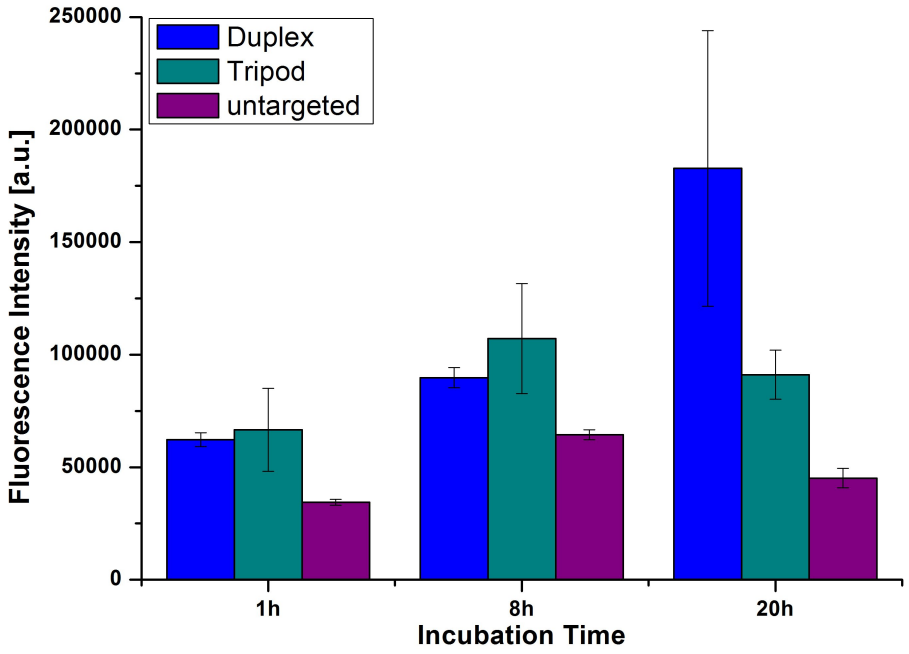

Figure 11.7: Uptake of AEA-targeted siRNA into RBL2H3 cells.
Whereas untargeted siRNA shows little uptake for all investigated time points, the targeted siRNA is internalized efficiently.

the later time points. Interestingly, the tripod siRNA-construct settles after 8 h at a medium level whereas the simple duplex construct is internalized further and exceeds the tripod siRNA-construct at an incubation time of 20 h. One can only speculate about the reasons. One possibility is that the tripod siRNA-construct is quite large ans bulky, making it difficult to internalize.
Next, we wanted to ensure that the AEA-targeted siRNA is really internalized via cannabinoid receptors and not, for example, unspecifically via attachment to the membrane: Since AEA is quite a hydrophobic molecule, this option must be taken into account. For this, we designed a competition experiment where we coincubated RBL2H3 cells with 125 nm fluorescently labeled duplex siRNA and 0, 125, 250, 500, and 750 nM non-fluorescent, but still AEA-targeted siRNA. If the uptake would be unspecific, one would expect no big difference between the different samples. However, when the uptake is receptor-mediated, fluorescent and non-fluorescent siRNA species will compete for binding which should decrease the intracellular fluorescence when increasing amounts of non-fluorescent siRNA is present. The result is given in Figure 11.8

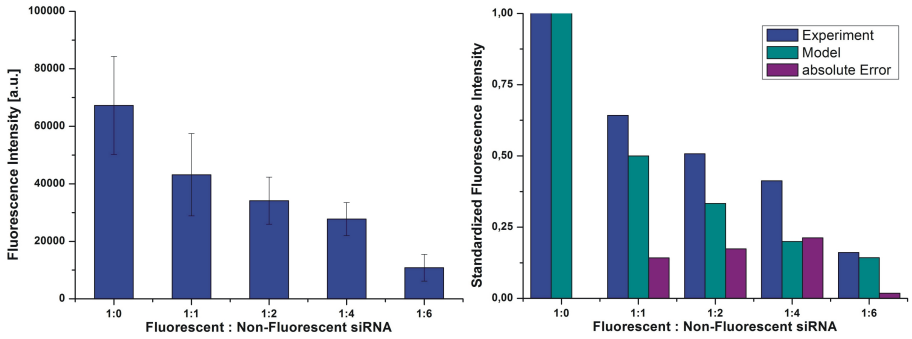

Figure 11.8: Quantification of fluorescent AEA-targeted duplex-siRNA in prescence of non-fluorescent, AEA-targeted duplex-siRNA.
Increasing amounts of non-fluorescent AEA-targeted duplex-siRNA decrease the amount of internalized fluorescent siRNA (left). The decrease corresponds well with the expected values (right).

As clearly visible, the presence of non-fluorescent, AEA-targeted siRNA-duplex decreases the intracellular fluorescence originating from AEA-targeted, fluorescently labeled siRNA-duplex. If the fluorescence is normalized and compared to the expected decrease (1:0, 1:1, 1:2, 1:4, and 1:6), a good agreement is observed. From these findings it is fair to assume that the uptake of AEA-targeted duplex-siRNA is not unspecific, but receptor-mediated since a clear competition effect is detected.

Having shown the specific, efficient uptake of AEA-targeted siRNA into model neuronal cells, we turned towards a more physiological setting. For this, we investigated again the uptake of AEA-targeted duplex- and tripod-siRNA, however, this time into murine neuronal stem cells. Again, we investigated the uptake of the duplex and the tripod siRNA-construct, however this time in a concentration-dependent manner: 125 and 250 nM siRNA was added to murine neuronal stem cells and the fluorescence was quantified after 24 hours. The result is shown in Figure 11.9 and representative fluorescent images in Figure 12.27.

Encouraged by these findings, we decided to investigate the uptake of the AEA-targeted duplex siRNA-construct in the most physiological environment: Inside a living animal. Since the cannabinoid receptors are highly expressed in the brain, AEA-targeted duplex siRNA and untargeted siRNA was injected into the brains of living mice. Moreover, as an additional control, AEA-targeted was injected into the brains of mice where

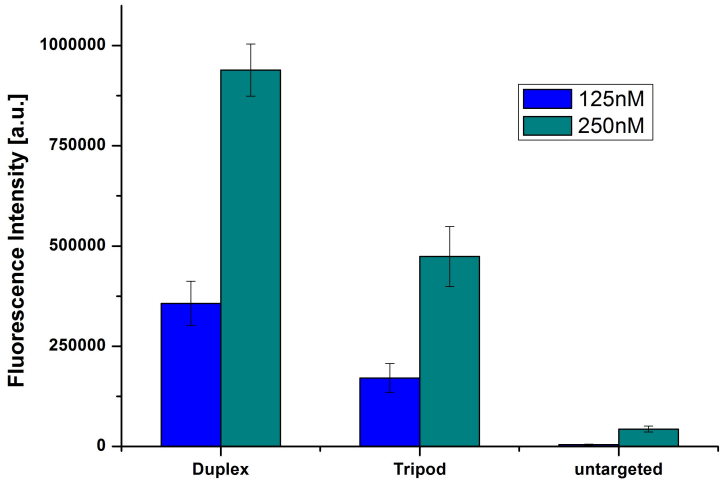

Figure 11.9: Quantification of duplex, tripod, and untargeted siRNA-constructs into murine neuronal stem cells.
Both for the duplex and tripod siRNA, strong uptake is detected. Doubling the concentration leads to about two to three times more internalized siRNA as expected. Furthermore, unspecific uptake was almost not present.

the cannabinoid receptors were knocked out. Then, fluorescent images of slices of brains were obtained. In case of specific uptake, siRNA should be found in the hippocampal region of the brain where cannabinoid are strongly expressed. Representative examples are given in Figure 11.10.

As it can be clearly seen, two conditions must be fulfilled in order for the siRNA to be enriched in the hippocampus: First, the siRNA must be targeted with AEA. Second, the receptors for AEA, the cannabinoid receptors, must be present. Interestingly, in case of targeted siRNA and cannabinoid receptor knockout (Figure 11.10 middle), the siRNA seems to be distributed around the brain whereas in case of untargeted siRNA the siRNA stays at the injection site (Figure 11.10 right). This indicates that the siRNA exhibits some mobility if modified with AEA. Presumably, this is due to diffusion in cell membranes due to the lipophilic nature of AEA. This would also indicate that only when the siRNA encounters the cannabinoid receptors present in the hippocampus, it is enriched there.
The specific internalization of AEA-targeted siRNA into the hippocampus of wild-type mice was clearly displayed by quantifying the siRNA-related fluorescence in the hippocampus as depicted in Figure 11.11. Here, the fluorescence in the hemisphere where siRNA was injected was compared to the fluorescence in the other hemisphere where

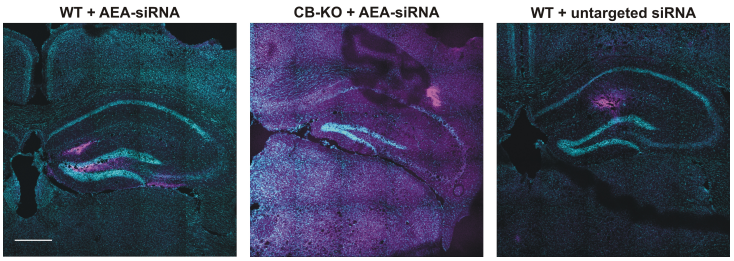

Figure 11.10: Uptake of targeted and untargeted siRNA into mouse brains.
Only when both the siRNA is targeted to the cannabinoid receptors with AEA and the cannabinoid receptors are present, the siRNA is found in the hippocampus (left). If the cannabinoid receptors are knocked out (middle) or siRNA lacks targeting (right), no enrichment of siRNA is found in the hippocampus. Scale bar = 500 µm.

no siRNA was injected. The separation between the two hemispheres does not allow for fast exchange of siRNA, therefore, the untreated hemisphere can be seen as internal control. As it is clearly visible, only when the siRNA is targeted and cannabinoid receptors are present, enrichment of siRNA in the hippocampus is detected.

11.4.2 Uptake Mechanism and Kinetics of Glucose-Targeted siRNA

The other modification that we investigated in detail was the glucose modification. The idea behind the attachment of glucose to the siRNA-constructs is that glucose is the primary source of energy for many cells and may therefore be used to induce fast internalization of siRNA. Hence, we tested several cell lines (Hela, HMEC, KB, HUH-7) for the uptake of glucose-modified siRNA. We compared it to the uptake of untargeted siRNA and, furthermore, investigated whether glucose present in the medium affects the internalization kinetics. Therefore, we turned to a medium where glucose as energy source was exchanged. The result of the quantification of the intracellular fluorescence caused by the internalized siRNA is given in Figure 11.12 and representative images are shown in Figure 12.28.

Interestingly, not only targeting by glucose, but also the presence of glucose in the medium is required for efficient internalization. This is to some extent not intuitive, since the presence of glucose should compete with the Glc-siRNA for the binding sites and hence depletion of glucose from the medium should increase the uptake. How-

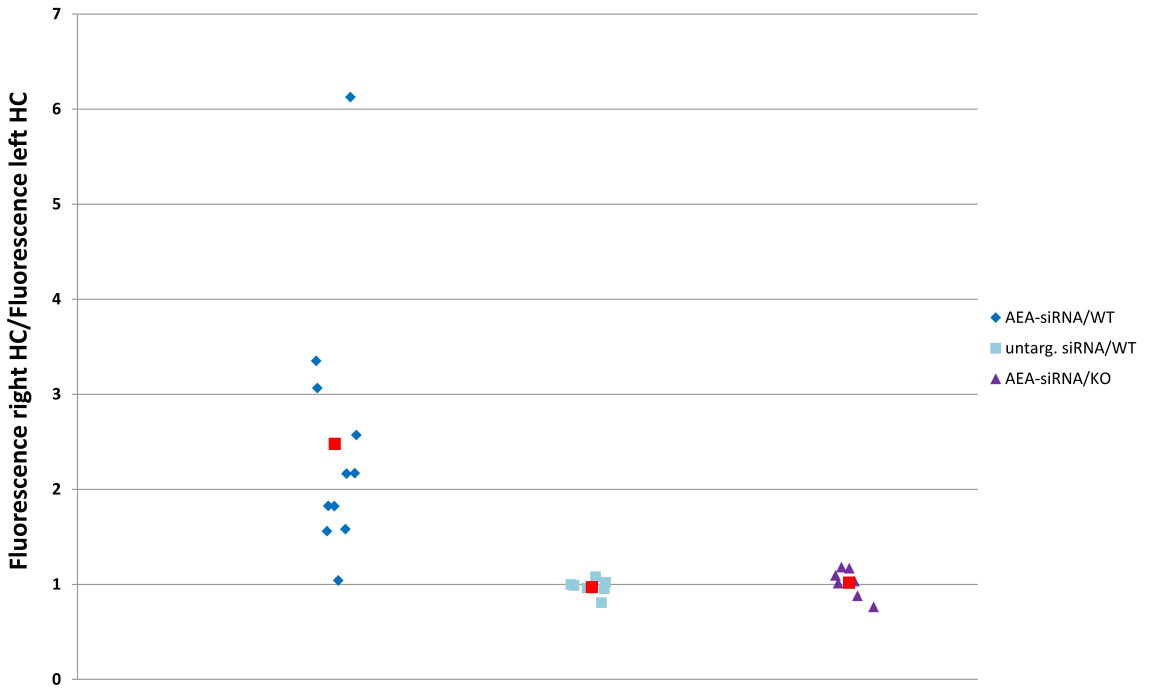

Figure 11.11: Quantification of AEA-siRNA uptake by the hippocampus
Only when both the siRNA is targeted to the cannabinoid receptors with AEA and the cannabinoid receptors are present, the ratio of the treated hippocampus to the untreated hippocampus is below one. The red square indicates the mean value.

ever, this is not the case. We speculated that upon glucose depletion, the cell stops the expression of proteins responsible for glucose uptake. Hence, the glucose-modified siRNA would then find no binding sites on the cell surface. To investigate this, we transfected cells with RNA encoding GFP-labeled GLUT1 which is the most important glucose transporter (Figure 12.29). Indeed, we detected much higher levels of GLUT1 expression in presence of glucose in the medium. Therefore, glucose depletion leads also to a depletion of binding sites for the glucose modification.
We now went on to prove that GLUT1 is indeed a receptor to which the glucose-modified siRNA binds. For this, we transfected Hela cells with RNA coding for GLUT1-GFP for 24 h, followed by incubation with fluorescently labeled Glc-siRNA for another 24 h. When we investigated the cells by fluorescence microscopy, we could clearly detect a colocalization between GLUT1-GFP and Glc-siRNA inside the cell as shown in Figure 11.13. This strongly indicates that Glc-siRNA indeed binds to GLUT1. Also,

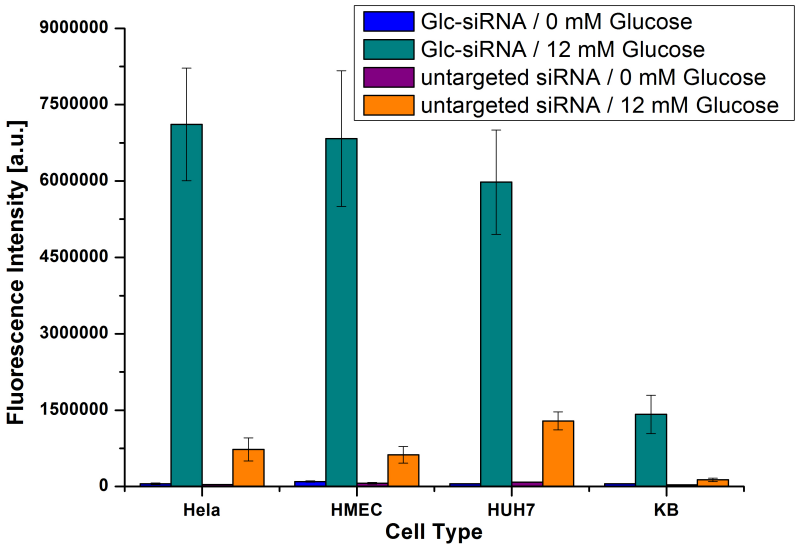

Figure 11.12: Quantification of Glc-siRNA uptake by Hela, HMEC, KB, and HUH-7 cells. In presence of glucose in the medium, glucose-modified siRNA is internalized very efficient. However, if no glucose is present in the medium or the siRNA is not targeted, uptake is very low.

this suggests that the Glc-siRNA blocks the transporter and is internalized together with it.

Since also glucose must be present in the cell medium for GLUT1 to be expressed, fast glucose transport through GLUT1 and high copy numbers are required to overcome the competition effect. Both features are reported in literature for GLUT1: Its processing rate belongs to the fastest among membrane proteins, and it is also present in high copy numbers. Hence, the competition effect is overcompensated. These two factors overcompensate the competition effect and lead to efficient uptake of Glc-siRNA into the investigated cells.

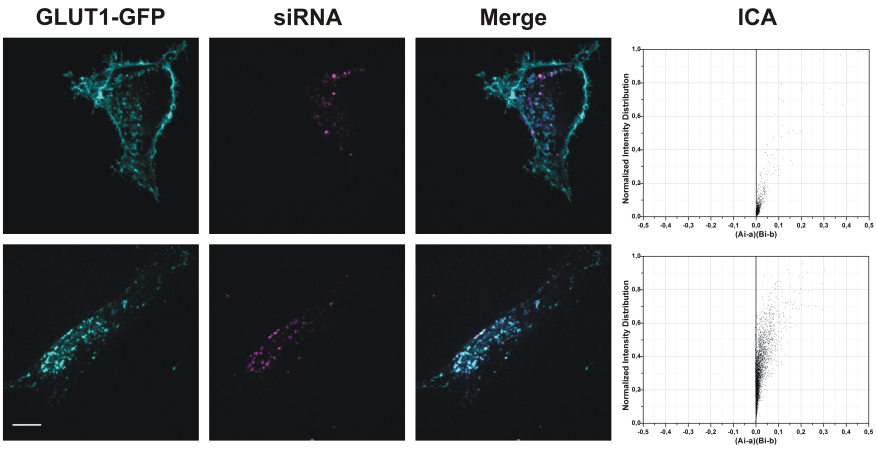

Figure 11.13: Colocalization between internalized Glc-siRNA and GLUT1
Internalized Glc-siRNA colocalizes clearly with the glucose transporter GLUT1 which is visualized using a GFP-tag. Scale bar = 10 μm.

12 Other Projects not Discussed in this Thesis

Two further projects not presented in detail in this thesis should be briefly mentioned here.

12.1 Intracellular Distribution and Action Mechanism of Antidepressants

This project was a collaboration between the MPI for psychiatry, Munich, the department of physical chemistry I, LMU Munich, the department of pharmacy, LMU Munich, and the HMNC GmbH, Munich. It was guided by Thomas Kirmeier, from the MPI for psychiatry.
We investigated the uptake, the distribution, and the action mechanism of a major class of antidepressants: Cationic amphiphilic drugs. Here, we employed azidobupramine, which can be fluorescently labeled via intracellular click chemistry, to monitor how the drug is internalized by the cell and spread afterward. We also used genetically incorporated fluorescent labels to visualize the cellular response. In the course of these experiments, we could reveal that the drug enriches very specifically inside the cell and induces characteristic transitions in the morphology of CD63- and LC3-carrying vesicles. With this, we could provide the basis to analyze the action of the drug inside the cell.
This work will be submitted to PlosOne.

12.2 Metabolic Labeling of *Mycobacterium tuberculosis*

This project was a collaboration between the CAU Kiel, the research center Borstel, and the department of physical chemistry I, LMU Munich. It was guided by Katharina Kolbe and Thisbe Lindhorst, CAU Kiel.
In this project, azido modified sugars that characteristically occur in the cell wall of certain bacteria were incorporated into *Mycobacterium tuberculosis* in order to specifically label them for diagnostic and therapeutic purposes. Here, we could determine that the cross-reactivity of these sugars with human cells, which is of course unwanted, can be neglected. In other word, the sugars do not label human cells. Furthermore, the cytotoxicity of the employed unnatural sugars was determined, another important aspect in order to realize this approach in a medicinal context.
This work will be submitted to Angewandte Chemie.

Bibliography

[1] K. Drickamer, M. E. Taylor, Evolving views of protein glycosylation, *Trends Biochem. Sci.* **1998**, *23*(9), 321–4.

[2] J. Cabezas, The origins of glycobiology, *Biochemical Education* **1994**, *22*, 3–7.

[3] J. D. Marth, P. K. Grewal, Mammalian glycosylation in immunity, *Nat. Rev. Immunol.* **2008**, *8*(11), 874–87.

[4] V. Restelli, M. D. Wang, N. Huzel, M. Ethier, H. Perreault, M. Butler, The effect of dissolved oxygen on the production and the glycosylation profile of recombinant human erythropoietin produced from CHO cells, *Biotechnol. Bioeng.* **2006**, *94*(3), 481–94.

[5] J. G. Leroy, Congenital disorders of N-glycosylation including diseases associated with O- as well as N-glycosylation defects, *Pediatr. Res.* **2006**, *60*(6), 643–56.

[6] C. Kranz, C. Jungeblut, J. Denecke, A. Erlekotte, C. Sohlbach, V. Debus, H. G. Kehl, E. Harms, A. Reith, S. Reichel, H. Grobe, G. Hammersen, U. Schwarzer, T. Marquardt, A defect in dolichol phosphate biosynthesis causes a new inherited disorder with death in early infancy, *Am. J. Hum. Genet.* **2007**, *80*(3), 433–40.

[7] A. Varki, Nothing in glycobiology makes sense, except in the light of evolution, *Cell* **2006**, *126*(5), 841–5.

[8] F. Crick, Central dogma of molecular biology, *Nature* **1970**, *227*(5258), 561–3.

[9] S. Toegel, D. Bieder, S. Andre, F. Altmann, S. M. Walzer, H. Kaltner, J. G. Hofstaetter, R. Windhager, H. J. Gabius, Glycophenotyping of osteoarthritic cartilage and chondrocytes by RT-qPCR, mass spectrometry, histochemistry with plant/human lectins and lectin localization with a glycoprotein, *Arthritis Res. Ther.* **2013**, *15*(5), R147.

[10] C. E. Grubenmann, C. G. Frank, A. J. Hulsmeier, E. Schollen, G. Matthijs, E. Mayatepek, E. G. Berger, M. Aebi, T. Hennet, Deficiency of the first mannosylation step in the N-glycosylation pathway causes congenital disorder of glycosylation type Ik, *Hum. Mol. Genet.* **2004**, *13*(5), 535–42.

[11] C. Korner, R. Knauer, U. Stephani, T. Marquardt, L. Lehle, K. von Figura, Carbohydrate deficient glycoprotein syndrome type IV: deficiency of dolichyl-P-Man:Man(5)GlcNAc(2)-PP-dolichyl mannosyltransferase, *EMBO J.* **1999**, *18*(23), 6816–22.

[12] A. Dell, H. R. Morris, Glycoprotein structure determination by mass spectrometry, *Science* **2001**, *291*(5512), 2351–6.

[13] W. Morelle, J. C. Michalski, Analysis of protein glycosylation by mass spectrometry, *Nat. Protoc.* **2007**, *2*(7), 1585–602.

[14] D. S. Dalpathado, H. Desaire, Glycopeptide analysis by mass spectrometry, *Analyst* **2008**, *133*(6), 731–8.

[15] C. S. Alphonsus, R. N. Rodseth, The endothelial glycocalyx: a review of the vascular barrier, *Anaesthesia* **2014**, *69*(7), 777–84.

[16] F. E. Curry, R. H. Adamson, Endothelial glycocalyx: permeability barrier and mechanosensor, *Ann. Biomed. Eng.* **2012**, *40*(4), 828–39.

[17] J. Blechinger, A. T. Bauer, A. A. Torrano, C. Gorzelanny, C. Brauchle, S. W. Schneider, Uptake kinetics and nanotoxicity of silica nanoparticles are cell type dependent, *Small* **2013**, *9*(23), 3970–80, 3906.

[18] A. Magrez, S. Kasas, V. Salicio, N. Pasquier, J. W. Seo, M. Celio, S. Catsicas, B. Schwaller, L. Forro, Cellular toxicity of carbon-based nanomaterials, *Nano Lett.* **2006**, *6*(6), 1121–5.

[19] G. Oberdörster, E. Oberdörster, J. Oberdörster, Nanotoxicology: an emerging discipline evolving from studies of ultrafine particles, *Environ. Health Perspect.* **2005**, *113*(7), 823–39.

[20] H. J. Busscher, H. C. van der Mei, How do bacteria know they are on a surface and regulate their response to an adhering state?, *PLoS Pathog.* **2012**, *8*(1), e1002440.

[21] M. Ribeiro, F. J. Monteiro, M. P. Ferraz, Infection of orthopedic implants with emphasis on bacterial adhesion process and techniques used in studying bacterial-material interactions, *Biomatter* **2012**, *2*(4), 176–94.

[22] T. Weber, V. Chandrasekaran, I. Stamer, M. B. Thygesen, A. Terfort, T. K. Lindhorst, Switching of bacterial adhesion to a glycosylated surface by reversible reorientation of the carbohydrate ligand, *Angew. Chem. Int. Ed. Engl.* **2014**, *53*(52), 14583–6.

[23] M. Hartmann, L. T., The Bacterial Lectin FimH, a Target for Drug Discovery - Carbohydrate Inhibitors of Type 1 Fimbriae-Mediated Bacterial Adhesion, *Eur. J. Org. Chem.* **2011**, *2011*(20-21), 3583–3609.

[24] B. Menchicchi, A. Hensel, F. M. Goycoolea, Polysaccharides as bacterial antiadhesive agents and "smart" constituents for improved drug delivery systems against Helicobacter pylori infection, *Curr. Pharm. Des.* **2015**.

[25] D. Cozens, R. C. Read, Anti-adhesion methods as novel therapeutics for bacterial infections, *Expert Rev. Anti Infect. Ther.* **2012**, *10*(12), 1457–68.

[26] R. I. Aminov, A brief history of the antibiotic era: lessons learned and challenges for the future, *Front. Microbiol.* **2010**, *1*, 134.

[27] J. M. Blair, M. A. Webber, A. J. Baylay, D. O. Ogbolu, L. J. Piddock, Molecular mechanisms of antibiotic resistance, *Nat. Rev. Microbiol.* **2015**, *13*(1), 42–51.

[28] C. Costelloe, C. Metcalfe, A. Lovering, D. Mant, A. D. Hay, Effect of antibiotic prescribing in primary care on antimicrobial resistance in individual patients: systematic review and meta-analysis, *BMJ* **2010**, *340*, c2096.

[29] M. Soyer, G. Dumenil, Introducing shear stress in the study of bacterial adhesion, *J Vis Exp* **2011**, *55*, e3241.

[30] W. E. Thomas, E. Trintchina, M. Forero, V. Vogel, E. V. Sokurenko, Bacterial adhesion to target cells enhanced by shear force, *Cell* **2002**, *109*(7), 913–23.

[31] W. A. Devane, L. Hanus, A. Breuer, R. G. Pertwee, L. A. Stevenson, G. Griffin, D. Gibson, A. Mandelbaum, A. Etinger, R. Mechoulam, Isolation and structure of a brain constituent that binds to the cannabinoid receptor, *Science* **1992**, *258*(5090), 1946–9.

[32] I. Svizenska, P. Dubovy, A. Sulcova, Cannabinoid receptors 1 and 2 (CB1 and CB2), their distribution, ligands and functional involvement in nervous system structures–a short review, *Pharmacol. Biochem. Behav.* **2008**, *90*(4), 501–11.

[33] R. C. Ryther, A. S. Flynt, r. Phillips, J. A., J. G. Patton, siRNA therapeutics: big potential from small RNAs, *Gene Ther.* **2005**, *12*(1), 5–11.

[34] E. Koutsilieri, A. Rethwilm, C. Scheller, The therapeutic potential of siRNA in gene therapy of neurodegenerative disorders, *J. Neural Transm. Suppl.* **2007**, *72*, 43–9.

[35] L. Johansson, G. Gafvelin, E. S. Arner, Selenocysteine in proteins-properties and biotechnological use, *Biochim. Biophys. Acta* **2005**, *1726*(1), 1–13.

[36] S. Prabakaran, G. Lippens, H. Steen, J. Gunawardena, Post-translational modification: nature's escape from genetic imprisonment and the basis for dynamic information encoding, *Wiley Interdiscip. Rev. Syst. Biol. Med.* **2012**, *4*(6), 565–83.

[37] C. Walsh, *Posttranslational modification of proteins : Expanding nature's inventory*, Englewood, Colo: Roberts and Co., **2006**.

[38] I. M. Ahearn, K. Haigis, D. Bar-Sagi, M. R. Philips, Regulating the regulator: post-translational modification of RAS, *Nat. Rev. Mol. Cell Biol.* **2012**, *13*(1), 39–51.

[39] E. J. Wagner, P. B. Carpenter, Understanding the language of Lys36 methylation at histone H3, *Nat. Rev. Mol. Cell Biol.* **2012**, *13*(2), 115–26.

[40] G. Burnett, E. P. Kennedy, The enzymatic phosphorylation of proteins, *J. Biol. Chem.* **1954**, *211*(2), 969–80.

[41] P. Cohen, The regulation of protein function by multisite phosphorylation–a 25 year update, *Trends Biochem. Sci.* **2000**, *25*(12), 596–601.

[42] M. K. Tarrant, P. A. Cole, The chemical biology of protein phosphorylation, *Annu. Rev. Biochem.* **2009**, *78*, 797–825.

[43] J. A. Ubersax, J. Ferrell, J. E., Mechanisms of specificity in protein phosphorylation, *Nat. Rev. Mol. Cell Biol.* **2007**, *8*(7), 530–41.

[44] L. N. Johnson, The regulation of protein phosphorylation, *Biochem. Soc. Trans.* **2009**, *37*(Pt 4), 627–41.

[45] M. A. Lemmon, J. Schlessinger, Cell signaling by receptor tyrosine kinases, *Cell* **2010**, *141*(7), 1117–34.

[46] E. Verdin, M. Ott, 50 years of protein acetylation: from gene regulation to epigenetics, metabolism and beyond, *Nat. Rev. Mol. Cell Biol.* **2015**, *16*(4), 258–64.

[47] P. Van Damme, K. Hole, A. Pimenta-Marques, K. Helsens, J. Vandekerckhove, R. G. Martinho, K. Gevaert, T. Arnesen, NatF contributes to an evolutionary shift in protein N-terminal acetylation and is important for normal chromosome segregation, *PLoS Genet.* **2011**, *7*(7), e1002169.

[48] V. G. Allfrey, R. Faulkner, A. E. Mirsky, Acetylation and Methylation of Histones and Their Possible Role in the Regulation of Rna Synthesis, *Proc. Natl. Acad. Sci. U. S. A.* **1964**, *51*, 786–94.

[49] L. Verdone, E. Agricola, M. Caserta, E. Di Mauro, Histone acetylation in gene regulation, *Brief Funct Genomic Proteomic* **2006**, *5*(3), 209–21.

[50] J. Du, L. M. Johnson, S. E. Jacobsen, D. J. Patel, DNA methylation pathways and their crosstalk with histone methylation, *Nat. Rev. Mol. Cell Biol.* **2015**, *16*(9), 519–32.

[51] K. K. Biggar, S. S. Li, Non-histone protein methylation as a regulator of cellular signalling and function, *Nat. Rev. Mol. Cell Biol.* **2015**, *16*(1), 5–17.

[52] G. E. Zentner, S. Henikoff, Regulation of nucleosome dynamics by histone modifications, *Nat. Struct. Mol. Biol.* **2013**, *20*(3), 259–66.

[53] K. L. Feijs, A. H. Forst, P. Verheugd, B. Luscher, Macrodomain-containing proteins: regulating new intracellular functions of mono(ADP-ribosyl)ation, *Nat. Rev. Mol. Cell Biol.* **2013**, *14*(7), 443–51.

[54] B. A. Gibson, W. L. Kraus, New insights into the molecular and cellular functions of poly(ADP-ribose) and PARPs, *Nat. Rev. Mol. Cell Biol.* **2012**, *13*(7), 411–24.

[55] K. M. Krueger, J. T. Barbieri, The family of bacterial ADP-ribosylating exotoxins, *Clin. Microbiol. Rev.* **1995**, *8*(1), 34–47.

[56] G. Goldstein, M. Scheid, U. Hammerling, D. H. Schlesinger, H. D. Niall, E. A. Boyse, Isolation of a polypeptide that has lymphocyte-differentiating properties and is probably represented universally in living cells, *Proc. Natl. Acad. Sci. U. S. A.* **1975**, *72*(1), 11–5.

[57] C. M. Pickart, M. J. Eddins, Ubiquitin: structures, functions, mechanisms, *Biochim. Biophys. Acta* **2004**, *1695*(1-3), 55–72.

[58] M. H. Glickman, A. Ciechanover, The ubiquitin-proteasome proteolytic pathway: destruction for the sake of construction, *Physiol. Rev.* **2002**, *82*(2), 373–428.

[59] K. Hofmann, Ubiquitin-binding domains and their role in the DNA damage response, *DNA Repair (Amst)* **2009**, *8*(4), 544–56.

[60] I. Hammond-Martel, H. Yu, B. Affar el, Roles of ubiquitin signaling in transcription regulation, *Cell. Signal.* **2012**, *24*(2), 410–21.

[61] J. D. Schnell, L. Hicke, Non-traditional functions of ubiquitin and ubiquitin-binding proteins, *J. Biol. Chem.* **2003**, *278*(38), 35857–60.

[62] H. Schachter, The joys of HexNAc. The synthesis and function of N- and O-glycan branches, *Glycoconj. J.* **2000**, *17*(7-9), 465–83.

[63] J. L. Mellquist, L. Kasturi, S. L. Spitalnik, S. H. Shakin-Eshleman, The amino acid following an asn-X-Ser/Thr sequon is an important determinant of N-linked core glycosylation efficiency, *Biochemistry* **1998**, *37*(19), 6833–7.

[64] E. Mohorko, R. Glockshuber, M. Aebi, Oligosaccharyltransferase: the central enzyme of N-linked protein glycosylation, *J. Inherit. Metab. Dis.* **2011**, *34*(4), 869–78.

[65] A. Varki, R. D. Cummings, J. D. Esko, H. H. Freeze, P. Stanley, C. R. Bertozzi, G. W. Hart, M. E. Etzler, *Essentials of Glycobiology*, 2nd Aufl., Cold Spring Harbor Laboratory Press, Cold Spring Harbor (NY), **2009**.

[66] L. W. Ruddock, M. Molinari, N-glycan processing in ER quality control, *J. Cell Sci.* **2006**, *119*(Pt 21), 4373–80.

[67] P. Hossler, B. C. Mulukutla, W. S. Hu, Systems analysis of N-glycan processing in mammalian cells, *PLoS One* **2007**, *2*(8), e713.

[68] A. Helenius, M. Aebi, Intracellular functions of N-linked glycans, *Science* **2001**, *291*(5512), 2364–9.

[69] K. W. Moremen, M. Tiemeyer, A. V. Nairn, Vertebrate protein glycosylation: diversity, synthesis and function, *Nat. Rev. Mol. Cell Biol.* **2012**, *13*(7), 448–62.

[70] K. Julenius, A. Molgaard, R. Gupta, S. Brunak, Prediction, conservation analysis, and structural characterization of mammalian mucin-type O-glycosylation sites, *Glycobiology* **2005**, *15*(2), 153–64.

[71] M. Tenno, K. Ohtsubo, F. K. Hagen, D. Ditto, A. Zarbock, P. Schaerli, U. H. von Andrian, K. Ley, D. Le, L. A. Tabak, J. D. Marth, Initiation of protein O glycosylation by the polypeptide GalNAcT-1 in vascular biology and humoral immunity, *Mol. Cell. Biol.* **2007**, *27*(24), 8783–96.

[72] K. Marino, J. Bones, J. J. Kattla, P. M. Rudd, A systematic approach to protein glycosylation analysis: a path through the maze, *Nat. Chem. Biol.* **2010**, *6*(10), 713–23.

[73] I. Brockhausen, Pathways of O-glycan biosynthesis in cancer cells, *Biochim. Biophys. Acta* **1999**, *1473*(1), 67–95.

[74] J. A. Letts, N. L. Rose, Y. R. Fang, C. H. Barry, S. N. Borisova, N. O. Seto, M. M. Palcic, S. V. Evans, Differential recognition of the type I and II H antigen acceptors by the human ABO(H) blood group A and B glycosyltransferases, *J. Biol. Chem.* **2006**, *281*(6), 3625–32.

[75] R. G. Spiro, Protein glycosylation: nature, distribution, enzymatic formation, and disease implications of glycopeptide bonds, *Glycobiology* **2002**, *12*(4), 43R–56R.

[76] K. G. Ten Hagen, T. A. Fritz, L. A. Tabak, All in the family: the UDP-GalNAc:polypeptide N-acetylgalactosaminyltransferases, *Glycobiology* **2003**, *13*(1), 1R–16R.

[77] K. A. Dill, S. B. Ozkan, M. S. Shell, T. R. Weikl, The protein folding problem, *Annu Rev Biophys* **2008**, *37*, 289–316.

[78] M. Bucciantini, C. Cecchi, Biological membranes as protein aggregation matrices and targets of amyloid toxicity, *Methods Mol. Biol.* **2010**, *648*, 231–43.

[79] P. Pamies, Amyloid fibrils: Forceful growth, *Nat Mater* **2015**, *14*(9), 857.

[80] C. J. Bustamante, C. M. Kaiser, R. A. Maillard, D. H. Goldman, C. A. Wilson, Mechanisms of cellular proteostasis: insights from single-molecule approaches, *Annu Rev Biophys* **2014**, *43*, 119–40.

[81] Y. E. Kim, M. S. Hipp, A. Bracher, M. Hayer-Hartl, F. U. Hartl, Molecular chaperone functions in protein folding and proteostasis, *Annu. Rev. Biochem.* **2013**, *82*, 323–55.

[82] J. J. Caramelo, A. J. Parodi, Getting in and out from calnexin/calreticulin cycles, *J. Biol. Chem.* **2008**, *283*(16), 10221–5.

[83] A. Ciechanover, Proteolysis: from the lysosome to ubiquitin and the proteasome, *Nat. Rev. Mol. Cell Biol.* **2005**, *6*(1), 79–87.

[84] K. Welinder, J. Tams, Effects of glycosylation on protein folding, stability and solubility. Studies of chemically modified or engineered plant and fungal peroxidases, *Prog. Biotechnol.* **1995**, *10*, 205–10.

[85] C. B. Anfinsen, Principles that govern the folding of protein chains, *Science* **1973**, *181*(4096), 223–30.

[86] D. Shental-Bechor, Y. Levy, Effect of glycosylation on protein folding: a close look at thermodynamic stabilization, *Proc. Natl. Acad. Sci. U. S. A.* **2008**, *105*(24), 8256–61.

[87] G. D. Rose, P. J. Fleming, J. R. Banavar, A. Maritan, A backbone-based theory of protein folding, *Proc. Natl. Acad. Sci. U. S. A.* **2006**, *103*(45), 16623–33.

[88] P. A. Alexander, Y. He, Y. Chen, J. Orban, P. N. Bryan, The design and characterization of two proteins with 88structure and function, *Proc. Natl. Acad. Sci. U. S. A.* **2007**, *104*(29), 11963–8.

[89] D. Shortle, The denatured state (the other half of the folding equation) and its role in protein stability, *FASEB J.* **1996**, *10*(1), 27–34.

[90] C. N. Pace, B. A. Shirley, M. McNutt, K. Gajiwala, Forces contributing to the conformational stability of proteins, *FASEB J.* **1996**, *10*(1), 75–83.

[91] R. J. Sola, W. Al-Azzam, K. Griebenow, Engineering of protein thermodynamic, kinetic, and colloidal stability: Chemical Glycosylation with monofunctionally activated glycans, *Biotechnol. Bioeng.* **2006**, *94*(6), 1072–9.

[92] R. J. Sola, J. A. Rodriguez-Martinez, K. Griebenow, Modulation of protein biophysical properties by chemical glycosylation: biochemical insights and biomedical implications, *Cell. Mol. Life Sci.* **2007**, *64*(16), 2133–52.

[93] K. Landsteiner, Zur Kenntnis der antifermentativen, lytischen und agglutinierenden Wirkungen des Blutserums und der Lymphe, *Centralblatt f. Bakteriologie, Parasitenkunde u. Infektionskrankheiten* **1900**, *27*, 357–62.

[94] A. S. Donald, J. M. Creeth, W. T. Morgan, W. M. Watkins, The peptide moiety of human-blood-group active glycoproteins associated with the ABO and Lewis groups, *Biochem. J.* **1969**, *115*(1), 125–7.

[95] K. Landsteiner, A. Wiener, An agglutinable factor in human blood recognized by immune sera for rhesus blood, *Proc. Soc. Exp. Biol. Med.* **1940**, *43*, 223–4.

[96] J. R. Storry, M. L. Olsson, The ABO blood group system revisited: a review and update, *Immunohematology* **2009**, *25*(2), 48–59.

[97] H. J. Gabius, S. Andre, J. Jimenez-Barbero, A. Romero, D. Solis, From lectin structure to functional glycomics: principles of the sugar code, *Trends Biochem. Sci.* **2011**, *36*(6), 298–313.

[98] H. Ghazarian, B. Idoni, S. B. Oppenheimer, A glycobiology review: carbohydrates, lectins and implications in cancer therapeutics, *Acta Histochem.* **2011**, *113*(3), 236–47.

[99] S. H. Barondes, D. N. Cooper, M. A. Gitt, H. Leffler, Galectins. Structure and function of a large family of animal lectins, *J. Biol. Chem.* **1994**, *269*(33), 20807–10.

[100] R. Y. Yang, G. A. Rabinovich, F. T. Liu, Galectins: structure, function and therapeutic potential, *Expert Rev. Mol. Med.* **2008**, *10*, e17.

[101] K. S. Lau, E. A. Partridge, A. Grigorian, C. I. Silvescu, V. N. Reinhold, M. Demetriou, J. W. Dennis, Complex N-glycan number and degree of branching cooperate to regulate cell proliferation and differentiation, *Cell* **2007**, *129*(1), 123–34.

[102] I. R. Nabi, J. Shankar, J. W. Dennis, The galectin lattice at a glance, *J. Cell Sci.* **2015**, *128*(13), 2213–9.

[103] O. B. Garner, L. G. Baum, Galectin-glycan lattices regulate cell-surface glycoprotein organization and signalling, *Biochem. Soc. Trans.* **2008**, *36*(Pt 6), 1472–7.

[104] J. Nieminen, A. Kuno, J. Hirabayashi, S. Sato, Visualization of galectin-3 oligomerization on the surface of neutrophils and endothelial cells using fluorescence resonance energy transfer, *J. Biol. Chem.* **2007**, *282*(2), 1374–83.

[105] J. W. Dennis, I. R. Nabi, M. Demetriou, Metabolism, cell surface organization, and disease, *Cell* **2009**, *139*(7), 1229–41.

[106] K. E. Wellen, C. Lu, A. Mancuso, J. M. Lemons, M. Ryczko, J. W. Dennis, J. D. Rabinowitz, H. A. Coller, C. B. Thompson, The hexosamine biosynthetic pathway couples growth factor-induced glutamine uptake to glucose metabolism, *Genes Dev.* **2010**, *24*(24), 2784–99.

[107] K. Ley, The role of selectins in inflammation and disease, *Trends Mol. Med.* **2003**, *9*(6), 263–8.

[108] R. P. McEver, Selectins: lectins that initiate cell adhesion under flow, *Curr. Opin. Cell Biol.* **2002**, *14*(5), 581–6.

[109] D. N. Granger, E. Senchenkova, *Inflammation and the Microcirculation*, Integrated Systems Physiology - From Cell to Function, Morgan and Claypool Life Sciences, San Rafael (CA), **2010**.

[110] S. Weinbaum, J. M. Tarbell, E. R. Damiano, The structure and function of the endothelial glycocalyx layer, *Annu. Rev. Biomed. Eng.* **2007**, *9*, 121–67.

[111] D. Chappell, M. Jacob, K. Hofmann-Kiefer, M. Rehm, U. Welsch, P. Conzen, B. F. Becker, Antithrombin reduces shedding of the endothelial glycocalyx following ischaemia/reperfusion, *Cardiovasc. Res.* **2009**, *83*(2), 388–96.

[112] S. Reitsma, D. W. Slaaf, H. Vink, M. A. van Zandvoort, M. G. oude Egbrink, The endothelial glycocalyx: composition, functions, and visualization, *Pflugers Arch.* **2007**, *454*(3), 345–59.

[113] C. B. Henry, B. R. Duling, Permeation of the luminal capillary glycocalyx is determined by hyaluronan, *Am. J. Physiol.* **1999**, *277*(2 Pt 2), H508–14.

[114] C. Desjardins, B. R. Duling, Heparinase treatment suggests a role for the endothelial cell glycocalyx in regulation of capillary hematocrit, *Am. J. Physiol.* **1990**, *258*(3 Pt 2), H647–54.

[115] A. A. Constantinescu, H. Vink, J. A. Spaan, Elevated capillary tube hematocrit reflects degradation of endothelial cell glycocalyx by oxidized LDL, *Am. J. Physiol. Heart Circ. Physiol.* **2001**, *280*(3), H1051–7.

[116] T. E. Woodcock, T. M. Woodcock, Revised Starling equation and the glycocalyx model of transvascular fluid exchange: an improved paradigm for prescribing intravenous fluid therapy, *Br. J. Anaesth.* **2012**, *108*(3), 384–94.

[117] M. J. Dane, B. M. van den Berg, D. H. Lee, M. G. Boels, G. L. Tiemeier, M. C. Avramut, A. J. van Zonneveld, J. van der Vlag, H. Vink, T. J. Rabelink, A microscopic view on the renal endothelial glycocalyx, *Am. J. Physiol. Renal Physiol.* **2015**, *308*(9), F956–66.

[118] E. E. Ebong, F. P. Macaluso, D. C. Spray, J. M. Tarbell, Imaging the endothelial glycocalyx in vitro by rapid freezing/freeze substitution transmission electron microscopy, *Arterioscler. Thromb. Vasc. Biol.* **2011**, *31*(8), 1908–15.

[119] M. M. Thi, J. M. Tarbell, S. Weinbaum, D. C. Spray, The role of the glycocalyx in reorganization of the actin cytoskeleton under fluid shear stress: a "bumper-car" model, *Proc. Natl. Acad. Sci. U. S. A.* **2004**, *101*(47), 16483–8.

[120] S. Weinbaum, Y. Duan, M. M. Thi, L. You, An Integrative Review of Mechanotransduction in Endothelial, Epithelial (Renal) and Dendritic Cells (Osteocytes), *Cell. Mol. Bioeng.* **2011**, *4*(4), 510–537.

[121] L. Hall-Stoodley, J. W. Costerton, P. Stoodley, Bacterial biofilms: from the natural environment to infectious diseases, *Nat. Rev. Microbiol.* **2004**, *2*(2), 95–108.

[122] N. Woodford, D. M. Livermore, Infections caused by Gram-positive bacteria: a review of the global challenge, *J. Infect.* **2009**, *59 Suppl 1*, S4–16.

[123] D. M. Monack, A. Mueller, S. Falkow, Persistent bacterial infections: the interface of the pathogen and the host immune system, *Nat. Rev. Microbiol.* **2004**, *2*(9), 747–65.

[124] J. Pizarro-Cerda, P. Cossart, Bacterial adhesion and entry into host cells, *Cell* **2006**, *124*(4), 715–27.

[125] A. Fabrega, J. Vila, Yersinia enterocolitica: pathogenesis, virulence and antimicrobial resistance, *Enferm. Infecc. Microbiol. Clin.* **2012**, *30*(1), 24–32.

[126] B. Coburn, G. A. Grassl, B. B. Finlay, Salmonella, the host and disease: a brief review, *Immunol. Cell Biol.* **2007**, *85*(2), 112–8.

[127] M. Ogawa, Y. Handa, H. Ashida, M. Suzuki, C. Sasakawa, The versatility of Shigella effectors, *Nat. Rev. Microbiol.* **2008**, *6*(1), 11–6.

[128] P. Klemm, M. A. Schembri, Bacterial adhesins: function and structure, *Int. J. Med. Microbiol.* **2000**, *290*(1), 27–35.

[129] G. Capitani, O. Eidam, R. Glockshuber, M. G. Grutter, Structural and functional insights into the assembly of type 1 pili from Escherichia coli, *Microbes Infect* **2006**, *8*(8), 2284–90.

[130] A. Kalita, J. Hu, A. G. Torres, Recent advances in adherence and invasion of pathogenic Escherichia coli, *Curr. Opin. Infect. Dis.* **2014**, *27*(5), 459–64.

[131] C. S. Hung, J. Bouckaert, D. Hung, J. Pinkner, C. Widberg, A. DeFusco, C. G. Auguste, R. Strouse, S. Langermann, G. Waksman, S. J. Hultgren, Structural basis of tropism of Escherichia coli to the bladder during urinary tract infection, *Mol. Microbiol.* **2002**, *44*(4), 903–15.

[132] E. V. Sokurenko, V. Vogel, W. E. Thomas, Catch-bond mechanism of force-enhanced adhesion: counterintuitive, elusive, but ... widespread?, *Cell Host Microbe* **2008**, *4*(4), 314–23.

[133] W. Thomas, Catch bonds in adhesion, *Annu. Rev. Biomed. Eng.* **2008**, *10*, 39–57.

[134] T. F. Landers, B. Cohen, T. E. Wittum, E. L. Larson, A review of antibiotic use in food animals: perspective, policy, and potential, *Public Health Rep.* **2012**, *127*(1), 4–22.

[135] D. I. Kisiela, H. Avagyan, D. Friend, A. Jalan, S. Gupta, G. Interlandi, Y. Liu, V. Tchesnokova, V. B. Rodriguez, J. P. Sumida, R. K. Strong, X. R. Wu, W. E. Thomas, E. V. Sokurenko, Inhibition and Reversal of Microbial Attachment by an Antibody with Parasteric Activity against the FimH Adhesin of Uropathogenic E. coli, *PLoS Pathog.* **2015**, *11*(5), e1004857.

[136] L. R. Rodrigues, Inhibition of bacterial adhesion on medical devices, *Adv. Exp. Med. Biol.* **2011**, *715*, 351–67.

[137] N. Sharon, H. Lis, History of lectins: from hemagglutinins to biological recognition molecules, *Glycobiology* **2004**, *14*(11), 53R–62R.

[138] N. Firon, I. Ofek, N. Sharon, Carbohydrate specificity of the surface lectins of Escherichia coli, Klebsiella pneumoniae, and Salmonella typhimurium, *Carbohydr. Res.* **1983**, *120*, 235–49.

[139] B. Fiege, S. Rabbani, R. C. Preston, R. P. Jakob, P. Zihlmann, O. Schwardt, X. Jiang, T. Maier, B. Ernst, The tyrosine gate of the bacterial lectin FimH: a conformational analysis by NMR spectroscopy and X-ray crystallography, *ChemBioChem* **2015**, *16*(8), 1235–46.

[140] J. Bouckaert, J. Berglund, M. Schembri, E. De Genst, L. Cools, M. Wuhrer, C. S. Hung, J. Pinkner, R. Slattegard, A. Zavialov, D. Choudhury, S. Langermann, S. J. Hultgren, L. Wyns, P. Klemm, S. Oscarson, S. D. Knight, H. De Greve, Receptor binding studies disclose a novel class of high-affinity inhibitors of the Escherichia coli FimH adhesin, *Mol. Microbiol.* **2005**, *55*(2), 441–55.

[141] G. Le Blay, I. Fliss, C. Lacroix, Comparative detection of bacterial adhesion to Caco-2 cells with ELISA, radioactivity and plate count methods, *J. Microbiol. Methods* **2004**, *59*(2), 211–21.

[142] Y. Wang, W. Knoll, J. Dostalek, Bacterial pathogen surface plasmon resonance biosensor advanced by long range surface plasmons and magnetic nanoparticle assays, *Anal. Chem.* **2012**, *84*(19), 8345–50.

[143] M. Hartmann, A. K. Horst, P. Klemm, T. K. Lindhorst, A kit for the investigation of live Escherichia coli cell adhesion to glycosylated surfaces, *Chem. Commun. (Camb.)* **2010**, *46*(2), 330–2.

[144] H. Kawashima, Generation of anti-sulfated glycan antibodies using sulfotransferase-deficient mice, *Methods Mol. Biol.* **2013**, *1022*, 51–60.

[145] H. Kayser, R. Zeitler, C. Kannicht, D. Grunow, R. Nuck, W. Reutter, Biosynthesis of a nonphysiological sialic acid in different rat organs, using N-propanoyl-D-hexosamines as precursors, *J. Biol. Chem.* **1992**, *267*(24), 16934–8.

[146] O. T. Keppler, P. Stehling, M. Herrmann, H. Kayser, D. Grunow, W. Reutter, M. Pawlita, Biosynthetic modulation of sialic acid-dependent virus-receptor interactions of two primate polyoma viruses, *J. Biol. Chem.* **1995**, *270*(3), 1308–14.

[147] E. M. Sletten, C. R. Bertozzi, Bioorthogonal chemistry: fishing for selectivity in a sea of functionality, *Angew. Chem. Int. Ed. Engl.* **2009**, *48*(38), 6974–98.

[148] E. M. Sletten, C. R. Bertozzi, From mechanism to mouse: a tale of two bioorthogonal reactions, *Acc. Chem. Res.* **2011**, *44*(9), 666–76.

[149] E. Saxon, C. R. Bertozzi, Cell surface engineering by a modified Staudinger reaction, *Science* **2000**, *287*(5460), 2007–10.

[150] P. Agarwal, B. J. Beahm, P. Shieh, C. R. Bertozzi, Systemic Fluorescence Imaging of Zebrafish Glycans with Bioorthogonal Chemistry, *Angew. Chem. Int. Ed. Engl.* **2015**, *54*(39), 11504–10.

[151] S. T. Laughlin, J. M. Baskin, S. L. Amacher, C. R. Bertozzi, In vivo imaging of membrane-associated glycans in developing zebrafish, *Science* **2008**, *320*(5876), 664–7.

[152] S. T. Laughlin, C. R. Bertozzi, Metabolic labeling of glycans with azido sugars and subsequent glycan-profiling and visualization via Staudinger ligation, *Nat. Protoc.* **2007**, *2*(11), 2930–44.

[153] J. A. Prescher, C. R. Bertozzi, Chemistry in living systems, *Nat. Chem. Biol.* **2005**, *1*(1), 13–21.

[154] R. Seth, S. Yang, S. Choi, M. Sabean, E. A. Roberts, In vitro assessment of copper-induced toxicity in the human hepatoma line, Hep G2, *Toxicol. In Vitro* **2004**, *18*(4), 501–9.

[155] V. Hong, N. F. Steinmetz, M. Manchester, M. G. Finn, Labeling live cells by copper-catalyzed alkyne–azide click chemistry, *Bioconjug. Chem.* **2010**, *21*(10), 1912–6.

[156] J. M. Baskin, J. A. Prescher, S. T. Laughlin, N. J. Agard, P. V. Chang, I. A. Miller, A. Lo, J. A. Codelli, C. R. Bertozzi, Copper-free click chemistry for dynamic in vivo imaging, *Proc. Natl. Acad. Sci. U. S. A.* **2007**, *104*(43), 16793–7.

[157] V. Bock, H. Hiemstra, J. Maarseveen, CuI-Catalyzed Alkyne-Azide "Click" Cycloadditions from a Mechanistic and Synthetic Perspective, *Eur. J. Org. Chem.* **2006**, *2006*(1), 51–68.

[158] F. Himo, T. Lovell, R. Hilgraf, V. V. Rostovtsev, L. Noodleman, K. B. Sharpless, V. V. Fokin, Copper(I)-catalyzed synthesis of azoles. DFT study predicts unprecedented reactivity and intermediates, *J. Am. Chem. Soc.* **2005**, *127*(1), 210–6.

[159] D. D. Licatalosi, R. B. Darnell, RNA processing and its regulation: global insights into biological networks, *Nat. Rev. Genet.* **2010**, *11*(1), 75–87.

[160] D. Semizarov, P. Kroeger, S. Fesik, siRNA-mediated gene silencing: a global genome view, *Nucleic Acids Res.* **2004**, *32*(13), 3836–45.

[161] A. J. Hamilton, D. C. Baulcombe, A species of small antisense RNA in posttranscriptional gene silencing in plants, *Science* **1999**, *286*(5441), 950–2.

[162] S. M. Elbashir, J. Harborth, W. Lendeckel, A. Yalcin, K. Weber, T. Tuschl, Duplexes of 21-nucleotide RNAs mediate RNA interference in cultured mammalian cells, *Nature* **2001**, *411*(6836), 494–8.

[163] E. Bernstein, A. A. Caudy, S. M. Hammond, G. J. Hannon, Role for a bidentate ribonuclease in the initiation step of RNA interference, *Nature* **2001**, *409*(6818), 363–6.

[164] R. Yi, Y. Qin, I. G. Macara, B. R. Cullen, Exportin-5 mediates the nuclear export of pre-microRNAs and short hairpin RNAs, *Genes Dev.* **2003**, *17*(24), 3011–6.

[165] L. Jaskiewicz, W. Filipowicz, Role of Dicer in posttranscriptional RNA silencing, *Curr. Top. Microbiol. Immunol.* **2008**, *320*, 77–97.

[166] R. I. Gregory, T. P. Chendrimada, N. Cooch, R. Shiekhattar, Human RISC couples microRNA biogenesis and posttranscriptional gene silencing, *Cell* **2005**, *123*(4), 631–40.

[167] F. V. Rivas, N. H. Tolia, J. J. Song, J. P. Aragon, J. Liu, G. J. Hannon, L. Joshua-Tor, Purified Argonaute2 and an siRNA form recombinant human RISC, *Nat. Struct. Mol. Biol.* **2005**, *12*(4), 340–9.

[168] K. Tiemann, J. J. Rossi, RNAi-based therapeutics-current status, challenges and prospects, *EMBO Mol. Med.* **2009**, *1*(3), 142–51.

[169] A. O. Garba, S. A. Mousa, Bevasiranib for the treatment of wet, age-related macular degeneration, *Ophthalmol. Eye Dis.* **2010**, *2*, 75–83.

[170] M. R. Barakat, P. K. Kaiser, VEGF inhibitors for the treatment of neovascular age-related macular degeneration, *Expert Opin Investig Drugs* **2009**, *18*(5), 637–46.

[171] L. F. Gebert, M. A. Rebhan, S. E. Crivelli, R. Denzler, M. Stoffel, J. Hall, Miravirsen (SPC3649) can inhibit the biogenesis of miR-122, *Nucleic Acids Res.* **2014**, *42*(1), 609–21.

[172] C. L. Jopling, M. Yi, A. M. Lancaster, S. M. Lemon, P. Sarnow, Modulation of hepatitis C virus RNA abundance by a liver-specific MicroRNA, *Science* **2005**, *309*(5740), 1577–81.

[173] R. Kanasty, J. R. Dorkin, A. Vegas, D. Anderson, Delivery materials for siRNA therapeutics, *Nat Mater* **2013**, *12*(11), 967–77.

[174] E. Wagner, Polymers for siRNA delivery: inspired by viruses to be targeted, dynamic, and precise, *Acc. Chem. Res.* **2012**, *45*(7), 1005–13.

[175] H. Ragelle, G. Vandermeulen, V. Preat, Chitosan-based siRNA delivery systems, *J. Control. Release* **2013**, *172*(1), 207–18.

[176] M. J. Wood, B. Trulzsch, A. Abdelgany, D. Beeson, Therapeutic gene silencing in the nervous system, *Hum. Mol. Genet.* **2003**, *12 Spec No 2*, R279–84.

[177] A. Biegon, I. A. Kerman, Autoradiographic study of pre- and postnatal distribution of cannabinoid receptors in human brain, *NeuroImage* **2001**, *14*(6), 1463–8.

[178] M. Glass, M. Dragunow, R. L. Faull, Cannabinoid receptors in the human brain: a detailed anatomical and quantitative autoradiographic study in the fetal, neonatal and adult human brain, *Neuroscience* **1997**, *77*(2), 299–318.

[179] R. Pepperkok, J. Ellenberg, High-throughput fluorescence microscopy for systems biology, *Nat. Rev. Mol. Cell Biol.* **2006**, *7*(9), 690–6.

[180] J. W. Lichtman, J. A. Conchello, Fluorescence microscopy, *Nat. Methods* **2005**, *2*(12), 910–9.

[181] L. Möckl, D. C. Lamb, C. Bräuchle, Super-resolved fluorescence microscopy: Nobel Prize in Chemistry 2014 for Eric Betzig, Stefan Hell, and William E. Moerner, *Angew. Chem. Int. Ed. Engl.* **2014**, *53*(51), 13972–7.

[182] A. Jablonski, Efficiency of Anti-Stokes Fluorescence in Dyes, *Nature* **1933**, *131*, 839–40.

[183] G. Stokes, On the Change of Refrangibility of Light, *Philos. Trans. R. Soc. London* **1852**, *142*, 463–562.

[184] J. Maxwell, A Dynamical Theory of the Electromagnetic Field, *Royal Society Transactions* **1865**, *155*, 459–512.

[185] E. Abbe, BeitrÃ¤ge zur Theorie des Mikroskops und der mikroskopischen Wahrnehmung, *Archiv fÃ¼r Mikroskopische Anatomie* **1873**, *9*(1), 413–68.

[186] S. Ram, E. S. Ward, R. J. Ober, Beyond Rayleigh's criterion: a resolution measure with application to single-molecule microscopy, *Proc. Natl. Acad. Sci. U. S. A.* **2006**, *103*(12), 4457–62.

[187] C. Sparrow, On Spectroscopic Resolving Power, *ApJ* **1916**, *44*, 76.

[188] K. Li, G. Li, F. Xiao, F. Lu, Z. Wang, A. Xu, Unidirectionally optical coupling from free space into silicon waveguide with wide flat-top angular efficiency, *Opt. Express* **2012**, *20*(17), 18545–54.

[189] J. R. Swedlow, M. Platani, Live cell imaging using wide-field microscopy and deconvolution, *Cell Struct. Funct.* **2002**, *27*(5), 335–41.

[190] L. Schermelleh, R. Heintzmann, H. Leonhardt, A guide to super-resolution fluorescence microscopy, *J. Cell Biol.* **2010**, *190*(2), 165–75.

[191] S. Kummer, T. Basche, C. BrÃ¤uchle, Terrylene in p-terphenyl: a novel single crystalline system for single molecule spectroscopy at low temperatures, *CPL* **1991**, *229*, 309–16.

[192] A. Kiraz, M. Ehrl, C. BrÃ¤uchle, A. Zumbusch, Low temperature single molecule spectroscopy using vibronic excitation and dispersed fluorescence detection, *JChPh* **2003**, *118*, 10821–24.

[193] http://zeiss-campus.magnet.fsu.edu/articles/livecellimaging/techniques.html, **2015**.

[194] N. Ruthardt, D. C. Lamb, C. Brauchle, Single-particle tracking as a quantitative microscopy-based approach to unravel cell entry mechanisms of viruses and pharmaceutical nanoparticles, *Mol. Ther.* **2011**, *19*(7), 1199–211.

[195] A. Kusumi, T. A. Tsunoyama, K. M. Hirosawa, R. S. Kasai, T. K. Fujiwara, Tracking single molecules at work in living cells, *Nat. Chem. Biol.* **2014**, *10*(7), 524–32.

[196] A. Fick, Ueber Diffusion, *AnP* **1855**, *94*, 59.

[197] E. Barkai, Y. Garini, R. Metzler, Strange kinetics of single molecules in living cells, *PhT* **2012**, *65*(8), 29.

[198] M. J. Saxton, K. Jacobson, Single-particle tracking: applications to membrane dynamics, *Annu. Rev. Biophys. Biomol. Struct.* **1997**, *26*, 373–99.

[199] M. Bates, B. Huang, X. Zhuang, Super-resolution microscopy by nanoscale localization of photo-switchable fluorescent probes, *Curr. Opin. Chem. Biol.* **2008**, *12*(5), 505–14.

[200] W. Moerner, A dozen years of single-molecule spectroscopy in physics, chemistry, and biophysics, *JPCB* **2002**, *106*, 910–27.

[201] A. Gahlmann, W. E. Moerner, Exploring bacterial cell biology with single-molecule tracking and super-resolution imaging, *Nat. Rev. Microbiol.* **2014**, *12*(1), 9–22.

[202] W. E. Moerner, New directions in single-molecule imaging and analysis, *Proc. Natl. Acad. Sci. U. S. A.* **2007**, *104*(31), 12596–602.

[203] H. Nyquist, Certain Topics in Telegraph Transmission Theory, *Trans. AIEE* **1928**, *47*, 617–644.

[204] C. Shannon, Communication in the Presence of Noise, *Proc. IRE* **1949**, *37*(1), 447–57.

[205] S. W. Hell, J. Wichmann, Breaking the diffraction resolution limit by stimulated emission: stimulated-emission-depletion fluorescence microscopy, *Opt. Lett.* **1994**, *19*(11), 780–2.

[206] T. Muller, C. Schumann, A. Kraegeloh, STED microscopy and its applications: new insights into cellular processes on the nanoscale, *Chemphyschem* **2012**, *13*(8), 1986–2000.

[207] S. J. Sahl, W. E. Moerner, Super-resolution fluorescence imaging with single molecules, *Curr. Opin. Struct. Biol.* **2013**, *23*(5), 778–87.

[208] A. Yildiz, J. N. Forkey, S. A. McKinney, T. Ha, Y. E. Goldman, P. R. Selvin, Myosin V walks hand-over-hand: single fluorophore imaging with 1.5-nm localization, *Science* **2003**, *300*(5628), 2061–5.

[209] M. A. Thompson, J. M. Casolari, M. Badieirostami, P. O. Brown, W. E. Moerner, Three-dimensional tracking of single mRNA particles in Saccharomyces cerevisiae using a double-helix point spread function, *Proc. Natl. Acad. Sci. U. S. A.* **2010**, *107*(42), 17864–71.

[210] E. Betzig, Proposed method for molecular optical imaging, *Opt. Lett.* **1995**, *20*(3), 237–9.

[211] A. M. van Oijen, J. Kohler, J. Schmidt, M. Muller, G. J. Brakenhoff, 3-Dimensional super-resolution by spectrally selective imaging, *Chem. Phys. Lett.* **1998**, *292*(183-187).

[212] R. M. Dickson, A. B. Cubitt, R. Y. Tsien, W. E. Moerner, On/off blinking and switching behaviour of single molecules of green fluorescent protein, *Nature* **1997**, *388*(6640), 355–8.

[213] G. H. Patterson, J. Lippincott-Schwartz, A photoactivatable GFP for selective photolabeling of proteins and cells, *Science* **2002**, *297*(5588), 1873–7.

[214] E. Betzig, G. H. Patterson, R. Sougrat, O. W. Lindwasser, S. Olenych, J. S. Bonifacino, M. W. Davidson, J. Lippincott-Schwartz, H. F. Hess, Imaging intracellular fluorescent proteins at nanometer resolution, *Science* **2006**, *313*(5793), 1642–5.

[215] S. T. Hess, T. P. Girirajan, M. D. Mason, Ultra-high resolution imaging by fluorescence photoactivation localization microscopy, *Biophys. J.* **2006**, *91*(11), 4258–72.

[216] M. J. Rust, M. Bates, X. Zhuang, Sub-diffraction-limit imaging by stochastic optical reconstruction microscopy (STORM), *Nat. Methods* **2006**, *3*(10), 793–5.

[217] M. A. Thompson, M. D. Lew, W. E. Moerner, Extending microscopic resolution with single-molecule imaging and active control, *Annu Rev Biophys* **2012**, *41*, 321–42.

[218] B. Huang, W. Wang, M. Bates, X. Zhuang, Three-dimensional super-resolution imaging by stochastic optical reconstruction microscopy, *Science* **2008**, *319*(5864), 810–3.

[219] S. R. Pavani, M. A. Thompson, J. S. Biteen, S. J. Lord, N. Liu, R. J. Twieg, R. Piestun, W. E. Moerner, Three-dimensional, single-molecule fluorescence imaging beyond the diffraction limit by using a double-helix point spread function, *Proc. Natl. Acad. Sci. U. S. A.* **2009**, *106*(9), 2995–9.

[220] H. Shroff, C. G. Galbraith, J. A. Galbraith, H. White, J. Gillette, S. Olenych, M. W. Davidson, E. Betzig, Dual-color superresolution imaging of genetically expressed probes within individual adhesion complexes, *Proc. Natl. Acad. Sci. U. S. A.* **2007**, *104*(51), 20308–13.

[221] F. Huang, T. M. Hartwich, F. E. Rivera-Molina, Y. Lin, W. C. Duim, J. J. Long, P. D. Uchil, J. R. Myers, M. A. Baird, W. Mothes, M. W. Davidson, D. Toomre, J. Bewersdorf, Video-rate nanoscopy using sCMOS camera-specific single-molecule localization algorithms, *Nat. Methods* **2013**, *10*(7), 653–8.

[222] L. Möckl, A. K. Horst, K. Kolbe, T. K. Lindhorst, C. Bräuchle, Microdomain Formation Controls Spatiotemporal Dynamics of Cell-Surface Glycoproteins, *ChemBioChem* **2015**.

[223] G. Vereb, J. Szollosi, J. Matko, P. Nagy, T. Farkas, L. Vigh, L. Matyus, T. A. Waldmann, S. Damjanovich, Dynamic, yet structured: The cell membrane three decades after the Singer-Nicolson model, *Proc. Natl. Acad. Sci. U. S. A.* **2003**, *100*(14), 8053–8.

[224] J. J. Sieber, K. I. Willig, C. Kutzner, C. Gerding-Reimers, B. Harke, G. Donnert, B. Rammner, C. Eggeling, S. W. Hell, H. Grubmuller, T. Lang, Anatomy and dynamics of a supramolecular membrane protein cluster, *Science* **2007**, *317*(5841), 1072–6.

[225] A. Kusumi, Y. Sako, Cell surface organization by the membrane skeleton, *Curr. Opin. Cell Biol.* **1996**, *8*(4), 566–74.

[226] S. Letschert, A. Gohler, C. Franke, N. Bertleff-Zieschang, E. Memmel, S. Doose, J. Seibel, M. Sauer, Super-resolution imaging of plasma membrane glycans, *Angew. Chem. Int. Ed. Engl.* **2014**, *53*(41), 10921–4.

[227] G. A. Rabinovich, L. G. Baum, N. Tinari, R. Paganelli, C. Natoli, F. T. Liu, S. Iacobelli, Galectins and their ligands: amplifiers, silencers or tuners of the inflammatory response?, *Trends Immunol.* **2002**, *23*(6), 313–20.

[228] J. W. Dennis, I. R. Nabi, M. Demetriou, Metabolism, cell surface organization, and disease, *Cell* **2009**, *139*(7), 1229–41.

[229] B. Belardi, G. P. O'Donoghue, A. W. Smith, J. T. Groves, C. R. Bertozzi, Investigating cell surface galectin-mediated cross-linking on glycoengineered cells, *J. Am. Chem. Soc.* **2012**, *134*(23), 9549–52.

[230] M. C. Miller, J. P. Ribeiro, V. Roldos, S. Martin-Santamaria, F. J. Canada, I. A. Nesmelova, S. Andre, M. Pang, A. A. Klyosov, L. G. Baum, J. Jimenez-Barbero, H. J. Gabius, K. H. Mayo, Structural aspects of binding of alpha-linked digalactosides to human galectin-1, *Glycobiology* **2011**, *21*(12), 1627–41.

[231] J. Dumic, S. Dabelic, M. Flogel, Galectin-3: an open-ended story, *Biochim. Biophys. Acta* **2006**, *1760*(4), 616–35.

[232] J. W. Dennis, K. S. Lau, M. Demetriou, I. R. Nabi, Adaptive regulation at the cell surface by N-glycosylation, *Traffic* **2009**, *10*(11), 1569–78.

[233] C. F. Brewer, M. C. Miceli, L. G. Baum, Clusters, bundles, arrays and lattices: novel mechanisms for lectin-saccharide-mediated cellular interactions, *Curr. Opin. Struct. Biol.* **2002**, *12*(5), 616–23.

[234] A. Homann, R. U. Qamar, S. Serim, P. Dersch, J. Seibel, Bioorthogonal metabolic glycoengineering of human larynx carcinoma (HEp-2) cells targeting sialic acid, *Beilstein J. Org. Chem.* **2010**, *6*, 24.

[235] X. Ning, J. Guo, M. A. Wolfert, G. J. Boons, Visualizing metabolically labeled glycoconjugates of living cells by copper-free and fast huisgen cycloadditions, *Angew. Chem. Int. Ed. Engl.* **2008**, *47*(12), 2253–5.

[236] D. Axelrod, D. E. Koppel, J. Schlessinger, E. Elson, W. W. Webb, Mobility measurement by analysis of fluorescence photobleaching recovery kinetics, *Biophys. J.* **1976**, *16*(9), 1055–69.

[237] P. H. Lommerse, G. A. Blab, L. Cognet, G. S. Harms, B. E. Snaar-Jagalska, H. P. Spaink, T. Schmidt, Single-molecule imaging of the H-ras membrane-anchor reveals domains in the cytoplasmic leaflet of the cell membrane, *Biophys. J.* **2004**, *86*(1 Pt 1), 609–16.

[238] T. Fujiwara, K. Ritchie, H. Murakoshi, K. Jacobson, A. Kusumi, Phospholipids undergo hop diffusion in compartmentalized cell membrane, *J. Cell Biol.* **2002**, *157*(6), 1071–81.

[239] V. Cattaneo, M. V. Tribulatti, J. Carabelli, A. Carestia, M. Schattner, O. Campetella, Galectin-8 elicits pro-inflammatory activities in the endothelium, *Glycobiology* **2014**.

[240] J. Etulain, S. Negrotto, M. V. Tribulatti, D. O. Croci, J. Carabelli, O. Campetella, G. A. Rabinovich, M. Schattner, Control of angiogenesis by galectins involves the release of platelet-derived proangiogenic factors, *PLoS One* **2014**, *9*(4), e96402.

[241] V. L. Thijssen, R. Postel, R. J. Brandwijk, R. P. Dings, I. Nesmelova, S. Satijn, N. Verhofstad, Y. Nakabeppu, L. G. Baum, J. Bakkers, K. H. Mayo, F. Poirier, A. W. Griffioen, Galectin-1 is essential in tumor angiogenesis and is a target for antiangiogenesis therapy, *Proc. Natl. Acad. Sci. U. S. A.* **2006**, *103*(43), 15975–80.

[242] C. Boscher, Y. Z. Zheng, R. Lakshminarayan, L. Johannes, J. W. Dennis, L. J. Foster, I. R. Nabi, Galectin-3 protein regulates mobility of N-cadherin and GM1 ganglioside at cell-cell junctions of mammary carcinoma cells, *J. Biol. Chem.* **2012**, *287*(39), 32940–52.

[243] J. Bonzi, O. Bornet, S. Betzi, B. T. Kasper, L. K. Mahal, S. J. Mancini, C. Schiff, C. Sebban-Kreuzer, F. Guerlesquin, L. Elantak, Pre-B cell receptor binding to galectin-1 modifies galectin-1/carbohydrate affinity to modulate specific galectin-1/glycan lattice interactions, *Nat Commun* **2015**, *6*, 6194.

[244] S. Bunse, S. Garg, S. Junek, D. Vogel, N. Ansari, E. H. Stelzer, E. Schuman, Role of N-cadherin cis and trans interfaces in the dynamics of adherens junctions in living cells, *PLoS One* **2013**, *8*(12), e81517.

[245] W. E. Moerner, M. Orrit, Illuminating single molecules in condensed matter, *Science* **1999**, *283*(5408), 1670–6.

[246] M. Orrit, J. Bernard, Single pentacene molecules detected by fluorescence excitation in a p-terphenyl crystal, *Phys. Rev. Lett.* **1990**, *65*(21), 2716–2719.

[247] W. E. Moerner, A Dozen Years of Single-Molecule Spectroscopy in Physics, Chemistry, and Biophysics, *J. Phys. Chem B* **2002**, *106*(5), 910–27.

[248] C. Hellriegel, E. Gratton, Real-time multi-parameter spectroscopy and localization in three-dimensional single-particle tracking, *J R Soc Interface* **2009**, *6 Suppl 1*, S3–14.

[249] J. Kirstein, B. Platschek, C. Jung, R. Brown, T. Bein, C. Brauchle, Exploration of nanostructured channel systems with single-molecule probes, *Nat Mater* **2007**, *6*(4), 303–10.

[250] H. Jiang, B. P. English, R. B. Hazan, P. Wu, B. Ovryn, Tracking surface glycans on live cancer cells with single-molecule sensitivity, *Angew. Chem. Int. Ed. Engl.* **2015**, *54*(6), 1765–9.

[251] K. Jaqaman, D. Loerke, M. Mettlen, H. Kuwata, S. Grinstein, S. L. Schmid, G. Danuser, Robust single-particle tracking in live-cell time-lapse sequences, *Nat Methods* **2008**, *5*(8), 695–702.

[252] N. Tarantino, J. Y. Tinevez, E. F. Crowell, B. Boisson, R. Henriques, M. Mhlanga, F. Agou, A. Israel, E. Laplantine, TNF and IL-1 exhibit distinct ubiquitin requirements for inducing NEMO-IKK supramolecular structures, *J. Cell Biol.* **2014**, *204*(2), 231–45.

[253] M. A. Rapsomaniki, P. Kotsantis, I. E. Symeonidou, N. N. Giakoumakis, S. Taraviras, Z. Lygerou, easyFRAP: an interactive, easy-to-use tool for qualitative and quantitative analysis of FRAP data, *Bioinformatics* **2012**, *28*(13), 1800–1.

[254] J. M. Bridger, N. Foeger, I. R. Kill, H. Herrmann, The nuclear lamina. Both a structural framework and a platform for genome organization, *FEBS J.* **2007**, *274*(6), 1354–61.

[255] D. A. Fletcher, R. D. Mullins, Cell mechanics and the cytoskeleton, *Nature* **2010**, *463*(7280), 485–92.

[256] J. Grove, D. J. Metcalf, A. E. Knight, S. T. Wavre-Shapton, T. Sun, E. D. Protonotarios, L. D. Griffin, J. Lippincott-Schwartz, M. Marsh, Flat clathrin lattices: stable features of the plasma membrane, *Mol. Biol. Cell* **2014**, *25*(22), 3581–94.

[257] M. R. Stachowiak, M. A. Smith, E. Blankman, L. M. Chapin, H. E. Balcioglu, S. Wang, M. C. Beckerle, B. O'Shaughnessy, A mechanical-biochemical feedback loop regulates remodeling in the actin cytoskeleton, *Proc. Natl. Acad. Sci. U. S. A.* **2014**, *111*(49), 17528–33.

[258] L. Guelen, L. Pagie, E. Brasset, W. Meuleman, M. B. Faza, W. Talhout, B. H. Eussen, A. de Klein, L. Wessels, W. de Laat, B. van Steensel, Domain organization of human chromosomes revealed by mapping of nuclear lamina interactions, *Nature* **2008**, *453*(7197), 948–51.

[259] J. Yang, W. S. Hlavacek, Scaffold-mediated nucleation of protein signaling complexes: elementary principles, *Math. Biosci.* **2011**, *232*(2), 164–73.

[260] J. W. Chu, G. A. Voth, Allostery of actin filaments: molecular dynamics simulations and coarse-grained analysis, *Proc. Natl. Acad. Sci. U. S. A.* **2005**, *102*(37), 13111–6.

[261] B. Fallqvist, A. Kulachenko, M. Kroon, Modelling of cross-linked actin networks - Influence of geometrical parameters and cross-link compliance, *J. Theor. Biol.* **2014**, *350*, 57–69.

[262] C. Zhang, C. Tian, F. Guo, Z. Liu, W. Jiang, C. Mao, DNA-directed three-dimensional protein organization, *Angew. Chem. Int. Ed. Engl.* **2012**, *51*(14), 3382–5.

[263] J. C. Sinclair, K. M. Davies, C. Venien-Bryan, M. E. Noble, Generation of protein lattices by fusing proteins with matching rotational symmetry, *Nat Nanotechnol* **2011**, *6*(9), 558–62.

[264] P. W. Rothemund, Folding DNA to create nanoscale shapes and patterns, *Nature* **2006**, *440*(7082), 297–302.

[265] H. Gradisar, S. Bozic, T. Doles, D. Vengust, I. Hafner-Bratkovic, A. Mertelj, B. Webb, A. Sali, S. Klavzar, R. Jerala, Design of a single-chain polypeptide tetrahedron assembled from coiled-coil segments, *Nat. Chem. Biol.* **2013**, *9*(6), 362–6.

[266] Y. Fujita, R. Furushima, H. Ohno, F. Sagawa, T. Inoue, Cell-surface receptor control that depends on the size of a synthetic equilateral-triangular RNA-protein complex, *Sci. Rep.* **2014**, *4*, 6422.

[267] R. Zidovetzki, I. Levitan, Use of cyclodextrins to manipulate plasma membrane cholesterol content: evidence, misconceptions and control strategies, *Biochim. Biophys. Acta* **2007**, *1768*(6), 1311–24.

[268] Y. Zhou, K. Yang, J. Cui, J. Y. Ye, C. X. Deng, Controlled permeation of cell membrane by single bubble acoustic cavitation, *J. Control. Release* **2012**, *157*(1), 103–11.

[269] A. Celedon, C. M. Hale, D. Wirtz, Magnetic manipulation of nanorods in the nucleus of living cells, *Biophys. J.* **2011**, *101*(8), 1880–6.

[270] H. Zhang, K. K. Liu, Optical tweezers for single cells, *J R Soc Interface* **2008**, *5*(24), 671–90.

[271] H. C. Kolb, M. G. Finn, K. B. Sharpless, Click Chemistry: Diverse Chemical Function from a Few Good Reactions, *Angew. Chem. Int. Ed. Engl.* **2001**, *40*(11), 2004–2021.

[272] J. A. Prescher, D. H. Dube, C. R. Bertozzi, Chemical remodelling of cell surfaces in living animals, *Nature* **2004**, *430*(7002), 873–7.

[273] D. H. Dube, J. A. Prescher, C. N. Quang, C. R. Bertozzi, Probing mucin-type O-linked glycosylation in living animals, *Proc. Natl. Acad. Sci. U. S. A.* **2006**, *103*(13), 4819–24.

[274] O. Livnah, E. A. Bayer, M. Wilchek, J. L. Sussman, Three-dimensional structures of avidin and the avidin-biotin complex, *Proc. Natl. Acad. Sci. U. S. A.* **1993**, *90*(11), 5076–80.

[275] A. T. Marttila, O. H. Laitinen, K. J. Airenne, T. Kulik, E. A. Bayer, M. Wilchek, M. S. Kulomaa, Recombinant NeutraLite avidin: a non-glycosylated, acidic mutant of chicken avidin that exhibits high affinity for biotin and low non-specific binding properties, *FEBS Lett.* **2000**, *467*(1), 31–6.

[276] M. Howarth, D. J. Chinnapen, K. Gerrow, P. C. Dorrestein, M. R. Grandy, N. L. Kelleher, A. El-Husseini, A. Y. Ting, A monovalent streptavidin with a single femtomolar biotin binding site, *Nat. Methods* **2006**, *3*(4), 267–73.

[277] P. C. Weber, D. H. Ohlendorf, J. J. Wendoloski, F. R. Salemme, Structural origins of high-affinity biotin binding to streptavidin, *Science* **1989**, *243*(4887), 85–8.

[278] A. Varki, Glycan-based interactions involving vertebrate sialic-acid-recognizing proteins, *Nature* **2007**, *446*(7139), 1023–9.

[279] T. Schmidt, G. J. Schutz, W. Baumgartner, H. J. Gruber, H. Schindler, Imaging of single molecule diffusion, *Proc. Natl. Acad. Sci. U. S. A.* **1996**, *93*(7), 2926–9.

[280] S. Rocha, J. A. Hutchison, K. Peneva, A. Herrmann, K. Mullen, M. Skjot, C. I. Jorgensen, A. Svendsen, F. C. De Schryver, J. Hofkens, H. Uji-i, Linking phospholipase mobility to activity by single-molecule wide-field microscopy, *Chemphyschem* **2009**, *10*(1), 151–61.

[281] F. Daumas, N. Destainville, C. Millot, A. Lopez, D. Dean, L. Salome, Confined diffusion without fences of a g-protein-coupled receptor as revealed by single particle tracking, *Biophys. J.* **2003**, *84*(1), 356–66.

[282] K. Jaqaman, S. Grinstein, Regulation from within: the cytoskeleton in transmembrane signaling, *Trends Cell Biol.* **2012**, *22*(10), 515–26.

[283] L. MÃ¶ckl, A. MÃ¼ller, C. BrÃ¤uchle, T. K. Lindhorst, Switching first contact: photocontrol of E. coli adhesion to human cells, *Chem. Commun. (Camb.)* **2016**, *52*(6), 1254–7.

[284] A. A. Khalili, M. R. Ahmad, A Review of Cell Adhesion Studies for Biomedical and Biological Applications, *Int. J. Mol. Sci.* **2015**, *16*(8), 18149–84.

[285] M. E. Taylor, K. Drickamer, Paradigms for glycan-binding receptors in cell adhesion, *Curr. Opin. Cell Biol.* **2007**, *19*(5), 572–7.

[286] C. R. Bertozzi, L. L. Kiessling, Chemical glycobiology, *Science* **2001**, *291*(5512), 2357–64.

[287] F. T. Liu, G. A. Rabinovich, Galectins as modulators of tumour progression, *Nat. Rev. Cancer* **2005**, *5*(1), 29–41.

[288] C. Xu, D. T. Ng, Glycosylation-directed quality control of protein folding, *Nat. Rev. Mol. Cell Biol.* **2015**.

[289] I. Ofek, D. Mirelman, N. Sharon, Adherence of Escherichia coli to human mucosal cells mediated by mannose receptors, *Nature* **1977**, *265*(5595), 623–5.

[290] K. Ohlsen, T. A. Oelschlaeger, J. Hacker, A. S. Khan, Carbohydrate receptors of bacterial adhesins: implications and reflections, *Top. Curr. Chem.* **2009**, *288*, 17–65.

[291] D. Ribet, P. Cossart, How bacterial pathogens colonize their hosts and invade deeper tissues, *Microbes Infect* **2015**, *17*(3), 173–83.

[292] K. E. Jones, N. G. Patel, M. A. Levy, A. Storeygard, D. Balk, J. L. Gittleman, P. Daszak, Global trends in emerging infectious diseases, *Nature* **2008**, *451*(7181), 990–3.

[293] A. Bernardi, J. Jimenez-Barbero, A. Casnati, C. De Castro, T. Darbre, F. Fieschi, J. Finne, H. Funken, K. E. Jaeger, M. Lahmann, T. K. Lindhorst, M. Marradi, P. Messner, A. Molinaro, P. V. Murphy, C. Nativi, S. Oscarson, S. Penades, F. Peri, R. J. Pieters, O. Renaudet, J. L. Reymond, B. Richichi, J. Rojo, F. Sansone, C. Schaffer, W. B. Turnbull, T. Velasco-Torrijos, S. Vidal, S. Vincent, T. Wennekes, H. Zuilhof, A. Imberty, Multivalent glycoconjugates as anti-pathogenic agents, *Chem. Soc. Rev.* **2013**, *42*(11), 4709–27.

[294] J. Lillington, S. Geibel, G. Waksman, Biogenesis and adhesion of type 1 and P pili, *Biochim. Biophys. Acta* **2014**, *1840*(9), 2783–93.

[295] V. Chandrasekaran, H. Jacob, F. Petersen, K. Kathirvel, F. Tuczek, T. K. Lindhorst, Synthesis and surface-spectroscopic characterization of photoisomerizable glyco-SAMs on Au(111), *Chemistry (Easton)* **2014**, *20*(28), 8744–52.

[296] G. Hartley, The Cis-form of Azobenzene, *Nature* **1937**, *140*, 281.

[297] J. Auernheimer, C. Dahmen, U. Hersel, A. Bausch, H. Kessler, Photoswitched cell adhesion on surfaces with RGD peptides, *J. Am. Chem. Soc.* **2005**, *127*(46), 16107–10.

[298] P. M. Mendes, Stimuli-responsive surfaces for bio-applications, *Chem. Soc. Rev.* **2008**, *37*(11), 2512–29.

[299] W. R. Browne, B. L. Feringa, Light switching of molecules on surfaces, *Annu. Rev. Phys. Chem.* **2009**, *60*, 407–28.

[300] M. M. Russew, S. Hecht, Photoswitches: from molecules to materials, *Adv. Mater.* **2010**, *22*(31), 3348–60.

[301] M. S. Siegrist, B. M. Swarts, D. M. Fox, S. A. Lim, C. R. Bertozzi, Illumination of growth, division and secretion by metabolic labeling of the bacterial cell surface, *FEMS Microbiol. Rev.* **2015**, *39*(2), 184–202.

[302] V. V. Rostovtsev, L. G. Green, V. V. Fokin, K. B. Sharpless, A stepwise huisgen cycloaddition process: copper(I)-catalyzed regioselective "ligation" of azides and terminal alkynes, *Angew. Chem. Int. Ed. Engl.* **2002**, *41*(14), 2596–9.

[303] M. Meldal, C. W. Tornoe, Cu-catalyzed azide-alkyne cycloaddition, *Chem. Rev.* **2008**, *108*(8), 2952–3015.

[304] M. Kleinert, T. Winkler, A. Terfort, T. K. Lindhorst, A modular approach for the construction and modification of glyco-SAMs utilizing 1,3-dipolar cycloaddition, *Org. Biomol. Chem.* **2008**, *6*(12), 2118–32.

[305] C. Grabosch, M. Kind, Y. Gies, F. SchweighÃ¶fer, A. Terfort, T. Lindhorst, A 'dual click' strategy for the fabrication of bioselective, glycosylated self-assembled monolayers as glycocalyx models, *Org. Biomol. Chem.* **2013**, *11*(24), 4006.

[306] G. Gustafson, C. Baldino, M. O'Donnell, A. Sheldon, R. Tarsa, C. Verni, D. Coffen, Incorporation of carbohydrates and peptides into large triazine-based screening libraries using automated parallel synthesis, *Tetrahedron* **1998**, *54*(16), 4051–65.

[307] V. Chandrasekaran, E. Johannes, H. Kobarg, F. D. Sonnichsen, T. K. Lindhorst, Synthesis and photochromic properties of configurationally varied azobenzene glycosides, *ChemistryOpen* **2014**, *3*(3), 99–108.

[308] G. Mantovani, V. Ladmiral, L. Tao, D. M. Haddleton, One-pot tandem living radical polymerisation-Huisgens cycloaddition process ("click") catalysed by N-alkyl-2-pyridylmethanimine/Cu(I)Br complexes, *Chem. Commun. (Camb.)* **2005**, *16*, 2089–91.

[309] G. Estrada-Gutierrez, N. Gomez-Lopez, V. Zaga-Clavellina, S. Giono-Cerezo, A. Espejel-Nunez, M. A. Gonzalez-Jimenez, S. Espino y Sosa, D. M. Olson, F. Vadillo-Ortega, Interaction between pathogenic bacteria and intrauterine leukocytes triggers alternative molecular signaling cascades leading to labor in women, *Infect. Immun.* **2010**, *78*(11), 4792–9.

[310] D. L. LaRock, A. Chaudhary, S. I. Miller, Salmonellae interactions with host processes, *Nat. Rev. Microbiol.* **2015**, *13*(4), 191–205.

[311] A. Persat, C. D. Nadell, M. K. Kim, F. Ingremeau, A. Siryaporn, K. Drescher, N. S. Wingreen, B. L. Bassler, Z. Gitai, H. A. Stone, The mechanical world of bacteria, *Cell* **2015**, *161*(5), 988–97.

[312] M. Totsika, D. G. Moriel, A. Idris, B. A. Rogers, D. J. Wurpel, M. D. Phan, D. L. Paterson, M. A. Schembri, Uropathogenic Escherichia coli mediated urinary tract infection, *Curr. Drug Targets* **2012**, *13*(11), 1386–99.

[313] T. R. Costa, C. Felisberto-Rodrigues, A. Meir, M. S. Prevost, A. Redzej, M. Trokter, G. Waksman, Secretion systems in Gram-negative bacteria: structural and mechanistic insights, *Nat. Rev. Microbiol.* **2015**, *13*(6), 343–59.

[314] A. J. Mathers, G. Peirano, J. D. Pitout, The role of epidemic resistance plasmids and international high-risk clones in the spread of multidrug-resistant Enterobacteriaceae, *Clin. Microbiol. Rev.* **2015**, *28*(3), 565–91.

[315] R. J. Pieters, Carbohydrate mediated bacterial adhesion, *Adv. Exp. Med. Biol.* **2011**, *715*, 227–40.

[316] M. Otto, Physical stress and bacterial colonization, *FEMS Microbiol. Rev.* **2014**, *38*(6), 1250–70.

[317] S. Kleeb, L. Pang, K. Mayer, D. Eris, A. Sigl, R. C. Preston, P. Zihlmann, T. Sharpe, R. P. Jakob, D. Abgottspon, A. S. Hutter, M. Scharenberg, X. Jiang, G. Navarra, S. Rabbani, M. Smiesko, N. Ludin, J. Bezencon, O. Schwardt, T. Maier, B. Ernst, FimH antagonists: bioisosteres to improve the in vitro and in vivo PK/PD profile, *J. Med. Chem.* **2015**, *58*(5), 2221–39.

[318] M. Hartmann, H. Papavlassopoulos, V. Chandrasekaran, C. Grabosch, F. Beiroth, T. K. Lindhorst, C. Rohl, Inhibition of bacterial adhesion to live human cells: activity and cytotoxicity of synthetic mannosides, *FEBS Lett.* **2012**, *586*(10), 1459–65.

[319] J. Zakrisson, K. Wiklund, O. Axner, M. Andersson, The shaft of the type 1 fimbriae regulates an external force to match the FimH catch bond, *Biophys. J.* **2013**, *104*(10), 2137–48.

[320] V. B. Rodriguez, B. A. Kidd, G. Interlandi, V. Tchesnokova, E. V. Sokurenko, W. E. Thomas, Allosteric coupling in the bacterial adhesive protein FimH, *J. Biol. Chem.* **2013**, *288*(33), 24128–39.

[321] J. Claes, L. Liesenborghs, M. Lox, P. Verhamme, T. Vanassche, M. Peetermans, In Vitro and In Vivo Model to Study Bacterial Adhesion to the Vessel Wall Under Flow Conditions, *J Vis Exp* **2015**, *100*, e52862.

[322] J. Meinders, H. van der Mei, H. Busscher, Deposition Efficiency and Reversibility of Bacterial Adhesion under Flow, *Journal of Colloid and Interface Sciences* **1995**, *176*, 329–42.

[323] J. Claes, T. Vanassche, M. Peetermans, L. Liesenborghs, C. Vandenbriele, K. Vanhoorelbeke, D. Missiakas, O. Schneewind, M. F. Hoylaerts, R. Heying, P. Verhamme, Adhesion of Staphylococcus aureus to the vessel wall under flow is mediated by von Willebrand factor-binding protein, *Blood* **2014**, *124*(10), 1669–76.

[324] S. E. Grubb, C. Murdoch, P. E. Sudbery, S. P. Saville, J. L. Lopez-Ribot, M. H. Thornhill, Adhesion of Candida albicans to endothelial cells under physiological conditions of flow, *Infect. Immun.* **2009**, *77*(9), 3872–8.

[325] J. D. Patel, M. Ebert, K. Stokes, R. Ward, J. M. Anderson, Inhibition of bacterial and leukocyte adhesion under shear stress conditions by material surface chemistry, *J. Biomater. Sci. Polym. Ed.* **2003**, *14*(3), 279–95.

[326] C. Fessele, T. K. Lindhorst, Effect of Aminophenyl and Aminothiahexyl alpha-D-Glycosides of the Manno-, Gluco-, and Galacto-Series on Type 1 Fimbriae-Mediated Adhesion of Escherichia coli, *Biology (Basel)* **2013**, *2*(3), 1135–49.

[327] R. Roy, F. Trooper, T. Morrison, J. Boratynski, Syntheses and transformations of glycohydrolase substrates into protein conjugates based on Michael additions, *J. Chem. Soc.* **1991**, *7*, 538–8.

[328] C. Grabosch, M. Hartmann, J. Schmidt-Lassen, T. K. Lindhorst, Squaric acid monoamide mannosides as ligands for the bacterial lectin FimH: covalent inhibition or not?, *ChemBioChem* **2011**, *12*(7), 1066–74.

[329] O. Sperling, A. Fuchs, T. K. Lindhorst, Evaluation of the carbohydrate recognition domain of the bacterial adhesin FimH: Design, synthesis and binding properties of mannoside ligands, *Org. Biomol. Chem.* **2006**, *4*(21), 3913–22.

[330] M. Virji, Ins and outs of microbial adhesion, *Top. Curr. Chem.* **2009**, *288*, 139–56.

[331] Y. Kikuchi, H. Toi, Y. Aoyama, Geometrical Requirement for the Intracomplex Sugar-Sugar Interaction, *Bull. Chem. Soc. Jpn.* **1993**, *66*, 1856–8.

[332] M. Dubber, T. K. Lindhorst, Syntheses of octopus glycosides: core molecules for the construction of glycoclusters and carbohydrate-centered dendrimers, *Carbohydr. Res.* **1998**, *310*, 35–41.

[333] K. Brunner, J. Harder, T. Halbach, J. Willibald, F. Spada, F. Gnerlich, K. Sparrer, A. Beil, L. Möckl, C. Bräuchle, K. K. Conzelmann, T. Carell, Cell-penetrating and neurotargeting dendritic siRNA nanostructures, *Angew. Chem. Int. Ed. Engl.* **2015**, *54*(6), 1946–9.

[334] A. Z. Fire, Gene silencing by double-stranded RNA (Nobel Lecture), *Angew. Chem. Int. Ed. Engl.* **2007**, *46*(37), 6966–84.

[335] C. C. Mello, Return to the RNAi world: rethinking gene expression and evolution (Nobel Lecture), *Angew. Chem. Int. Ed. Engl.* **2007**, *46*(37), 6985–94.

[336] H. Yin, R. L. Kanasty, A. A. Eltoukhy, A. J. Vegas, J. R. Dorkin, D. G. Anderson, Non-viral vectors for gene-based therapy, *Nat. Rev. Genet.* **2014**, *15*(8), 541–55.

[337] H. Lv, S. Zhang, B. Wang, S. Cui, J. Yan, Toxicity of cationic lipids and cationic polymers in gene delivery, *J. Control. Release* **2006**, *114*(1), 100–9.

[338] Z. Ma, J. Li, F. He, A. Wilson, B. Pitt, S. Li, Cationic lipids enhance siRNA-mediated interferon response in mice, *Biochem. Biophys. Res. Commun.* **2005**, *330*(3), 755–9.

[339] S. Akhtar, I. F. Benter, Nonviral delivery of synthetic siRNAs in vivo, *J. Clin. Invest.* **2007**, *117*(12), 3623–32.

[340] J. Godfray, P. Estibeiro, The potential of antisense as a CNS therapeutic, *Expert Opin. Ther. Targets* **2003**, *7*(3), 363–76.

[341] I. Posadas, F. J. Guerra, V. Cena, Nonviral vectors for the delivery of small interfering RNAs to the CNS, *Nanomedicine (Lond)* **2010**, *5*(8), 1219–36.

[342] A. O'Mahony, B. Gofinho, J. Ogier, M. Dvocelle, R. Darcy, J. Cryan, C. O'Driscoll, Click-Modified Cyclodextrins as Nonviral Vectors for Neuronal siRNA Delivery, *ACS Chem. Neurosci.* **2012**, *3*(10), 744–52.

[343] J. Willibald, J. Harder, K. Sparrer, K. K. Conzelmann, T. Carell, Click-modified anandamide siRNA enables delivery and gene silencing in neuronal and immune cells, *J. Am. Chem. Soc.* **2012**, *134*(30), 12330–3.

[344] E. Paredes, S. R. Das, Click chemistry for rapid labeling and ligation of RNA, *ChemBioChem* **2011**, *12*(1), 125–31.

[345] J. Gierlich, G. Burley, P. Gramlich, D. Hammond, T. Carell, Click Chemistry as a Reliable Method for the High-Density Postsynthetic Functionalization of Alkyne-Modified DNA, *Org. Lett.* **2006**, *8*(17), 3639–42.

[346] P. M. Gramlich, C. T. Wirges, A. Manetto, T. Carell, Postsynthetic DNA modification through the copper-catalyzed azide-alkyne cycloaddition reaction, *Angew. Chem. Int. Ed. Engl.* **2008**, *47*(44), 8350–8.

[347] T. Yamada, C. Peng, S. Matsuda, H. Addepalli, N. Jayaprakash, M. Alam, K. Mills, M. Maier, K. Charisse, M. Sekine, M. Manoharan, K. Rajeev, Versatile Site-Specific Conjugation of Small Molecules to siRNA Using Click Chemistry, *J. Org. Chem.* **2011**, *76*(5), 1198–211.

[348] E. Paredes, S. R. Das, Optimization of acetonitrile co-solvent and copper stoichiometry for pseudo-ligandless click chemistry with nucleic acids, *Bioorg. Med. Chem. Lett.* **2012**, *22*(16), 5313–6.

[349] S. E. Averick, E. Paredes, S. K. Dey, K. M. Snyder, N. Tapinos, K. Matyjaszewski, S. R. Das, Autotransfecting short interfering RNA through facile covalent polymer escorts, *J. Am. Chem. Soc.* **2013**, *135*(34), 12508–11.

[350] M. Oishi, Y. Nagasaki, K. Itaka, N. Nishiyama, K. Kataoka, Lactosylated poly(ethylene glycol)-siRNA conjugate through acid-labile beta-thiopropionate linkage to construct pH-sensitive polyion complex micelles achieving enhanced gene silencing in hepatoma cells, *J. Am. Chem. Soc.* **2005**, *127*(6), 1624–5.

[351] Y. Wang, S. Juranek, H. Li, G. Sheng, G. S. Wardle, T. Tuschl, D. J. Patel, Nucleation, propagation and cleavage of target RNAs in Ago silencing complexes, *Nature* **2009**, *461*(7265), 754–61.

[352] F. Czauderna, M. Fechtner, S. Dames, H. Aygun, A. Klippel, G. J. Pronk, K. Giese, J. Kaufmann, Structural variations and stabilising modifications of synthetic siRNAs in mammalian cells, *Nucleic Acids Res.* **2003**, *31*(11), 2705–16.

[353] Y. L. Chiu, T. M. Rana, RNAi in human cells: basic structural and functional features of small interfering RNA, *Mol. Cell* **2002**, *10*(3), 549–61.

[354] J. P. Shaw, K. Kent, J. Bird, J. Fishback, B. Froehler, Modified deoxyoligonucleotides stable to exonuclease degradation in serum, *Nucleic Acids Res.* **1991**, *19*(4), 747–50.

[355] C. Richardson, Influence of Glucosylation of Deoxyribonucleic Acid on Hydrolysis by Deoxyribonucleases of Escherichia coli, *J. Biol. Chem.* **1966**, *241*, 2084–92.

[356] J. M. Layzer, A. P. McCaffrey, A. K. Tanner, Z. Huang, M. A. Kay, B. A. Sullenger, In vivo activity of nuclease-resistant siRNAs, *RNA* **2004**, *10*(5), 766–71.

[357] Y. Ikeda, D. Kubota, Y. Nagasaki, Simple solid-phase synthesis and biological properties of carbohydrate-oligonucleotide conjugates modified at the 3'-terminus, *Bioconjug. Chem.* **2010**, *21*(9), 1685–90.

[358] H. Bagci, A. G. Fisher, DNA demethylation in pluripotency and reprogramming: the role of tet proteins and cell division, *Cell Stem Cell* **2013**, *13*(3), 265–9.

[359] S. Ito, L. Shen, Q. Dai, S. C. Wu, L. B. Collins, J. A. Swenberg, C. He, Y. Zhang, Tet proteins can convert 5-methylcytosine to 5-formylcytosine and 5-carboxylcytosine, *Science* **2011**, *333*(6047), 1300–3.

[360] T. Pfaffeneder, B. Hackner, M. Truss, M. Munzel, M. Muller, C. A. Deiml, C. Hagemeier, T. Carell, The discovery of 5-formylcytosine in embryonic stem cell DNA, *Angew. Chem. Int. Ed. Engl.* **2011**, *50*(31), 7008–12.

[361] A. Nath, K. L. Tyler, Novel approaches and challenges to treatment of central nervous system viral infections, *Ann. Neurol.* **2013**, *74*(3), 412–22.

[362] M. J. Schnell, J. P. McGettigan, C. Wirblich, A. Papaneri, The cell biology of rabies virus: using stealth to reach the brain, *Nat. Rev. Microbiol.* **2010**, *8*(1), 51–61.

[363] P. K. Gupta, A. A. Sonwane, N. K. Singh, C. D. Meshram, S. S. Dahiya, S. S. Pawar, S. P. Gupta, V. K. Chaturvedi, M. Saini, Intracerebral delivery of small interfering RNAs (siRNAs) using adenoviral vector protects mice against lethal peripheral rabies challenge, *Virus Res.* **2012**, *163*(1), 11–8.

[364] Y. J. Yang, P. S. Zhao, T. Zhang, H. L. Wang, H. R. Liang, L. L. Zhao, H. X. Wu, T. C. Wang, S. T. Yang, X. Z. Xia, Small interfering RNAs targeting the rabies virus nucleoprotein gene, *Virus Res.* **2012**, *169*(1), 169–74.

[365] G. Castel, M. Chteoui, G. Caignard, C. Prehaud, S. Mehouas, E. Real, C. Jallet, Y. Jacob, R. W. Ruigrok, N. Tordo, Peptides that mimic the amino-terminal end of the rabies virus phosphoprotein have antiviral activity, *J. Virol.* **2009**, *83*(20), 10808–20.

[366] E. Real, J. C. Rain, V. Battaglia, C. Jallet, P. Perrin, N. Tordo, P. Chrisment, J. D'Alayer, P. Legrain, Y. Jacob, Antiviral drug discovery strategy using combinatorial libraries of structurally constrained peptides, *J. Virol.* **2004**, *78*(14), 7410–7.

[367] P. E. Brandao, J. G. Castilho, W. Fahl, J. Carnieli, P., N. Oliveira Rde, C. I. Macedo, M. L. Carrieri, I. Kotait, Short-interfering RNAs as antivirals against rabies, *Braz. J. Infect. Dis.* **2007**, *11*(2), 224–5.

[368] K. Brzozka, S. Finke, K. K. Conzelmann, Identification of the rabies virus alpha/beta interferon antagonist: phosphoprotein P interferes with phosphorylation of interferon regulatory factor 3, *J. Virol.* **2005**, *79*(12), 7673–81.

[369] M. Rieder, K. Brzozka, C. K. Pfaller, J. H. Cox, L. Stitz, K. K. Conzelmann, Genetic dissection of interferon-antagonistic functions of rabies virus phosphoprotein: inhibition of interferon regulatory factor 3 activation is important for pathogenicity, *J. Virol.* **2011**, *85*(2), 842–52.

[370] X. Liu, J. Zhou, T. Yu, C. Chen, Q. Cheng, K. Sengupta, Y. Huang, H. Li, C. Liu, Y. Wang, P. Posocco, M. Wang, Q. Cui, S. Giorgio, M. Fermeglia, F. Qu, S. Pricl, Y. Shi, Z. Liang, P. Rocchi, J. J. Rossi, L. Peng, Adaptive amphiphilic dendrimer-based nanoassemblies as robust and versatile siRNA delivery systems, *Angew. Chem. Int. Ed. Engl.* **2014**, *53*(44), 11822–7.

Appendix

Membrane Protein Glycosylation and its Relevance in Cell Biology

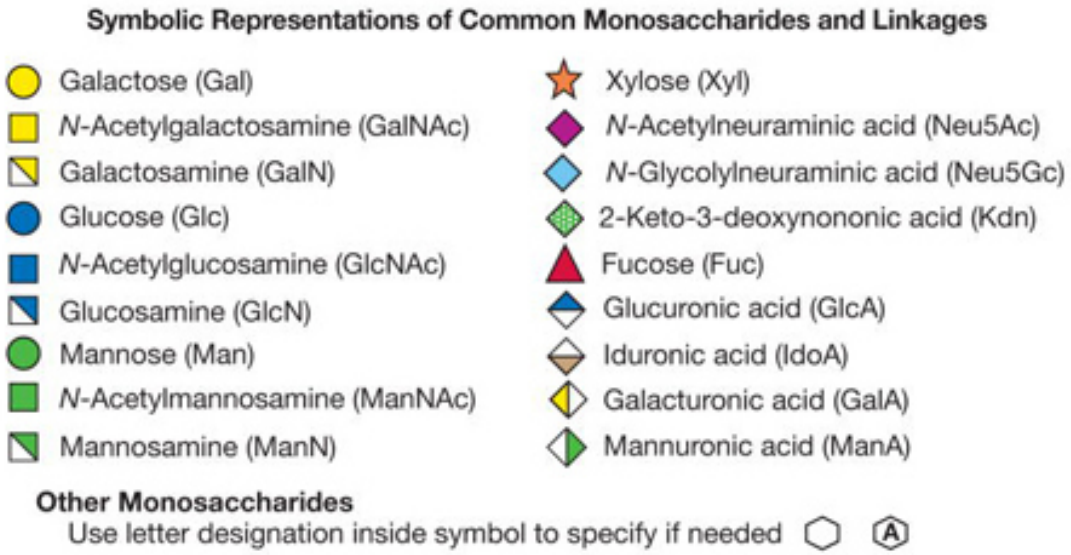

Figure 12.1: Key for sugar symbols.

Glycosylation Influences Spatiotemporal Membrane Protein Dynamics

ESI to "Microdomain Formation Controls Spatiotemporal Dynamics of Cell-Surface Glycoproteins" by Leonhard Möckl, Andrea K. Horst, Katharina Kolbe, Thisbe K. Lindhorst, and Christoph Bräuchle; *ChemBioChem* 2015

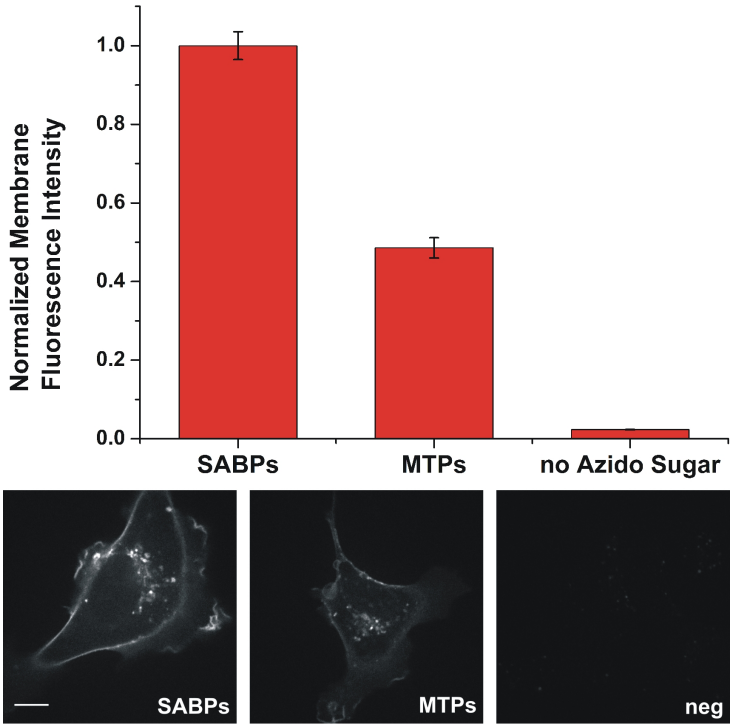

Figure 12.2: Specificity of the labeling reaction.
In presence of Ac_4ManNAz or Ac_4GalNAz, sialic acid-bearing proteins (SABPs, left column) or mucin-type proteins (MTPs, middle column) on the cell membrane are fluorescently labeled by incubation with the AlexaFluor647-cyclooctyne-conjugate (DIBO647). In contrast, the lack of an azido sugar leads to no labeling (right column). This is nicely displayed in the fluorescence images (contrast settings are equal for all images). Note that the fluorescent endosomes inside the cell in the left and middle image are caused by internalization of already labeled glycans during incubation with the labeling solution and not by uptake of the DIBO647 itself since the negative control does not exhibit any significant intracellular fluorescence. Scale bar=10 μm.

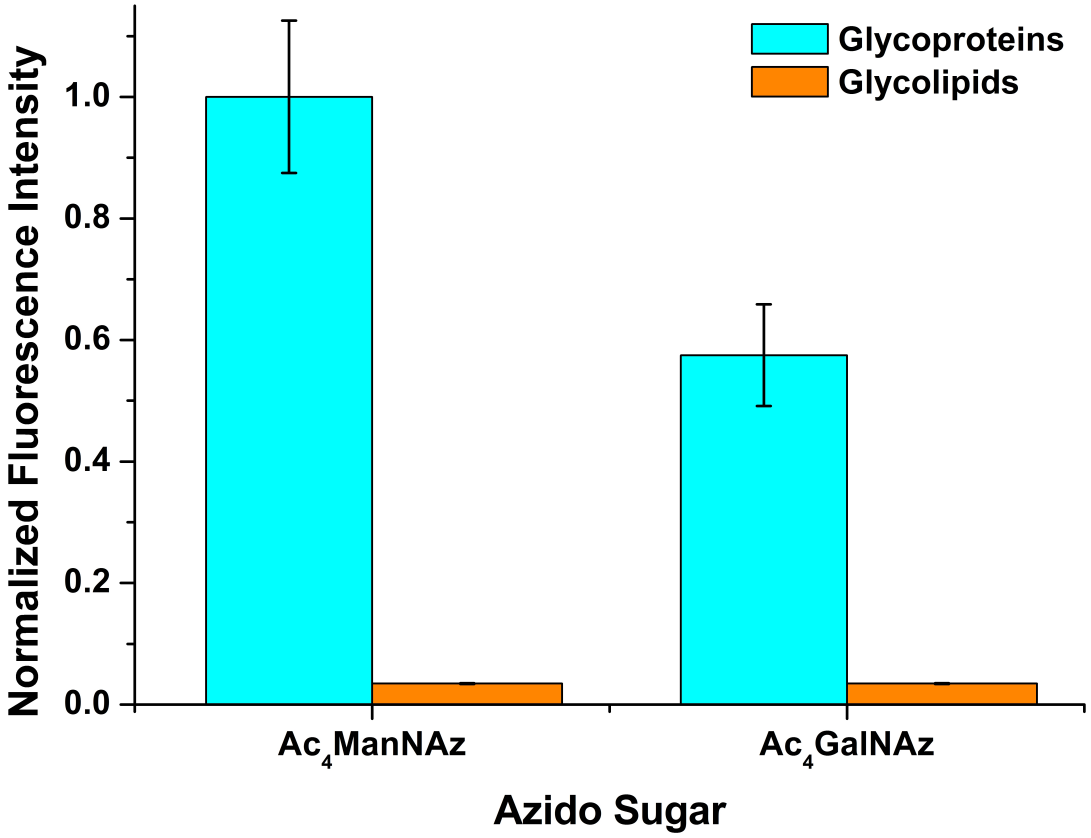

Figure 12.3: Identity of the labeled species.
To check if the metabolic labeling approach targets predominantly glycoproteins and not glycolipids, we seeded $1.5 \cdot 10^6$ cells in a six-well plate and cultivated them as described in presence of 50 µM of the indicated azido sugar for two days. Then, we labeled them for 45 minutes with 35 µM DIBO647 and isolated proteins and lipids using the Mem-PER- and the Lipid Extraction-kit (Thermo Scientific, Waltham, Massachusetts, USA/Sigma Aldrich, St. Louis, Missouri, USA). The isolated species were solubilized in equal amounts of solvents. 20 µL were transferred onto a microscope slide and the fluoresence was quantified using a Zeiss spinning disk confocal microscope. Clearly, only glycoproteins (cyan) are labeled whereas no significant labeling of glycolipids (orange) was detected. The experiments were carried out in triplicate. Errors are given as SEM.

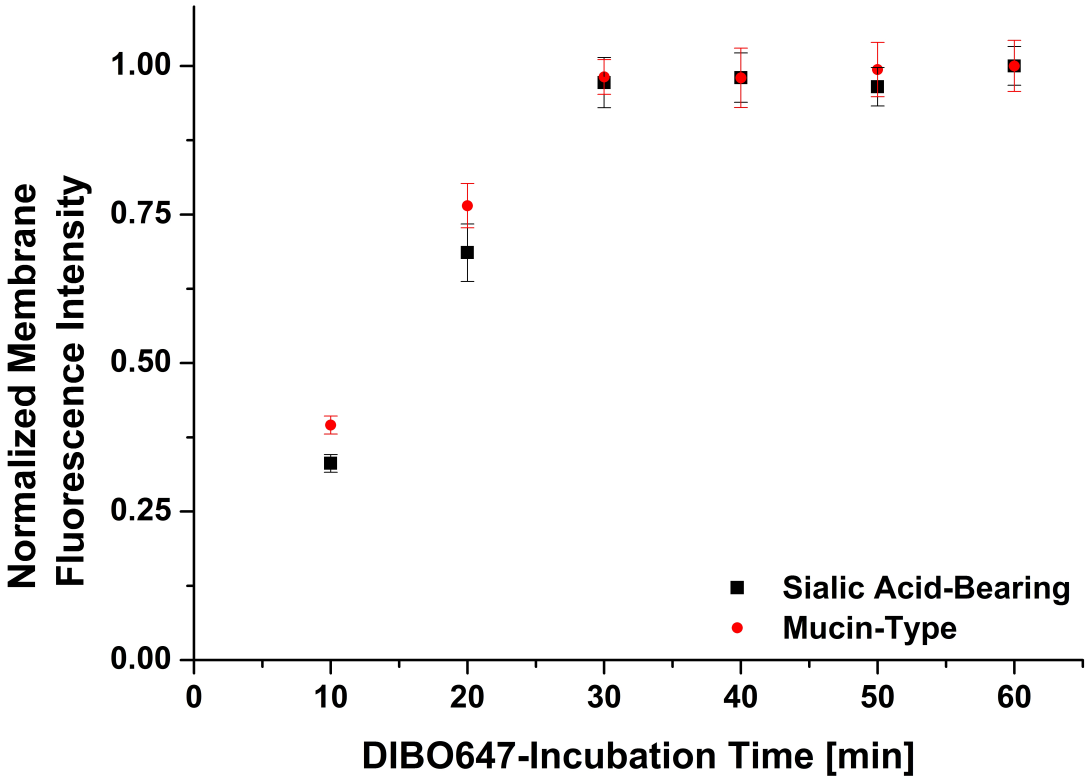

Figure 12.4: Minimum labeling duration.
To ensure that all available azide groups on the cell membrane after incubation with the respective azido sugar are addressed by the labeling reagent DIBO647, we varied the incubation time as indicated. It is clearly visible that after 30 minutes no further increase in membrane fluorescence intensity occurs. n=30, errors are given as SEM.

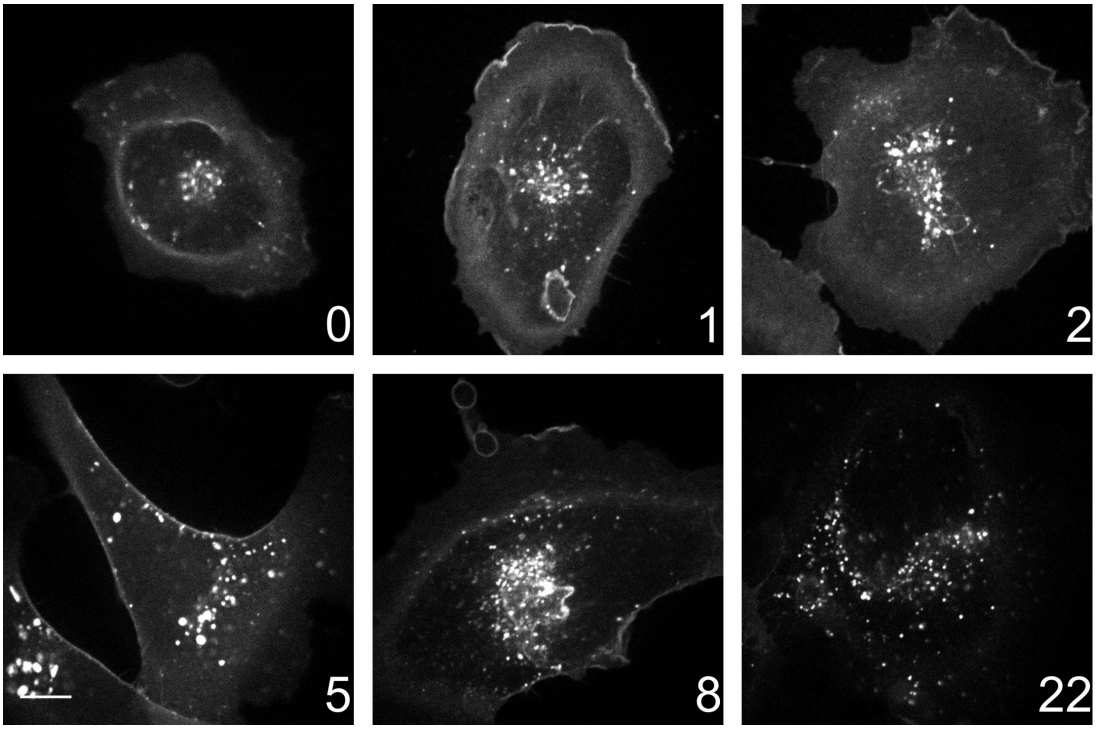

Figure 12.5: Glycans are localized in endosomes after internalization.
The depicted cells were incubated with Ac_4ManNAz to incorporate an azide group into SABPs and incubated for the indicated time periods (hours) after labeling with DIBO647. During this time, fluorescent SABPs are internalized into the cell. The decrease in membrane fluorescence and the increasingly bright, perinuclear fluorescence of endosomes is obvious. Scale bar=10 μm.

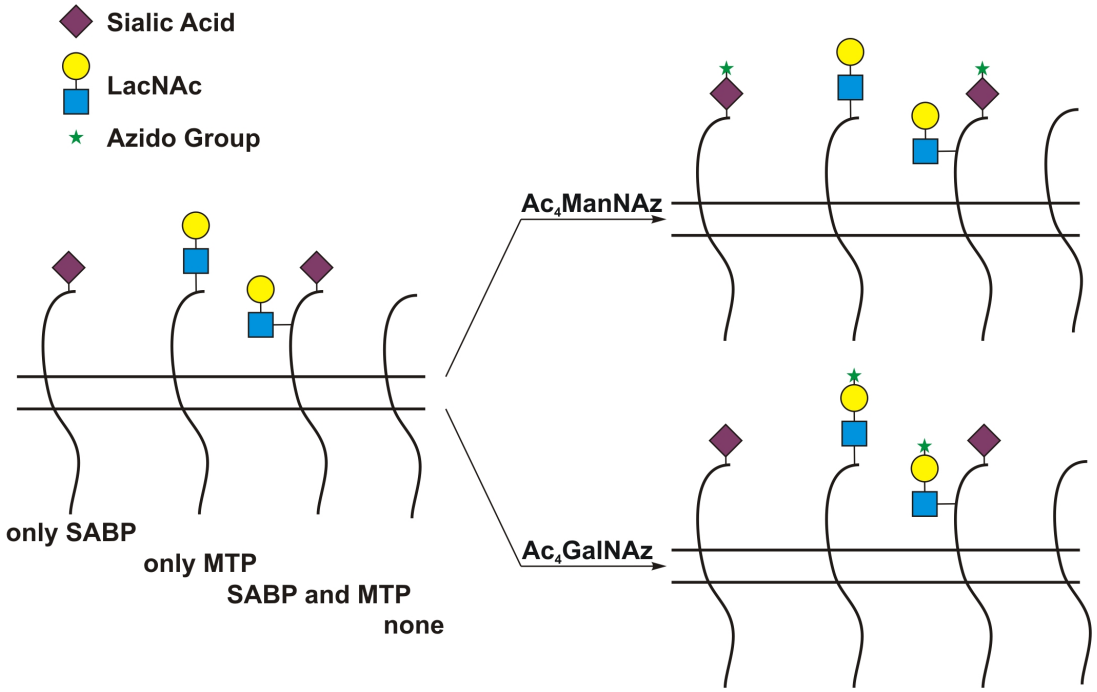

Figure 12.6: Classes of labeled glycans.
Four principle types of proteins are depicted as relevant for our study: SABPs, MTPs (carrying sialic acids or LacNAc, respectively), SABPs and MTPs (carrying both sialic acid and LacNAc), or none of the two classes (carrying no or different glycosylation). Metabolic labeling with Ac_4ManNAz targets SABPs whereas metabolic labeling with Ac_4GalNAz targets MTPs. The possible overlap between SABPs and MTPs has an important consequence: One may detect and MTP-specific effect while visualizing SABPs and vice versa. However, we were able to show that the two classes can be very well separated using metabolic labeling and fluorescence visualization, indicating that the overlap is not dominant. Glycosylation pattern simplified, other sugars are omitted for clarity.

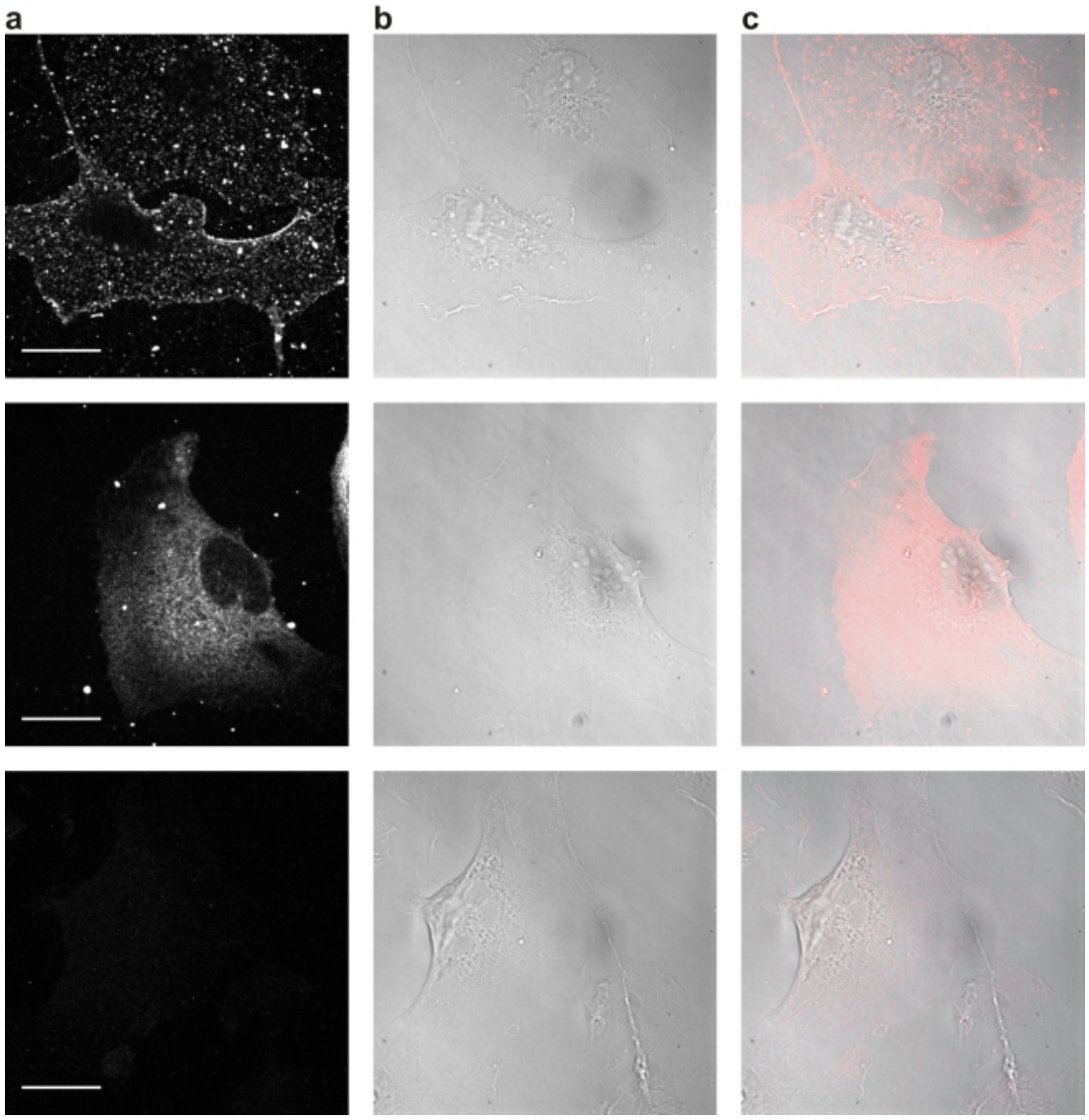

Figure 12.7: Galectin-1 and -3 are present on the membrane of HMEC-1.
(a) Fluorescence images of immunostaining against galectin-1 (top), galectin-3 (middle), and isocontrol (bottom). (b) Differential interference contrast images corresponding to a). (c) Merge of a) and b) Scale bar = 25 μm, contrast settings identical for all fluorescence images.

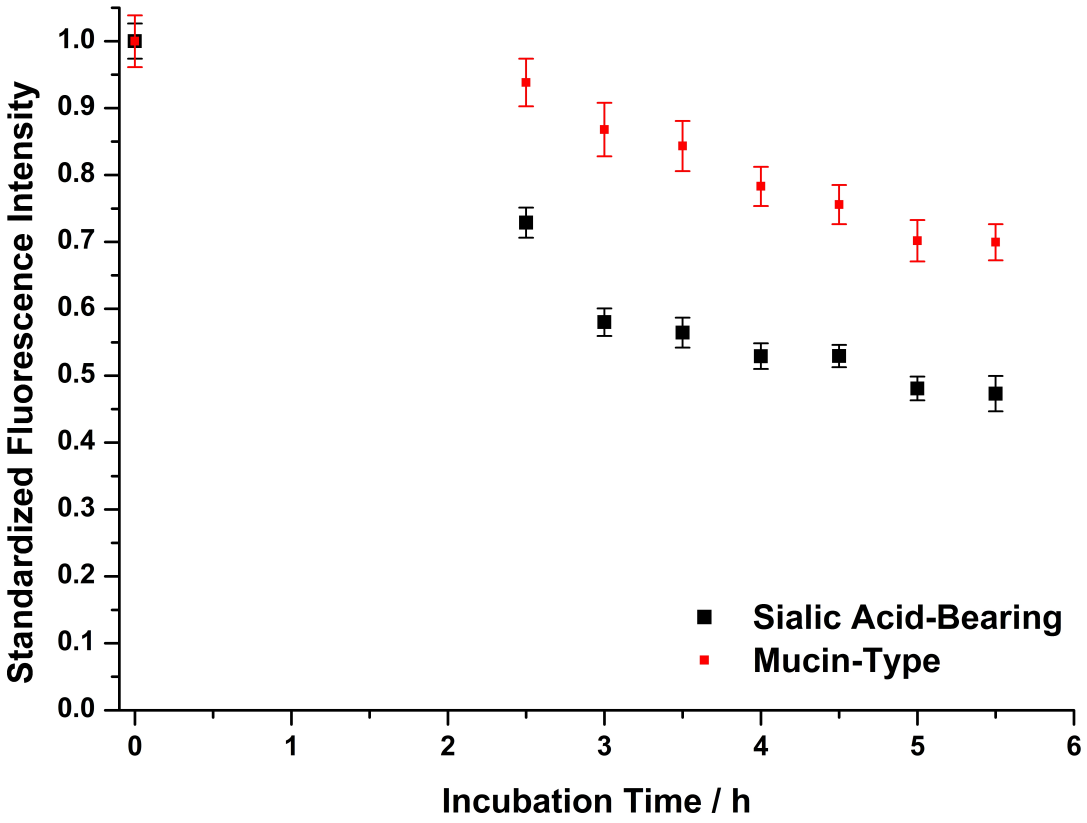

Figure 12.8: Internalization of MTPs and SABPs into untreated HMEC-1.
Decrease in membrane fluorescence of HMEC-1 through internalization of fluorescently labeled sialic acid-bearing and mucin-type proteins. Note that within 5.5 h the membrane fluorescence decreases strongly in both cases. However, SABPs show faster decrease owing to less involvement in galectin-lattice formation, thus corroborating the data on spatial mobility. Errors=SEM, n=26-30, black=SABPs, red=MTPs.

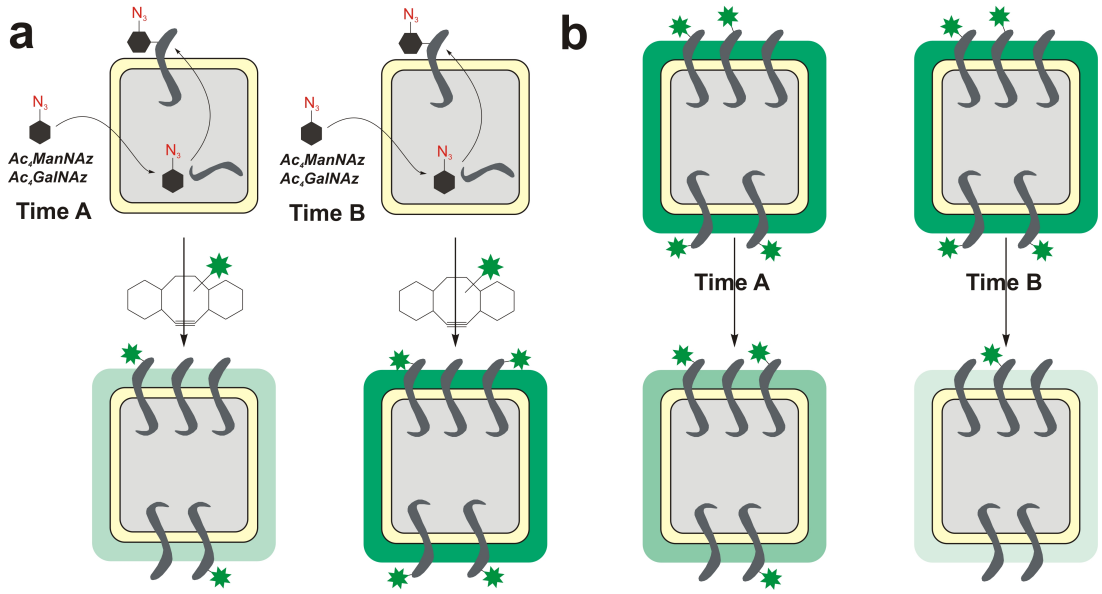

Figure 12.9: Experimental design to investigate temporal dynamics of membrane proteins. (a) To measure the incorporation of glycans into the cell membrane, HMEC-1 were incubated with Ac_4ManNAz or Ac_4GalNAz, respectively, which are internalized and metabolized in glycan biosynthesis. After an incubation time, the azido group appears in cell surface glycoproteins. There, it can be bioorthogonally reacted with DIBO647, covalently linking a fluorescent dye to membrane glycoproteins. As with increasing incubation time (Time B) the number of azido groups on the cell surface increases, membrane fluorescence is enhanced accordingly. (b) Correspondingly, after incubation with Ac_4ManNAz or Ac_4GalNAz and subsequent fluorescent labeling, the decrease in membrane fluorescence is a measure for the internalization of membrane glycoproteins into the cell.

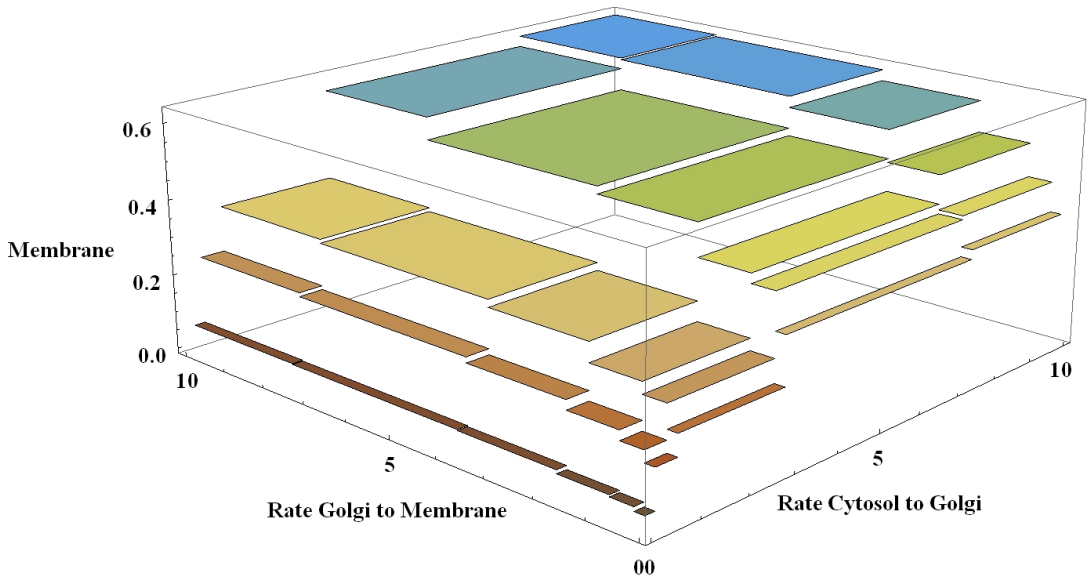

Figure 12.10: Final metabolite concentration on the cell membrane in dependence of rates from cytosol to Golgi apparatus and Golgi apparatus to membrane.
All rates occurring inFigure 6.7 are set to 1 except for the two rates that transport metabolites from the cytosol via the Golgi apparatus to the membrane. If these rates increase, the final metabolite concentration on the membrane rises, too. However, this is not physiological since the membrane cannot arbitrarily increase its capacity (cf. Figure 12.11).

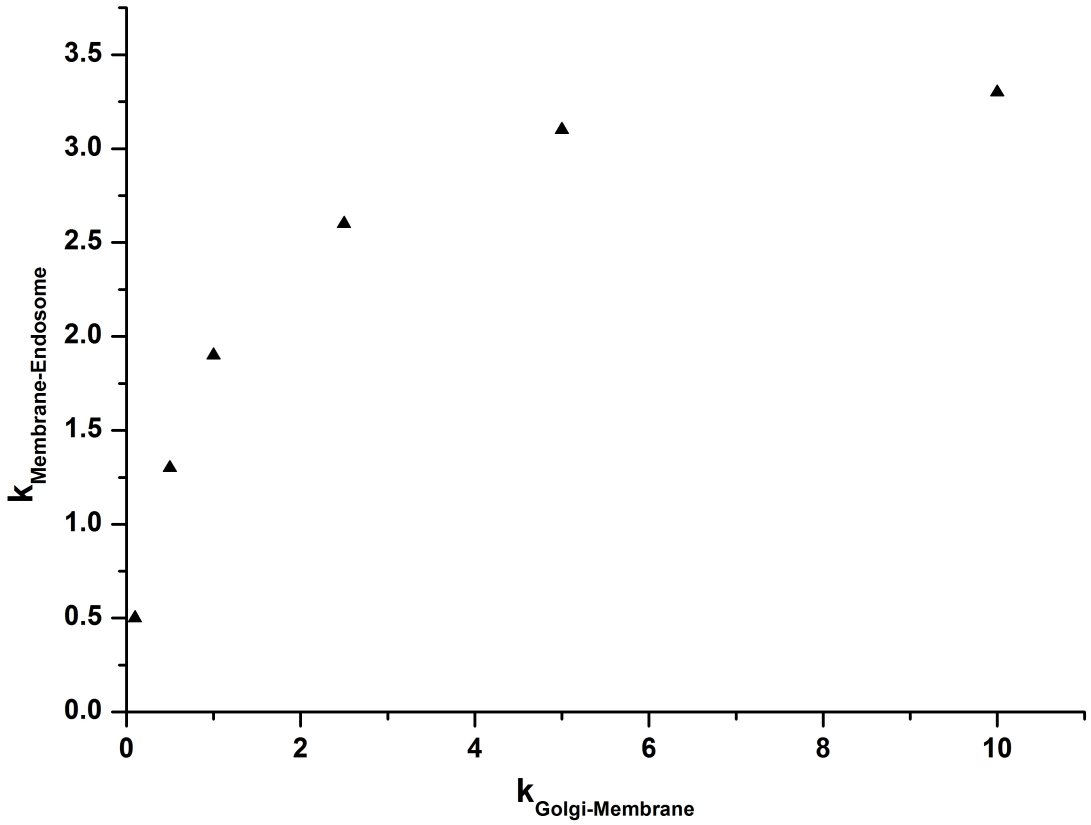

Figure 12.11: Mutual dependence of $k_{Golgi\text{-}Membrane}$ and $k_{Membrane\text{-}Endosome}$.
If the rate Golgi apparatus-membrane increases and the final membrane metabolite concentration should stay constant, the rate membrane-endosome must increase accordingly (all other rates are kept constant). For very high values of $k_{Golgi\text{-}Membrane}$, the rate $k_{Membrane\text{-}Endosome}$ does not change much because in this region an increase in the rate $k_{Golgi\text{-}Membrane}$ no longer increases the final membrane metabolite concentration: In this case, every metabolite that arrives at the Golgi apparatus is almost immediately transferred to the membrane.

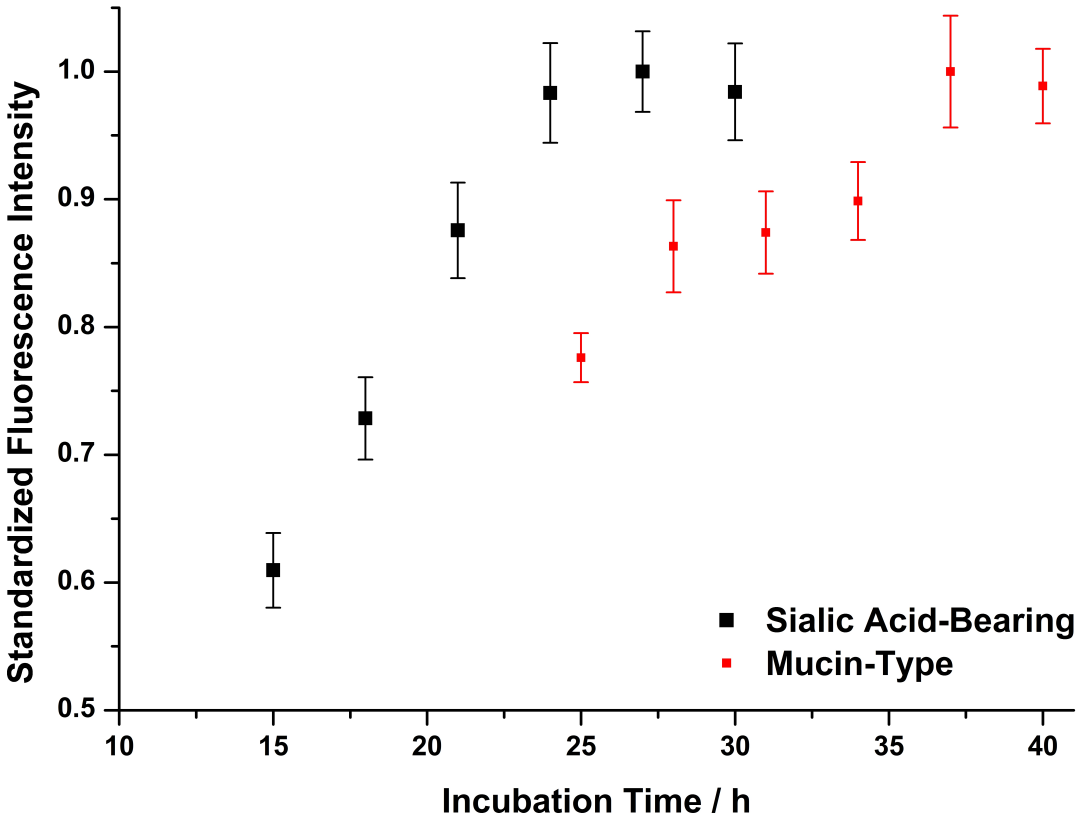

Figure 12.12: Incorporation of MTPs and SABPs into the membrane of untreated HMEC-1. Cells were treated for the indicated incubation time with Ac_4ManNAz or Ac_4GalNAz, addressed by DIBO647, and fixed. Membrane fluorescence was quantified. It is clearly visible that the steady state (every azide-bearing membrane protein is replaced by another azide-bearing membrane protein, net change zero) is earlier reached for SABPs than for MTPs. This development was also obtained using the above described model (cf. Figure 6.7 and Figure 12.13).

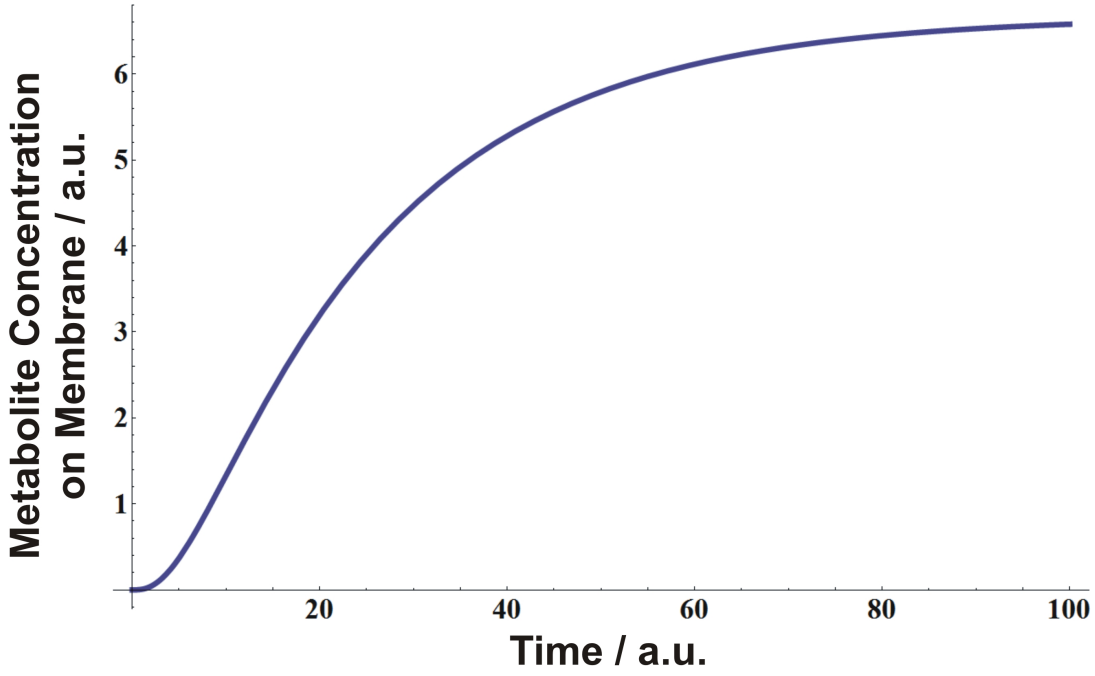

Figure 12.13: Development of membrane metabolite concentration.
Note the sigmoidal development and the steady state reached. Rates: All rates are set to 0.1 with the exception of $k_{\text{Extracellular Space-Cytosol}}=1$ and $k_{\text{Cytosol-Golgi apparatus}}=0.5$

Artificial, Tunable Interconnection of Membrane Glycans

ESI to "Artificial Formation and Tuning of Glycoprotein Networks on Live Cell Membranes: A Single-Molecule Tracking Study" by Leonhard Möckl, Thisbe K. Lindhorst, and Christoph Bräuchle; *ChemPhysChem* 2015

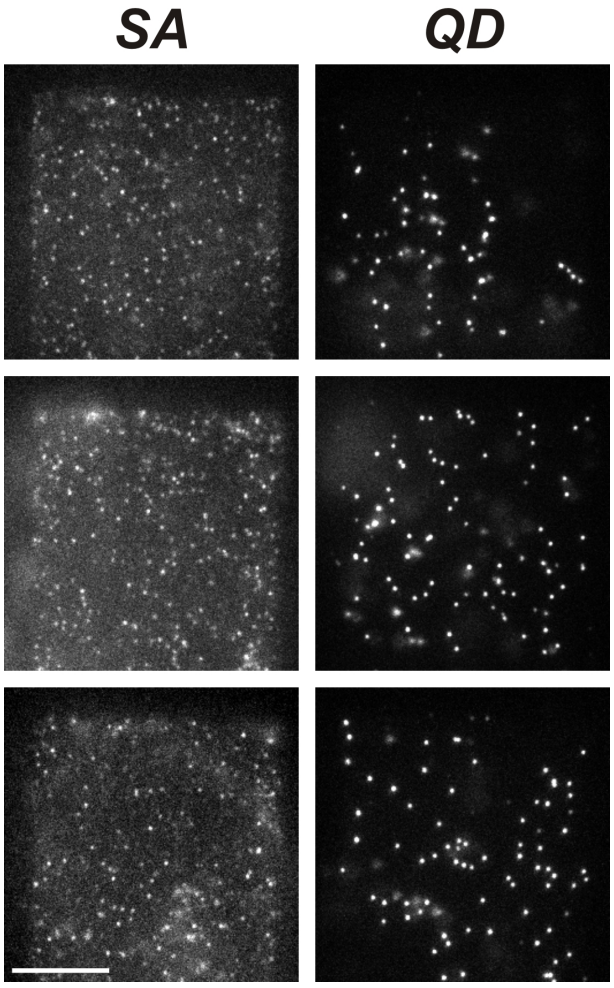

Figure 12.14: Representative images of single SA molecules (left) or SA-coated quantum dots (QDs, right) on the membrane of HMEC-1.
Shown are three representative frames obtained in our measurements with clearly visible signals of single SA molecules and single QDs, respectively. Scale bar = 10 μm

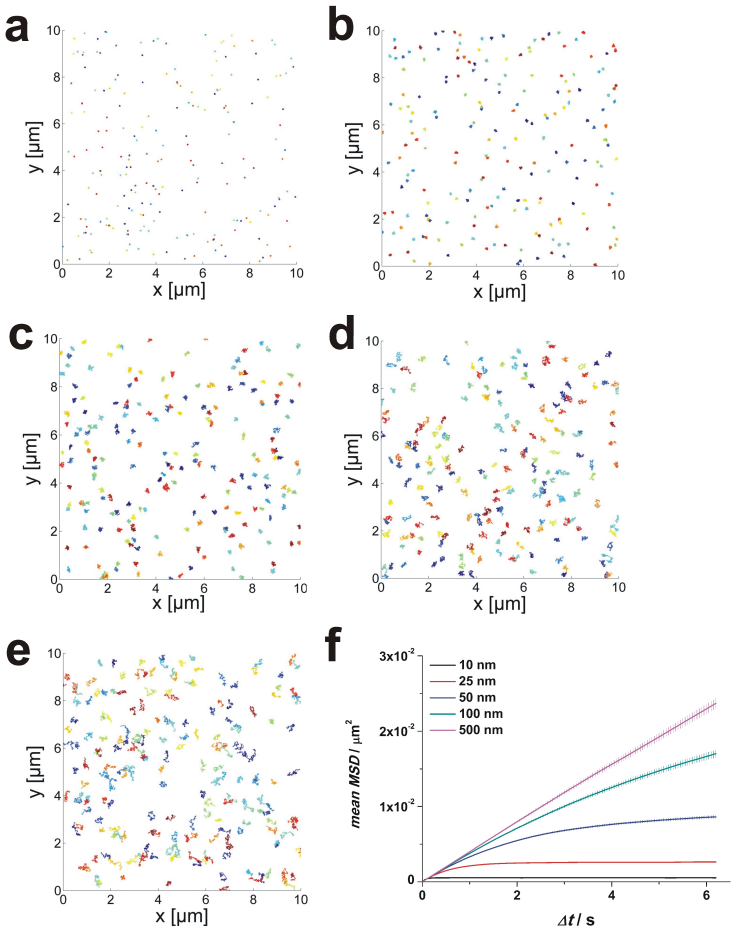

Figure 12.15: Simulation of confined diffusion.
For the simulation of confined diffusion, we slightly modified the approach described in the online documentation of the Matlab class @msdanalyzer that we also used for the MSD analysis of the obtained trajectories.[252]

Briefly, particles were set to a starting position from where they can diffuse freely. However, a restoring force drives them towards their starting position which increases with increasing distance. This approach resembles the situation of interconnected particles in a very basic, but still useful way: Particles inside a network are pushed or pulled back as if they were attached to the equilibrium position. The higher the interconnection, the higher the restoring force. In the simulation, the restoring force is realized by a parabolic potential around the starting position of the particle, exhibiting a certain width. With this, different restoring forces are chosen, corresponding to different interconnection strengths of the network: the more narrow the potential is, the higher is the restoring force at a certain distance, corresponding to stronger interconnection. The other important parameters of the simulation were set to reasonable values, e.g. a temperature of 20°C, a frame time of 50 ms, a dimensionality of 2, and a diffusion constant of $10 \cdot^{-3}$ μ^2/s. The width of the potential was varied between 10 and 500 nm. The results

depicted above show clearly that a narrower potential, i.e. stronger interconnection, leads to increased confinement (trajectories shown in a)-e) with potentials of 10/25/50/100/500 nm width, respectively). Consistently, the MSD curves are stronger bent (f). Note that the error bars of the MSD curves are very small because the particles move according to a theoretical model. The only reason that there is an error at all is the use of random numbers to simulate particles undergoing Brownian motion. Error bars are given as the weighted standard deviation divided by the square root of the number of degrees of freedom. Coloring in a)-e) is used only for easier discrimination of single trajectories.

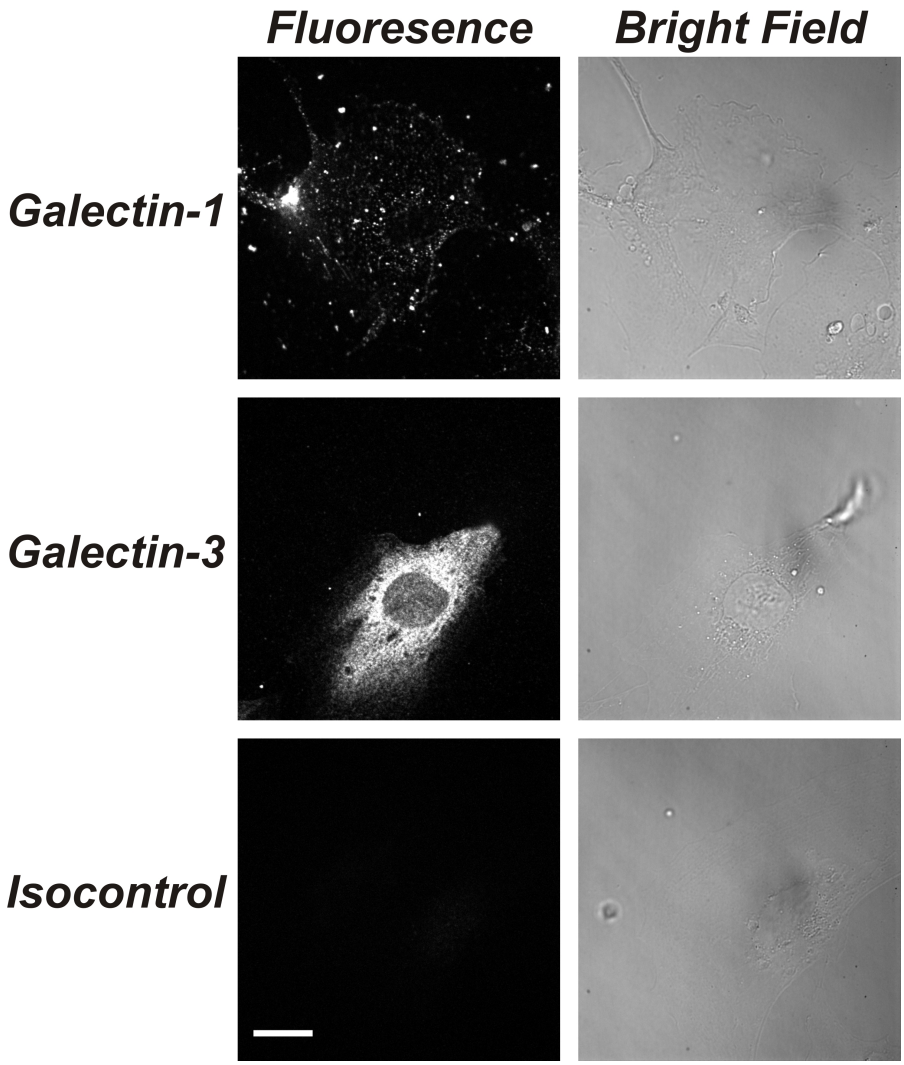

Figure 12.16: Immunostaining confirms the expression of galectin-1 and -3 on cultured HMEC-1
As it can be clearly seen from the fluorescent images, a strong signal for galectin-1 and -3 is obtained whereas the isocontrol does not show any fluorescence. Contrast settings are equal for all three fluorescent images, scale bar = 20 μm

Photocontrol of E. Coli Adhesion to Human Cells

ESI to "Switching first contact: photocontrol of E. coli adhesion to human cells" by Leonhard Möckl, Anne Müller, Christoph Bräuchle, and Thisbe K. Lindhorst; *ChemComm* 2015

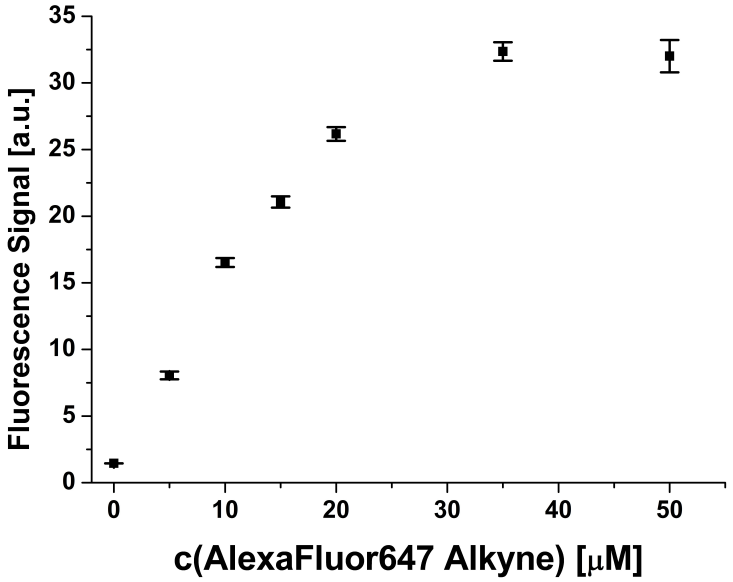

Figure 12.17: Required alkyne concentration for saturation.
HMEC-1 were cultivated in presence of 50 μM Ac_4ManNAz for two days as described. Instead of an azobenzene derivate, a fluorescent alkyne was coupled at various concentrations to the incorporated azido groups under identical conditions. The membrane fluorescence was determined. It can be clearly seen that at 35 μM a plateau is reached. Hence, the concentration of 200 μM azobenzene derivate that we used in our experiment ensures that all available azido groups are tagged.

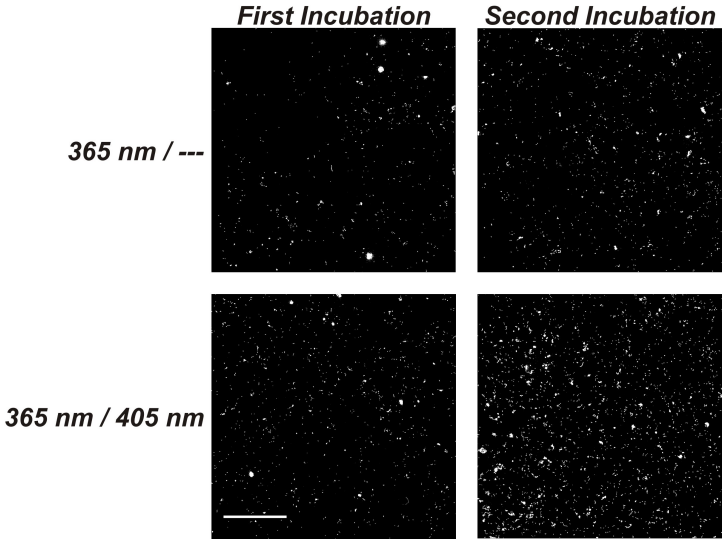

Figure 12.18: Adhesion of *E. coli* to *Z* and *E*-configured 5
Two sets of HMEC-1 with sialic acids modified with *Z*-azobenzene mannoside were incubated with bacteria (after irradiation with light of 365) (left column). Next, only one set of HMEC-1 was irradiated with light of 405 nm to effect $Z \rightarrow E$ isomerisation. Then, both sets of HMEC were incubated again with bacteria. By high-resolution fluorescence microscopy it can be seen that the number of adhered bacteria increases strongly for HMEC-1 in the *E*-state (bottom right), whereas it does not change significantly when HMEC-1 were not irradiated with 405 nm light (leaving **5** in the *Z*-state) (top right). Scale bar = 250 μm.

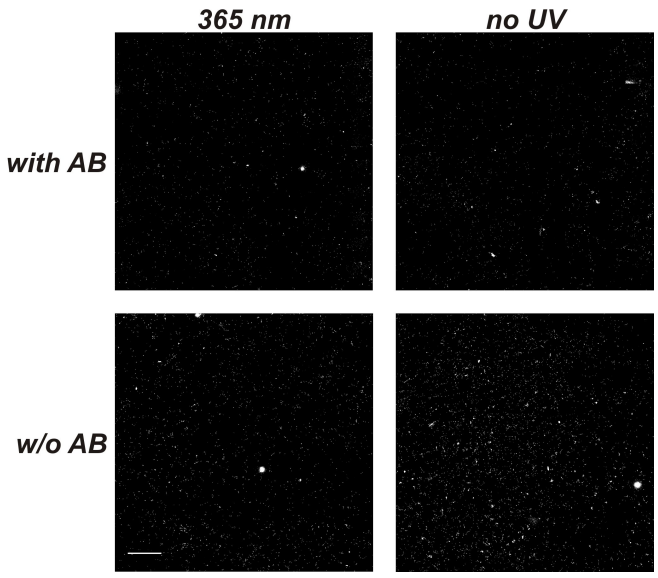

Figure 12.19: Adhesion of *E. coli* to *Z* and *E*-configured AB
HMEC-1 were modified at sialic acids with AB or remained untreated as control. Next, one set of cells was irradiated with 365 nm light in order to switch the azobenzenes to the *Z*-state. The other set was not irradiated. After incubation with bacteria, fluorescence images were obtained. It can be clearly seen that the presence of **7** in both *Z*- and *E*-configuration reduced adhesion of bacteria. Scale bar = 250 μm.

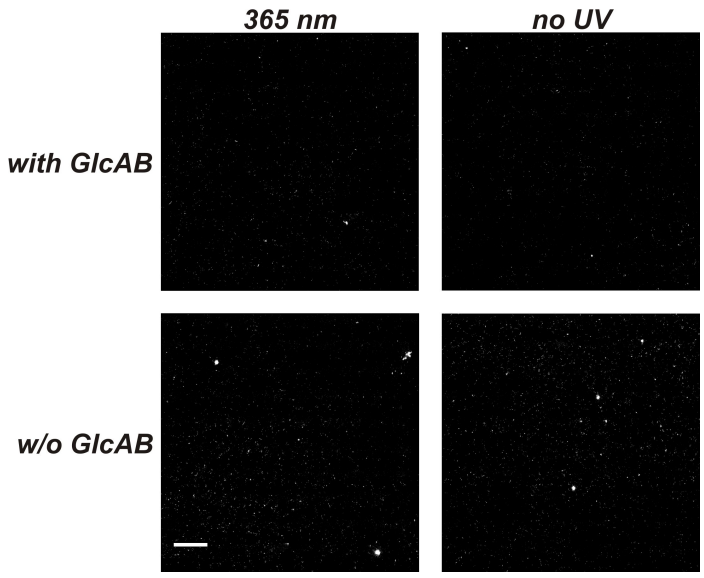

Figure 12.20: Adhesion of *E. coli* to *Z* and *E*-configured 6
HMEC-1 were modified at sialic acids with **6** or remained untreated as control. Next, one set of cells was irradiated with 365 nm light in order to switch the azobenzenes to the Z-state. The other set was not irradiated. After incubation with bacteria, fluorescence images were obtained. As for **7**, adhesion of bacteria was decreased. Therefore, the glucose modification of **6** cannot serve as ligand. Also, unspecific interactions are not increased. Scale bar = 250 μm.

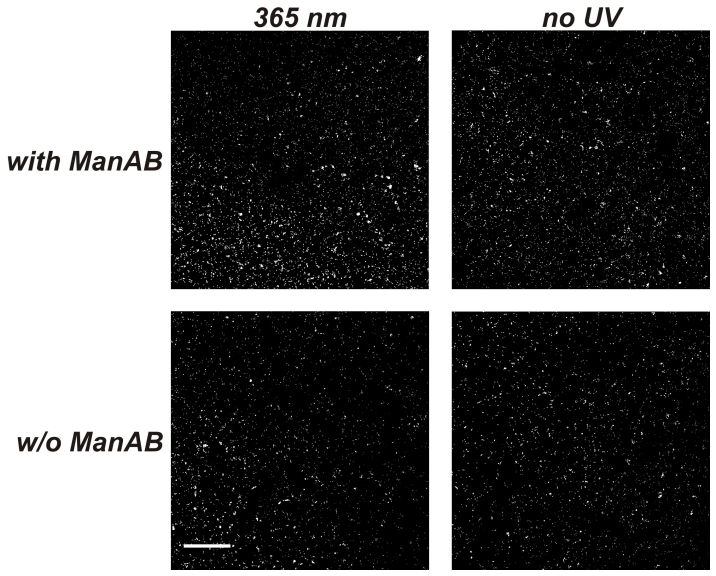

Figure 12.21: Adhesion of *E. coli* to *Z* and *E*-configured 5 linked to mucin-type proteins. HMEC were modified with **5** at mucin-type proteins or remained untreated as control. In comparison to labelling of sialic acids, this leads to attachment of **5** deeper within the glycan tree. Next, one set of cells was irradiated with 365 nm light in order to switch the azobenzenes to the Z-state. The other set was not irradiated. After incubation with bacteria, fluorescence images were obtained. It can be seen that the additional mannose groups increased adhesion in comparison to cells not treated with **5**, however, switching had no effect. This is reasonable since the change in orientation upon switching is small compared to the distance the azobenzene-mannoside is away from the incoming bacteria in this case. Scale bar = 250 μm.

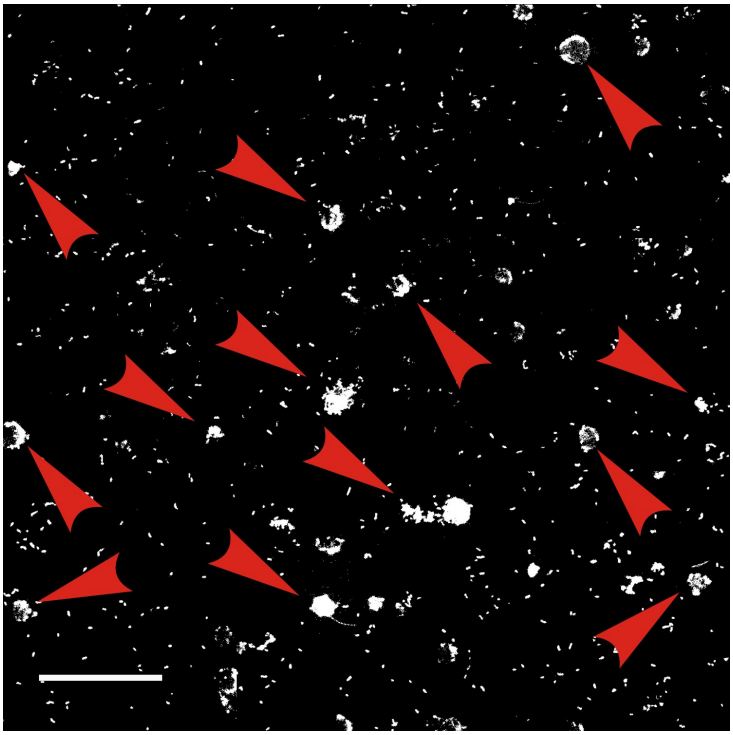

Figure 12.22: Clumps of *E. coli* under flow conditions.
With increasing time of flow, bacteria more and more adhere to already adhered bacteria and not to HMEC-1, forming clumps (some of them indicated by red arrow heads). Scale bar = 250 μm.

Flow Changes the Properties of E. coli Adhesion Inhibitors

ESI to "En route from artificial to natural: Evaluation of inhibitors of mannose-specific adhesion of *E. coli* under flow" by Leonhard Möckl, Claudia Fessele, Christoph Bräuchle, and Thisbe K. Lindhorst; under revision at *Biochimica Biophysica Acta (BBA)*

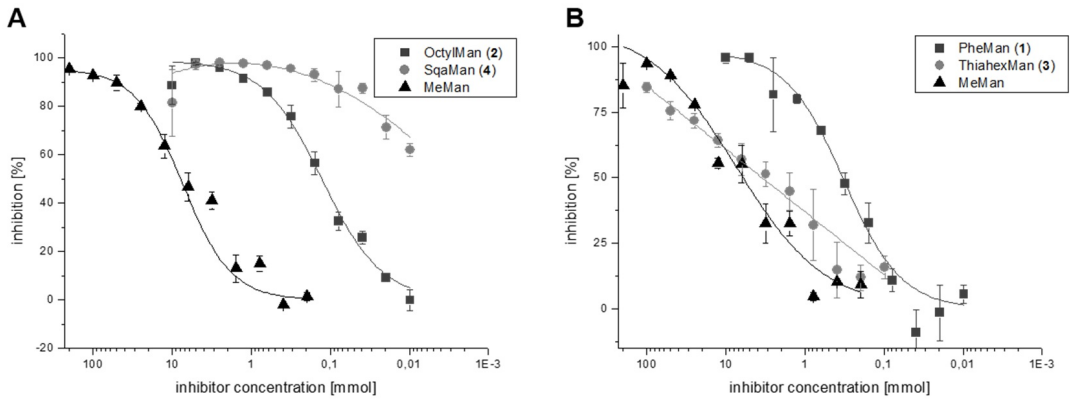

Figure 12.23: **Inhibition of bacterial adhesion to mannan surfaces under static conditions.** Solutions of the respective glycosides were prepared and serial dilutions were added to mannan-coated microtiter plate wells. The prepared bacterial solution (OD600 0.4) was added and the plate incubated for 1 h at 37°C and 100 rpm. The plates were washed with PBS buffer and then the wells were filled with PBS for the fluorescence read out (485 nm/535 nm). (A) Inhibition tested with mannoside **2** and **4**. (B) Inhibition tested with mannoside **1** and **3**. The depicted binding curves are representative examples from several (>3x) independent experiments. Error bars result from duplicate values on one plate.

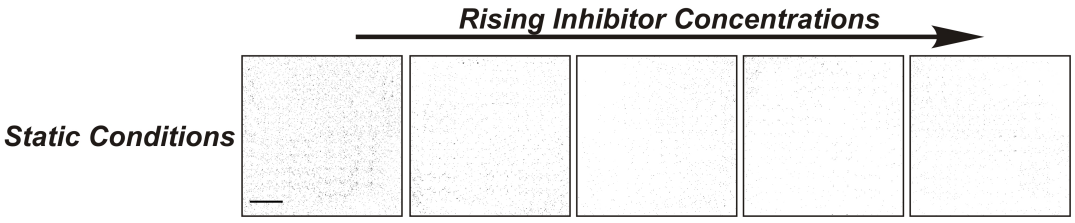

Figure 12.24: Bacterial adhesion to HMEC-1 under static conditions using SAMan as inhibitor.
WThe images clearly show that under static conditions, bacteria can adhere up to high inhibitor concentrations (0 / 0.001 / 0.01 / 0.1 / 1 mM). Contrast is inverted for clarity. Contrast settings are equal for all images. Scale bar = 200 μm.

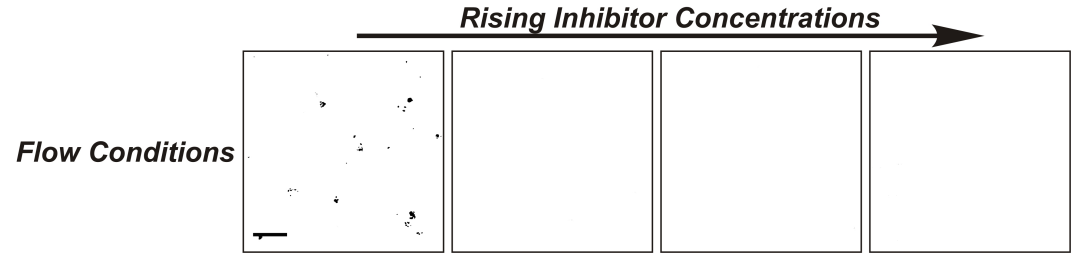

Figure 12.25: Bacterial adhesion to HMEC-1 under flow conditions using SAMan as inhibitor.
Under flow conditions, no adhesion was detected already at low inhibitor concentrations (0 / 0.1 / 1 / 2 mM). Contrast is inverted for clarity. Contrast settings are equal for all of images. Depicted adhesion is after five minutes of bacterial flow. Scale bar = 100 μm.

Uptake of Targeted siRNA into Model Cells and *in vivo*

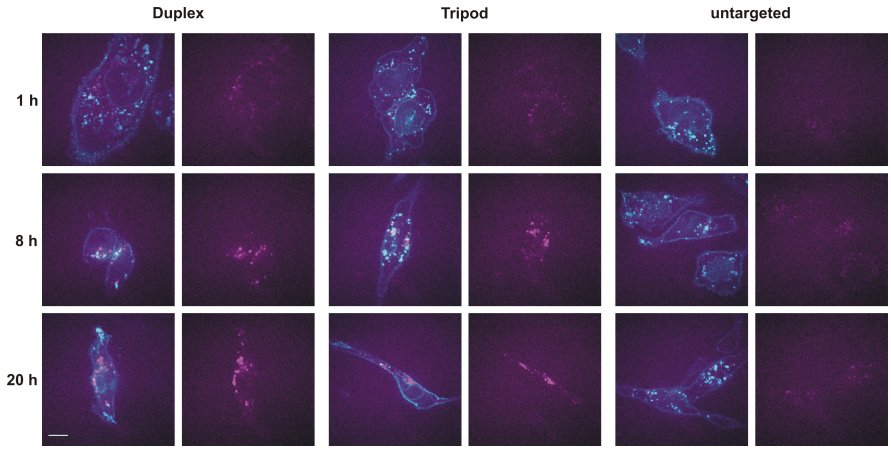

Figure 12.26: Representative fluorescence images showing the uptake of AEA-siRNA duplex, AEA-siRNA tripod, and untargeted siRNA duplex into RBL2H3 cells. newline Scale bar 10 μm

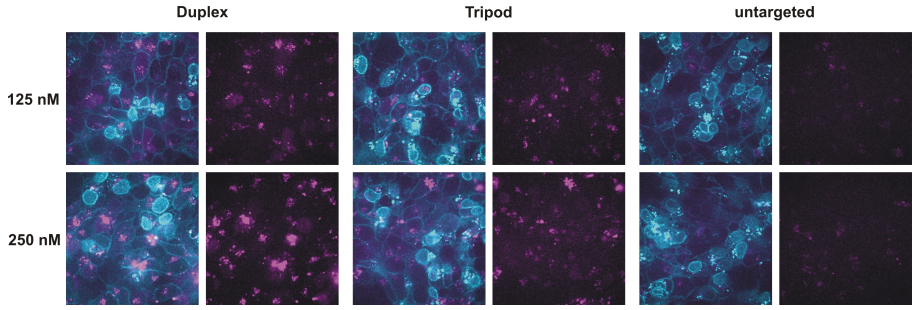

Figure 12.27: Representative fluorescence images showing the uptake of AEA-siRNA duplex, AEA-siRNA tripod, and untargeted siRNA duplex into murine neuroanl stem cells. newline Scale bar 10 μm

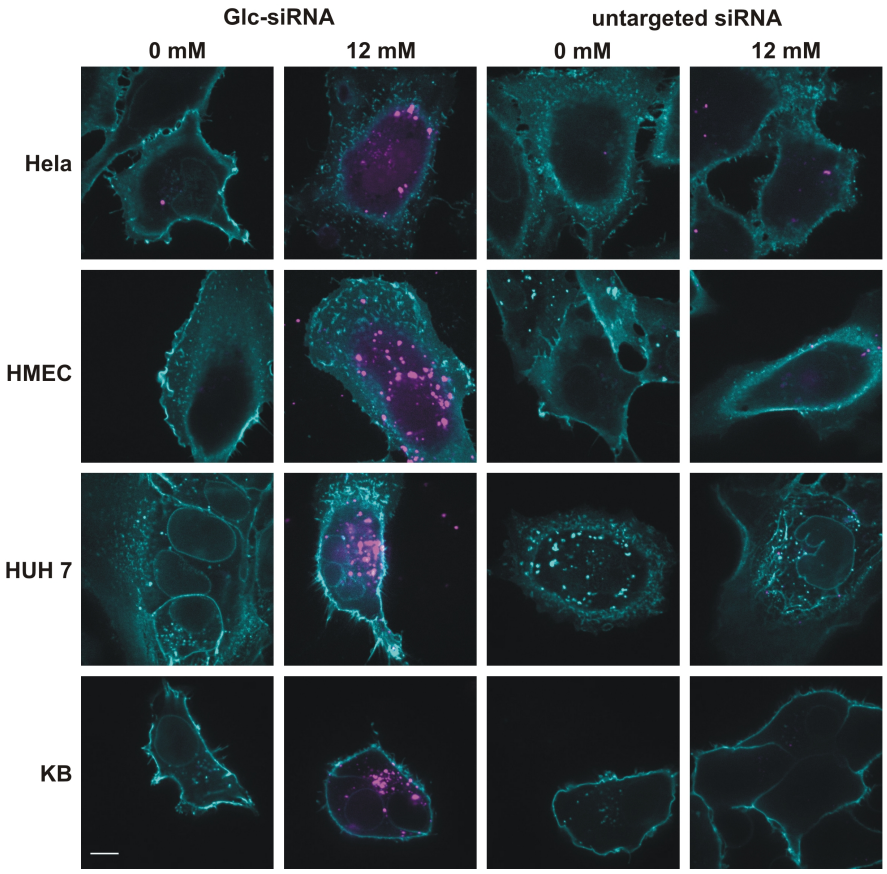

Figure 12.28: Representative fluorescence images showing the uptake of Glc-siRNA into Hela, HMEC, KB, and HUH-7 cells. newline Scale bar 10 μm

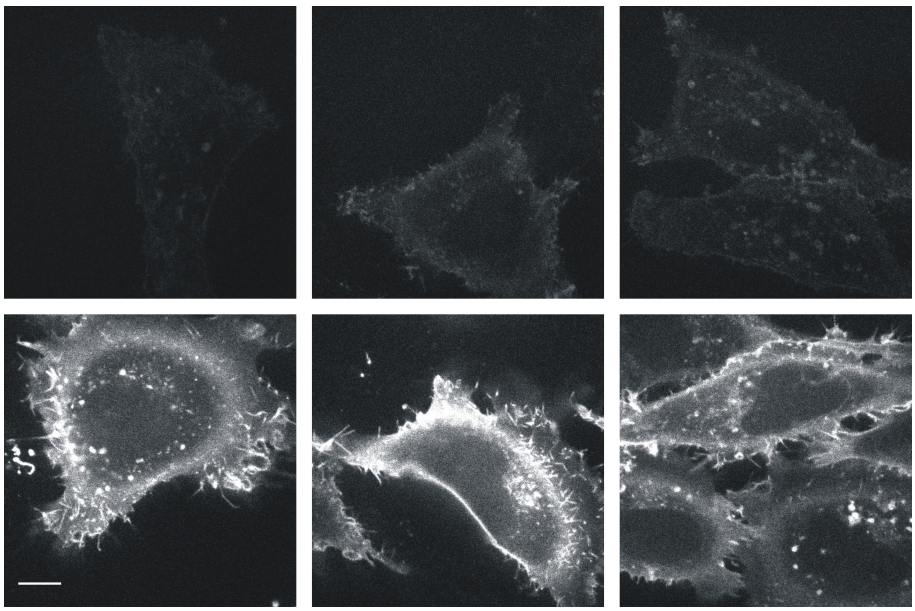

Figure 12.29: Representative fluorescence images showing GLUT1 expression in presence (top) or absence (bottom) of glucose in the medium
Contrast settings are equal for all images.
Scale bar 10 μm

List of Figures

List of Tables

Contributions

Publications

- **12/2015** Artificial Formation and Tuning of Glycoprotein Networks on Live Cell Membranes: A Single-Molecule Tracking Study
  Leonhard Möckl, Thisbe Lindhorst, Christoph Bräuchle, *ChemPhysChem*
- **11/2015** Switching first contact: photocontrol of E. coli adhesion to human cells
  Leonhard Möckl, Anne Müller, Christoph Bräuchle, Thisbe Lindhorst, *ChemComm* **52**, 1254 (2016) - recieved the back cover of the issue
- **9/2015** Microdomain Formation Controls Spatiotemporal Dynamics of Cell-Surface Glycoproteins
  Leonhard Möckl, Andrea Horst, Katharina Kolbe, Thisbe Lindhorst, and Christoph Bräuchle, *ChemBioChem* **16 (14)**, 2023 (2015) - recieved the inside cover of the issue
- **2/2015** Mit Logischer Schärfe und Systhematischer Unbeugsamkeit: Wichard von Moellendorff (1881-1937)
  Leonhard Möckl and Jürgen Evers, *Chemie in Unserer Zeit* **49 (4)**, 236 (2015)
- **1/2015** Two High-Pressure Phases of SiS_2: Missing Links between the Extremes of Only Edge- and Only Corner-Sharing Tetrahedra
  Jürgen Evers, Peter Mayer, Leonhard Möckl, Gilbert Oehlinger, Ralf Köppe, and Hansgeorg Schnöckel, *Inorganic Chemistry* **54 (4)**, 1240 (2015)

- **12/2104** Cell-Penetrating and Neurotargeting Dendritic siRNA Nanostructures
  Korbinian Brunner, Johannes Harder, Tobias Halbach, Julian Willibald, Fabio Spada, Felix Gnerlich, Konstantin Sparrer, Andreas Beil, Leonhard Möckl, Christoph Bräuchle, Karl-Klaus Conzelmann, and Thomas Carell, *Angewandte Chemie* **127 (6)**, 1968 (2015)/*Angewandte Chemie International Edition* **54 (6)**, 1946 (2015)
- **11/2014** Super-resolved Fluorescence Microscopy: Nobel Prize in Chemistry 2014 for Eric Betzig, Stefan Hell, and William E. Moerner
  Leonhard Möckl, Don Lamb, and Christoph Bräuchle, *Angewandte Chemie* **126 (51)**, 14192 (2014)/*Angewandte Chemie International Edition* **53 (51)**, 13972 (2014)
- **12/2012** Der Wittelsbacher und der Hope Diamant
  Jürgen Evers, Leonhard Möckl, and Heinrich Nöth, *Chemie in unserer Zeit* **46 (6)**, 356 (2012)
- **5/2012** Tuning Nanoparticle Uptake: Live-Cell Imaging Reveals Two Distinct Endocytosis Mechanisms Mediated by Natural and Artificial EGFR Targeting Ligand
  Frauke Mickler, Leonhard Möckl, Nadia Ruthardt, Manfred Ogris, Ernst Wagner, and Christoph Bräuchle, *NanoLetters* **12 (7)**, 3417 (2012)

Submitted/In Preparation

- Under revision En route from artificial to natural: Evaluation of inhibitors of mannose-specific adhesion of *E. coli* under flow
  Leonhard Möckl, Claudia Fessele, Christoph Bräuchle, Thisbe K. Lindhorst; under revision at *Biochimica et Biophysica Acta (BBA)*
- In Preparation Unraveling the action mechanism of antidepressants
  Leonhard Möckl, Christoph Bräuchle, Thomas Kirmeier *et al.*; to be submitted to *PlosONE*

- In Preparation Azido-pentoses, a novel tool to label the cell wall of *Mycobacterium tuberculosis*
  Katharina Kolbe, Leonhard Möckl, Victoria Sohst, Regina Engel, Christoph Bräuchle, Stefan Niemann, Otto Holst, Thisbe K. Lindhorst, Norbert Reiling; to be submitted to *Angewandte Chemie*
- In Preparation The endothelial glycocalyx protects cells from nanoparticle entry
  Leonhard Möckl, Stefanie Hirn, Adriano de Andrade Torrano, Christoph Bräuchle, and Fritz Krombach

Conference Contributions

- **2015** Poster at the Engineering Life conference, Leipzig
- **2015** Selected talk at the EuroCarb XVIII, Moscow
- **2014** Poster at the iPoLS conference, LMU Munich
- **2014** Poster at the Paris Workshop on Membranes
- **2014** Poster at the Nanosystems Initiative Munich conference
- **2013** Poster at the CeNS conference, Venice International University
- **2012** Poster at the CeNS conference, Venice International University

Acknowledgements

Diese Arbeit wäre nicht ohne die Unterstützung einer Reihe von hilfsbereiten Menschen entstanden. Ihnen gilt mein tiefer Dank.

An erster Stelle möchte ich meinem Betreuer, Herrn Professor Bräuchle, danken. Er setzte sehr früh großes Vertrauen in mich und hatte zu jeder Zeit ein offenes Ohr, sowohl für fachliche als auch für persönliche Fragen. Darüber hinaus gestand er mir große Freiräume zu und ließ mich immer neugierig sein. Wenn ich mich aber verzettelte, griff er behutsam ein und brachte mich wieder auf die richtige Spur. Ich habe mich stets hervorragend betreut und aufgehoben gefühlt.

Der engagierten und begeisternden Darstellung der Zuckerchemie durch meine zweite Betreuerin, Frau Professorin Lindhorst, verdanke ich das Thema meiner Dissertation. Obwohl es manchmal schwerer als gedacht war, bin ich sehr froh, dass sie mir diese Welt eröffnet hat. Auch sie war jederzeit für mich da und ließ mich, obwohl räumlich weit entfernt, nie allein und baute mich auf, wenn die Motivation manchmal zwischen gescheiterten Experimenten verloren zu gehen drohte.

Bei Herrn Professor Evers legte ich mein Fortgeschrittenenparktikum in Anorganischer Chemie ab. Es bereitete mir größte Freude, unter seiner kundigen Anleitung an Fragen der Festkörperchemie und der Geschichte der Chemie zu arbeiten. Sein väterlicher Rat begleitete mich durch alle kleinen und großen Tiefen der Promotion. Ohne ihn wäre diese Zeit nicht die gleiche gewesen.

Frau Horst trägt eine gehörige "Mitschuld" an meinem Weg in die Zuckerchemie. Dafür möchte ich danken - und dafür, dass sie mir durch ihre einfühsahme Art und ihr riesiges Fachwissen dabei half, in diesem Feld auch Fuß zu fassen.

Thomas Kirmeier möchte ich sehr herzlich für die Möglichkeit danken, an seinem faszinierenden Projekt an der Schnittstelle zwischen Chemie, Medizin und Neurowissenschaften mitzuarbeiten.

Dem "amicus specialis" Andreas sei für das gemeinsame Leeren unzähliger Flaschen und Teller gedankt, für die Diskussionen über Gott und die Welt währenddessen, für eine großartige Kooperation über siRNA-Uptake und schonmal für unser nächstes Forschungsprojekt, was es auch immer sein mag!

Meinen Kooperationspartnern Hanna und Adriano; Professor Fritz Krombach und Dr. Stephanie Hirn; Professor Thomas Carell und seinen Doktoranden/-innen Nada Raddaoui, Korbinian Brunner und Johannes Harder; sowie Katharina, Anne und Claudia, Doktorandinnen von Frau Professorin Lindhorst, möchte ich für die herzliche und effiziente Zusammenarbeit danken. Es ist gewiss nicht selbstverständlich, dass gemeinsames Experimentieren und Schreiben von Publikationen so reibungslos und entspannt vonstatten geht.

Allen Mitarbeitern des Arbeitskreises Bräuchle und Lamb sei für die motivierende Arbeitsatmosphäre gedankt, insbesondere meiner Bachelorbetreuerin Frauke und meinen Bürkollegen/-innen Meli, Ellen, Stephan und Adriano.

Ich bin Hanna, Andreas und Gerald für das Korrekturlesen meiner Disseration sehr zu Dank verpflichtet - hoffentlich wirkte dieser Kontakt mit Glycobiologie nicht zu abschreckend;)

Einige bleiben hier unerwähnt, weil ich ihnen mehr schulde, als ich an dieser Stelle schreiben möchte.